



UNIVERSIDADE DE SÃO PAULO  
INSTITUTO DE ASTRONOMIA GEOFÍSICA E CIÊNCIAS ATMOSFÉRICAS  
DEPARTAMENTO DE GEOFÍSICA

**Paleomagnetism, magnetic stratigraphy and sedimentology  
of the Ediacaran Avellaneda Formation (Argentina)**

Jhon Willy Lopes Afonso

Advisor: Prof. Dr. Ricardo Ivan Ferreira Da Trindade

São Paulo

2022

Jhon Willy Lopes Afonso

“Versão Corrigida. O original encontra-se disponível na Unidade.”

**Paleomagnetism, magnetic stratigraphy and sedimentology  
of the Ediacaran Avellaneda Formation (Argentina)**

Doctoral thesis presented to the Instituto de Astronomia Geofísica e Ciências Atmosféricas da Universidade of São Paulo (IAG-USP), to obtain the title of Doctor of Geophysics.

Advisor: Prof. Dr. Ricardo I. F. Da Trindade

São Paulo

2022

Dedicado à minha família

## **Agradecimentos**

Ao CNPq e CAPES pela bolsa de fomento durante o desenvolvimento da tese de doutorado.

Agradeço ao Prof. Ricardo Trindade por sua orientação e incentivo ao longo desses anos. Muito obrigado também pela oportunidade de participar de discussões e debater ideias dentro das geociências. Foi uma honra, Ricardo!

Aos professores do IAG/USP, em especial a Prof. Leila Soares para quem deixo minha imensa gratidão aos seus puxões de orelha e conselhos.

Aos amigos paleomágicos do Laboratório de Paleomagnetismo (USPmag) que tornaram o processo do doutorado um tanto mais leve. Muito obrigado Janine, Dani, Plínio, Will, Grazi, Paul, Gigio, Thiago, Caio, Karine, Lívia, Gelson e Ualisson (cuidem bem da sala), e tantos outros que graças ao USPmag tive a felicidade de conhecer.

Sou imensamente grato ao Prof. Augusto Rapalini por me apresentar a Formação Avellaneda, tornando essa tese realidade. Ao amigo Pablo Franceschini com quem dividi longas horas de trabalho no laboratório e discussões. Agradecimentos especiais vão para María Julia Arrouy, Lucía Gómez-Peral e Daniel Poiré por suas sugestões, críticas e revisões realizadas nos manuscritos. Também sou grato a companhia Cementos Avellaneda S/A por ceder gentilmente as amostras utilizadas aqui.

Minha gratidão aos geólogos Msc. Luciano Castro (CPRM-PA), Dr. Pedro Augusto (GSED-UFPA) e o Dr. Sergio Caetano Filho (IGc-USP) por suas valiosas colaborações com o desenvolvido desta tese.

Um agradecimento especial para Kamilla Borges Amorim, namorada e companheira de uma longa e tortuosa aventura. Kamilla, sem você isso não seria possível. Obrigado.

Por fim, gostaria de agradecer aos meus pais, Selma e Jorge, por todo esforço empregado para realização de um sonho. Obrigado pelo incentivo e me ensinarem o valor de estudar. Também agradeço minhas irmãs, Jenny e Jully, fundamentais na continuidade de minha carreira. Amo vocês coisas lindas.

## Resumo

O Período Ediacarano registrou notáveis perturbações em quase todos os elementos do Sistema Terra. Este intervalo é pontuado por largas oscilações nas razões isotópicas de  $\delta^{13}\text{C}$ . No Ediacarano os oceanos tornaram-se progressivamente oxigenados e capazes de abrigar organismos macroscópicos complexos. O aparecimento da vida macroscópica foi acompanhado por expressivas mudanças na configuração paleogeográfica dos continentes. O comportamento do campo magnético terrestre durante o Ediacarano é controverso. Estudos recentes sugerem uma baixa intensidade e uma frequência de alta taxa de reversão do campo geomagnético. Acessar o registro do Ediacarano é fundamental para compreender estes eventos e suas consequências na modernização do planeta. A cobertura sedimentar do Cráton do Río de la Plata (RPC) representa uma oportunidade de acessar informações significativas sobre este momento crítico da história da Terra. Esta tese investiga as rochas sedimentares da Formação Avellaneda (Grupo La Providencia) na porção noroeste do Sistema Tandilia (Argentina). A Formação Avellaneda por seu posicionamento estratigráfico entre 580-560 Ma é uma janela de observação importante para uma fatia de tempo de baixo nível de conhecimento. O foco da tese é fornecer de informações sobre as condições paleodeposicionais, adquirir novos dados de isótopos de carbono e combinar com estratigrafia magnética além de fornecer um contexto paleogeográfico da Formação Avellaneda. Para fazer isso foram investigados três furos de sondagem de espessura variável entre 11 e 20 metros. O estudo de microfácies auxiliada por novos dados de isótopos de carbono permitiu refinar o cenário deposicional da Formação Avellaneda, indicando um ambiente submaré/intermaré a intermaré/supramaré. Pela primeira vez foram relatados pseudomorfos de sulfatos de cálcio além de texturas evaporíticas, indicando alguma restrição na bacia ou uma zona de alta evaporação. Os dados de  $\delta^{13}\text{C}$  revelam uma excursão negativa localizada próximo ao topo da Formação Avellaneda. Esta excursão é de natureza primária e interpretada como uma expressão da excursão isotópica Shuram. Apesar de não atingir valores negativos extremos, esta excursão isotópica é consistente se comparada com outras seções coevas. A presença da excursão Shuram na Formação Avellaneda implica em uma idade para sua deposição em torno de ~570 Ma. As rochas da Formação Avellaneda forneceram direções magnéticas estáveis, portadas por magnetita e hematita, que são consistentes nos três furos estudados. Esses dados, junto com os registros de outras unidades fora do RPC, permitiram construir um arcabouço magneto-estratigráfico para o Ediacarano médio, englobando todo o período de ocorrência da excursão Shuram. Os novos dados paleomagnéticos contribuíram para definir

uma curva de deriva polar aparente (APWP) mais robusta para o cráton Río de la Plata (RPC) de 600 a 560 Ma. O polo paleomagnético não se assemelha a nenhum outro polo previamente determinado para o RPC fornecendo, portanto, um novo vínculo paleogeográfico para um dos blocos continentais mais importantes do Gondwana Ocidental. De acordo com os novos dados, durante o intervalo de 580-560 Ma, o RPC migrou para paleolatitudes moderadamente altas (entre cerca de 50° e 42°S). Estas latitudes estão próximas daquelas esperadas para a ocorrência de evaporitos. Além disso, os dados paleomagnéticos sugerem uma grande rotação no sentido anti-horário para o RPC, mas pouco deslocamento paleolatitudinal entre 580 e 570 Ma. Por fim, os dados obtidos na Formação Avellaneda fornecem novas informações sobre o paleoambiente, geoquímica de isótopos de carbono e oxigênio, estratigrafia magnética e paleogeográfica que podem contribuir na compreensão dos eventos ocorridos no Ediacarano.

## Abstract

The Ediacaran Period records remarkable perturbations in almost all components of the Earth's system. This interval is punctuated by large oscillations in  $\delta^{13}\text{C}$  signal. During Ediacaran oceans became progressively oxygenated sheltering macroscopic complex life. The appearance of macroscopic animals was accompanied by sudden changes in the configuration of the continents. The behavior of the Earth's magnetic field during the Ediacaran is controversial, appears to be characterized by low intensity and high reversal frequencies. Accessing the Ediacaran record is critical to understand these events and their consequences for the modernization of the planet. The sedimentary cover of the Río de la Plata craton (RPC) represents an opportunity to access significant information about this critical time on Earth's history. This thesis investigates the sedimentary succession of the Avellaneda Formation (La Providencia Group), preserved in the northwestern portion of the Tandilia System (Argentina). The Avellaneda Formation, due to its stratigraphic position between 580-560 Ma, is an important window for access a poor-knowledge time slice. This thesis provides integrated information about the sedimentary settings, carbon isotopes, magnetic stratigraphy and paleogeography of the Avellaneda Formation. For this, three drilling core of varying thickness between 11 and 20 meters were investigated. Microfacies analysis combined with new carbon isotopes data were used to refine its depositional setting, indicating a subtidal/intertidal to intertidal/supratidal carbonate-dominated depositional environment. Pseudomorphs after Ca-sulfate and evaporite textures are reported for the first time in this unit and suggest some restriction in the basin or a high evaporative zone. The  $\delta^{13}\text{C}$  isotopes reveal a negative excursion located near the top of the Avellaneda Formation. This excursion is primary and has been interpreted as an expression of the Shuram isotope excursion. Although not reaching extreme negative values, the Avellaneda record is consistent with other coeval successions worldwide. The presence of the Shuram excursion in the Avellaneda Formation implies an age of deposition around 570 Ma. The Avellaneda formation rocks provided stable magnetic directions carried by magnetite and hematite that are consistent for the three drill cores studied. Together with other records worldwide, it was possible to build a magnetic stratigraphic framework for the mid-Ediacaran period encompassing the whole Shuram CIE. The new paleomagnetic data contributed to define a more robust apparent polar wander path (APWP) for the Río de la Plata craton (RPC) from 600 to 560 Ma. The paleomagnetic pole does not resemble other any previously determined poles from the RPC, therefore providing a critical new constraint to an important block of the Western Gondwana. According to the new

data, the RPC drifts towards moderately high paleolatitudes (between around 50° and 42°S) for the interval 580-560 Ma. These latitudes are close to those expected for the occurrence of evaporites. In addition, paleomagnetic data suggest a large counterclockwise rotation for the RPC, but minor palaeolatitudinal displacement between 580 and 570 Ma. Lastly, the Avellaneda Formation provides new information about depositional setting, carbon and oxygen isotope geochemistry, new paleomagnetic and magnetostratigraphic data that can help to understand the events that took place in the Ediacaran.

## SUMMARY

---

Dedicatory	iii
Acknowledgements	iv
Resume	v
Abstract	vii
<b>CHAPTER I</b>	<b>10</b>
1.1 Motivation	
1.2. Main goals	
1.3. Organization of this Thesis	
<b><u>CHAPTER II</u></b>	<b>12</b>
2.1. The Ediacaran Period, an overview	
2.2. Ediacaran environments	
2.3. Carbon isotopes excursions	
2.4. The Earth's magnetic field during the Ediacaran	
<b><u>CHAPTER III</u></b>	<b>22</b>
Microfacies of the Avellaneda Formation (Argentina), a tidal flat facing the Shuram Excursion	
<b><u>CHAPTER IV</u></b>	<b>66</b>
Paleomagnetism of the Ediacaran Avellaneda Formation (Argentina), Part I: Paleogeography of the Río de la Plata craton at the dawn of Gondwana	
<b><u>CHAPTER V</u></b>	<b>109</b>
Paleomagnetism of the Ediacaran Avellaneda Formation (Argentina), Part II: Magnetic and chemical stratigraphy constraints on the onset of the Shuram carbon excursion	
<b><u>CHAPTER VI</u></b>	<b>141</b>
Conclusions and perspectives	
<b>REFERENCES</b>	<b>146</b>
Supplementary material 1	170

# **CHAPTER I**

## 1.1 Motivation

The Ediacaran Period, 635 to 539 million years ago, represents a critical period in Earth's history. It began immediately after the extreme ice-ages (Snowball Earth events) that marked the Cryogenian period and amid several perturbations to the carbon cycle. These perturbations have been documented worldwide and are characterized by large  $\delta^{13}\text{C}$  isotope excursions (CIEs) in marine carbonate (Och and Shields-Zhou, 2012). Due to their global nature, they are commonly used to establish regional to global stratigraphic correlations (Xiao and Narbonne, 2020; Rooney et al., 2020). These times have also probably witnessed rapid changes in continental configurations related to the Gondwana paleocontinent formation (Robert et al., 2017; Antonio et al., 2021). The geomagnetic field also showed an anomalous behavior during the Ediacaran with an anomalously high reversal frequency in the late Ediacaran (Shatsillo et al., 2015; Bazhenov et al., 2016; Meert et al., 2016; Bono et al., 2019). These radical changes in likely impacted the biosphere, with Ediacaran strata marking the transition between an anoxic, microscopic dominated world to a predominantly oxic ocean containing a diversified macroscopic life (Xiao and Narbonne, 2020).

By their multiples and irreversible events, the Ediacaran Period has attracted the attention of several reserachers. The debate is centred on the causes, timing and possible interconnections of the changes registered during the Ediacaran. Connections between biological and environments changes are speculated, but Ediacaran succession still need detailed information about their sedimentological, biological and geochemical traits. We also must know better how feedbacks between life and the environment operate. The lack of reliable chronostratigraphic hallmarks impose a barrier to unraveling causal relationships. The palaeogeographic configuration during Ediacaran is also uncertain and open to debate. It is likely that changes in paleogeography may have provoked modifications in seawater chemistry and affected directly or not the biological evolution. A consistent reconstruction of the global palaeogeography and the local environments is therefore crucial to check the distribution of macroscopic organisms and the influence of oscillating redox conditions at the dawn of animal life (Bowyer et al., 2017).

Amidst the large cartons that make up the Gondwana paleocontinent, the Río de la Plata craton (RPC) preserves part of the main Ediacaran events in its sedimentary cover (Rapalini et al., 2013; Arrouy et al., 2016; Gómez-Peral, 2019). The present study focuses on the Avellaneda Formation. This unit is positioned just after the Gaskiers glaciation (580 Ma) and precedes the appearance of the first macroscopic life (White Sea fauna, Droser and

Gehling 2015), encompassing at least in part the period of the largest carbon isotope excursion ever recorded, the Shuram CIE. Therefore, the Avellaneda Formation offers an opportunity to investigate a critical interval within the Ediacaran Period.

## **1.2. Main goals**

This thesis is dedicated to the study of the sedimentology, paleomagnetism, and magnetic and chemical stratigraphy of the Avellaneda Formation (Argentina). This unit represents a window into the mid-Ediacaran Period. The main goals of the work are:

(i) Refine the description of sedimentary facies and depositional settings of the Avellaneda Formation in order to reconstruct its depositional history with accuracy, providing the basis for a local and global perspective on the Ediacaran sedimentary record;

(ii) Obtain new paleomagnetic data in the Avellaneda Formation to better constrain the drift of Gondwana through the Ediacaran and improve global paleogeographic reconstructions for this time period;

(iii) Test the effectiveness of magnetostratigraphic studies in the Ediacaran in addition to the often used carbon isotopes records, with the aim of producing a high resolution framework for local and global correlations.

## **1.3. Organization of this Thesis**

The results obtained in this thesis are presented in three manuscripts (Chapter 3 to 5), all of them submitted for publication in international journals. Before presenting these chapters, a synthesis of the Ediacaran period is present in Chapter 2.

Chapter 3 presents the manuscript entitled “Microfacies of the Avellaneda Formation (Argentina), an Ediacaran tidal flat recording the onset of the Shuram Excursion” submitted to *The Depositional Record*. This chapter provides a detailed microfiches investigation combining petrography, electron microscopy and cathodoluminescence observations, geochemistry and carbon-oxygen stable isotopes, and improves the understanding about the depositional setting of the Avellaneda Formation. Furthermore, this study also provides new carbon isotope data that help in constraining the spatio-temporal record of the Shuram anomaly.

Chapter 4 presents the manuscript entitled “Paleomagnetism of the Ediacaran Avellaneda Formation (Argentina), Part I: Palaeogeography of the Río de la Plata craton at the dawn of Gondwana” submitted to Precambrian Research. This paper provides new paleomagnetic information for the mid to late Ediacaran in the Río de la Plata craton. With these new data, the apparent polar wander path of the Río de La Plata cartoon is refined and its Ediacaran segment is now almost almost complete. Furthermore, this study also suggests a significant motion of the Rio de La Plata craton, that appears to also occurs in other cratonic blocks worldwide.

Chapter 5 explores the potential of magnetostratigraphy as a tool to establish high-resolution correlation among Ediacaran strata worldwide. The corresponding manuscript is entitled “Paleomagnetism of the Ediacaran Avellaneda Formation (Argentina), Part II: Magnetic and chemical stratigraphy constrains on the onset of the Shuran carbon excursion” also submitted to Precambrian Research as a companion paper to Chapter 4. This chapter proposes that the polarity magnetic pattern recorded in the Avellaneda Formation can be used to track the beginning of the globally synchronous Shuram CIE. Together with the record of other successions worldwide that present both carbon isotopes and magnetic stratigraphy, it provides a magnetic stratigraphy framework for the entire Shuram excursion.

To conclude, Chapter 6 summarizes results and discussions developed in the previous chapters, the related problems that remain open and presents some perspective for future investigations of the Avellaneda Formation and the Ediacaran period as a whole.

## **CHAPTER II**

### **2.1. The Ediacaran Period, an overview**

The Ediacaran Period encompasses the latest of the three periods of the Neoproterozoic Era, extending from approximately 635 million to 541 million years ago (Knoll et al., 2006). It comprises the longest duration among all stratigraphically defined geological periods (Xiao and Narbonne, 2020). The Ediacaran represents a critical transition in Earth's history, marking the transition between the Proterozoic and the Phanerozoic, and as such shares attributes of both eons. The period witnessed several environmental changes and evolutionary innovations that transformed climate, oceans, the atmosphere and the biosphere (Xiao and Narbonne, 2020). These modifications are archived in several sedimentary successions, and their sedimentary record includes glaciogenic intervals, carbon isotope excursions, a stepwise transition from anoxic to oxic oceans besides the paleontological record of the rise of the first large-scale life and the advent of burrowing and of biomineralizing metazoans. These times have also probably witnessed rapid changes in continental configurations related to the Gondwana paleocontinent formation and the establishment of the modern plate tectonics regime that prevails until the present (Hamilton 2011; Cordani et al., 2020; Palin et al., 2020). Inside the planet, the molten core probably began to solidify during the Ediacaran (~565 Ma) marking the onset of inner core growth (Bono et al., 2019). The inner core nucleation affects the geomagnetic field (Bono et al., 2019). The rapid flip-flopping of the geomagnetic field during the Ediacaran decrease of field intensity was ventilated like a response to unusually ultra-low geomagnetic field intensity (Bono et al., 2019). The anomalous behavior of the geomagnetic field could also play an important role in the appearance of animals due to Ediacaran organism vulnerability to harmful cosmic radiation attaining the surface of the Earth due to the weak magnetic field (Meert et al., 2016).

### **2.2. Ediacaran environments**

The worldwide sedimentary record of the Neoproterozoic Era is punctuated by glaciogenic deposits with diamictites containing faceted and striated clasts and stratified siltstones with dropstones (Fairchild and Kennedy, 2007). Cryogenian glacial successions attain great thicknesses and cover wide areas along the continental margins. Glacial deposits were recognized on most continents and are organized in two events termed Sturtian (720 Ma) and Marinoan (635 Ma) based on chronostratigraphic units from South Australia. Both

glaciations are in accordance with the fundamental predictions of the snowball Earth hypothesis (Kirschvink, 1992; Hoffman et al., 1998; Hoffman & Schrag, 2002). Paleomagnetic data suggest that Cryogenian glaciations attained near-palaeoequatorial latitudes close to  $\leq 10^\circ$  (Schmidt et al., 1991; Schmidt and Williams, 1995; Schmidt et al., 2009). Subsequent studies have yielded low palaeolatitudes for other Cryogenian glacial deposits, with most results between  $0-20^\circ$  and no result  $> 40^\circ$  palaeolatitude (Evans and Raub, 2011).

A third younger ice-age within the Ediacaran period, called Gaskiers glaciation event, is recognized on at least 8 palaeocontinents, but its global extension is still contentious (Etienne et al., 2007; Gostin et al., 2010). The Gaskiers glaciation in Newfoundland is dated at ca. 580 Ma (Pu et al., 2016) and the Fauquier Formation in Virginia at ca. 571 Ma (Hebert et al., 2010), but without further radiometric ages their relation to glacial episodes elsewhere remains unclear. The main difficulty in acceptance of Ediacaran snowball Earth events rests on the poor age constraints that would attest that these glacial episodes were synchronous (Hoffman and Li, 2009). In addition, available paleomagnetic data are insufficient and unreliable to infer the latitudinal extent of ice sheets (Pisarevsky et al., 2012). Ediacaran glaciation spanned wide palaeolatitudes: ice rafting and glacial deposition in Australia occurred at  $10-15^\circ$  (Gostin et al., 2010) and glaciation elsewhere ranged from ca.  $50^\circ$  to a palaeolatitudes of  $78 \pm 12^\circ$  for the Fauquier Formation (Evans and Raub, 2011).

The sedimentary record from Ediacaran is rich in carbonate successions with some record of calcium sulfate minerals (CAS) in evaporitic deposits. Obviously, it is important to bear in mind the preservation bias, however the widespread occurrence of shallow carbonates can be considered as an indication of warm climatic conditions prevailing at that time. Carbonates, as a general rule, occur in near-equatorial latitudes and warm waters. While evaporites commonly occur in restricted basins, arid conditions and tropical latitudes ( $30-60^\circ$ ; see Warren 2010). The occurrence of large carbonate successions punctuated by short glaciogenic intervals reflect dramatic temperature fluctuations in the Ediacaran. Global temperatures estimates using  $\delta^{18}\text{O}$  composition of Precambrian oceans suggest of tropical paleotemperatures for the late Precambrian (Ediacaran) was higher ( $>50^\circ\text{C}$ ) than in the Phanerozoic periods (Bergmann et al., 2018; Scotese et al., 2021). The improve in recognized of sulfate phases minerals in Ediacran depositis can be help to better contains paleoclimatic conditions (Cui et al., 2022).

Geochemical evidence from Ediacaran sedimentary rocks suggest that oxygen levels increased in that period, reaching modern levels. This Neoproterozoic Oxygenation Event (Och and Shields-Zhou, 2012) has been considered as the second major increase in photosynthetic oxygen in the history of the Earth and is linked with the first true phosphorite giants (Pufahl and Hiatt, 2012) and probably led to the diversification of multicellular animals (Canfield et al., 2007; Och and Shields-Zhou, 2012). The appearance of mobile animals capable and new feeding styles amongst late Ediacaran-early Cambrian metazoans (McIlroy and Logan, 1999; Erwin et al., 2011) changed the chemical nature and the physical landscape of marine ecosystem. The “substrate revolution” (Bottjer et al., 2000) represents the growth in bioturbation intensity which drastically reduced the thickness and distribution of previously ubiquitous microbial facies and mats (Garrett, 1970; Hagadorn and Bottjer, 1997). Consequently, Phanerozoic seafloors developed large mixed layers with higher water contents, which produced an increasingly heterogeneous sediment-water interface (Seilacher and Pflüger, 1994; Hagadorn and Bottjer, 1997; Seilacher, 1999; Plotnick et al., 2010).

The Ediacaran record also mark the first appearance of biomineralized metazoans (Porter and Knoll, 2000; Cohen et al., 2011). The ability to create calcified hard parts was a key competitive innovation in benthic metazoans (Wood and Penny, 2018). Biomineralization by eukaryotes was another major innovation of the Ediacaran–Cambrian radiation (Darroch et al., 2021). Biomineralized hard parts include bilaterian plates, spines and shells (Bengtson, 1992; Maloof et al., 2010). The advent of biogenic hard-part deposits for the first time in Earth’s history played an important role on the environmental and ecological dynamics (Warren et al., 2013). As a consequence, previously bioclast-free environments started to contain unprecedented autochthonous inputs of biogenic hard parts. Oversized hard-particles produce a generalized bioclast scouring of the marine floor eventually eroding the benthic microbial mats and preventing the establishment of new ones (Pratt, 1982). A further implication of the new rigid framework is the formation of new, bioclast-rich local topographic highs, creating a new niche for potential colonization by benthic, skeletonized forms (Wood, 2011). The diversification in biomineralizing organisms was followed by an increase in overall skeletal contribution to shallow-water carbonate facies in the Ordovician, especially by heavily calcified corals, bryozoans, brachiopods, and echinoderms (Pruss et al., 2010).

### 2.3. Carbon isotopes excursions

Ediacaran strata from several localities record noticeable fluctuations in the signal of carbon isotopes, which are putatively linked with dramatic shifts in the paleoclimate and redox state of the Earth's atmosphere-ocean (Halverson et al., 2010). Basal successions of Ediacaran age (cap dolostone) are characterized by negative  $\delta^{13}\text{C}$  in carbonate values (Knoll et al., 2006), representing a negative excursion designated as EN1 in South China (Zhou and Xiao, 2007). Negative values initiate immediately above the contact with late-Cryogenian glaciogenic deposits. Basal Ediacaran successions ('cap carbonates') show values of  $\delta^{13}\text{C}$  of about -5‰ (Hoffman et al., 2007), after which they return to near -0‰ within about 3 million years (Condon et al., 2005). Many sections record a subsequent rise to highly positive  $\delta^{13}\text{C}$  values ranging from +6‰ to +10‰. This isotopic behavior is reported in sections from Namibia (Cui et al., 2018), NE Svalbard (Halverson et al., 2005), South China (McFadden et al., 2008) and Brazil (Sial et al., 2016). Ediacaran sedimentary successions in South China display a regionally consistent negative excursions (named EN2) in the middle Doushantuo Formation punctuated the highly positive  $\delta^{13}\text{C}$  values (Zhou and Xiao, 2007). Additional negative excursions are documented in some sections (Sawaki et al., 2010; Zhu et al., 2013), but they are not regionally consistent and may represent diagenetic alterations.

The most prominent feature in the Ediacaran  $\delta^{13}\text{C}$  record is an unusually negative  $\delta^{13}\text{C}$  excursion on carbonate, known as the Shuram excursion (SE). This isotope anomaly is characterized by the most depleted C values ever recorded reaching up to -12‰ (Grotzinger et al., 2011). A poorly determined chronostratigraphic framework makes the SE difficult to correlate and compare globally. Yet, negative excursions of similar magnitude have been observed in several units, including the upper Doushantuo Formation (EN3 interval) in South China, the Wonoka Formation in South Australia, the Gametrail excursion in northwestern Canada, and the Rainstorm Member in Death Valley (Xiao and Narbonne, 2020). Despite being widely recognized in several basins, the evolution of the excursion, its genesis and meaning still remain in debate. The complexity of the anomaly is not a consensus. Some authors suggest it is a simple negative anomaly (Fike et al., 2006; Le Guerroue et al., 2006) whereas other authors suggest that the SE comprises several small-scale negative anomalies (Condon et al., 2005).

The origin of the SE excursion has been attributed to the mineralization of a large global ocean dissolved inorganic carbon (DIC) reservoir due to oxidation of organic carbon or methane (Rothman et al., 2003; Fike et al., 2006; Kaufman et al., 2007; McFadden et al.,

2008; Bjerrum and Canfield, 2011), or to large authigenic carbonate precipitation (Grotzinger et al., 2011; Macdonald et al., 2013; Schrag et al., 2013; Cui et al., 2017), or yet from burial or meteoric diagenesis (Knauth and Kennedy, 2009; Derry, 2010). More recently Cui et al., (2022) propose a complex interplay of biogeochemical process involving bacterial sulfate reduction and C, S and Ba cycles in response to the Shuram oxygenation event. The age and duration of the anomaly are poorly constrained. Some authors suggest that it lasted a few million years (Minguez and Kodama 2017; Gong et al., 2019; Gong and Li, 2020) while others propose a 50 million years duration for it (Le Guerroue et al., 2006).

Finally, the stratigraphic relationships of the anomaly with the ~580 Ma Gaskiers glaciation is also contentious (Xiao and Narbonne, 2020). Anomalous negative excursions equivalent to the SE are found stratigraphically below glaciogenic deposits interpreted as equivalent to the Gaskiers record. Witkosky and Wernicke (2018), for example, estimated that the SE recorded in the Rainstorm Member occurred between 585-579 Ma, being thus older than the c. 580 Ma Gaskiers glaciation. A similar relation is also observed in the uppermost Nyborg Formation that present a strong negative anomaly and underlies the Mortensnes diamictite in northern Norway, which has been correlated to the Gaskiers glaciation (Halverson et al., 2005). These stratigraphic relations lead some author to suggest that the Gaskiers glaciation postdated the initiation or even the entirety of the Shuram negative  $\delta^{13}\text{C}$  excursion. However, most occurrences related to the Shuram isotopic anomaly are stratigraphically above Gaskiers-equivalent records. Evidence for that comes from Scotland and Ireland where ice-rafted debris beds in the Dalradian Supergroup (Gaskiers glaciation) are covered by the Girdle Limestone that records a negative  $\delta^{13}\text{C}$  excursion correlated to the SE. Other localities, like Newfoundland (Canada) also contain evidences that the Gaskiers glacial event predates the Shuram-like excursion (Canfield et al., 2020). In addition, high-precision radioisotopic dates from Ediacaran successions in Newfoundland constrained the SE excursion to between c. 570 and 560 Ma (Rooney et al., 2020). In South China, the SE is thought to be correlated to the EN3 interval of the upper Doushantuo Formation. The EN3 in the upper Doushantuo Formation contains a 551 Ma volcanic ash (Condon et al., 2005), and this has been taken by some geologists as evidence that the Shuram Excursion is 551 Ma and thus younger than the 580 Ma Gaskiers glaciation. However, this interpretation is not secure because recent studies have shown that the EN3 is succeeded by additional  $\delta^{13}\text{C}$  variations before being capped by the 551 Ma ash (Xiao et al., 2017; Zhou et al., 2017), suggesting the SE may be significantly older than 551 Ma.

Carbon isotopes profiles are usually applied to establish regional and global correlations of Ediacaran successions. As previously mentioned, the lack of high-precision radioisotopic ages to constrain the SE and its purported equivalents is an important challenge for more precise stratigraphic correlations using this feature. Likewise, an accurate age constraint on the glacial deposits related to the Gaskiers Glaciation (580 Ma) are still scarce. For instance, the uncertain stratigraphic relationship between the Shuram and the Gaskiers is the main reason behind the two different versions of Ediacaran correlations and subdivision presented in Narbonne et al. (2012) and Xiao et al. (2016).

The Ediacaran Period is closed by another negative  $\delta^{13}\text{C}$  anomaly, dubbed BACE or Basal Cambrian Carbon Isotope Excursion (Zhu et al., 2006). This excursion has been used to approximate the Precambrian-Cambrian boundary (Kaufman and Knoll, 1995; Amthor et al., 2003), but the precise relationship between the BACE and the basal Cambrian boundary needs additional refinement.

#### **2.4. The Earth's magnetic field during the Ediacaran**

The geomagnetic field is one of the key components of the complex integrated system of our planet, because it interacts with all Earth's shells: atmosphere, biosphere, crust, mantle and core, also shielding life from the harmful effects of cosmic radiation. The Earth's magnetic field has repeatedly reversed polarity through time (Opdyke and Channel, 1996). In the last 160 million of years, sedimentary successions and seafloor magnetic anomalies provide the basis for a robust polarity chart. Based on these data, the observed reversal rates are variable, but the usually around 2–3 reversals per million years and always below 5 reversals per million years (Opdyke and Channell, 1996; Melott et al., 2018).

For periods older than 200 Myr magnetostratigraphic data obtained from sedimentary sections suggest that the geomagnetic field may have operated in three modes (Gallet and Pavlov, 2016): 1) a normal reversing state showing frequency of flipping around 1 to 3 reversals per million years, 2) a long-term non-reversing interval also called “superchron” mode. Superchron intervals (normal or reversed) extends out for tens of millions of years (Opdyke and Channell, 1996; Gradstein et al., 2004). Reverse polarity superchrons intervals have been reported during the early-mid Ordovician (Moyero superchron) and during the late Carboniferous-mid Permian (Kiaman superchron) and normal polarity superchrons during the late Cretaceous (CNPS) and Proterozoic. 3) a third mode of high-frequency of reversals, was

noted recently where intervals of more than 10 reversals per million of years have been recorded in some units (Biggin et al., 2012; Gallet and Pavlov, 2016; Meert et al., 2016).

Previous research has suggested that Earth's magnetic field underwent a period of hyperactive reversals during Ediacaran-Cambrian boundary (Meert et al., 2016; Bazhenov et al., 2016; Levashova et al., 2021). Well-documented cases of high reversal rates are known in Cambrian age successions from Siberia (Pavlov and Gallet, 2001; Gallet et al., 2003; Gallet et al., 2019). Ediacaran-aged (~550 Ma) sedimentary rocks in the Ural Mountains in western Russia, indicate a reversal rate then was 20 times faster than it is today (Bazhenov et al., 2016; Levashova et al., 2021). Late Ediacaran rocks of the Lopata Formation from Baltica also suggested a high reversal frequency of geomagnetic field (Shatsillo et al., 2015). The cause of hyperactivity in the Ediacaran was linked with low dipole intensity and perhaps nucleation of the inner core (Meert et al., 2016; Biggin et al., 2019). Restricted paleointensity data from Ediacaran igneous rocks support this anomalous behaviour of the field in the Ediacaran and Cambrian (Bono et al., 2019; Lluhiliier et al., 2019; Shcherbakova et al., 2020). More magnetostratigraphic studies developed on Ediacaran stratigraphic section and acquisition of new paleointensity data are, however, needed to confirm the extent of this anomalous behaviour of the field in the Ediacaran and Cambrian.

## **CHAPTER III**

### 3. Microfacies of the Avellaneda Formation (Argentina), a tidal flat facing the Shuram Excursion

**Jhon W.L. Afonso**, María Julia Arrouy, Lucía E. Gómez-Peral, Victoria Penzo, Daniel G. Poiré, Pedro Augusto, Luciano Castro, Sergio Caetano-Filho, Augusto E. Rapalini, Pablo Franceschinis, Ricardo I.F. Trindade

**Abstract:** Middle to Late Ediacaran is a dynamic time transition, hosting sudden changes in the sedimentary environments, pronounced carbon geochemical disturbances and biological innovations. The Avellaneda Formation (~580-565 Ma, Argentina) provides a valuable window into this interval. Here, we present a detailed description of microfacies coupled electron microscope observations, cathodoluminescence, elementary geochemistry and carbon-oxygen stable isotopes. These tools were combined to improve previously assigned depositional settings for the Avellaneda Formation. Our findings suggest a shallow marine setting range from subtidal/intertidal zone and intertidal/supratidal environments. Evaporite textures, sulfate minerals and crack reveal short and episodic subaerial exposure. Carbon stable isotopes show a likely primary nature negative excursion in the Avellaneda Formation. Although not reaching extreme nadir values, this isotopic excursion is interpreted as an expression of the Shuram negative C isotope excursion. At the same time, we document a new occurrence of sulfate minerals occurring near the SE interval, extending the global dataset. The coincidence of evaporite textures, sulfate minerals (barite) with  $\delta^{13}\text{C}_{\text{carb}}$  excursion in the study sections reinforce the potential link between rising oxygen levels, enhanced sulfate weathering fluxes, transient increases of  $\text{SO}_4^{2-}$  and concurrent oxidation likely cause of the SE.

#### 3.1-Introduction

The Late Neoproterozoic was a key time in Earth's history. This period witnessed remarkable modifications in the marine environment by progressive but dynamic oxygenation pulses and nutrient availability (Wood et al., 2019; Mitchel et al., 2020). During this interval, completely new organisms arose in the marine ecosystem, previously, essentially dominated by microbial mats communities (Grotzinger and Knoll, 1999). The shift in marine environment and diversification of early biota was accompanied by dramatic perturbations in global biogeochemical cycles, including some of the largest excursions in the carbon and

sulfur isotope ratios (Halverson et al., 2005; Shields et al., 2019; Cui et al., 2022). All these innovations are attributed to irreversible changes on Earth's surface environments.

Pronounced isotope anomalies have been reported in Ediacaran succession worldwide. Due to the proximity with the appearance and disappearance of fossil assemblages intervals, many believe in an eventual connection between environmental changes, biogeochemical cycles, and evolutionary innovation or extinctions. Indeed, most taxa of the Ediacara biota (such as the White Sea and the Nama assemblages, Waggoner, 2003) appear to be bracketed by two negative carbon isotope excursions raising the intriguing possibility that the rise and fall of the Ediacara biota may have been related to environmental and ecological events (Xiao et al., 2016; Darroch et al., 2018; Xiao and Narbonne 2020). However, a unique interpretation for isotope excursions is a matter of considerable debate. For instance, the largest carbon isotope excursion recorded at the time has been interpreted in a variety of ways, including local or global scales (Grotzinger et al., 2011). Mechanisms involve diagenetic overprints (Knauth and Kennedy, 2009; Derry, 2010), destabilization of methane hydrate (Bjerrum and Canfield, 2011), a spike in mantle CO<sub>2</sub> degassing (Paulsen et al., 2017), eruption of carbonatite volcanic ash (Liu et al., 2021) and/or the sudden increase in the ocean sulfate reservoir stimulating microbial sulfate reduction and anaerobic oxidation of organic matter (Shields et al., 2019; Cui et al., 2022). Therefore, to better separate global from local processes and understand the feedbacks between life evolution and environmental changes, it is of utmost importance to characterize in detail key Ediacaran successions in different paleo continents and the sedimentary product of these processes.

The sedimentary cover of the Río de La Plata craton encompasses part of the events related to the Late Neoproterozoic and therefore provides access to key information about this critical time on Earth's history. Here we present a description of microfacies from the mid to late Ediacaran Avellaneda Formation (~580-560 Ma) a shallow-marine depositional system developed in a tidal flat setting (Arrouy et al., 2015). Petrographic results were combined with electron microscope observations, cathodoluminescence, geochemistry and carbon-oxygen stable isotopes to improve the depositional conditions of the Avellaneda Formation, at the margin of the southwestern Gondwana supercontinent. We compare the obtained results with other mid-Ediacaran successions worldwide, supporting the idea that this particular time-interval within Ediacaran experienced a potential major oxygenation event.

## 3.2 – Geological context

### 3.2.1. Geological setting

The Tandilia System is a NW-trend orogenic belt that stretches along 350 km in the province of Buenos Aires, Argentina (Figure 3.1a). It encompasses an igneous-metamorphic basement covered by a thick sequence of sedimentary rock formations that can reach 455 meters (Figure 3.1 b-3.1 c). Basement rocks are mainly granitoids, orthogneisses and migmatites from the Buenos Aires Complex (2234 to 2065 Ma; U-Pb SHRIMP; Cingolani et al., 2002; Hartmann et al., 2002; Cingolani, 2011). The main tectonomagmatic episodes that occurred in the Tandilia belt were dated to about 2.2–2.1 Ga and are linked to Trans-Amazonian events (Hartmann et al., 2002; Cingolani et al., 2002). The sedimentary cover ranges from Neoproterozoic to Early Paleozoic (Poiré 1993; Gómez-Peral et al., 2014; Arrouy et al., 2015). The Sierras Bayas Group marks the onset of depositional infill and rests unconformably on the crystalline basement (Poiré, 1993; Poiré and Spalletti, 2005; Poiré and Gaucher, 2009). This group is limited at the top by a regional erosive karstic surface (Barrio et al., 1991) that marks the contact with the units of La Providencia Group (Middle to Late Ediacaran age, Arrouy et al., 2015; Arrouy et al., 2016). La Providencia Group comprises the terminal sedimentary record of the Precambrian in the region of the Tandilia System and is covered by clastic units of Lower Paleozoic, plus sediments of Tertiary and Quaternary age.

### 3.2.2. The Avellaneda Formation

The Avellaneda Formation (Arrouy et al., 2015) is a subsurface unit defined from stratigraphic boreholes and positioned at the base of the La Providencia Group (Figure 3.1c). This group was recently proposed to include several successions accumulated along shallow-water marine settings (Arrouy et al., 2015). Sedimentary deposits of the Avellaneda Formation lay above carbonate rocks of the Loma Negra Formation, the upper unit of the Sierras Bayas Group. The contact between Loma Negra and Avellaneda formations is marked by an irregular karst surface, called Barker Surface (Barrio et al., 1991; Poiré and Gaucher, 2007), developed during a sea level fall thought as a response to the Gaskiers glacial event (Gómez-Peral et al., 2014; 2017). The Avellaneda Formation is conformably overlain by fine grained sediments of the Alicia Formation (Arrouy et al., 2015; Arrouy and Gómez-Peral, 2021).

The Avellaneda Formation varies from 4 to 25 m in thickness. According to Arrouy et al., (2015), this unit consists mainly of three sedimentary facies: purple-gray-greenish

laminated marl and massive marl at the base, which grade vertically into red massive mudstone. Sedimentary features also include sporadic mudcracks (Arrouy et al., 2015). The presence of illite as the main clay mineral was indicated by X-ray diffraction data (Arrouy et al., 2015). Previous investigations also recognized phosphate as nodules and lenses and chert breccias in the basal section of Avellaneda Formation (Leanza and Hugo, 1987; Gómez-Peral et al., 2014). These phosphorite concretionary levels were formed under well-oxygenated sea-floor conditions in a fully ventilated ocean (Gómez-Peral et al., 2014). Currently, it is proposed that sedimentary deposits of the Avellaneda Formation were accumulated in a tidal flat environment (Arrouy et al., 2015).

### 3.2.3. Age

The tentative age of Avellaneda Formation was constrained by its stratigraphic relationships (Figure 3.1c). This is underlying by the Loma Negra Formation, which is considered Ediacaran based on the correlation of  $\delta^{13}\text{C}$  and  $^{87}\text{Sr}/^{86}\text{Sr}$  initial ratios to global reference curves. The Loma Negra Formation shows  $^{87}\text{Sr}/^{86}\text{Sr}$  initial ratios of 0.7064–0.7082 (Gómez-Peral et al., 2018). Such  $^{87}\text{Sr}/^{86}\text{Sr}$  ratios were considered as indirect evidence for an age around 590–580 Ma (Gómez-Peral et al., 2018; 2019). Furthermore, the erosional surface that marks the contact between both formations is interpreted as a response to sea-level fall linked to the ~580 Ma Gaskiers glaciation (Arrouy et al., 2015; Gómez-Peral et al., 2018).

The overlying units of the Avellaneda Formation are Alicia and Cerro Negro formations (La Providencia Group). These units contain a rich organic-walled microfossil assemblage that consists of acritarchs and filamentous microfossils, as well as taxonomically unidentified forms of colonial spheroids (Arrouy et al., 2019). The absence of large complex acanthomorphs and the dominance of leiospheres are attributed to the Late Ediacaran Leiosphere Palynoflora (LELP; Arrouy et al., 2019). Additionally, the discovery and description in the Cerro Negro Formation of *Aspidella* sp., an Ediacaran disk-shaped fossil of uncertain affinity and related to the Ediacaran White Sea assemblage (560–550 Ma; Droser and Gehling, 2015; Droser et al., 2017), imposes a minimal age of 560 Ma for the unit (Arrouy et al., 2016). Considering this, it is reasonable to accept an age between 580–560 Ma for the Avellaneda Formation.

### 3.3. Methods

#### 3.3.1. Samples and petrography

The studied cores were recovered from three stratigraphic drill cores in the Olavarría area (Figure 3.1b). Drilling was undertaken by Cementos Avellaneda S.A. with a rotary drilling method and reached depths of 200 meters below surface (mbs). These three continuous drill cores E7, E34 and H9, provide an overlapping composite record covering the entire Avellaneda Formation. Individual cores were logged as the physical expression of vertical stacking of sedimentary rocks. The measuring and subsequent correlation of different columns along the cores allow obtain a general stratigraphic framework with different lateral relationships between different strata sets (cf. Walker, 1984). Stratigraphic logs also provided sedimentological data that allowed their interpretation in terms of depositional processes.

Due to the difficulties imposed by the very fine granulometry of sedimentary rocks from Avellaneda Formation, the macroscopic descriptions were supplemented by standard petrographic analysis. The microfacies are best described and classified based on grain size, lithology, color, nature of contact, physical sedimentary structures and content of organic material (Tucker, 1988; Flügel, 2010) at microscopic scale. Emphasis was placed on petrographic analysis as the basis for understanding paleoenvironments and regional stratigraphic trends. Polished and uncovered thin-sections were observed and analyzed with a polarized microscope Olympus BX51P at the Institute of Astronomy, Geophysics and Atmospheric Sciences (IAG), University of São Paulo, Brazil. Thin-sections were stained with a mixed Alizarin Red-S and potassium ferricyanide solution to distinguish carbonate minerals (Dickson, 1966). Optical microscopy observations were complemented with cathodoluminescence techniques (CL). CL provided data on the paragenetic relationships, recrystallization and eventual mineral replacements (e.g., calcite by dolomite) (Budd, 2000; Götze, 2012; Hiatt and Pufhall, 2014). CL data were acquired with an optical microscope (Leica DM4500 P LED) coupled to a color cathodoluminescence optical station (model CCL Mk5-2) from Cambridge Image Technology Ltd. CL analyses were performed in the Cathodoluminescence Laboratory of the Geosciences Institute at Federal University of Pará (LabCatodo-UFPa). CL images were acquired with an electron beam current ranging from 348 to 508  $\mu\text{A}$  and a constant acceleration voltage of 15.2 kV with an exposure time ranging from 4.2 to 6.0 s to carbonate-dominated samples. The main structures and textures of carbonate-evaporite deposits recognized in thin-section were then imaged using a scanning electron microscope (SEM) coupled with energy dispersive X-ray spectroscope (EDS) at the

Geological Survey of Brazil (CPRM). Such analyses provided critical information on the morphological structures, size and shape of crystals, chemical composition and other components that collectively control the textures of carbonates. Gold-coated samples were imaged in a JEOL JSM 6400 scanning electron microscope (SEM) (JEOL Limited, Tokyo, Japan) with a Carl Zeiss MERLIN™ EDS (Carl Zeiss Group, Jena, Germany) at 3–5 kV and 150–500 pA.

### 3.2. Carbon and oxygen stable isotopes and elemental geochemistry

About 10 mg of carbonate powder was obtained by microdrilling carbonate matrix from polished slabs. We focused on well-preserved carbonate rich-layers, free of fractures or any post-depositional feature. Layers with siliciclastic grains were also avoided. Carbonate powders were reacted with  $\text{H}_3\text{PO}_4$  at 72 °C and the released  $\text{CO}_2$  was extracted through a continuous flow in a Thermo Finnigan GasBench II. C and O isotope compositions were obtained at the Stable Isotope Laboratory of the Center for Geochronological Research, University of São Paulo (CPGeo/USP). Stable isotope compositions are expressed in delta notation relative to the Vienna Pee-Dee Belemnite (V-PDB – ‰). Standard deviations in the analyzed samples are 0.04 ‰ for carbon and 0.04 to 0.06 ‰ for oxygen.

Elemental geochemical analysis focused on Ca, Sr, Fe, and Mn measurements for investigation of Fe/Sr, Mn/Sr and Ca/Sr relationships against carbon and oxygen isotope compositions to assess post-depositional effects. Elemental concentrations were measured using a portable Olympus Delta XRF Analyzer in the Marine Inorganic Chemistry Laboratory of the Institute of Oceanography, University of São Paulo. XRF analyses were performed in homogeneous surfaces of polished slabs. A blank (pure  $\text{SiO}_2$ ) and the reference material NIST SRM 2711A were measured for each 30 samples. The blank for Ca, Mn, Fe, and Sr contents were below the detection limit of the equipment. The standard material NIST SRM 2711A was measured 35 times during the period of analyses, with average uncertainties below  $\pm 0.4\%$  for Ca and Fe,  $\pm 92$  mg/kg for Mn and below  $\pm 7$  mg/kg for Sr. Reproducibility are in a range below  $\pm 0.05\%$  for Ca and Fe,  $\pm 9$  mg/kg for Mn, and  $\pm 5$  mg/kg for Sr.

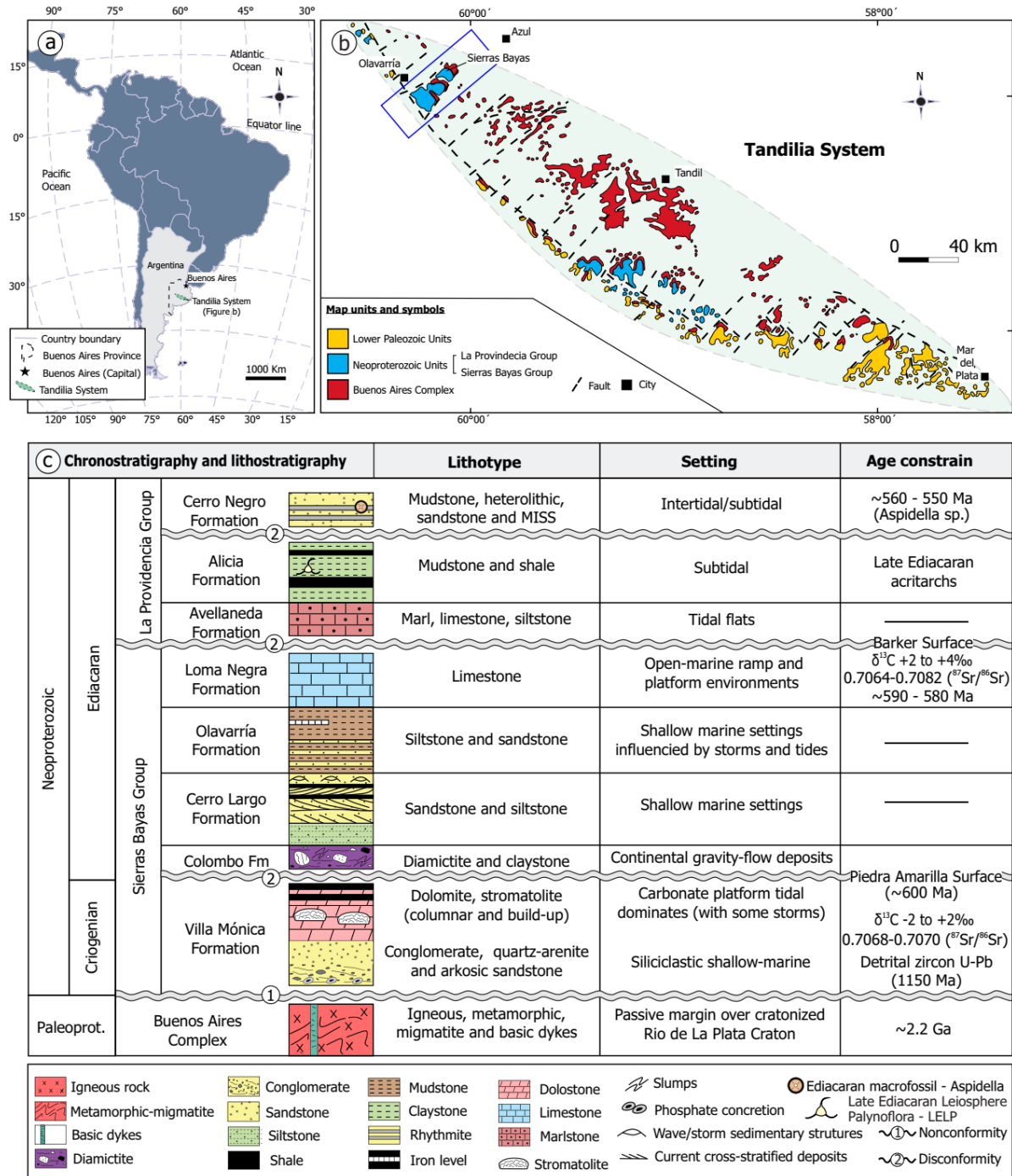


Figure 3.1: Geological context and stratigraphy of the Neoproterozoic-Paleozoic sedimentary cover of Río de La Plata Craton. (a) Location of the Tandilia System belt. (b) Simplified geological map of the Tandilia System displaying outcrop regions of Sierras Bayas and La Providencia Groups, and the Buenos Aires Complex basement (modified from Iñiguez 1999 and Rapela et al., 2007). In (b) the blue rectangle delineates the study area. (c) Stratigraphic column of Sierras Bayas and La Providencia Groups (modified from Arrouy and Gómez-Peral, 2021; Gómez-Peral et al., 2021). Age constraints are based on Poiré, (1987), Rapela et al., (2007), Gómez-Peral et al., (2007; 2014), Rapalini et al., (2013), Arrouy et al., (2016).

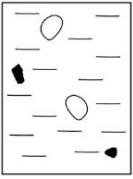
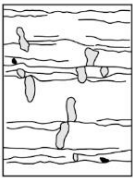
### 3.4. Results

#### 3.4.1. Sedimentary microfacies of the Avellaneda Formation

The sedimentary record of the Avellaneda Formation was accessed from stratigraphic boreholes located on the outskirts of Olavarría, Argentina. All these drilling sites completely trespass this unit, with different depths and variable thickness between 11 and 22 meters (Figure 3.2). The studied material is fresh and well-preserved with cores frequently exhibiting a well continuity. Each borehole was individually logged with emphasis in the sedimentary microfacies, vertical changes and lateral correlation (Figure 3.2). Drill core E7 comprises about 18 meters of the Avellaneda Formation, beginning at 40 mbs (meters below surface) and ending at 58 mbs (Figure 3.2). In core E34 the unit occurs between 80 and 91 mbs, totalling 11 meters (Figure 3.2). The H9 core contains the most expressive record of the Avellaneda Formation with 22 meters between 55 and 77 mbs (Figure 3.2).

The main carbonate and siliciclastic components were individualized based on composition, grain size, sedimentary structures, and diagenetic features. Regardless of the common recrystallization, much of the original fabric elements of the studied carbonate successions remain preserved within the neoformed textures. From thin-section analysis were recognized six sedimentary microfacies in the Avellaneda Formation. All these microfacies may occur in different proportions through the succession and may show different facies relationships between them. from the studied sections are summarized in Table 3.1.

Table 3.1: Summary of sedimentary microfacies present in the Avellaneda Formation

Microfacies (MF)	Description	Process/interpretation	Representation
Clayey carbonate (MF1)	MF1 is mostly formed by microcrystalline calcite with low grade of recrystallization. Presence of anastomosing and bifurcated lamination. Spherical to oval fibro-radial spherulite (200 to 500µm of diameters)	Suspension fall out within low energy waters; precipitation from supersaturated solution related to restricted settings	
Massive limestone (MF2)	Consist of dense dark micrite composed of anhedral calcite crystals smaller than 4 µm. After treatment of Alizarin Red S and potassium ferricyanide protocol reveal sub-rhombic calcite crystals similar in size (80-120µm). Presence of spherical, sub-spherical to oblate gypsum nodules. Dispersed detrital quartz grains. Calcite fiber vein	Precipitation in quiet waters; nodular grow displacing host sediment;	
Laminated limemudstone (MF3)	Comprise carbonate dominated layers interlayered argillaceous/clay laminae. Quartz grains are dispersed and range from 125 to 150µm. Carbonate nodules sometimes truncating the laminations. Single and, more rarely, aggregates of rhombohedral calcite crystals	Deposition from suspension; nodular masses that displaced the surrounding host sediment.	
Laminated microbial mats (MF4)	Thinly-laminated microfacies characterized by dark organic-rich layers and carbonate-rich layer. Laminations are laterally persistent with wavy crinkly appearance and sometimes complexly anastomosed. Laminations are superimposed and exhibit a finely wrinkled surface morphology. Fenestral fabric. Presence of vertical crack like sedimentary structures. Sparse crystals with acicular and/or lens-shaped with bitermination (Barite pseudomorphs after gypsum)	Biogenic sedimentary structures produced by microbial mat builders (likely cyanobacteria); Metabolic activities; disruption due sporadic periods of subarea exposition; subaqueous gypsum precipitates replaced by barite	
Laminated limestone with nodular anhydrite (MF5)	Encompass a very thin alternation composed of millimetric darker gray organic-rich laminae alternated with light carbonate-rich layers. Carbonates are cryptocrystalline to microcrystalline mudstones. Presence of nodules of variable morphology which include ovoid or lenticular shapes, sometimes forming coalesced structure. Fine felted mass of lath crystals likely anhydrite (100 µm long). Convolutions and deformation on laminations. Quartz grains are rare. Large barium sulphate crystal likely gypsum-anhydrite. Fe-Cu sulphides associated.	Organo-sedimentary structure associated to microbial mats accretion; displacive growth of nodular mosaic and microenterolithic layers show anhydrite replaced by calcite; pseudomorphic replacement of tabular prismatic gypsum by barite.	
Massive claystone to siltstone (MF6)	Mf6 consist of mostly dark to brown layers made of silt- and clay-sized particles. Mud-rich intervals showing plastic deformation of centimetre-scale.	Subaqueous sediment flow (clastic gravitational flows) to suspension/mud plumes (?); Reworking of microbial mats deposits.	

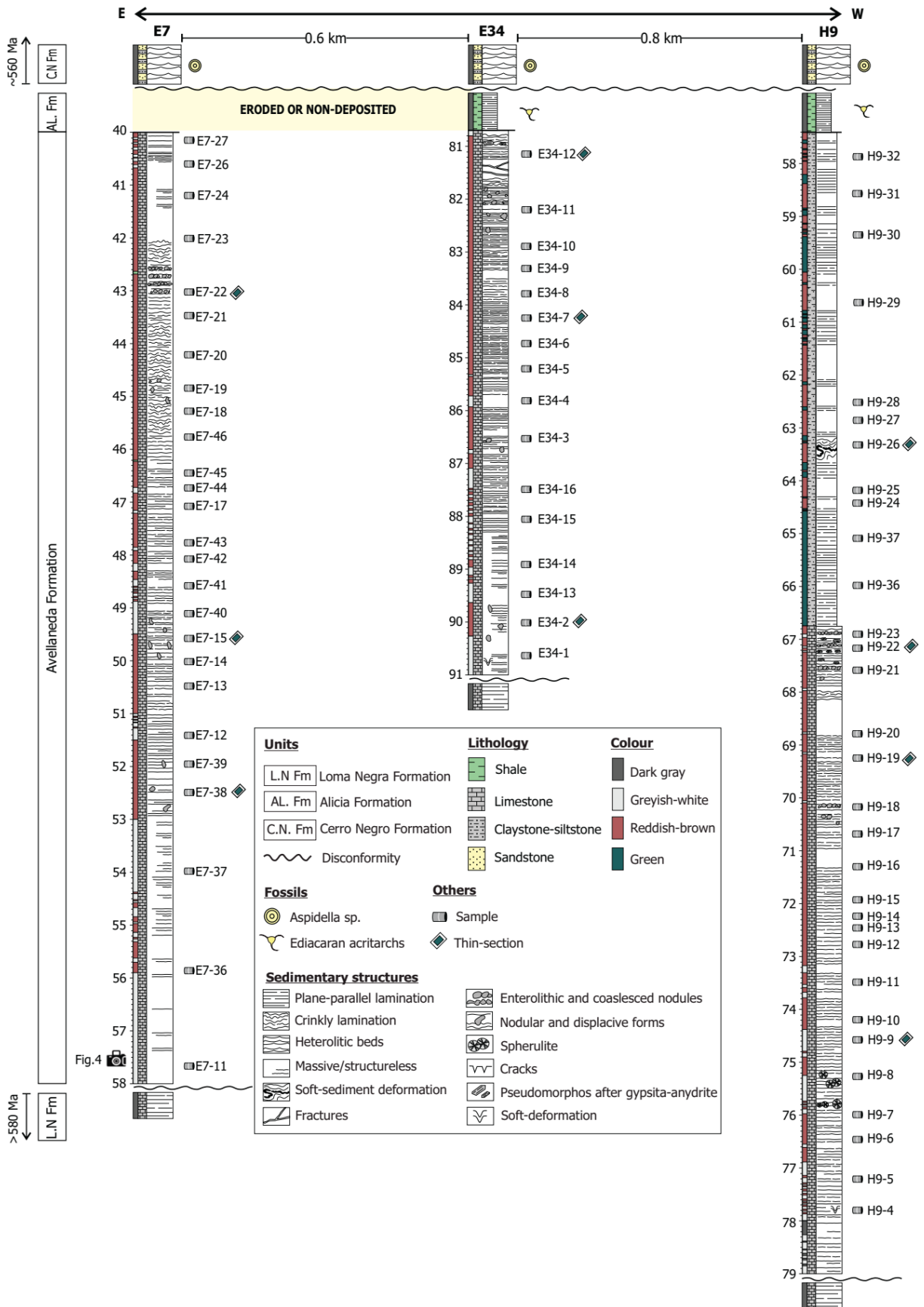


Figure 3.2: Sedimentary logs performed in the Avellaneda Formation for three drill cores recovered in Olavarría region, Argentina (see Figure 3.1). Drill-cores are spatially oriented from East to West and distance between each borehole is indicated.

#### 3.4.1.1. MF1 - Clayey-carbonate microfacies

##### **Description**

Clayey-carbonate microfacies are present at the base of the Avellaneda Formation (Figures 3.2 and 3.3) interbedded with carbonate. Macroscopic samples are gray to brownish gray (Figure 3.3a). Optical microscopy shows the light laminae are composed of microcrystalline calcite and the dark ones are clayey and likely rich in organic matter (Figure 3.3a). The fine-grained sediments are mostly composed of microcrystalline calcite but may also show some degree of recrystallization (Figure 3.3b). Microscopic observations demonstrate the presence of anastomosing and bifurcated lamination (Figure 3.3c). In addition, there are embedded spherulites (Figure 3.3a and 3.3d), consisting of radial fibrous calcite, like ray-crystal fans, with intracrystalline inclusions (Figure 3.3d). The spherulite particles observed do not show nuclei (Figure 3.3d). They are spherical to oval (Figure 3.3e), commonly up to 100  $\mu\text{m}$  in diameter, ranging from 200 to 500  $\mu\text{m}$ . In CL images they sometimes display a compound form, where two spherulites grow together, as well as incomplete spherulites exhibiting hemispherical to fan shapes. The matrix laminae bend and wrap around the spherulites (Figure 3.3d and 3.3e).

##### **Interpretation**

The presence of clay minerals and mud-rich carbonate suggest a low-energy and/or restricted environment. The presence of spherulite particles is usually associated with Mg-rich clays and can be found in marine peritidal settings (Sumner and Grotzinger, 2000, 2004) and restricted settings (Mercedes-Martin et al., 2017; Gomes et al., 2020; Claes et al., 2021). Laboratory experimentation demonstrates that nucleation of spherulite can be associated with bacterial and cyanobacterial activity (Verrecchia et al., 1995; Rodríguez-Navarro et al., 2007; Sanchez-Navas et al., 2009), but an abiotic origin cannot be discarded (Tosca and Wright, 2018; Mercedes-Martin et al., 2019).

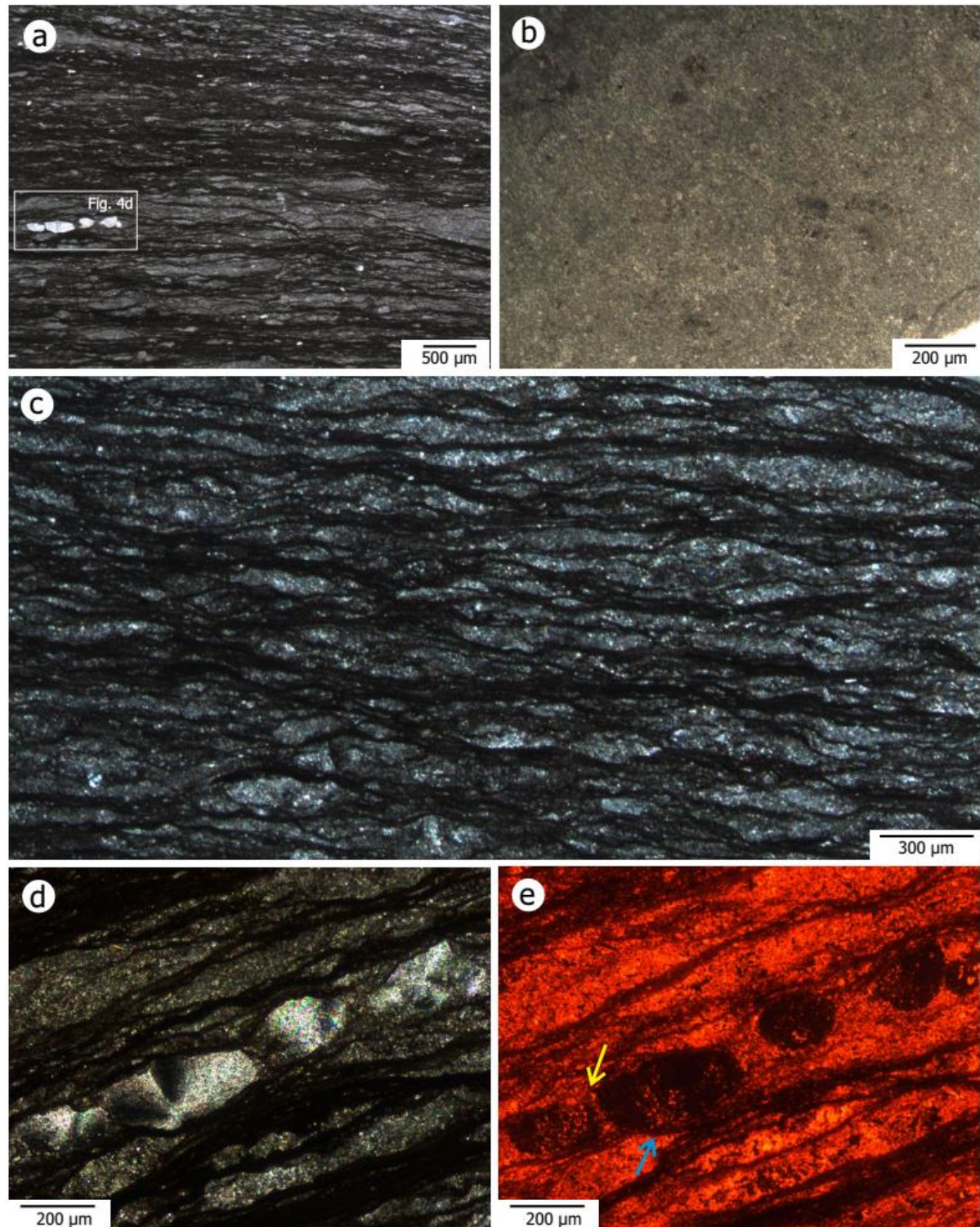


Figure 3.3: Argillaceous-carbonate facies. (a) Micrite carbonate facies intercalated with clay-enriched darkest layers presumably with some organic matter. (b) Micritic limestone composed of interlocking mosaics of micron-sized and equant calcite crystals. (c) Fine anastomosing and bifurcating laminations present in the argillaceous-carbonate facies. (d) Petrographic images of spherulite and surrounding matrix. (e) CL image highlighting the spherical to oval shape. On the same image, note the presence of a compound form (yellow arrow) and isolated form embedded in carbonate-rich layers. Note how laminations wrap round the spherulites (blue arrow).

### 3.4.1.2. MF2 - Massive limestone microfacies

#### *Description*

The massive limestone microfacies is better exposed in the basal section of the E7 and E34. In drill core H9, the massive limestone is poorly developed (Figure 3.2). Macroscopic samples usually show brownish, greenish and gray to dark grayish colors (Figure 3.4a and 3.4b). Limestone mud is composed dominantly of dense micrite matrix without visible lamination under the microscope (Figure 3.4c). The micrite is dark, formed by anhedral calcite crystals smaller than 4  $\mu\text{m}$  (microcrystalline calcite), but also occur as calcite crystals 5 to 8  $\mu\text{m}$  in size (microsparitic calcite). In thin section, after staining with Alizarin Red S and potassium ferricyanide these crystals appear with no discernible nucleus and range in size commonly between 80  $\mu\text{m}$  and 120  $\mu\text{m}$  showing sub-rhombic contours separated by a micritic matrix (Figure 3.4d). They also occur as aggregates of sub-rhombic crystals with similar sizes. Gypsum crystals occur scattered in the surrounding matrix as nodules with shapes varying from spherical, sub-spherical to oblate (Figure 3.4e). These nodules range in size from 70 $\mu\text{m}$  to 200 $\mu\text{m}$ . Under CL, we also identified nodules with the same size, but composed of microsparitic calcite (Figure 3.4f and 3.4g). They can show a nucleus constituted of micrite (Figure 3.4f) or no visible core (Figure 3.4g). The most common terrigenous component found in the lime mudstone is quartz floating in the microcrystalline matrix (Figure 3.4e and 3.4h). The quartz grains are moderately sorted, rounded to subrounded and occasionally angular (Figure 3.4h). Grain size ranges from coarse silt to fine sand, with a predominance of silt-sized grains. Microfractures cut across these samples and are filled/cemented by coarse calcite spar (Figure 3.4i). Furthermore, bedding-parallel veins composed of fibrous calcite with fibers of roughly 1 mm in diameter, arranged nearly perpendicular to the vein walls (Figure 3.4j).

#### *Interpretation*

Massive lime-mudstone is indicative of mud deposition through settling from suspension in low-energy flows or a slack water environment (Shinn, 1983; Tucker and Wright, 1990). Massive limestone facies are reported in shallow subtidal zones in restricted environments under low energy conditions (Shinn, 1983; Tucker and Wright, 1990). Individual round-oval nodules are interpreted as possible evaporite textures replaced by carbonate during early diagenesis (Poch et al., 2010).

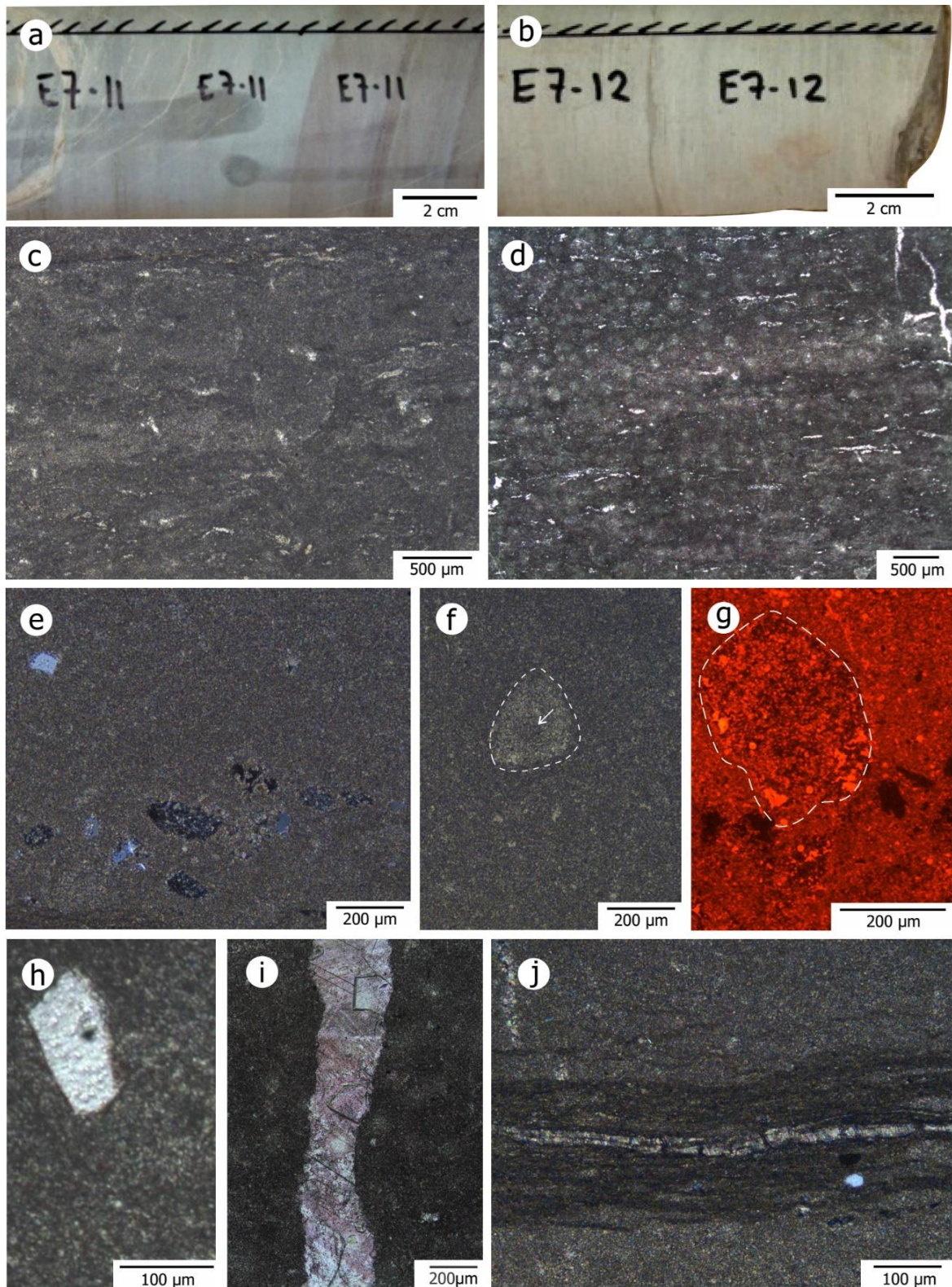


Figure 3.4: Macroscopic sample and main petrographic features of the massive limestone facies of the Avellaneda Formation. (a) Greenish to reddish purple massive carbonate (58-57 mbs). (b) Light-gray massive centimeter-scale muddy-carbonate beds (52-51 mbs). (c) General aspects of carbonate mud rich facies. (d) Contours of sub-rhombic calcite separated by micritic matrices (after alizarin red-S and potassium ferricyanide protocol). Purple colour in (d) denotes the presence of ferroan calcite. (e) Nodular features likely formed gypsum replaced by carbonate. (f) Rounded carbonate nodule marked

by lighter microspar (white dashed line) with a dark core of microcrystalline lime-mud (indicated by white arrow). (g) CL image helps to delineate the carbonate nodule (no visible nucleus) and within display partial recrystallization. The CL image also suggests a ferrous composition. In the same image, note the presence of cavities (non luminescent). (h) Angular to sub-angular detrital quartz grains with corroded borders. (i) Microfractures are filled/cemented by coarse calcite spar. (j) Bedding-parallel fibrous calcite veins.

### 3.4.1.3. MF3 - Laminated lime mudstone microfacies

#### Description

This microfacies is better expressed in E34 but is also recognized in the intermediate section of E7 (Figure 3.2). Beds range in thickness from a few centimeters up to 20 cm and are typified by gray to pale brownish lime mudstone showing faintly parallel laminae in hand samples (Figure 3.5a). In thin-section, they consist of alternating brown argillaceous/clay-dominated laminae and argillaceous/clay-poor mud-supported laminae (Figure 3.5b). The laminae are evenly spaced with carbonate dominated layers thicker than argillaceous/clay laminae (Figure 3.5c). Lenses of blocky microspar morphology appear to follow the laminae (Figure 3.5d). Siliciclastic components consist essentially of quartz grains of fine sand size ( $< 125 \mu\text{m}$ ) and rarely exceeding  $150 \mu\text{m}$ . Detrital quartz consist of mostly subangular to subrounded grains floating on the carbonate matrix (Figure 3.5b).

The presence of nodular fabric showing displaced growth is a relevant feature of this facies (Figure 3.5e - 3.5f). These nodules exhibit preferred orientation sub-perpendicular to the original bedding plane of the carbonate and are usually arranged laterally, resulting in a columnar appearance (Figure 3.5e and 3.5f). These patches commonly grow and push the lamination leading to soft deformation (Figure 3.5g). The vertically elongated nodules described in MF3 may vary from  $250$  to  $1000 \mu\text{m}$ , on their longest axis. Generally, it demonstrates a subspherical to ellipsoidal shape, or shows a polygonal pattern like triangular shape with the apex pointing upwards (Figure 3.5f). Other nodular types comprise more or less rounded features with no evidence of a polygonal pattern (Figure 3.5g). Nodules are mainly composed of calcite that form an interlocking mosaic of anhedral equant crystals of different sizes. However, nodules can also contain smaller ( $\sim 50\text{-}80 \mu\text{m}$ ) interlocked plates of gypsum. Sometimes, prismatic crystals, likely of anhydrite, showing high birefringence colors can be found associated with nodules.

SEM-EDS analysis demonstrates that both microcrystalline and large mosaics of rhombic crystals are chemically composed of  $\text{CaCO}_3$  (Figure 3.6a). Under CL, the

microcrystalline phase is mostly orange-dull reddish colored. From CL petrography we can identify nucleus or inclusions inside individual crystals composed of patches of much finer crystalline calcite (Figure 3.6b – 3.6c). These inclusions generally show a dull red to dark response involved by bright orange-red bands under CL. Textured crystals reach 20–60  $\mu\text{m}$  in size (occasionally up to 80  $\mu\text{m}$ ). Laminated lime-mudstone facies exhibit inter-particle and mainly vuggy porosities (Figure 3.6d - 3.6e) filled by single and, more rarely, aggregates of rhombohedral calcite crystals (Figure 3.6d). The crystals are clean, without nucleus or inclusions (Figure 3.6e). Fractures are rare and filled by large mosaic calcite spar.

### **Interpretation**

MF3 microfacies are compatible with a continuous sediment accumulation by suspension settling under relatively weak and slow flow under bottom-water deposition conditions (Tucker and Wright, 1990). Physical conditions like that are commonly reported in subtidal and/or protected coastal settings (Tucker and Wright, 1990). In the Avellaneda Formation, elongated nodules appear to contain gypsum plates and anhydrite, and still preserve the original morphologies. The presence of displacive and vertically aligned nodules forming columnar features are similar to bottom growth evaporites developing in subaqueous conditions (Warren, 1982; Schreiber, 1988; De Putter et al., 1994). Another alternative to the genesis of the nodules and columnar displacive features involve crystallization in early diagenetic stages at shallow subsurface (Warren and Kendall, 1985; Lokier, 2013; Warren, 2016). However, for MF3 deposits the lack of any evidence of subaerial features rules out this possibility.

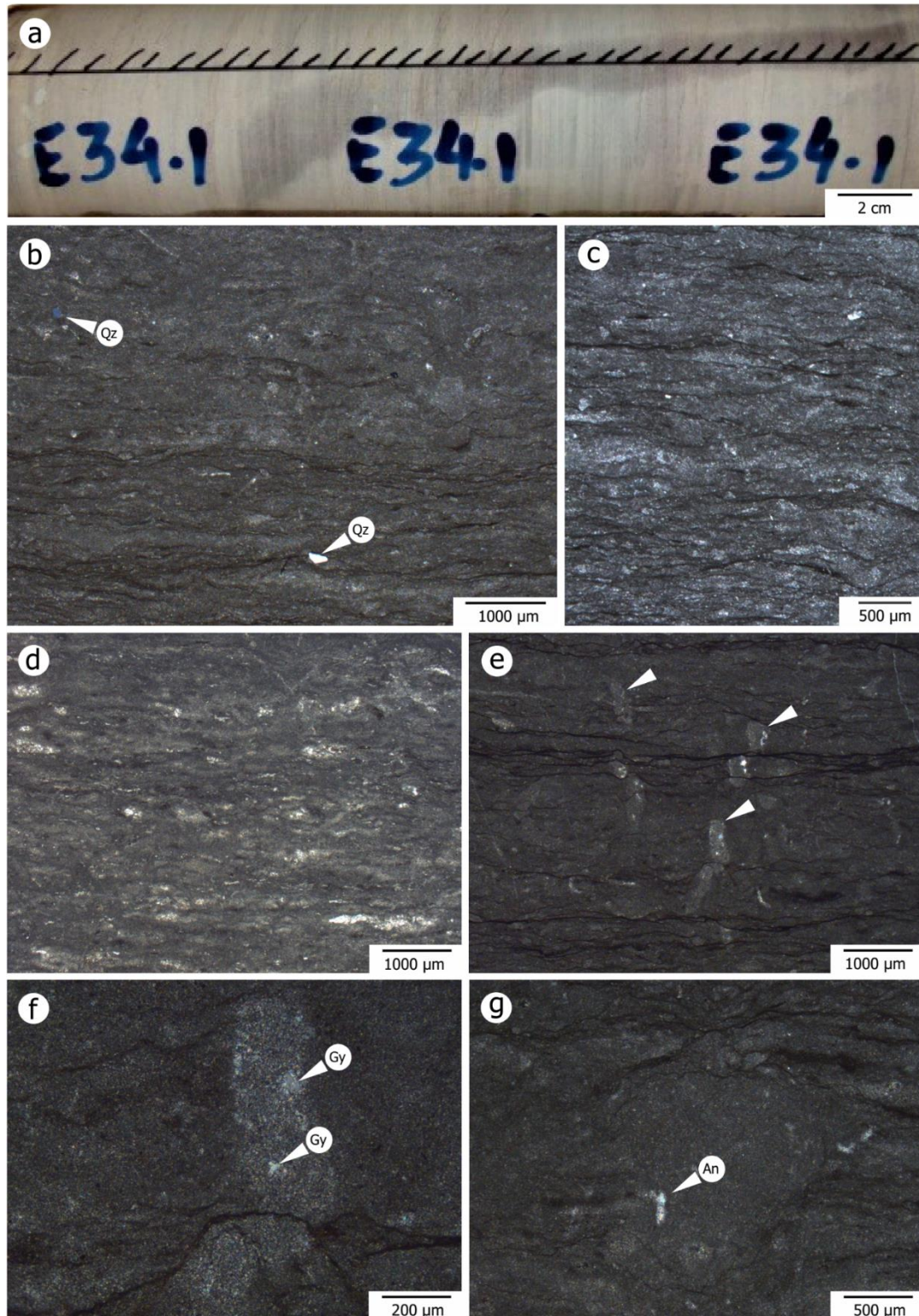


Figure 3.5: Laminated lime mudstone facies. (a) Core sample with plane-parallel laminae. (b) General aspect of MF2 marked by occurrence of millimeter-scale lamination. White arrow points out the presence of quartz grains. (c) Note how each lamina is regularly spaced. (d) Blocky microspar morphology that accompanies the laminae. (e) Vertically oriented nodules developing a columnar arrangement (highlighted by white arrows). (f) Detail of nodules displaying internally anhedral equant crystal of calcite and locally, probably relict crystal of calcium sulfate minerals. (g) Nodular carbonate feature that interrupts the lamination.

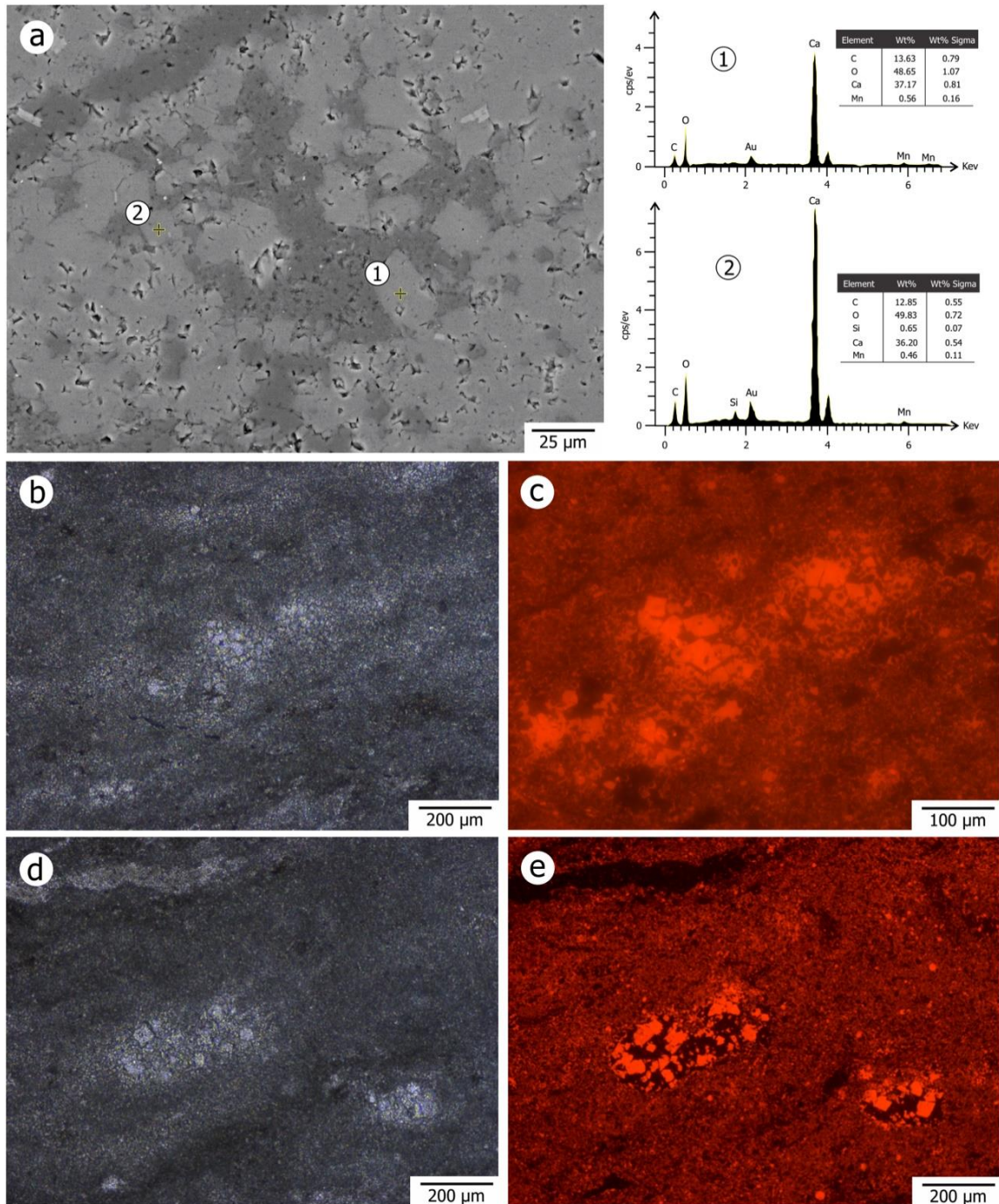


Figure 3.6: SEM-EDS analysis, petrography and cathodoluminescence images of the laminated lime-mudstone. (a) Scanning electron microscopy (SEM) image showing rhombic crystals aggregated. Energy dispersive X-ray spectrometer (EDS) spectrum of 1 to 2 showing the typical composition of the calcite crystals, with minor amounts of Si. (b) Recrystallized carbonate constituents. (c) CL image, note the presence of finer crystalline calcite as nucleus or inclusion. (d) Likely vuggy porous. (e) Aggregates of rhombohedral calcite crystals filling vug porosity. Observe the clear aspect of crystals, with no nucleus and free of inclusions.

#### 3.4.1.4. MF4 - Laminated microbial mats microfacies

##### Description

This microfacies occurs dominantly in the intermediate portion of the Avellaneda Formation (Figure 3.2 and 3.3). Overall, representative core samples display well-developed mm- to cm-thick lamination with close spacing, but irregularly spaced (Figure 3.7a and 3.7b). In closer view, gray/whitish and dark brown laminae form alternate couplets giving a striped pattern to some core samples (Figure 3.7a). Dark laminae are likely rich in organic matter and relatively thin, and commonly show a crenulated or pustular aspect, whereas white-clear layers comprise carbonate-rich layers and are typically thicker (Figure 3.7b). A detailed description indicates that laminae is laterally persistent with wavy-crinkly appearance and sometimes anastomosed (Figure 3.7c). Laminations are usually enhanced by almond shapes (fenestrae laminae) characterized by aligned flat to rounded-shape cavities filled by cements (Figure 3.7d and 3.7e). Occasionally, we observe that dark laminae form small reliefs of <10  $\mu\text{m}$  in height that may evolve into domical microstructure (Figure 3.7f). Micropeloids range from 50-100  $\mu\text{m}$  in diameter and structures similar to grumous microstructure are also described (Figure 3.7f). Laminations can show vertical ruptures sealed by recrystallized carbonate phases. In other cases, there are small protuberances capable of arching the laminations without causing their rupture (Figure 3.7g).

Microfacies of laminated microbial mats exhibit delicate structures characterized by vertical orientation and disposed perpendicular to the lamination of frayed edges in crinkly laminae (Figure 3.8a and 3.8b). Locally, we observed small spherical features with diameter around 250  $\mu\text{m}$ , resembling bubbles surrounded by darker laminae (Figure 3.8c and 3.8d). CL images show these putative bubbles are entirely filled by microspar and/or blocky spar (Figure 3.8d). These structures occur associated with fenestrae composed of 'birds eye'-shaped cavities, usually 1–5 mm across (Figure 3.8d). Under the petrographic microscope, we note the presence of vertical cracks that cut through the horizontal thin lamination. Cracks display an isolated spindle shaped and sinuous morphology (Figure 3.8e). Vertical cracks can reach up to 500  $\mu\text{m}$  in size. They are filled by a mosaic of equant calcite crystals (Figure 3.8f).

We also found in these facies small, but well formed, doubly terminated crystals ca. 50 to 100  $\mu\text{m}$  wide and 200 to 250  $\mu\text{m}$  in length (Figures 3.9a, 3.9b). These crystals are scattered, embedded in carbonate and organic-rich layers. The composition of these crystals, analyzed by EDS, shows that they are essentially composed of Ba, S and O (Figure 3.9b). The SEM image also shows another lamellar to platy mineral phase that appears to cut the barite crystal

(Figure 3.9b). X-ray spectroscopy indicates the presence of Mg-Fe-Al, together with O-Si in these crystals.

### **Interpretation**

Laterally continuous thin, wrinkled, and curled laminations is widely used as a diagnostic of stratified microbial communities (Noffke et al., 2013). Dark micritic crinkled laminae laterally merging or fusing together and locally having frayed edges are also typical features related to microbial mats (Schieber et al., 2007). These sedimentary textures are reported for the first time in the Avellaneda Formation and indicate a participation of microbial activity during its deposition. Microbial mats facies are also commonly recorded in peritidal environments associated with siliciclastic facies (Warren et al., 1985; Tucker and Wright, 1990; Noffke et al., 2003, 2006; Jahnert and Collins, 2012). Fenestrae fabric (Figure 3.8d) are common in peritidal deposits and typically form because of desiccation and gas generation resulting from the decay of microbial mat-derived organic matter (Shin, 1968; Shin 1998b; Tucker and Wright, 1990; Tucker, 2001; Duda et al., 2016). In periods of low energy, microbial carpets colonize and spread along the seabed (Bose et al., 2012). The persistence of microbial mats in the Avellaneda Formation is a solid indicator of low-energy settings. Flat laminated microbial mats are frequently associated with the photic zone in flattened and undisturbed areas (Schieber et al., 2007; Franks and Stolz, 2009). Periods of drying out and eventual subaerial exposure could cause breaks and ruptures in the microbial mat tissue (Tucker and Wright, 1990; Schieber et al., 2007; Pratt 2010). Cracks with sinuous morphology are related to burial responses in muddy beds (Lindholme 1987). Short-time wetting and drying cycles are inferred by pseudomorphs after gypsum-anhydrite crystals replaced by BaSO<sub>4</sub> and desiccation cracks reported here (Forjanés et al., 2020; Lakhdar et al., 2020; McMahan et al., 2021).

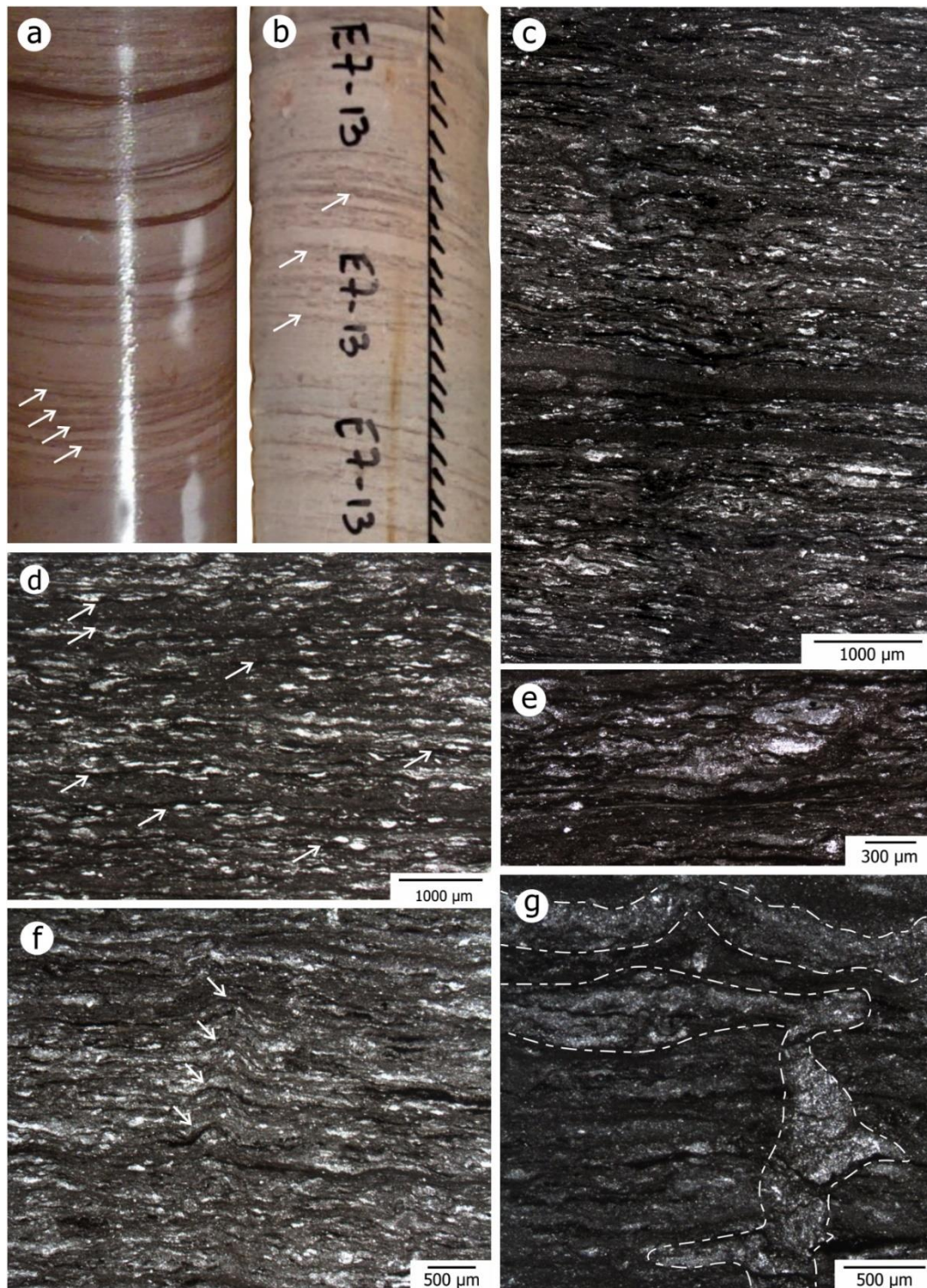


Figure 3.7: Examples of laminated microbial mats from Avellaneda Formation. (a) Alternate dark brown putative organic rich layers and calcium rich layers forming a striped pattern. (b) Thin-lamination showing a crenulated or pustular aspect. (c) Vertical section showing dark layers composed of organic remains of microbial mats interbedded with massive limestone. (d) Stratiform microbial mats show laminoid fenestral cavities occluded by calcite cementation. (e) Detail of irregular anastomosing microbial lamination. (f) Domical microstructure or pinnacles of spherical morphology of amorphous organic matter. Note the clotted peloids textures. (g) Discontinuities and break in microbial mat layers (dashed white line).

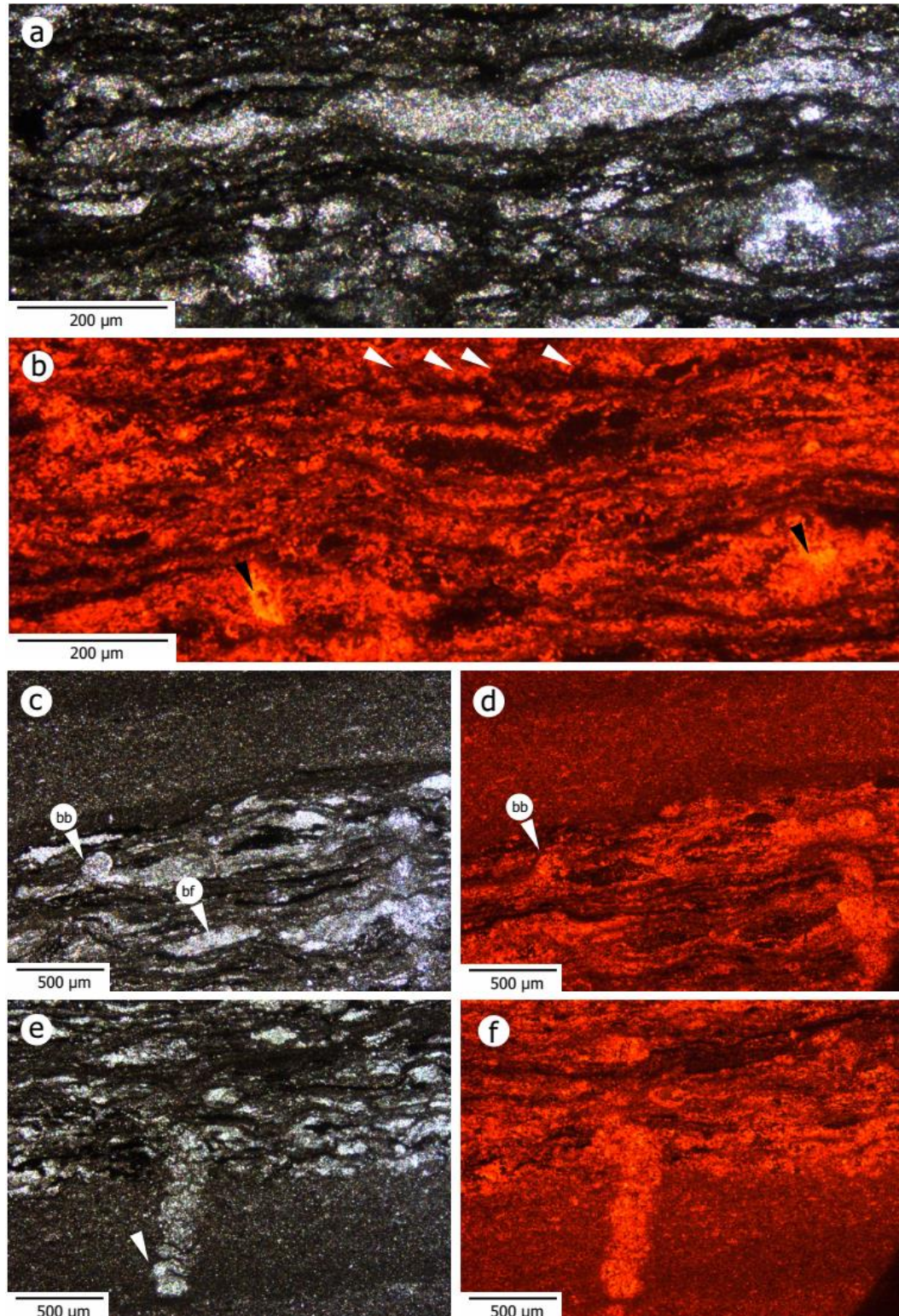


Figure 3.8: Petrography detail and CL imagens produced from microbial mat facies. (a) Large fenestral porosity. (b) CL image helps to reveal frayed edges arranged perpendicular to lamination (see white arrow). Note how voids are occluded by precipitates (black arrow). (c) Spherical putative bubbles (bb) and fenestral 'birdseye'-shaped cavities (bf). (d) CL imagens show a recrystallized carbonate conforming bubble (bb) and fenestral cavities. (e) Cross section view of shrinkage crack. Look at the sinuous or tight ptygmatic folds (see white arrow). (f) CL image display that crack fill is formed by microspar calcite.

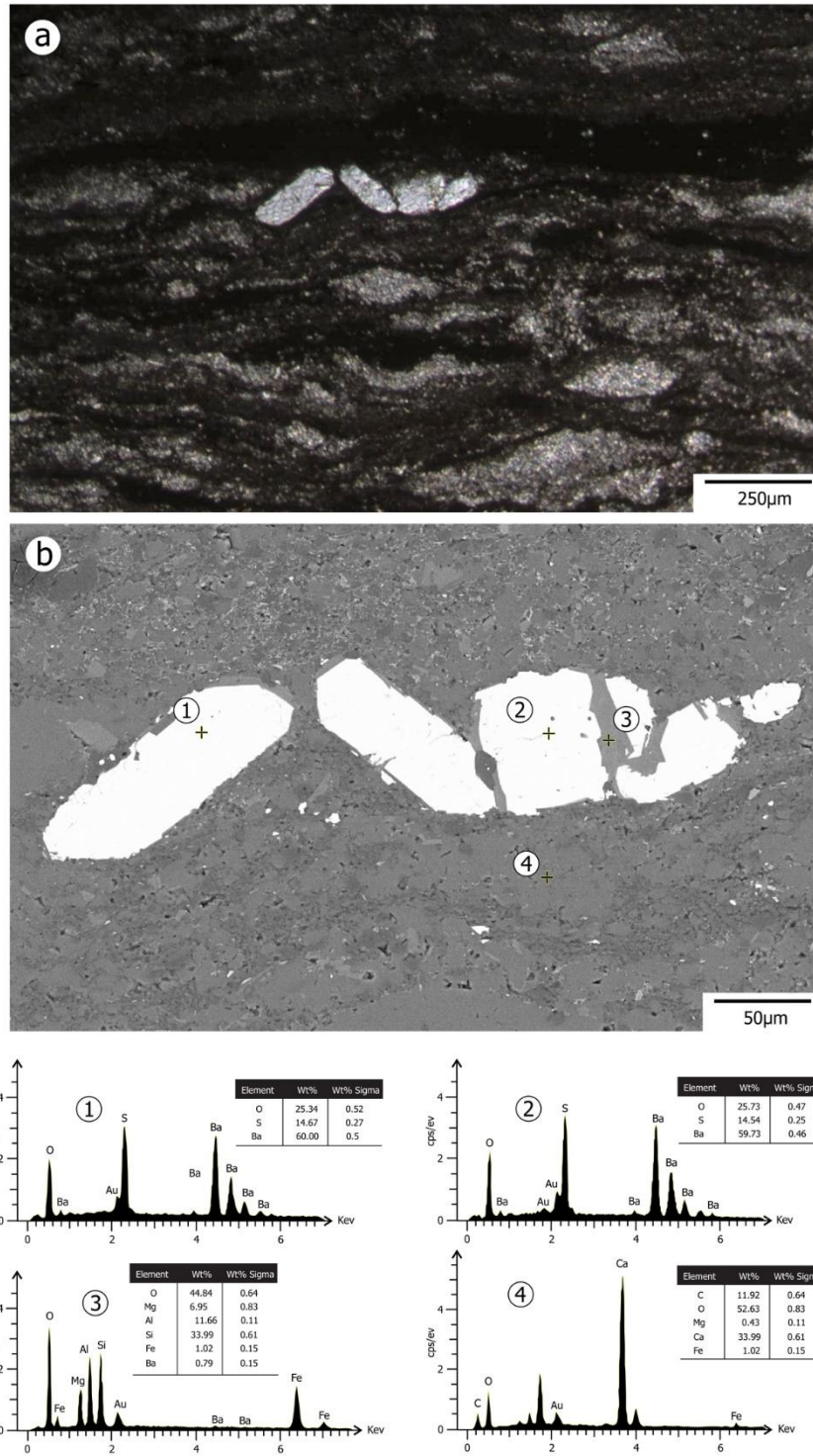


Figure 3.9: Petrography and SEM images coupled with EDS analysis of crystal aggregates associated with microbial mats. (a) Euhedral cluster of barite nanocrystals embedded in carbonate rich sediments. (b) SEM images showing details about crystal aggregates. Note the presence of inclusion located on the border of crystal and small inclusion inside of some crystal. EDS spectrum of the crystal aggregates – black cross with ‘1’ and ‘2’ in (b) – indicates the relatively equal proportion of Ba, S and O in both crystal samples selected, showing the typical composition of the barite crystals. Black cross with ‘3’ in (b) – specifies a composition with Fe-Mg-Al plus Si-O, suggesting some mineral platy mica minerals, likely chlorite. ‘4’ in (b) – show the presence of carbonate-rich phases around the crystal of barite.

#### 3.4.1.5. MF5 - Laminated lime mudstone with nodular to microenterolithic gypsum/anhydrite microfacies

##### Description

MF5 occurs at the upper portion of drill cores E7 and E34 (Figure 3.2). In drill core H9, this microfacies is described between 68 and 66 mbs (Figure 3.2). Core samples show a brown to gray color, and finely laminated fabric with nodular forms (Figure 3.10a), sometimes connected (Figure 3.10b). This microfacies seems to mark the end of the deposition of carbonate layers and hosted evaporites. MF5 deposits are overlaid by sedimentary clastic deposits of MF6. This contact is sharp, forming an abrupt and irregular surface (Figure 3.10c and 3.10d). Microscopic analysis demonstrates that the lamination corresponds to a very thin alternation of millimetric thickness, composed of dark gray, organic-rich laminae alternated with light carbonate-rich layers (Figure 3.10e). Organic-rich intervals form a continuous thin lamina with wavy and irregular aspects (Figure 3.10f). Carbonate phases comprise cryptocrystalline to microcrystalline mudstones and typically have a light to dark brown appearance in crossed polars. Carbonate-rich areas consist of anhedral,  $\leq 10$  mm in size, sub-spherical crystals and more rarely subhedral to euhedral. In addition, there are sub-rhombic to rhombic calcite crystals, many with cloudy cores and more clear rims (Figure 3.10f). Occasionally, there are some single floating quartz sand grains randomly distributed throughout the facies.

The nodules display a variable morphology that include ovoid to irregular shapes (Figure 3.10c), lenticular or almond shapes (Figure 3.10g), or even large coalescent forms, resembling microenterolithic structures (Figure 3.10i). The nodules are flattened and elongated parallel to the lamination (Figure 3.10g). The diameter of the nodules varies from a few millimeters for isolated forms to centimeters for those with coalesced/microenterolithic arrangement (Figure 3.10g). The nodules push and bend the laminations into the surrounding (Figure 3.10g). Small scale convolutions are also observed, even without the presence of nodules. Nodules are made of a fine felted mass of 100  $\mu\text{m}$  long lath crystals, likely anhydrite, enveloped by cohesive carbonate mud or hosted in more organic-rich laminae (Figure 3.10h). CL images reveal that despite the thin lath crystals found inside the nodular features, these nodules are essentially made of  $\text{CaCO}_3$ . Non-luminescent phases under CL are associated with sulfate minerals (Figure 3.10h).

Petrographic microscope thin-section analysis combined with SEM-EDS shows the presence of large and well-developed crystals preserved within the sediment (Figure 3.11a).

SEM-EDS analysis indicates a composition of barium sulfate. Crystals are subhedral, exhibiting a lenticular and/or tabular morphology, and have a preferred alignment concordant with the horizontal lamination (Figure 3.11a). More rarely barite crystals can be randomly orientated (Figure 3.11). Tabular crystals have flat faces with an elongate parallelogram shape (Figure 3.11a-3.11d). Crystal sizes range in length from 100  $\mu\text{m}$  to 650  $\mu\text{m}$ , and width from 10  $\mu\text{m}$  to 100 $\mu\text{m}$ . They may enclose variable amounts of sediment or be clear and free of inclusions. Inclusions are primarily of carbonate minerals. The impurities range in composition from carbonate to the clay of the surrounding matrix. Such impurities may occur with a random orientation, resembling a poikilotopic texture, or yet be aligned parallel to the growth faces of the gypsum crystals. In some cases, barite encloses tabular, platy crystals or radiating crystals shaped like a fan associated with chlorite (Figure 12c). In addition, EDS analysis indicates that large barite crystals are also associated with copper-iron sulfides (Figure 12d). Subhedral to eudreal chalcopyrite, up to 30- $\mu\text{m}$ -sized occurs as inclusions.

### **Interpretation**

Flat, thinly-laminated sediments composed of alternated organic-rich and carbonate-rich layers are commonly associated with algal mats (Warren and Kendall, 1985). The presence of isolated nodules enveloped by cohesive clayey carbonate mud and coalesced nodules resembling thin microenterolithic structures, indicates intra-sediment growth of anhydrite that may have taken place above the water table in a partially exposed surface of an arid region (Warren 2010; Warren 2016). Displaced growth causes gentle bends on laminations and reinforces an intra-sediment growth. Crystal morphologies such as prismatic, felted laths and satellite-shaped laths are locally present in the nodular portions and are likely derived from the precursor anhydrite fabric of the nodules (Kendall, 2010; Warren 2010; Warren 2016). Thus, the nodular structures at the top of the laminated gypsum indicate the end of the sporadic desiccation episodes. This type of deposit was attributed to coastal flats development in supratidal conditions (Kinsman, 1969; Schreiber et al., 1976). Supratidal records are also characterized by the presence of penecontemporaneous anhydrite and are often capped by an erosion surface (Pratt, 2010; Kendall, 2010; Quijada et al., 2020). This last scenario is similar to the vertical arrangement of microfacies in Avellaneda Formation. The conversion of gypsum to anhydrite can take place at any stage of burial. However, the presence of well-preserved depositional fabric, the alignment of crystals and micronodules and the lack of diagenetic indicators suggesting deep burial (veins, fractures and stylolitizations) implies that evaporites hosted in carbonates in the Avellaneda Formation

likely precipitated during early diagenesis and are therefore penecontemporaneous to deposition. The occurrence of large prismatic crystals of barite ( $\text{BaSO}_4$ ) is probably related to gypsum-anhydrite replacements (Forjanes et al., 2020; Györi et al., 2020).

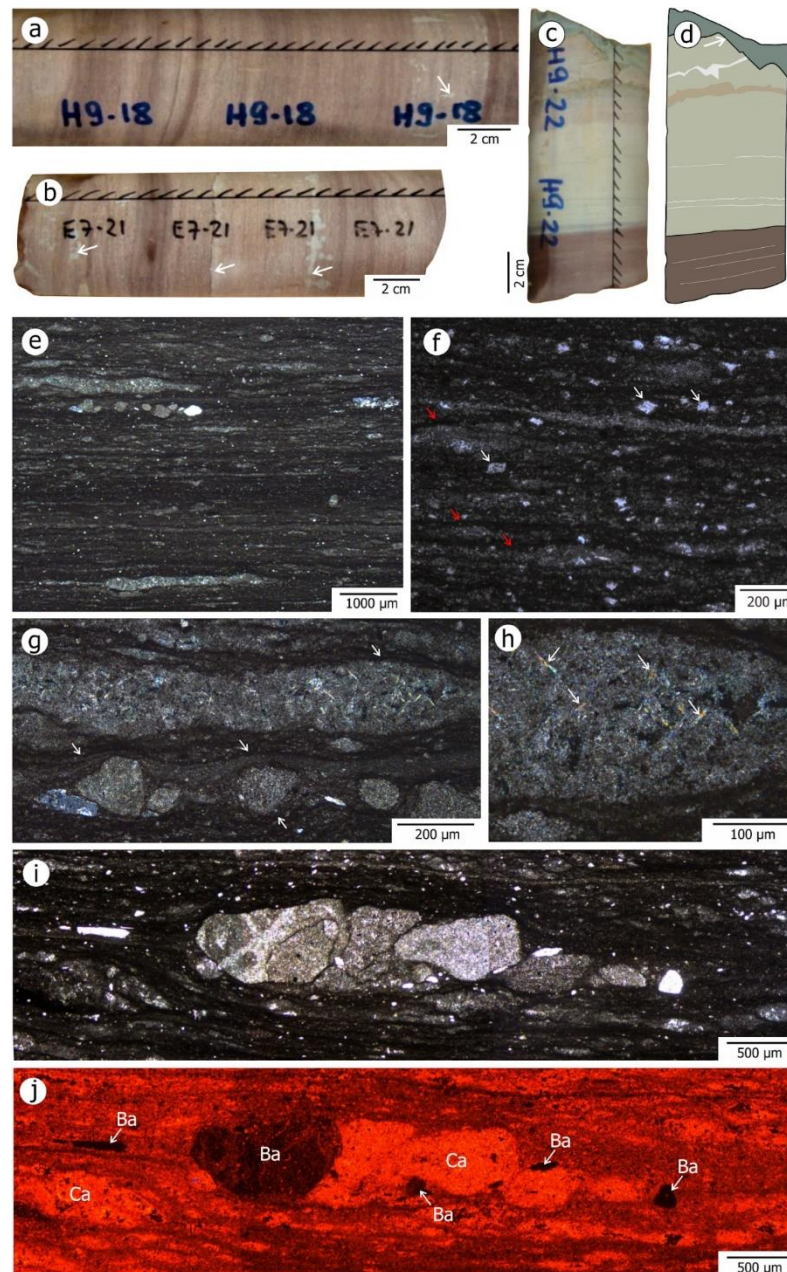


Figure 3.10 – Main macroscopic features and microscopic sedimentary textures of MF5. (a) Core samples display a brown to gray color and thinly-laminated aspects with forms like nodules (see white arrow). (b) Isolated and bands of nodular features in hand sample (white arrow). (c) Contact between MF5 deposits and sedimentary clastic sediments of the MF6. (d) Representative illustration of abrupt contact between MF5 and detrital deposits of the MF6. (e) Overview of typical thinly laminated appearance of the facies, show nodules and large tabular-prismatic crystal aligned with lamination. (f) Detail of putative organic-rich intervals (red arrow), which define continuous dark-thin lamina. Also note the presence of sub-rhombic to rhombic calcite with cloudy cores (stands out by white arrow). (g) Laminated fabric with separated nodules and lenticular to stretched shaped nodules. Note as nodular

features induce bending in surrounding lamination (white arrow). (h) Details from nodular features indicate dusty inclusions outlining felted lath texture typically of anhydrite (see white arrow). (i) Coalesced nodules/microenterolithic structure that deform and truncate enclosing laminae. (j) Coalesced/microenterolithic viewed with the aid of cathodoluminescence technique. Note how nodules are partially, or sometimes completely replaced by carbonate (Ca). Also observe the non-luminescent portions that indicate authigenic, possibly relics of evaporites, in this case barite (Ba).

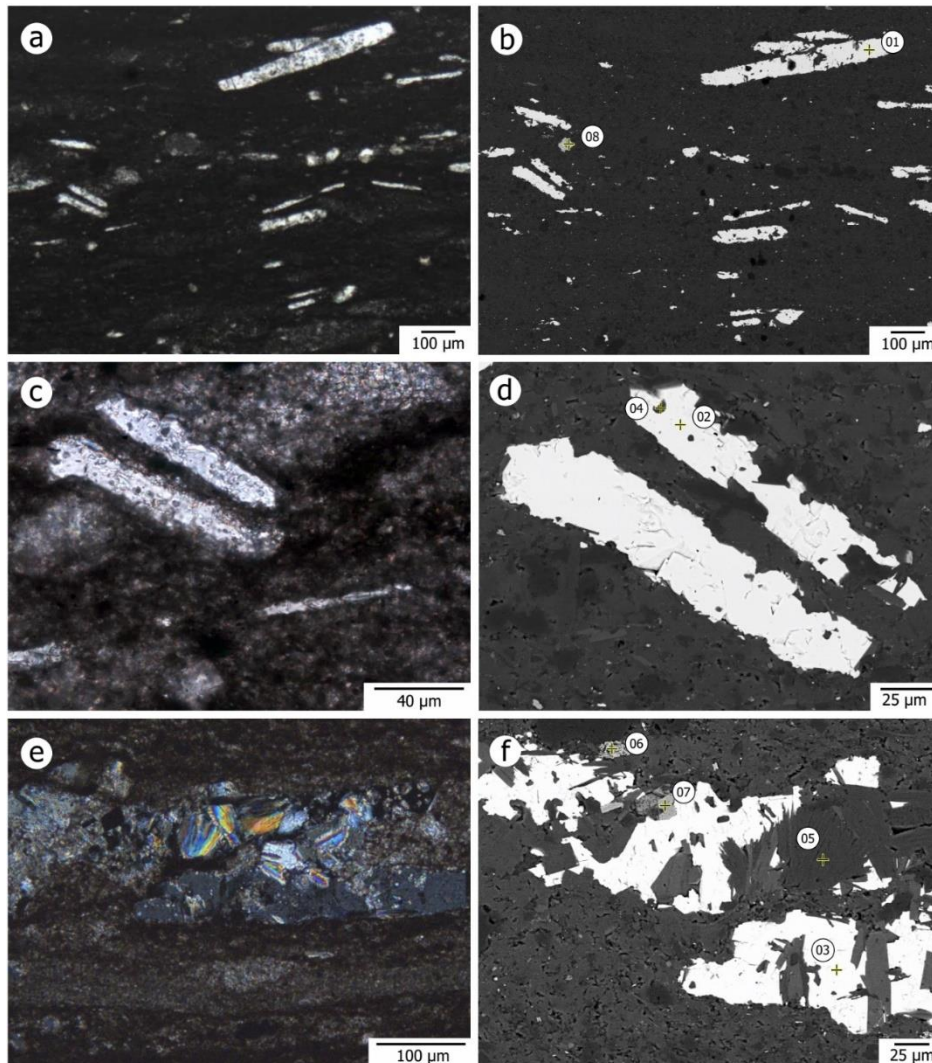


Figure 3.11: Petrography and SEM-EDS analysis. (a) Crystals accumulate as layered to laminated sulfate phases. (b) SEM-EDS reveal large barium sulfate crystals up to 120μm. EDS analysis is indicated by numbers (01: BaSO<sub>4</sub> - barite; 08: CuFeS<sub>2</sub> - chalcopyrite). (c) Optical image of prismatic, double terminated crystals also shows the occurrence of carbonate inclusions. (d) SEM image of the same crystals. EDS analyses are indicated by numbers (1: BaSO<sub>4</sub> crystal; 2: CaCO<sub>3</sub> inclusion). (e) Large prismatic crystal covered by plate minerals and mosaic of microspatic calcite; note the occurrence of opaque minerals showing subhedral to euhedral shape. (f) SEM image of barite crystal showing several inclusions. EDS analyses are indicated by numbers (3: large prismatic crystals of BaSO<sub>4</sub>; 7 and 8: Fe-Ti oxides and 5: chlorite).

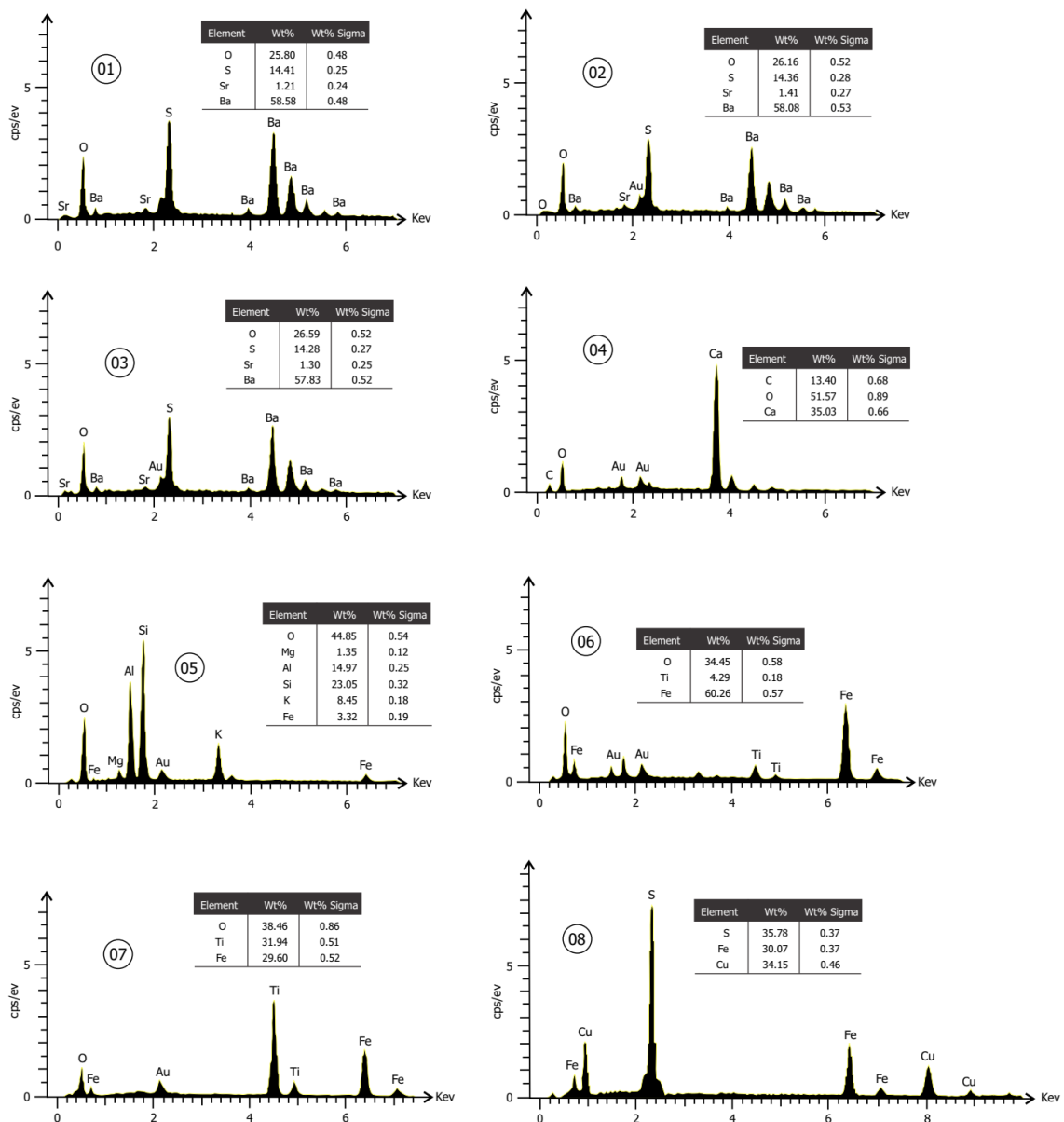


Figure 3.11 (continuation): Petrography and SEM-EDS analysis. 01, 02 and 03: BaSO<sub>4</sub> - barite; 04: calcite; 05: chlorite; 06 and 07: Fe-Ti oxides; 08: CuFeS<sub>2</sub> – chalcopyrite)

### 3.4.1.6. MF6 - Claystone to massive siltstone microfacies

#### Description

Clastic sedimentary rocks occupy the upper part of the Avellaneda Formation and were described exclusively in the upper portion of drill core H9 (Figure 3.2). Siliciclastic sediments start at around 66 mbps and dominate the rest of the succession (Figure 3.2). At hand sample, rocks range from gray through brown and reddish to brownish color, commonly structureless and homogeneous (Figure 3.12a and 3.12b).

The petrographic thin-sections revealed a mixture of clay, silt and very fine sand (Figure 3.12c-3.12e). This mixture is mainly composed of quartz, micaceous minerals and feldspar grains. Quartz is the major component, comprising more than 80% of the rock. It is generally poorly sorted and exhibits angular to subangular shape (Figure 3.12d). The size of quartz grains typically ranges from very fine silt size to fine sand (Figure 3.12d). Micaceous minerals may display a platy to elongated tabular shape, or even curved shapes. The size of platy micaceous minerals is around 40-60  $\mu\text{m}$  in length, while elongated tabular shape can reach 120  $\mu\text{m}$ . Micas occur chaotically distributed (Figure 3.12d). Feldspar grains are often tabular, subrounded shapes with edges partially corroded. The size of feldspar grains varies from 20-35  $\mu\text{m}$ . Black to brown, contorted, and tangled fragments resembling filaments also represent a widespread component (Figure 3.12d). They are uniserial (unbranched) and can reach up to 200  $\mu\text{m}$  in length and up to 30-45  $\mu\text{m}$  in width (Figure 3.12d). Plastic deformation structures (Figure 3.12e) are characterized by contorted and asymmetrical folds in mud-rich layers (Figure 2.12f). Slightly muddy organic matter is also observed occupying the space between the grains. Calcite appears as a cement (Figure 2.12g) that commonly occurs as optically continuous patches, less than one millimeter in diameter, some of which enclosing detrital grains and forming a poikilotopic texture (Figure 2.12h). Opaque minerals, likely Ti-Fe oxides, are observed locally. Black to brown organic fragments are accessory components.

### ***Interpretation***

Detrital sediments included in MF6 were probably transported into the depositional site. The occurrence of contorted and tangled fragments interpreted as putative remains of previously stabilized microbial mats also suggest potential transport and reworking. The source areas of filamentous microbial mat may be shallow peritidal lakes, lagoons and their adjacent flats, on the other hand, accumulation areas may be subaqueous (Schieber, 1999; Schieber et al. 2007). The rework from partially lithified microbial mats and re-deposition can be triggered by marine flooding on top of microbial mats laminated facies, especially in tidal dominated environments (Pratt, 2010; Kendall, 2010). Massive structures in fine sediments can be caused by very uniform and possibly rapid deposition (Lindholm 1987; Collinson and Thompson, 1982).

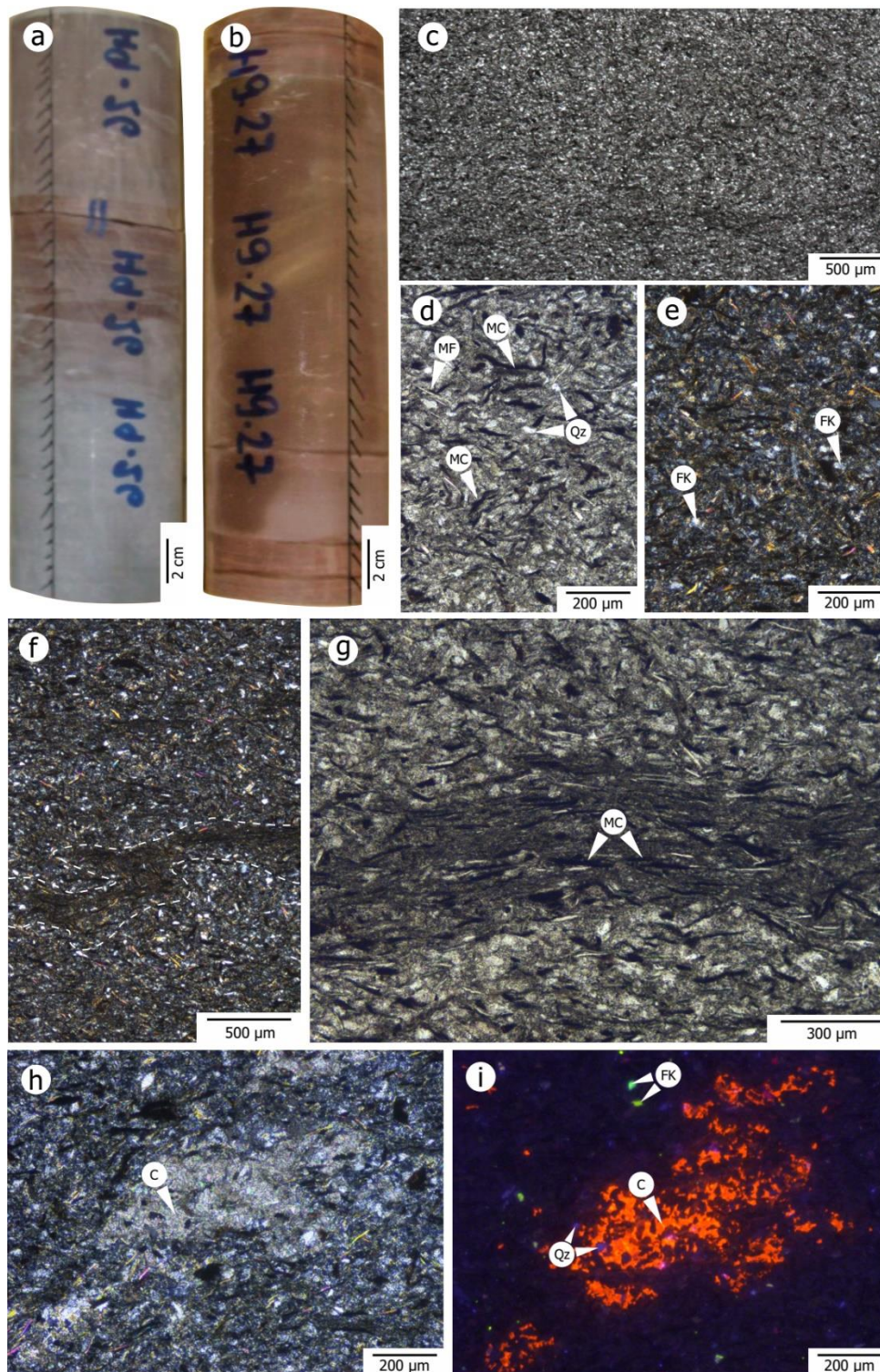


Figure 3.12: Thin-section photomicrographs and CL image of detrital components and main features in claystone to siltstone facies of the Avellaneda Formation. In (a) and (b) show structureless and homogeneous hand samples. (c) Thin-section showing a fine-grained rock with relatively even grain size. (d) Details exhibit the main constituents that include quartz (Qz), mica flakes (MF) and mat chips fragments (MC). (e) Feldspar grains (FK). (f) Plastic deformed layers (white dashed line) found in claystone to siltstone facies. (g) Note the preferential orientation of mat chips fragments. (h) Sparry carbonate cements fill irregular pockets. (i) CL image showing poikilotopic calcite cement replacing the grains margins. In (i) Qz is quartz, C is carbonate and FK is grains of feldspar.

### 3.4.2 - Carbon and oxygen isotopes

Each core was sampled for carbon and oxygen stable isotope analyses. Samples selected for isotopic analyses were taken from fine-grained micrite/microsparite fabric, a ubiquitous characteristic of Avellaneda Formation. Carbon and oxygen stable isotopes were plotted against the stratigraphic height favoring the observation of trends (Figure 3.13). The E7 core displays  $\delta^{13}\text{C}$  values ranging from  $-2.53\text{‰}$  to  $+4.65\text{‰}$  and  $\delta^{18}\text{O}$  values from  $-15.47\text{‰}$  to  $-13.59\text{‰}$  (Figure 3.13). In the E34 core,  $\delta^{13}\text{C}$  values extend from  $+0.97\text{‰}$  to  $+4.45\text{‰}$  and  $\delta^{18}\text{O}$  values vary from  $-15.49\text{‰}$  to  $-14.72\text{‰}$  (Figure 3.13). For samples recovered from H9 core,  $\delta^{13}\text{C}$  values vary from  $-3.31\text{‰}$  to  $+4.49\text{‰}$  and  $\delta^{18}\text{O}$  values vary from  $-15.47\text{‰}$  to  $-13.44$  (Figure 3.13).

By comparison all drill cores show a similar isotopic behavior marked by a decrease in  $\delta^{13}\text{C}$  values toward the up section, which ends as a negative excursion at the top of sections. This negative trend is clearly reproduced in E7 and H9 stratigraphic sections (Figure 3.13). A comparable behavior is also observed in the  $\delta^{18}\text{O}$  signal, however, as a major and gradual negative excursion along the whole studied interval, in a narrow range of variation. The cross-plot of  $\delta^{13}\text{C}$  versus  $\delta^{18}\text{O}$  shows weak correlation (Figure 3.14a). Stable isotopes plotted against the stratigraphy reveal that different facies show a distinct isotopic signal. The upper section described in the Avellaneda Formation is composed of microbial mats and gypsum-anhydrite bearing carbonates. Samples taken from these facies of the Avellaneda Formation are more negative in both  $\delta^{13}\text{C}$  and  $\delta^{18}\text{O}$  when compared with the massive to poorly laminated facies from the base of the unit.

### 3.4.3 – Element concentrations (Ca, Mn, Fe and Sr)

In this study, some carbonate samples were analyzed for elemental concentrations (Figure 3.14). The main goals of this analysis were to evaluate the diagenetic history of the samples (based on Mn/Sr, Fe/Sr and Sr/Ca ratios) of the depositional basin. Generally, the Mn/Sr, Fe/Sr are very low, except for a few outliers (Figure 3.14b). All samples have Mn/Sr ratio  $< 8$  with many samples showing values  $< 6$ . Samples display Fe/Sr ratios range from 0.2 to 400, with most samples around 50. The Sr/Ca ratios of the limestone samples collected from the Avellaneda Formation were also calculated (Figure 3.14c). The Sr/Ca ratios show a wide range from 0.0001 to 0.0070, with most samples below 0.0020.

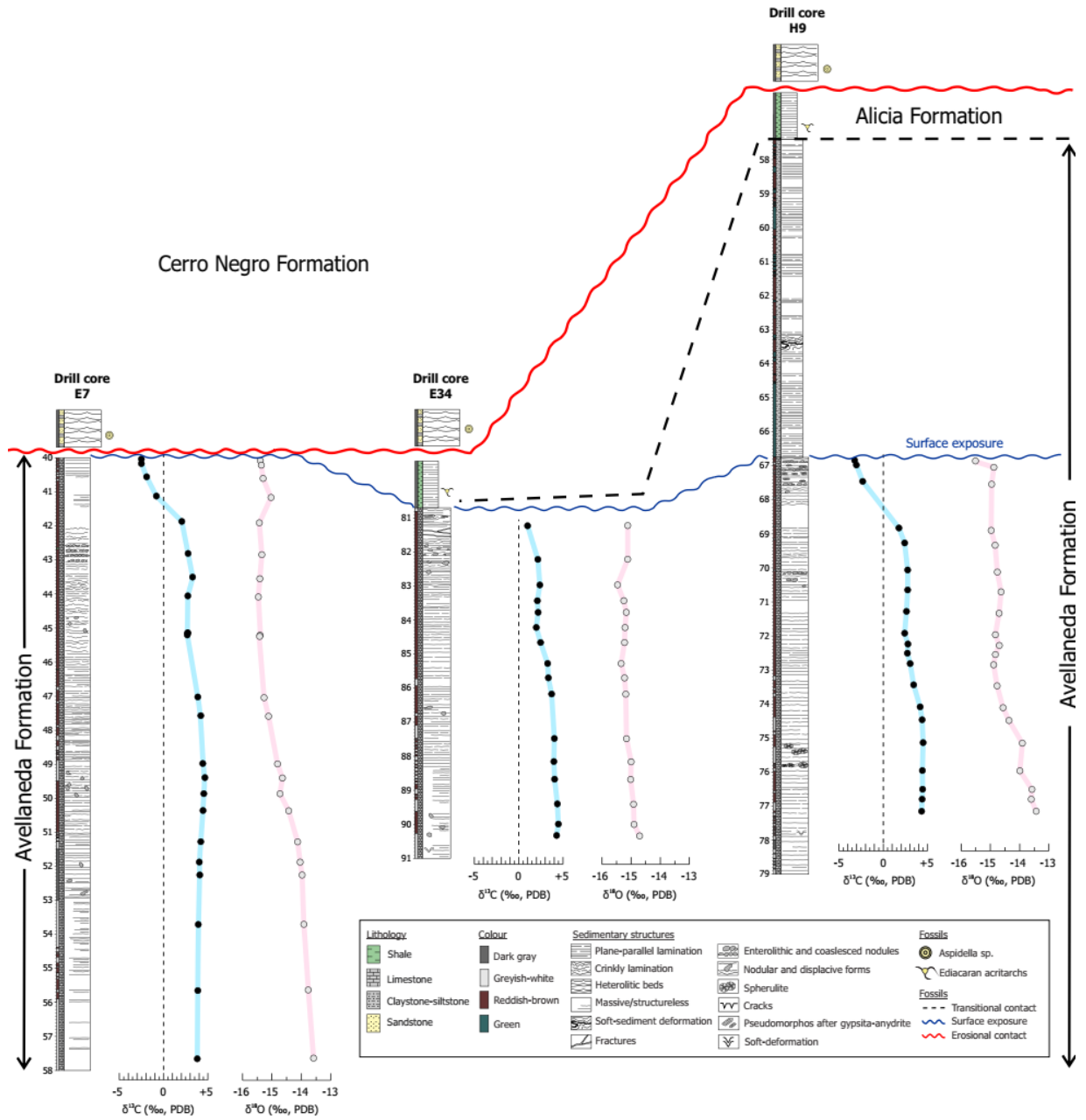


Figure 3.13 – Microfacies and carbon and oxygen isotope variations across the Avellaneda Formation.

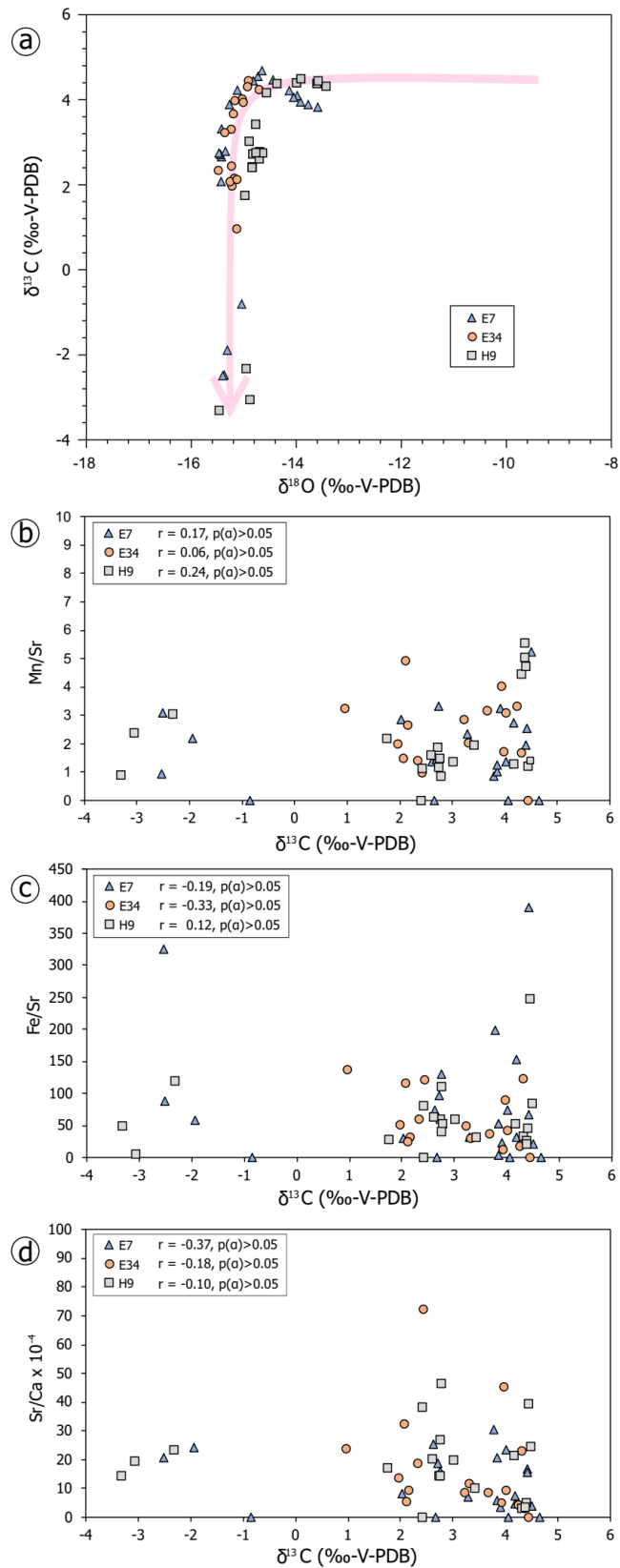


Figure 3.14: Diagrams relating element concentrations and  $\delta^{13}\text{C}$  for samples from the Avellaneda Formation. (a)  $\delta^{13}\text{C}$  versus  $\delta^{18}\text{O}$  cross-plots. (b)  $\delta^{13}\text{C}$  vs Sr/Ca ( $10^{-4}$ ). (c)  $\delta^{13}\text{C}$  vs Mn/Sr. (d)  $\delta^{13}\text{C}$  vs Fe/Sr.

### 3.5. Discussion

#### 3.5.1 – Depositional environment

The analysis of microfacies from the Avellaneda Formation allows us to recognize key depositional features, including primary laminated structures and internal crystal fabrics, grain size and texture of carbonate, as well as the sedimentary structures related to microbial mat activity and pseudomorphs after evaporite minerals. The lateral and vertical microfacies arrangement show that massive to crudely laminated mudstone passes to thin laminated microbial mats, and then are capped by nodular and microenterolithic features enveloped by cohesive micritic carbonate mud (Figure 3.2). These microfacies are commonly reported in low energy muddy tidal flat environments and point to deposition through suspension settling (Wright, 1984). Moreover, the presence of pseudomorphs after gypsum crystals and after anhydrite nodules disrupting the carbonate facies located close to subaerially exposed surface at the top of the Avellaneda Formation suggests these tidal flats experienced certain dryness by evaporation (Wright 1984; Warren 2016, James and Jones 2015). The vertical microfacies distribution is divided into subtidal/intertidal and intertidal/supratidal superimposed by relatively deep-water siliciclastic-rich deposits (Figure 3.15).

The Avellaneda Formation starts with micritic and massive carbonate microfacies of MF1 and MF2 likely related to the subtidal/intertidal zone. The low grain/mud ratio in these microfacies point to deposition in calm waters and low energy environments through suspension settling. This circumstance is found in restricted and protected settings or in a tidal flat setting, such as that already proposed for this unit (e.g. Gómez-Peral et al., 2014; Arrouy et al., 2015). The general lack of sedimentary structures indicative of tractive flow and the predominance of micritic microfacies in the carbonates corroborates the calm water scenario. Fibro-radial calcite spherulite hosted in mud-rich carbonate facies and clay sediments (MF1, basal H9) corroborate a deposition in non-agitated water scenario and also suggests an alkaline-marine water (Mercedes-Martín et al., 2021). Elongated nodules reported in MF3 exhibiting a preferred orientation perpendicular-sub perpendicular to the original bedding of the carbonate structures (Figure 3.5e and 3.5f) point to a subaqueous precipitation growth at the bottom and match the interpretation of a subtidal/intertidal zone depositional setting (Warren, 1982; Schreiber, 1988; De Putter et al., 1994).

The intermediate portion of the Avellaneda Formation is dominated by well-developed lamination consisting in the alternation of dark organic layers and carbonate-rich layers (MF4), which are interpreted as microbial mats. The persistence of microbial mats in the

Avellaneda Formation is a solid indicator of low-energy settings with microbial carpets colonizing the seabed (Bose et al., 2012). Fenestral fabric can be attributed to photosynthetic respiration of microbial mats and is usually considered evidence of tidal influence (Shin 1968; Shin 1986). Laminated microbial mats with wavy-crenulate features and small domes are commonly found in the intertidal zone (Homann et al., 2015). The presence of doubly terminated crystals of sporadic occurrence embedded in MF4 also suggests a shallow subsurface sediment and point to deposition in the upper inter- to supratidal zone (James and Janes, 2015). The sporadic occurrence of vertical cracks attests to the closeness of the surface and corroborates occasional periods of subaerial exposure with desiccation (Warren, 1983; Alsharhan and Kendall, 2003).

The microbial mats (MF4) are capped by layers marked by the ubiquitous presence of anhydrite nodules (MF5; calcitized nodules) which are typical of supratidal flats (Warren and Kendall, 1985; Alsharhan and Kendall, 2003; Warren, 2016). Isolated and coalesced anhydrite nodules are strong evidence for a supratidal zone subjected to sporadic evaporation in very shallow water settings, leading to the precipitation of intrasediment capillary evaporites and episodes of partial drying (Warren, 2016; James and Jones, 2015). Moreover, nodular sulfate horizons (supratidal) are truncated by a sharp surface (see photo E9). These features appear to mark the end of carbonate deposition in the Avellaneda Formation. Several authors consider that these erosive surfaces in ancient deposits constitute unequivocal evidence that anhydrite precipitation occurred shortly after deposition in a supratidal environment (see Warren and Kendall, 1985; Warren, 1991; Kirkham, 1997; Alsharhan and Kendall, 2003; Warren, 2016). Evaporitic minerals, particularly those of group Ca-sulfates are recognized by their low preservation potential, especially when they are in contact with subsaturated fluids like brackish water conditions (Tucker 1976; Schreiber 2000; Warren 2016). This interaction results in a vanished Ca-sulfate phase, but can preserve the shape of crystals and textures (Schreiber 2000; Warren 2016).

After deposition of the carbonate sediments, the supratidal zone was covered by siliciclastic deposits (MF6). The carbonates hosting sporadic evaporitic minerals were terminated by an episode of relative sea-level rise, which resulted in deeper water deposition of MF6. Petrography in thin-section shows that these clastic deposits are mainly composed of clay-silty and very fine sand. Detrital composition of clastic sediments includes quartz grains, mica flakes and weathered minerals (especially feldspar grains).

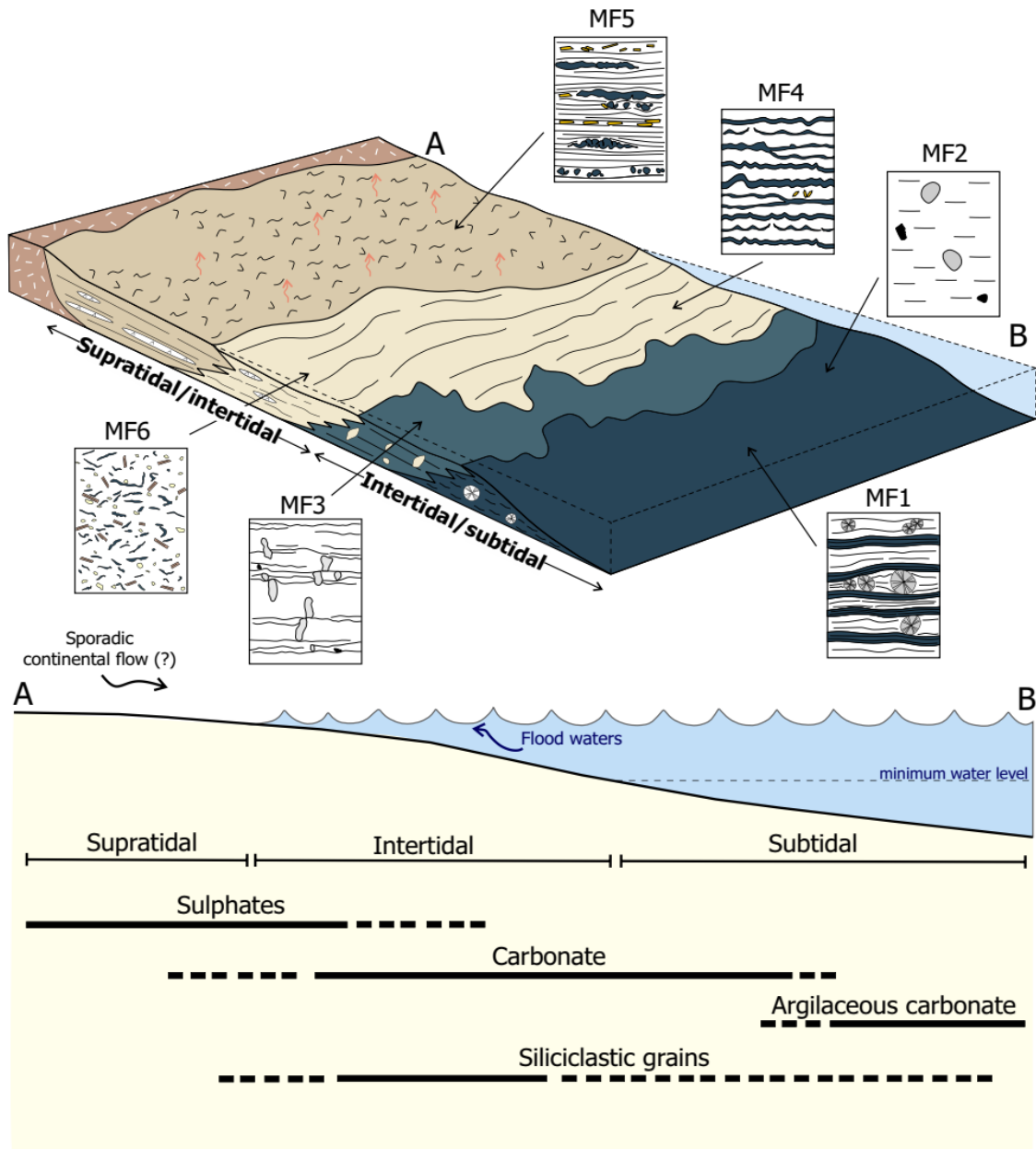


Figure 3.15 – Interpretative depositional model proposed for the Avellaneda Formation. The number representing the corresponding microfacies. The location of each microfacies (MF) is indicated by black arrow.

### 3.5.2 – Diagenesis evaluation

The C–O isotope and empirical element concentrations provide a window to evaluate the evolution of the diagenetic environment imprints in the Avellaneda Formation. A wide range of later postdepositional processes (authigenic components, burial diagenesis, and/or meteoric diagenesis), can potentially modify the primary signal of carbon isotopic composition, particularly for Precambrian successions with long and complex geological histories (Kaufman and Knoll, 1995; Knauth and Kennedy, 2009; Derry, 2010; Schrag et al.,

2013). The magnitude of diagenetic pathways can be estimated using stable isotope ratios and elemental concentrations. Relationships between Sr/Ca, Mn/Sr, Fe/Sr ratios and  $\delta^{18}\text{O}/\delta^{13}\text{C}$  are accepted as diagnosis of diagenesis effects (Brand and Veizer, 1980; Banner, 1995; Kaufman and Knoll, 1995). Post-depositional diagenesis of sedimentary carbonates usually causes an enrichment in Fe and Mn and depletion in Sr, resulting in a decrease in Sr/Ca ratios and higher Mn/Sr and Fe/Sr ratios (Brand and Veizer, 1980; Veizer et al., 1983; Derry et al., 1992; Narbonne et al., 1994). During meteoric diagenesis values of  $\delta^{13}\text{C}$  or  $\delta^{18}\text{O}$  can be progressively lowered from meteoric fluids of more lighter isotope compositions; the same occurs when fresh water is mixed with seawater either during post-glacial periods or due to the contribution of continental fluids in the shallow marine environments (Gómez-Peral et al., 2018). In addition, meteoric diagenesis generates a strong linear correlation between these elements (Sr/Ca, Mn/Sr and Fe/Sr) and isotope values (Kaufman and Knoll, 1995). It is interpreted that samples with a Mn/Sr ratio  $< 10$  and a Fe/Sr ratio  $< 50$  generally indicate minimal diagenetic alteration of  $\delta^{13}\text{C}$  signatures (Kaufman and Knoll, 1995; Veizer, 1983). Applying this empirical constraint in the Avellaneda Formation, all samples are characterized by Mn/Sr  $< 6$  and most samples show Fe/Sr  $< 50$ , which are expected in mixed environments. Furthermore, cross-correlations between element ratios (Sr/Ca, Mn/Sr or Fe/Sr) versus  $\delta^{13}\text{C}$  show a weak correlation suggesting that the carbon isotope trends are close to their primary composition. Stable isotopes, elementary data and weak cross-correlations obtained in samples from Avellaneda Formation point out to a minor degree of diagenetic alteration, and thus, it is likely and safe that data represent the composition of contemporaneous seawater.

The  $\delta^{18}\text{O}$  values cross plotted with respect to  $\delta^{13}\text{C}$  values from the same sample are widely applied proxies used to infer paleoenvironmental conditions (depositional and diagenetic) in ancient carbonate sediments. Oxygen isotope values are prone to diagenesis owing to the high concentration of oxygen in diagenetic fluids and their higher sensitiveness to thermodynamic fractionation (Banner and Hanson, 1990; Kaufman and Knoll, 1995). Overall,  $\delta^{18}\text{O}$  values  $< -5\text{‰}$  are pointed as probably altered and those with  $\delta^{18}\text{O} < -10\text{‰}$  are generally considered inappropriate for stratigraphic analysis because of post depositional alteration (Kaufman and Knoll, 1995; Xiao et al., 1997). However, the  $\delta^{18}\text{O}$  record in most Precambrian carbonate rocks indicates a more depleted  $\delta^{18}\text{O}$  signal than those of the Phanerozoic (Shields et al., 2003; Kasting et al., 2006). Consequently, negative values of  $\delta^{18}\text{O}$  obtained from Precambrian carbonate successions not only reflect the post-depositional conditions, but can preserve an isotopic signature of ancient seawater (Shields et al., 2003;

Kasting et al., 2006). In the case of Avellaneda Formation, samples show  $\delta^{18}\text{O}$  values marked by a narrow variation ranging from -13% to -16%, without a clear lateral trend consistency, which may have resulted from the paleoenvironmental conditions described. Meteoric fluids containing dissolved inorganic carbon from oxidized organic matter can lead to decreases in  $\delta^{13}\text{C}_{\text{carb}}$  as well as  $\delta^{18}\text{O}_{\text{carb}}$ , yielding a corresponding positive covariation between the two values (Knauth and Kennedy, 2009). A lack of  $\delta^{13}\text{C}$  and  $\delta^{18}\text{O}$  covariation in studied successions further indicates reliable carbon isotopic compositions of depositional seawater in the Avellaneda Formation despite possible alteration of oxygen values.

Meteoric diagenesis comprises a major and common obstacle in use of carbonates as paleoproxies for ancient seawater chemistry, particularly at times of frequent and large-scale changes in sea level (Allan and Matthews, 1982; Swart and Eberli, 2005). Despite this, geochemical data suggest minimal interaction of diagenetic fluid and the difference between the original carbonate and the diagenetic fluid was small and/or the diagenetic system was buffered by the rock composition (low water–rock ratio) also considering the high degree of preservation of the primary texture. The  $\delta^{13}\text{C}$  excursion in the Avellaneda Formation is thus interpreted as a primary marine signal.

### 3.5.3 - Origin of barite at Avellaneda Formation

The Avellaneda Formation shows petrographic evidence of  $\text{BaSO}_4$  crystals. However, the genesis of this mineral is not so clear and the above description raises the question of how barite crystal was formed. Barite can be formed in the water column, or within marine sediments or around hydrothermal vents and cold seeps or yet by deposition of older barite deposits as detrital material (Paytan et al, 2002; Griffith and Paytan, 2012; Okubo et al., 2018; Widanagamage et al., 2018; Martinez-Ruiz et al., 2019). The shape and size of barite crystals are useful to determine its environment formation (Bishop, 1988; Paytan et al., 1993; Paytan et al., 2002; Cui et al., 2022; Cheng et al., 2022).

In this study barite crystals were recognized in all drill cores analyzed (Figure 3.2). Best occurrences are found between 70 and 66 meters deep in drill core H9 (Figure 3.2), and around 60 meters deep in the drill core E7 (Figure 3.2). Barite is hosted in thin laminated intervals with original textures still preserved (see MF4 and MF5). Microfacies analyses indicate that barite crystals occur together with evaporite textures (Figure 3.9, 3.10 and 3.11). Features related to evaporite relics consist of lenticular biterminated crystal and isolated/coalesced nodular features with acicular-lath crystals (Figure 3.10). These features

are associated with gypsum or anhydrite phase formed in the surface environment and require a sulfate enrichment process such as evaporative brine formation or oxidative sulfide weathering (Nabhan et al., 2020). Indeed, barite (as well as carbonate) appears as a substitute for likely calcium sulfate phases (Figure 3.10). Our identification was supported by CL and fully confirmed by electron probe microscope. Barite crystals reported here are typically tabular and often elongate, subhedral to euhedral, may show double terminated like a lensoidal morphology crystal (Figure 3.11). Nodules originally composed of calcium-sulfate can be partially or fully replaced by barite (Figura 3.10). Crystals of barite may be uniform sizes or can show sizes ranging 100-650  $\mu\text{m}$  in length and 10-100  $\mu\text{m}$  of width (Figura 3.11). Often crystal occurs preferentially concordant with the horizontal lamination (Figure 3.9, 3.10 and 3.11). In general, barite minerals described are clear and relatively free of inclusions (Figure 3.11). Carbonate is mainly inclusion trapped in barite minerals (Figure 3.11b). Any conceptual mechanism proposed in order to clarify the genesis of barite in Avellaneda Formation should cover all sedimentary aspects previously stood out. Several scenarios can be invoked to provide meaningful interpretations of barite occurrences reported in Avellaneda Formation. Following, we focus on a potential explanation about the origin of barite. It is important to keep in mind that these scenarios are not mutually exclusive.

The Avellaneda Formation occupies the basal stratigraphy of the La Providencia Group and lies immediately above the Barker Surface (Arrouy et al., 2015). The Avellaneda Formation occupies the basal stratigraphy of the La Providencia Group and lies immediately above the Barker Surface (Arrouy et al., 2015). This surface comprises a remarkable karstic discontinuity that separates the La Providencia Group and Sierras Bayas Group (Arrouy et al., 2015). A surface discontinuity is recognized as prone to dissolution, brecciation and hot fluid-circulation that favors local mineralization events (Rob, 2005; Ridley, 2013). Likewise, as in Barker-Villa Cacique area, were described in studied area, a similar association composed of Fe-Cu sulfides – barite – chlorite. This fact may argue a hydrothermal origin for association found in the Avellaneda Formation and described here. If this turns out to be correct, then, hydrothermal activity extends out not laterally but vertically on Barker surface, reaching in some case, the entire record of the Avellaneda Formation. However, no expressive brecciated intervals, multidirectional injections veins or any indications of hydraulic fracturing that generally accompany hydrothermal alteration occurs in investigated sections. Moreover, sections investigated here demonstrate a well-preserved original rock texture. The state of

preservation is attested by presence of soft-tissue related to microbial mat (see MF4 and MF5).

Barite involves supersaturated conditions resulting from an increased supply of Ba or sulfate (Cheng et al., 2022). In described sections, barite crystals occur together with microbial mats and evaporite textures (Figure 3.10). It is recognized that barite, would be a likely result of the interaction of heated Ba-rich formation water with sedimentary calcium-sulfate beds. At the Avellaneda Formation, the juxtaposition and close association with deposits formed by calcium-sulfate beds point out for possible source of  $\text{SO}^{4-}$ . Further, barite appear as a pseudomorph substitute for crystal and nodules of evaporites (Figure 3.11j). This replacement can be partial or complete (Figure 3.11j). This replacement process would be enabled by the retrograde solubility of gypsum and anhydrite in the diagenetic temperature window. This mechanism was invoked to explain barite replacements of early diagenetic calcium sulfate nodules in supratidal deposits from Windsor Group (Mossman and Brown, 1986; Melvin et al., 1991) and after lenticular gypsum in a buried soil from central Australia (Sullivan and Koppi, 1993). The horizontal alignment of crystals regarding the sedimentary bedding surface and nodular configuration pushing aside the adjacent lamination is a strong argument for an early-diagenetic origin (Figure 3.11j). Furthermore, size and morphology are key criteria to constraint the environment of barite formation (Cheng et al., 2022). Barite crystals at Avellaneda Formation show large sizes (frequently up 150  $\mu\text{m}$ ) with flat and tabular shapes, thus, these criterions also agree with a diagenetic origin. However, in a merely diagenetic scenario it is quite difficult to explain the presence of metal sulfides and chlorite associated with barite.

#### **3.5.4 - Is the Avellaneda Formation $\delta^{13}\text{C}$ excursion an expression of the Shuran Excursion (SE)?**

Recently, Cui et al., (2022) suggests that the Ediacaran Period saw at least two presumed-global scale episodes of enhanced barite burial: the first episode is linked with cap carbonate deposition and the second episode is connected with the SE. Both episodes contain negative  $\delta^{13}\text{C}$  excursions and enhanced barite mineralization which are probably driven by intensive oxidative weathering and greater influx of sulfate and barium into the depositional basin. As consequence the higher seawater sulfate concentrations during the SE not only promoted the deposition of gypsum and anhydrite, but also appear to have facilitated barite mineralization and burial (Shields et al., 2019; Wei et al., 2021; Cui et al., 2022). The last

episode, positioned in the Middle Ediacaran Period, has attracted special attention because it offers an opportunity to clarify the relationship between a redox event and the rise of the Ediacara biota.

Evaluating mineralogical and geochemical data in several sedimentary successions of the same age but geographically separated demonstrate that the middle Ediacaran episode supports a probable global carbon perturbation, which is potentially linked to major disturbances in sulfur and barium biogeochemical cycles as well (Cui et al., 2022). The Shuram-Wonoka carbon excursion in several succession across the globe, reported in Wonoka Formation in South Australia (Calver et al., 2000; Husson et al., 2015; Minguez and Kodama, 2017), the Shuram Formation in Oman (Fike et al., 2006), the Nama Group in southern Namibia (Wood et al., 2015); the Krol Group in India (Jiang et al., 2003), the Rainstorm Member of the Johnnie Formation in western USA (Corsetti and Kaufman, 2003; Kaufman et al., 2007), Upper Clemente Formation in Mexico (Loyd et al., 2012, 2013; Cui et al., 2022), Doushantuo Formation (Cui et al., 2017; Shi et al., 2018; Cui et al., 2022) and sections from Siberia (Russia) also report large fluctuations in C-curves (Melezhik et al., 2009; Zhang et al., 2019). Several of these successions not only share a pronounced  $\delta^{13}\text{C}$  negative excursion but show sulfate minerals or textures of evaporites that are closely associated with the SE (including China, Oman, Australia, India, Namibia and Russia).

The results reported in Avellaneda Formation match with predictions recently proposed by Cui et al., (2022). The juxtaposition of evaporite textures, barium sulfate and subaerial exposure features are consistent with increased weathering hypotheses for the SE, which boosted oxidation of reduced carbon and sulfur reservoirs in land, resulting in increased deliver of  $^{13}\text{C}$ -depleted and sulfate ions in proximal areas (Kaufman et al., 2007; Shi et al., 2018; Shields et al. 2019; Cui et al., 2022). Enhanced oxidative weathering, evaporite recycling, microbial sulfate reduction and pyrite burial may have formed a biogeochemical loop with positive feedback, contributing to the long-lasting oxygenation event recorded by the SE (Cui et al., 2022). This fact is consistent with published geochemical profiles of Ce/Ce\* performed at the base of the unit (Gómez-Peral et al., 2014) and also the global oxygenation event recorded in the underlied Loma Negra Formation (Gómez-Peral et al., 2019; Arrouy et al., 2021). The negative anomaly of Ce/Ce\* strongly argues for an oceanic oxygenation event recorded at the base of the Avellaneda Formation (Gómez-Peral et al., 2014).

The Avellaneda Formation seems to gather ideal conditions to preserve some form of sulfate. Until now, evaporative sulfate minerals were exclusively found in the Doushantuo Formation at relatively shallow water depths, including both the inner shelf and rimmed outer shelf shoal sections (Cui et al., 2022). Models made from Doushantuo Formation suggest an increase in Ba content during middle Ediacaran with major concentration close to expression of Shuram isotopic excursion. Accordantly with these idealized models Shuram excursion occurred or are recorded preferentially in much shallower settings. Our finding also supports an enrichment in Ba reservoir closeness or during the SE. Moreover,  $\delta^{13}\text{C}_{\text{carb}}$  values obtained in the upper portion of this unit comprises a challenging to pinpoint whether it is or not an expression of the SE using only the  $\delta^{13}\text{C}_{\text{carb}}$  profiles because C-isotope values do not seem to reach as low values as other coeval successions. The occurrence of an episodic subaerial exposure surface located in the upper erosive contact of the Avellaneda Formation is a potential explanation of why negative excursions reported here are not so large as those described in contemporaneous units.

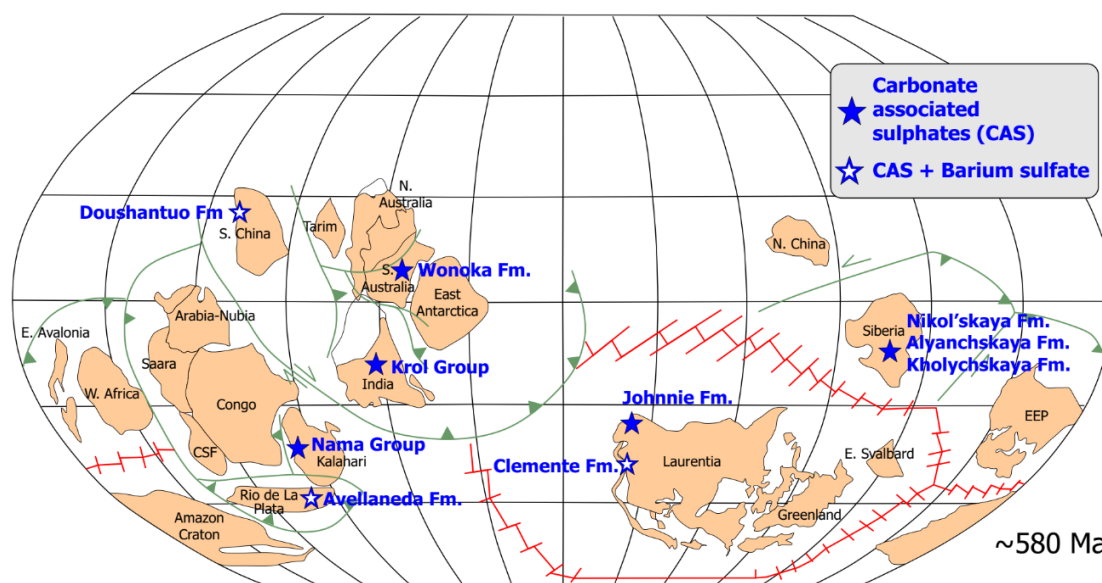


Figure 3.1: Paleogeographic map showing the locations of Shuram sections at the global scale. Key sections for the SE are indicated by stars. Blue star closed represents sulfate mineral or textures (CAS). Open stars symbolize sections that show CAS and Ba-sulfate. The map is modified from Li et al., (2013). Carbon isotope data, sulfate minerals content (CAS) and Ba enrichment for each section and references are hereafter listed: Avellaneda Formation (this study), Wonoka Formation (Calver et al., 2000; Husson et al., 2015; Minguez and Kodama, 2017), Shuram Formation (Fike et al., 2006), Nama Group (Wood et al., 2015), Krol Group (Jiang et al., 2003), Johnnie Formation (Corsetti and Kaufman, 2003; Kaufman et al., 2007), Clemente Formation (Loyd et al. 2012, 2013; Cui et al., 2022), Doushantuo Formation (Cui et al., 2017; Shi et al., 2018; Cui et al., 2022) and sections performed in Nikol'skaya, Alyanchskaya and Kholychskaya formations (Melezhik et al., 2009; Zhang et al., 2019).

### 3.6. Conclusion

Microfacies analysis performed in Avellaneda Formation allowed recognition of a shallow marine setting range from subtidal/intertidal zone and intertidal/supratidal environments. Shallow-marine system is corroborated by episodic subaerial exposure. Evaporite textures and sulfate minerals reveal the prevailed conditions of deposition in a mixed carbonate-siliciclastic system with short periods of desiccation during subaerial exposure which are more frequent upwards the unit. A middle Ediacaran carbon isotope excursion has been documented in the c.a. 580-560 Ma Avellaneda Formation. Although not reaching extreme nadir values, this isotopic excursion displays similarities with the other coeval sections based on age constraints for the Avellaneda Formation and, most important, its sedimentary expression (see Cui et al., 2022). This excursion predates the earliest appearance of discoidal forms and can be potentially significant to subsequent biological events. The coincidence of sulfate minerals (barite) with  $\delta^{13}\text{C}_{\text{carb}}$  excursion in the study sections reinforce the link between rising oxygen levels, enhanced sulfate weathering fluxes, transient increases of  $\text{SO}_4^{2-}$  and concurrent oxidation of a reduced carbon reservoir how a probably cause of the SE. This process may have played a pivotal role in the genesis of the largest globally recorded  $\delta^{13}\text{C}$  negative excursion in Earth history. New data reported here complements the global dataset of sulfate minerals occurring near the SE interval. Furthermore, this study also suggest that further investigations are still needed to fully understand changing seawater chemistry and biogeochemical cycles during apparently pulsed events, considering that several late Ediacaran to early Paleozoic successions seem to resemble anoxic and sulfate-limited conditions. The acquisition of sulfate can shed light and solve some questions about a larger sulfate pool in the Ediacaran ocean than previously thought.

## **CHAPTER IV**

#### 4. Paleomagnetism of the Ediacaran Avellaneda Formation (Argentina), Part I: Paleogeography of the Río de la Plata craton at the dawn of Gondwana

Pablo Franceschinis, Jhon W.L. Afonso, María Julia Arrouy, Lucía E. Gómez-Peral, Daniel G. Poiré, Ricardo I.F. Trindade, Augusto E. Rapalini

**Abstract:** A paleomagnetic and rock magnetic study was carried out in the Ediacaran Avellaneda (~570 Ma) and Cerro Negro (~560 Ma) formations belonging to the La Providencia Group, in the upper part of the Neoproterozoic sedimentary cover of the Tandilia region, in the Río de la Plata craton. The Avellaneda formation was studied at outcrop level and in three drill cores, obtaining a mean characteristic remanence direction of Dec: 21.4°, Inc: 67.1°,  $\alpha_{95}$ : 4.2°, k: 23.9, N: 51 and a paleomagnetic pole at 1.0° S, 313.4° E, A95: 5.9°. The Cerro Negro formation yielded a mean characteristic direction of Dec: 19.8°, Inc: 60.7°,  $\alpha_{95}$ : 7.7°, k: 27.7, N: 14 obtained from a single bore core, from which a paleomagnetic pole at 7.0° N, 314.4°E, A95: 9.5° was computed. Rock magnetic data indicates that remanence is mainly associated with magnetite and hematite. The paleomagnetic information present here results in a change in the previously accepted Late Ediacaran apparent polar wander path of the Río de la Plata craton. The newly obtained poles indicate a rapid drift from a low latitude location (ca. 19° S) at ca. 600 Ma to moderately higher latitudes (between 50° and 42°S) from around 580 to 560 Ma.

##### 4.1. Introduction

The Ediacaran period (635-541 Ma), at the end of the Proterozoic, witnessed a series of events of great importance such as the appearance and diversification of a complex biota (Erwin et al., 2011; Xiao et al., 2014, among others). At the same time, significant climatic changes occurred affecting the atmosphere composition and the chemistry of the oceans (eg. Canfield et al., 2008; Ader et al., 2009, 2014; Lyons et al., 2014; Sperling et al., 2015; Smith et al., 2016), which include a global glaciation (Gaskiers, Pu et al., 2016; Gómez Peral et al., 2017; Poiré et al., 2018) and the largest excursion recorded in carbon isotopic composition (Shuram excursion, Macdonald et al., 2013; Gómez Peral et al., 2018; Li et al., 2020). It has been speculated that all these processes have been directly related to global palaeogeographic changes due to the final dispersion of the Rodinia supercontinent and the formation of Gondwana (eg. Collins and Pisarevsky, 2005; Li et al., 2013). In addition, the Ediacaran could

have experimented very particular geomagnetic or geodynamic phenomena based on different non-actualist hypotheses. For example, geodynamic processes that led to episodes of inertial interchange true polar wander (IITPW) have been proposed (eg. Evans, 2003; Mitchell et al., 2012; Robert et al., 2017, 2018), or very peculiar geomagnetic patterns, such as the existence of a magnetic field with an equatorial dipole (Abrajevitch and Van der Voo, 2010) or a very weak geodynamo with permanent non-dipole configurations of the field (Driscoll, 2016). These hypotheses question the ability of the paleomagnetic method through the geocentric axial dipole (GAD) hypothesis to determine the paleolatitude and paleorientation of the continents in the Ediacaran. These views may have been reinforced by recent absolute paleointensity determinations suggesting that during this period the Earth experienced an ultra-low geomagnetic field (e.g. Bono et al., 2019; Thallner et al., 2021). In contrast to those findings, some Ediacaran-Cambrian polar positions, with a high degree of reliability, have shown coherence along a relatively simple Gondwana apparent polar path, suggesting that the GAD hypothesis may still be valid for several intervals within, if not across most of the Ediacaran (for example, Tohver et al., 2006; Rapalini, 2018).

One of the major questions regarding the paleogeography of Western Gondwana from the Early Ediacarian to the Early Cambrian is the hypothesis, based on paleomagnetic data, of the existence of a large Clymene Ocean between Amazonia-West Africa and Congo-São Francisco-Rio de la Plata (Trindade et al., 2006; Cordani et al., 2013; Tohver and Trindade, 2014; Rapalini et al., 2015). According to this hypothesis, the Amazon-West Africa block should have been the last major landmass to join Gondwana in the Early Cambrian. The existing paleomagnetic information in volcanic units of the middle Ediacaran of West Africa (Robert et al., 2017), allows a comparison of high quality contemporaneous paleomagnetic poles for the ~575 Ma of the Río de la Plata, West Africa and Congo-São Francisco cratons. The superposition of the poles of these cratons suggests that they were already united or very close to each other in the middle Ediacaran (Rapalini et al., 2021), weakening the model of a large Clymene Ocean for those times (eg. Rapalini et al., 2015). On the other hand, sedimentological and paleontological evidence has recently been interpreted as evidence for a still open Clymene Ocean in the late Ediacaran (Arrouy et al., 2016; Warren et al., 2014).

Paleomagnetic constraints on the paleogeographic evolution of the Río de la Plata craton (RPC) in the Precambrian is limited to three time-spans (Rapalini et al., 2021). The first of them is restricted to the Rhyacian, between 2.11 and 2.05 Ga (Rapalini et al., 2015; Franceschinis et al., 2019). The second time span occurs during the Statherian and correspond

to the 1790 Ma pole of Teixeira et al. (2013) obtained from the Florida tholeiitic dyke swarm exposed in the Piedra Alta terrane, Uruguay. Finally, a third group of paleomagnetic poles and VGPs (Rapalini et al., 2013, 2015, 2021) correspond to the Ediacaran, coeval with the assembly of Gondwana (600-550 Ma, Meert, 2014). The first paleomagnetic studies in Precambrian units of the Tandilia system, southern Río de la Plata craton, were carried out by Valencio et al. (1980) in sedimentary units assigned at that time to the La Tinta Formation (current Sierras Bayas group). However, Rapalini and Sánchez Bettucci (2008) and Rapalini et al. (2013) demonstrated that these first studies had isolated a secondary remanence, likely related to a Permian to Triassic remagnetization. In the last twenty years, an apparent polar wander path (APWP) has been constructed with a total of six polar positions from paleomagnetic poles and VGPs for the Rio de la Plata craton (Rapalini et al., 2013; 2015; Rapalini, 2018). This path suggests that the craton was at low, nearly equatorial, latitudes at around 600 Ma and drifted to intermediate latitudes by 575 Ma, possibly already attached to or very close to the Congo-São Francisco and NW Africa cratons (Rapalini et al., 2021). By around 550 Ma, the RPC was apparently still at intermediate latitudes. During the Ediacaran, besides this latitudinal migration, the RPC underwent a large counterclockwise rotation. Lack of Neoproterozoic paleomagnetic data older than 600 Ma has prevented to paleomagnetically test the position of this craton within Rodinia (e.g. Li et al., 2013). However, the available data has been interpreted as incompatible with a mid-Ediacaran rifting of RPC from the eastern margin of Laurentia (Rapalini et al., 2015). Despite this progress on the Ediacaran apparent polar wander path of the Río de la Plata craton that has placed some constraints on its paleogeographic evolution and the timing and kinematics of Western Gondwana assembly (e.g. Rapalini, 2018; Rapalini et al., 2021), the paleomagnetic database is still scarce for robust and precise paleogeographic reconstructions.

In order to provide better constraints on the paleogeographic and paleoenvironmental evolution of the southern Río de la Plata craton during Ediacaran times, a multidisciplinary study was initiated by a collaboration between researchers of the University of Buenos Aires, National University of La Plata and University of São Paulo on the sedimentary cover of the Tandilia system. The first results of this collaboration are here present in the form of two companion papers, reporting paleomagnetic, rock magnetic, magnetic stratigraphy and isotope stratigraphy data for the Avellaneda Formation. The present paper is the first one, and describes in detail the paleomagnetic and rock magnetic study carried out on nearly two hundred and fifty oriented samples of the Avellaneda Formation, mainly from three bore

cores drilled near the city of Olavarria, in the Buenos Aires province. Preliminary data from the younger Cerro Negro Formation are also presented. These results permit to determine two new high quality paleomagnetic poles for the Rio de la Plata craton at approximate ages of 570 and 560 Ma providing new evidence on the paleogeography of this cratonic unit during Gondwana assembly.

#### **4.2 The Tandilia system**

The Tandilia System (Figure 4.1) is exposed along a 300 km long NW-SE belt in the Buenos Aires province, in central eastern Argentina. The oldest rocks are represented by gneiss, migmatites, granitoids and dykes of the Paleoproterozoic Buenos Aires Complex (Marchese and Di Paola, 1975; Cingolani et al., 2002). This is intruded by a swarm of Paleoproterozoic tholeiitic dykes (Teixeira et al., 2002 and references therein) and covered by a Neoproterozoic sedimentary succession of unmetamorphosed and scarcely deformed clastic and carbonate rocks. These have been subdivided into the Sierras Bayas (see Poiré and Gaucher, 2009) and La Providencia Groups (Arrouy et al., 2015). The Sierras Bayas group is made up of the following units, from the oldest to the youngest: Villa Mónica (dolostones and quartzites), Colombo (diamictite), Cerro Largo (sandstones and pelites), Olavarría (pelites) and Loma Negra (limestones) Formations (Figure 4.2a). The youngest formation of the Sierras Bayas Group, the Loma Negra Formation (Borrello, 1966), consists of a sequence of approximately 40 m of reddish and black micritic limestones deposited in a marine or lagoon ramp environment (Poiré and Gaucher, 2009). Gómez Peral et al. (2007) suggested an age between 580-590 Ma for this formation. A major regression marks the end of the Sierras Bayas Group, with the development of the erosive Barker surface (Poiré and Gaucher, 2007) on the Loma Negra limestones. This big drop in sea-level has been assigned to the Gaskiers glaciation (Gómez Peral et al., 2018; Poiré et al., 2018), dated at 580 Ma (Pu et al., 2016). This surface has been correlated with similar features in other regions of southwestern Gondwana, like in Uruguay, Brazil, South Africa, and Namibia (Poiré et al., 2018 and references therein).

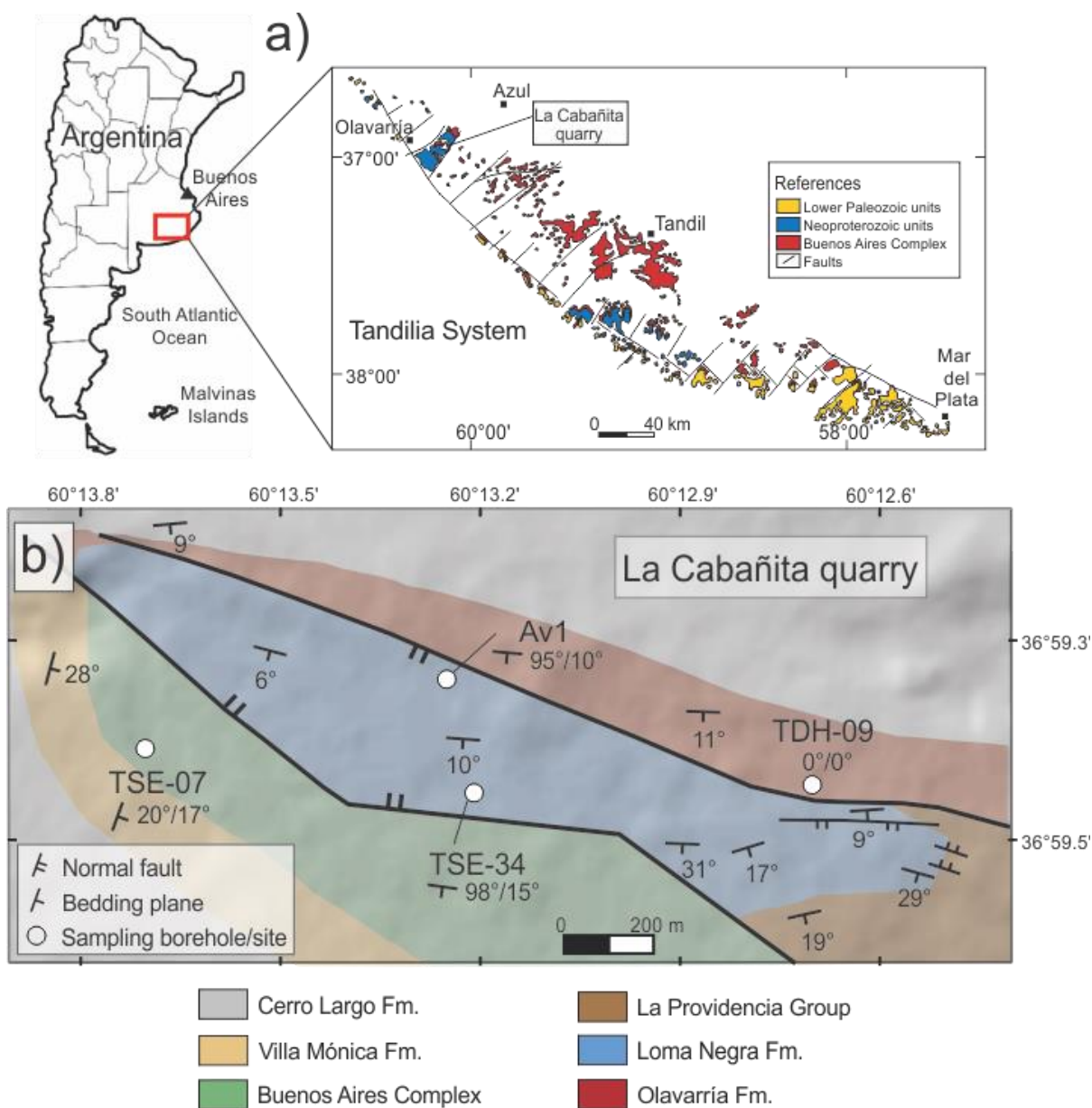


Figure 4.1: a) Location of the study area, “La Cabañita” quarry in the Tandilia System, close to the Olavarría city; b) Simplified geological map of the “La Cabañita” quarry where the location of the bore cores and the sampled site are indicated. Modified map from Hernández et al. (2017). Note: the map published by Hernandez et al. (2017) was carried out after the sampling of the AV1 site. The outcrops in the quarry changing due to the extraction work carried out in the quarry. In this way, the site AV1 is located in the Loma Negra formation currently outcrops.

Arrouy et al. (2015) proposed a new stratigraphic scheme for the Late Neoproterozoic cover of the Tandilia system based on the subsurface recognition of a sedimentary succession of 150 meters of shales and siltstones. The succession on top of the Barker Surface was included into the La Providencia Group, which is integrated from base to top by the Avellaneda, Alicia and Cerro Negro formations (Figure 4.2). The Avellaneda Formation

(Arrouy et al., 2015) is deposited directly on the erosive Barker Surface. It consists of an association of facies, starting from the base with a mixed composition of massive and laminated marls, increasing the siliciclastic content towards the top where it is composed of massive red clays. The palaeoenvironment proposed for its deposition is tidal flat with evidence of subaerial exposure (Arrouy et al., 2015). The age of the Avellaneda Formation is restricted stratigraphically between the Barker Surface and the Late Ediacaran fossils found in the Cerro Negro Formation (see below). This suggests the Avellaneda Formation to be constrained somewhat between 580 Ma and 560 Ma. Accordingly, the carbon isotope profile of the Avellaneda Formation displays a negative excursion correlated to the onset (575 Ma) of the global Shuram carbon isotope excursion (see Afonso et al., companion paper). The Alicia Formation (Arrouy et al., 2015) consists of a clastic succession of black shales in the lower levels that grade into a succession of heterolytic facies of black to gray siltstones and sandstones, both with wavy and lenticular stratification. Massive gray siltstones appear towards the top of the unit. A distal subtidal, with anoxic to suboxic conditions, has been inferred for this unit based on its dark color and the presence of pyrite. The Cerro Negro Formation (Iñiguez and Zalba, 1974), redefined by Arrouy et al. (2015), consists of a succession of massive, fine- to medium-grained sandstones with symmetric waves and swalley cross lamination, black to gray heterolytic facies with wavy stratification, and massive red shales. This formation is associated with a subtidal to intertidal zone with frequent structures associated with tractive processes alternating with subordinate processes of decantation by suspension. Arrouy et al. (2016) reported discoidal structures in fine sandstones of this formation that were assigned to the genus *Aspidella* sp. The characteristics of these fossil remains in the upper levels of the Cerro Negro Formation have been interpreted as corresponding to the “White Sea” Assemblage (Arrouy et al., 2016), with a most probable age between 550 and 558 Ma (Cracknell et al., 2021).

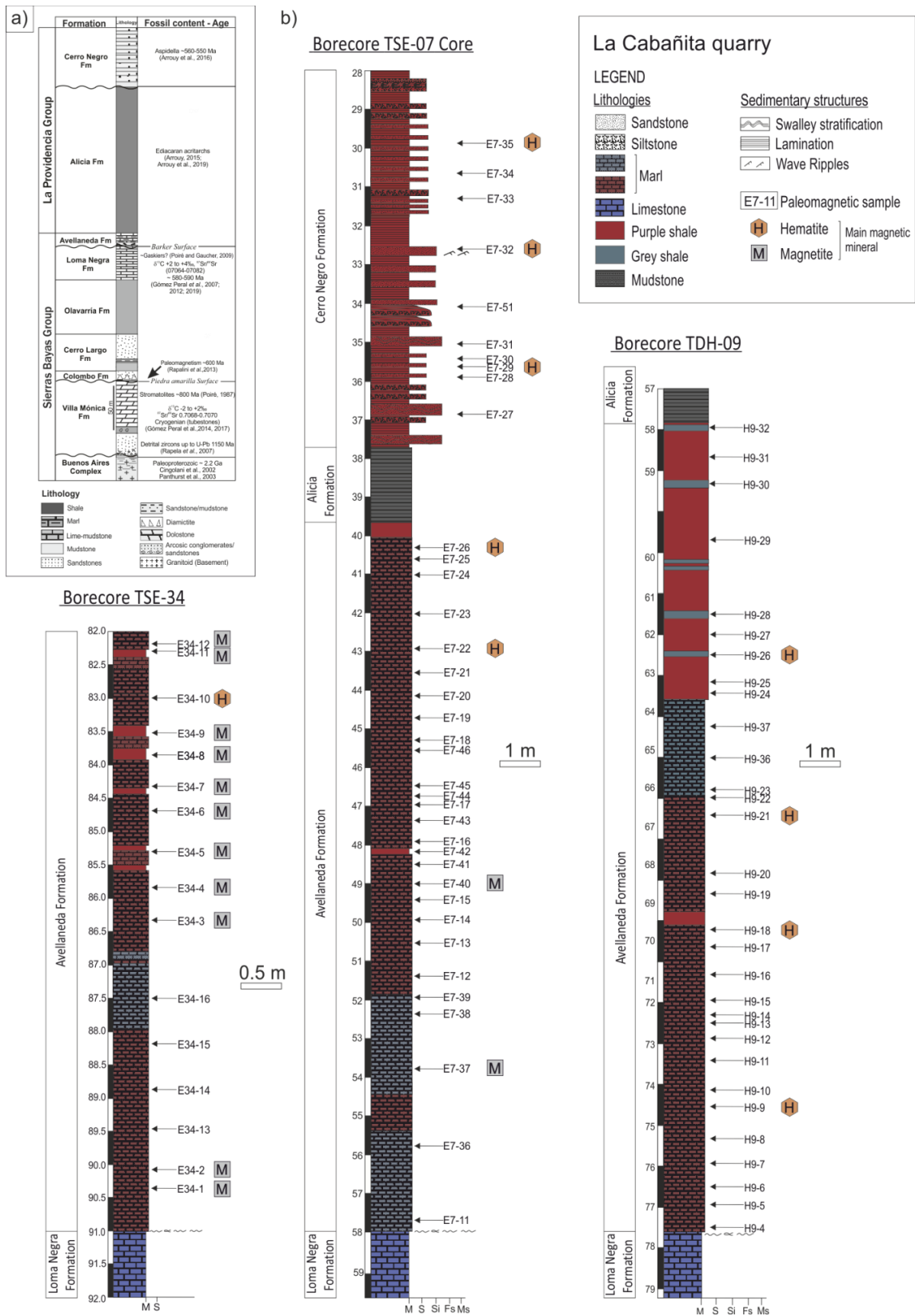


Figure 4.2: a) Regional stratigraphic profile from Tandilia System. Modified from Arrouy et al. (2019); b) Stratigraphic profiles of bore cores TSE-34, TSE-07 and TDH-09. Stratigraphic position of each sample is indicated. The main magnetic mineral

### 4.3. Methodology

#### 4.3.1. Outcrop sampling

The outcrop sampling was carried out in the “La Cabañita” quarry (Cementos Avellaneda SA), near Olavarría city. The outcrop consists of a fairly monotonous succession of purple marls with intercalations of lighter levels (Figure 4.3a, b). We collected four oriented cores using a portable drill and five oriented hand samples (Site AV1: 36.988780° S, 60.220840° W, Figure 4.1b). Whenever possible, samples were oriented with both solar and magnetic compasses. The sampled stratigraphic thickness was just over 6 m.

#### 4.3.2. Drill core sampling

A detailed study of the Avellaneda formation was carried out in samples from three vertical drill cores (E34, E07 and H09, Figure 4.1). Sections of these cores have already been studied for their sedimentological and isotopic aspects by Arrouy et al. (2015) and Gómez Peral et al. (2018), respectively. Segments of these drill core samples, approximately 10-30 cm in length, were selected for paleo magnetic sampling (see Figure 4.3). From each sample, between three to seven cylindrical cores 2.54 cm in diameter and approximately 3 cm in height were extracted, from which a specimen of 2.2 cm high was obtained (Figure 4.3). The core segments were drilled centered on the fiduciary mark, which allowed defining their x and y axes. Since the dip of the lamination could be observed and measured along the samples, the relative orientation of the core fiduciary mark was determined with respect to this structural feature. This made possible to azimuthally orient the samples spatially assuming a bedding strike equivalent to the mean strike observed at the nearby AV1 site. This first orientation was later improved using the low-temperature natural remanent magnetization (NRM) component (see section below).

#### 4.3.3. Core E34 (Avellaneda Formation)

The bore core TSE-34 (Figure 4.2, 4.3c, d, e) is located approximately 260 meters SSE of the AV1 site, (36.991059° S, 60.220154° W, Figure 4.1b). It consists of a succession of massive red marls with some gray color alternations. In the upper half of the profile there are intercalations of massive levels of clays with reddish tones (Figure 4.2). The measured vertical thickness of the Avellaneda Formation in this core is 9 m, extending from 91 m to 82 meters below the surface (mbs). Sixteen samples were selected in this bore core (Figure 4.2).

Dipping of the lamination was measured in the laboratory, on each sample fragment. Dip values ranged between  $14^{\circ}$  and  $23^{\circ}$ , obtaining an average of  $15^{\circ}$  for the bore core.

#### **4.3.4. Core H09 (Avellaneda Formation)**

Bore core TDH-09 (Figure 4.1b,  $36.990898^{\circ}$  S,  $60.211683^{\circ}$  W) is located just over 750 meters east of bore core TSE-34. Thickness of the Avellaneda formation at this bore core reaches 19.7 m, with its base at 77.7 m. and its top at 57.6 m (mbs). It consists of a succession dominated by reddish marls, with a change into a succession of massive shales with red and gray tones in the upper 7 meters (Figure 4.2). Thirty-one samples were collected from this bore core (Figure 4.3f, g). Lamination is sub-horizontal.

#### **4.3.5. Core E07 (Avellaneda and Cerro Negro formations)**

Bore core TSE-07 (Figure 4.1b,  $36.99017^{\circ}$  S,  $60.228392^{\circ}$  W) is located just over 740 meters to the west from TSE-34 bore core. The succession belonging to the Avellaneda formation consists almost exclusively of marls, being mostly reddish, with few intercalations of massive reddish shales (Figure 4.2). The vertical thickness determined for the Avellaneda formation is 18.3 m, with its base at 57.9 meters and its top at 39.7 m (mbs). Twenty-seven samples were collected from this formation (Figure 4.3h, i, j). The average dip determined for the laminations is  $17^{\circ}$ , ranging between  $14^{\circ}$  and  $24^{\circ}$ .

On top of the Avellaneda Formation is a very thin level (1.5 m) of the greenish to greyish clastics of the Alicia formation, which is overlain by the Cerro Negro Formation. It consists of reddish heterolithic facies of fine sandstones and shales. The shales show parallel lamination and the sandstones wave ripples and swalley stratification (Figure 4.2). It has a vertical thickness of 7.1 m (between 36.9 and 29.8 m mbs). Ten samples were collected from this formation. These sediments show an average dip of the lamination of  $17^{\circ}$ , identical to that measured in the underlying Avellaneda Formation. Dip values ranged between  $14^{\circ}$  and  $21^{\circ}$ .

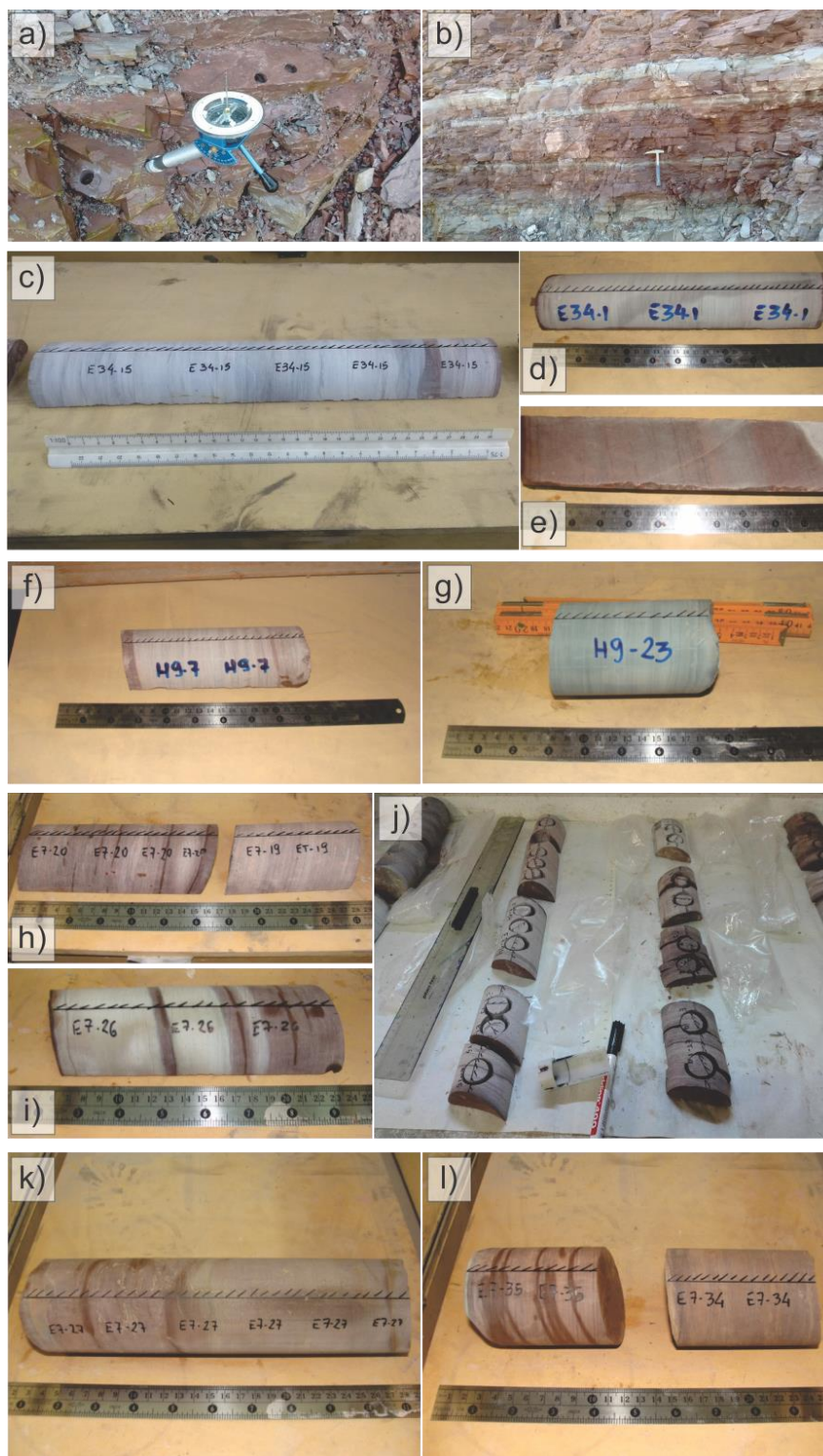


Figure 4.3: a) and b) Quarry front where the Avellaneda formation (site AV1) was sampled; c), d) and e) Samples extracted from the Avellaneda formation in bore core TSE-34. Photos d) and e) belong to the same sample, showing the observed laminations in greater detail; f) and g) samples extracted from the Avellaneda formation in bore core TDH-09; h) and i) samples extracted from the Avellaneda formation in bore core TSE-07; j) drilled samples from the same formation with the individual cores; k) and l) samples extracted from the Cerro Negro formation in bore core TSE-07. Note the fiduciary mark along the samples and the well-developed laminations, used for azimuthal orientation of the samples. See text for more information.

### 4.3.6 Laboratory Procedures

Bulk magnetic susceptibility ( $k$ ),  $k$  vs. temperature curves were performed using a Kappabridge MFK1-A (AGICO) susceptibility-meter with CS-L and CS3 devices. These instruments are located at the “Daniel A. Valencio” Paleomagnetism Laboratory (IGEBA) of the University of Buenos Aires. Hysteresis loops, IRM (isothermal remanent magnetization) and IRM back-field curves were performed using a Molspin Ltd. vibration sample magnetometer (VSM) and the paleomagnetic processing of the AV1 site samples using a 2G-550R-DC cryogenic magnetometer, at the same institution. A single chamber ASC48-TD furnace was used for the thermal demagnetization stages, meanwhile a 2G static 3 axes alternating field (AF) demagnetization attached to the cryogenic magnetometer was used for AF demagnetization. Paleomagnetic processing of all drill core samples was conducted at the Laboratory of Paleomagnetism of the University of São Paulo (USPmag), using a cryogenic long-core magnetometer 2G 755-4K and an ASC48-TD furnace for thermal desmagnetization. Another batch of hysteresis cycles, IRM and IRM back-field curves were performed in this laboratory using a MicroMag-VSM, Model 3900 (Princeton Measurements Corporation).

## 4.4. Paleomagnetic results

### 4.4.1 Site AV1

Samples from AV1 site were submitted to a first stage of demagnetization by alternating magnetic fields (AF) in steps of 3, 6, 9, 12, 15, 20, 25, 30, 40, 50, 60, 70, 80 and 90 mT, followed by a second stage of high temperature demagnetization in steps of 100, 150, 300, 400, 500, 530, 560, 590, 620 °C. Each sample demagnetization behavior was analyzed independently and principal component analysis (PCA, Kirschvink, 1980) was used to determine the magnetic components. A “soft” magnetic component, labelled "a", with low to medium coercivities was defined at alternating magnetic fields under 40 mT. The directions obtained between 50 and 90 mT show a random distribution. A second stable component, "b", could be defined by high-temperature demagnetization showing a trend towards the origin of coordinates in Zijderveld diagrams. In some cases, unblocking temperatures close to or greater than 600° C were observed, while in other samples the unblocking temperature is lower, between 500 and 550° C (Figure 4.4a). “In situ” mean direction of component “a” was Dec: 5.5°, Inc: -60.2°,  $\alpha_{95}$ : 3.6°,  $k$ : 43.4,  $n$ : 37 (specimens) (Figure 4.4b). Component “b”,

interpreted as the characteristic remanent magnetization, presented a consistent direction in the analyzed specimens, with moderate to high positive inclinations, pointing to the N, obtaining a mean “in situ” direction of Dec:  $8.5^\circ$ , Inc:  $47.6^\circ$ ,  $\alpha_{95}$ :  $6.9^\circ$ , k: 14.3, n: 33 (specimens). After application of the bedding correction, the characteristic mean direction for “b” at AV1 is Dec:  $9.5^\circ$ , Inc:  $57.6^\circ$ ,  $\alpha_{95}$ :  $6.9^\circ$ , k: 14.3 (Figure 4.7b, Table 4.1 and 4.2).

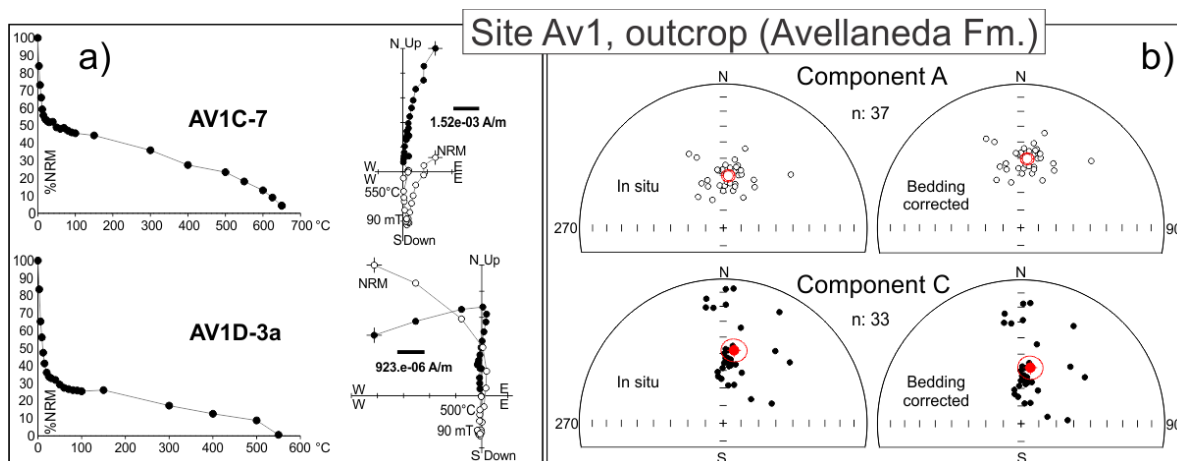


Figure 4.4: a) Representative specimens of the Avellaneda formation at site AV1 demagnetized by alternating fields plus high temperatures. Demagnetization plots and Zijderveld diagrams are shown. In the latter open (full) symbols correspond to projection in the vertical (horizontal) plane; b) Stereographic projections of the specimens directions obtained from the low coercivity component "a" and the high temperature component "b". Open (full) circles represent upward (downward) directions. The components are shown in “in situ” coordinates and after bedding correction.

#### 4.4.2. Drill core E34

Sixteen samples were collected from this drill core. The measured vertical thickness for the Avellaneda Formation was  $\sim 9$  m (Figure 4.2). All paleomagnetic specimens (n: 58) were demagnetized with high temperatures according to the following steps: 90, 120, 150, 200, 250, 300, 350, 400, 450, 500, 525, 550, 575, 600, 620 and  $640^\circ$  C. (Figure 4.5a). The behavior during thermal demagnetization was very similar in all specimens. Up to approximately  $250$ - $350^\circ$  C, a NW to NE directed magnetic component (component "a") of moderate negative inclination was isolated. The maximum angular deviation (MAD) values were always below  $12^\circ$ . This component was used to refine the azimuthal orientation of the sampled fragments of the core. As a reference, we used component “a” isolated in the specimens obtained in the outcrops of the quarry (site AV1). To achieve that we rotated the mean “a” in situ direction around a vertical axis so that its mean declination matches that obtained for the same component at AV1. After this we were able to determine with more confidence the dip direction of the layers observed in the core ( $Az=188^\circ$ ), in order to perform

a more reliable bedding correction. Figure 8b shows the directions of component "a" isolated from each specimen "in situ" (after this azimuthal correction) and after bedding correction (mean dip  $15^\circ$  towards Az:  $188^\circ$ ). The average of these directions "in situ" is: Dec:  $5.5^\circ$ , Inc:  $-51.6^\circ$ , k: 69.2,  $\alpha95$ :  $2.1^\circ$ , n: 67, while corrected to the paleohorizontal is: Dec:  $6.0^\circ$ , Inc:  $-36.7^\circ$ , k: 69.2,  $\alpha95$ :  $2.1^\circ$ . Between 350 and 575° C the characteristic remanent magnetization (ChRM or component "b") was isolated, generally trending towards the origin of coordinates (Figure. 4.5a). Maximum accepted MAD was of  $15^\circ$ , but most (80%) were less than  $10^\circ$ . The minimum number of demagnetization steps to determine components was 6. At temperatures of 600° C or higher all specimens showed an abrupt increase in the intensity of magnetic remanence and random directions. At this temperature, the samples also presented an increase in bulk magnetic susceptibility, sometimes of one order of magnitude. Forty-seven specimens showed a ChRM pointing NNE and downwards, while eleven specimens (from samples E34-14, E34-15 and E34-16) presented nearly antipodal, SSW and upwards directions. Component "b" (Figure 4.5b) "in situ" mean direction is: Dec:  $15.7^\circ$ , Inc:  $53.3^\circ$ ,  $\alpha95$ :  $3.2^\circ$ , k: 35.4, n: 58 and after bedding correction: Dec:  $20.4^\circ$ , Inc:  $68.1^\circ$ ,  $\alpha95$ :  $3.2^\circ$ , k: 35.4. It is interesting to note that the mean bedding-corrected direction of component b is very similar to that of the same component determined at AV-1. None of these two mean directions are similar to any expected post-Cambrian directions for the study area (eg. Torsvik et al., 2012).

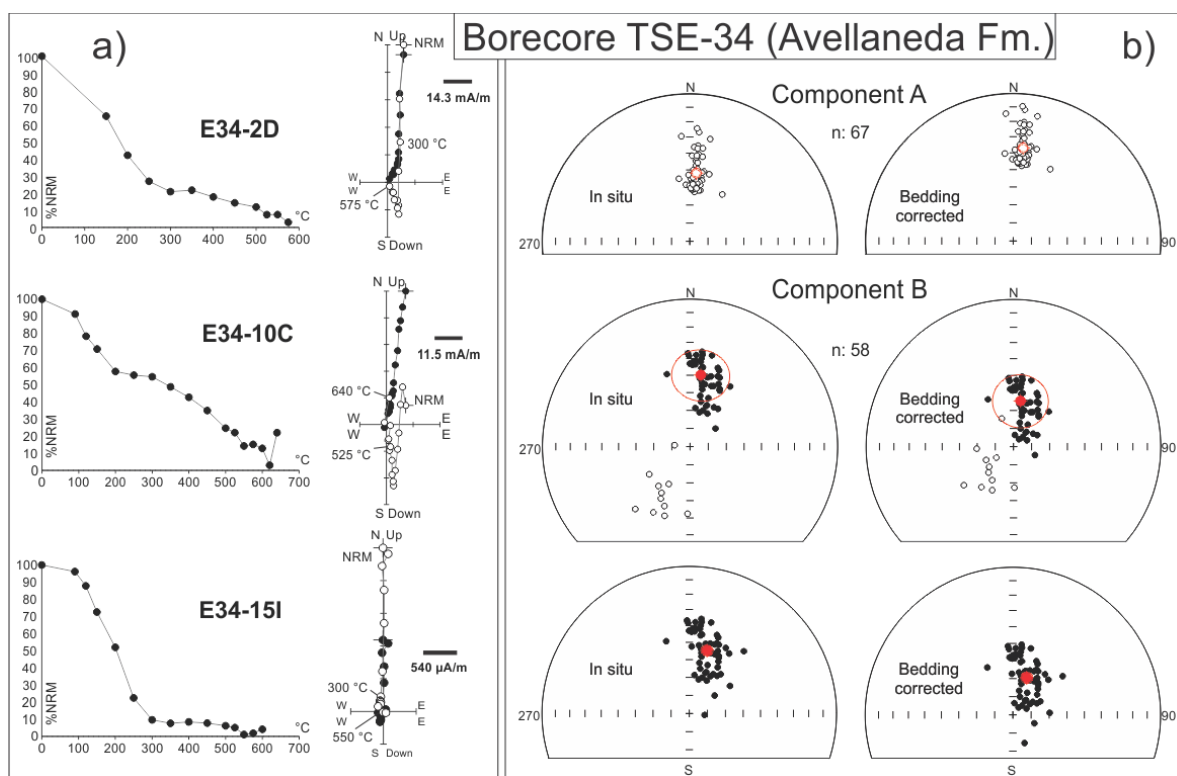


Figure 4.5: a) Representative specimens of the Avellaneda formation in TSE-34 bore core demagnetized by high temperatures. Demagnetization plots and Zijderveld diagrams are shown; b) Stereographic projections of the specimens directions obtained from the low coercivity component "a" and the high temperature component "b". The components are shown in "in situ" geographic coordinates and after bedding correction. Lowermost stereonet shows specimen ChRM directions after inverting those of negative inclinations references as in Figure 4.4.

#### 4.4.3. Drill core H09

Thirty-one samples were collected from this drill core, where the measured vertical thickness for the Avellaneda formation was 19.7 m (Figure 4.2). The paleomagnetic processing consisted of high-temperature demagnetization following the same steps as in the previous case. A low temperature component "a" was isolated at temperatures below 200-300° C in most specimens. A second component "b" of high unblocking temperature was generally determined between 350 and 575° C, or up to 600° C in some cases (Figure 4.6a). In this collection, all except two specimens showed a NW to NE downward directed ChRM. The demagnetization behavior was very similar to that observed in samples from core E34. Unlike the other two cores, the H09 presented subhorizontal laminations. Azimuthal orientation of the samples was therefore only achieved by rotating each sample around a vertical axis so that the component "a" mean sample declination coincides with that obtained for the same component at AV-1. The mean direction of component "a" is, Dec: 5.4°, Inc: -48.2°,  $\alpha_{95}$ : 2.8°, k: 28.9, n: 89. Component "b" yielded a mean direction: Dec: 20.5°, Inc: 58.0°,  $\alpha_{95}$ : 3.9°, k: 18.3, n: 76 (Figure 4.6b, Table 4.1 and 4.2).

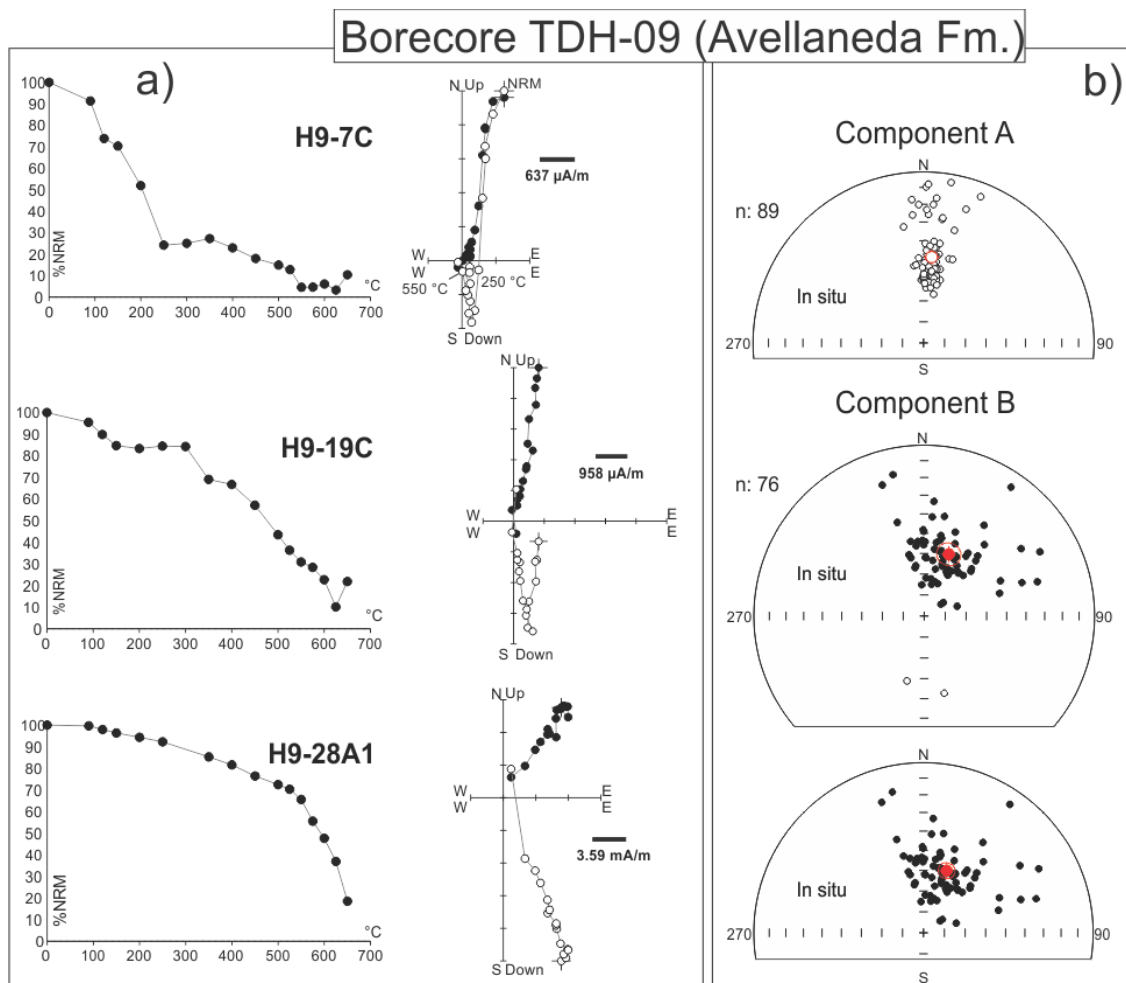


Figure 4.6: a) Representative specimens of the Avellaneda formation in TDH-09 bore core demagnetized by high temperatures. Demagnetization plots and Zijderveld diagrams are shown; b) Sterographic projections of the specimens directions obtained from the low coercivity component "a" and the high temperature component "b". The components are shown only in "in situ" geographic coordinates as bedding is horizontal. Lowermost stereonet shows specimen ChRM directions after inverting those of negative inclinations. References as in Figure 4.4.

#### 4.4.1 Drill core E07

Twenty-seven samples were collected for the Avellaneda formation from this bore core. Measured vertical thickness of this unit was 17.5 m. All specimens were demagnetized by high temperatures. Heating steps were the same as those applied to the other bore cores specimens. Component "a" was determined between 100-350° C. The high temperature, characteristic component "b" was isolated between 350-550° C in most cases. In just few specimens unblocking temperatures reached 575°C or even 600° C (Figure 4.7a). Both polarities of component "b" were recorded. As in TSE-34, in situ mean direction of Component "a" for each sample was used to check and correct the azimuthal orientation of the core, by comparison with mean declination of this component at AV1. Negative

inclinations were found for Component “b” at samples E7-26, E7-36, E7-40, E7-42, E7-43, E7-44 and E7-45. The measured dip of the laminations ranged between 14 and 23° with an average inclination of 17°. The mean direction obtained for Component “a” in “in situ” coordinates is: Dec: 5.4°, Inc: -56.0°,  $\alpha_{95}$ : 1.5°, k: 101.1, n: 88 while after bedding correction is Dec: 345.1°, Inc: -48.8°,  $\alpha_{95}$ : 1.5°, k: 101.1. On the other hand, mean direction of Component “b” in “in situ” coordinates is, Dec: 336.9°, Inc: 66.1°,  $\alpha_{95}$ : 3.7°, k: 19.5, n: 79 while after bedding correction the mean direction is Dec: 20.5°, Inc: 72.8°,  $\alpha_{95}$ : 3.7°, k: 19.5 (Figure 4.7b, Table 4.1 and 4.2).

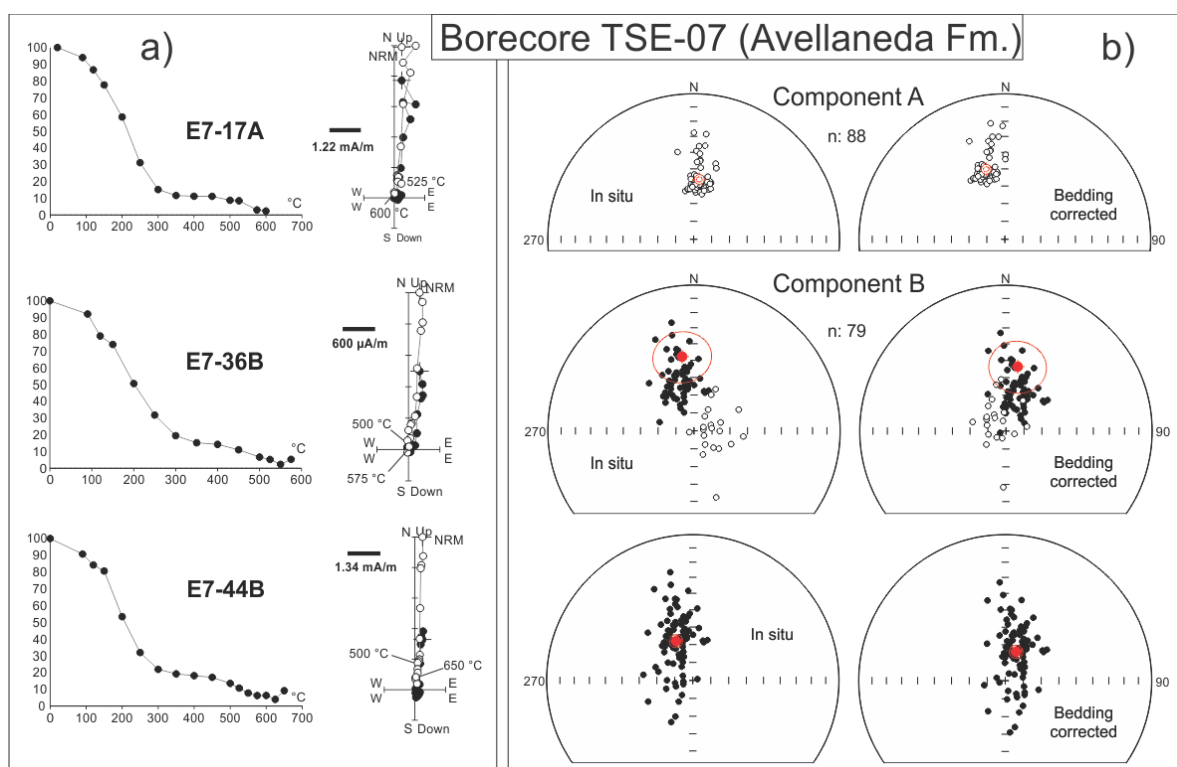


Figure 4.7: a) Representative specimens of the Avellaneda formation in TSE-07 bore core demagnetized by high temperatures. Demagnetization plots and Zijderveld diagrams are shown. b) Stereonographic projections of the specimens directions obtained from the low coercivity component "a" and the high temperature component "b". Components are shown in “in situ” geographic coordinates and after bedding correction, lowermost stereonet shows specimen ChRM directions after inverting those of negative inclinations. References as in Figure 4.4.

The Cerro Negro formation was also sampled in this bore core. Ten samples were collected from this formation encompassing a vertical thickness of 7.1 m. Samples were oriented by the lamination dip directions. Since the same mean dip was measured for the Cerro Negro and Avellaneda formations, the same bedding attitude determined for the latter was used for the Cerro Negro samples (Strike Az: 20°, dip: 17°). Demagnetization of the specimens proceeded following the same scheme applied to samples from the Avellaneda

Formation. Only high temperature demagnetization with steps similar to those described above for the Avellaneda formation was applied. A low temperature component "a" was isolated between 90 and 300°/350°C. The mean direction of component "a" isolated was virtually identical to that from the Avellaneda formation in this borecore confirming the validity of the same bedding correction. This component was isolated between 350 and 575° C, although in some occasions unblocking temperatures above 600° C were found (Figure 4.8a). With a single exception, all specimens carried a NNW downward directed component "b" with moderate to high inclinations. The mean direction obtained for component "a" "in situ" was: Dec: 4.9°; Inc: -30.0°;  $\alpha_{95}$ : 5.1°; k: 39.8; n: 21 and after bedding correction: Dec: 356.6°; Inc: -24.3°;  $\alpha_{95}$ : 5.1°; k: 39.8. For the directional analysis of the Cerro Negro formation, both components obtained in the bore core were joined with the components determined in Rapalini et al. (2013) for the same formation. In this manner, the low temperature component "a" (n: 13) and the high temperature component "c" (n: 17) obtained at sites OV-9, OL-20, OL-21 and OV-22 were also considered (see Rapalini et al., 2013) for a fully directional analysis. Component "a" isolated in this paper and in Rapalini et al. (2013) yielded, in geographical coordinates, a mean direction of n: 34, Dec: 4.8°, Inc: -39.1°,  $\alpha_{95}$ : 5.4°, k: 21.6, worsening their statistical parameters when performing the correction to the paleohorizontal: Dec: 350.5°, Inc: -36.7°,  $\alpha_{95}$ : 8.1°, k: 10.2. The mean "in situ" direction obtained from the "b" component plus the same component isolated by Rapalini et al. (2013), is n: 49, Dec: 359.8°, Inc: 55.8°,  $\alpha_{95}$ : 5.9°, k: 13.0, while after bedding correction a slight improvement in the statistical parameters is observed: Dec: 22.9°, Inc: 60.4°,  $\alpha_{95}$ : 5.2°, k: 16.1 (Figure 4.11b, Table 4.1 and 4.2).

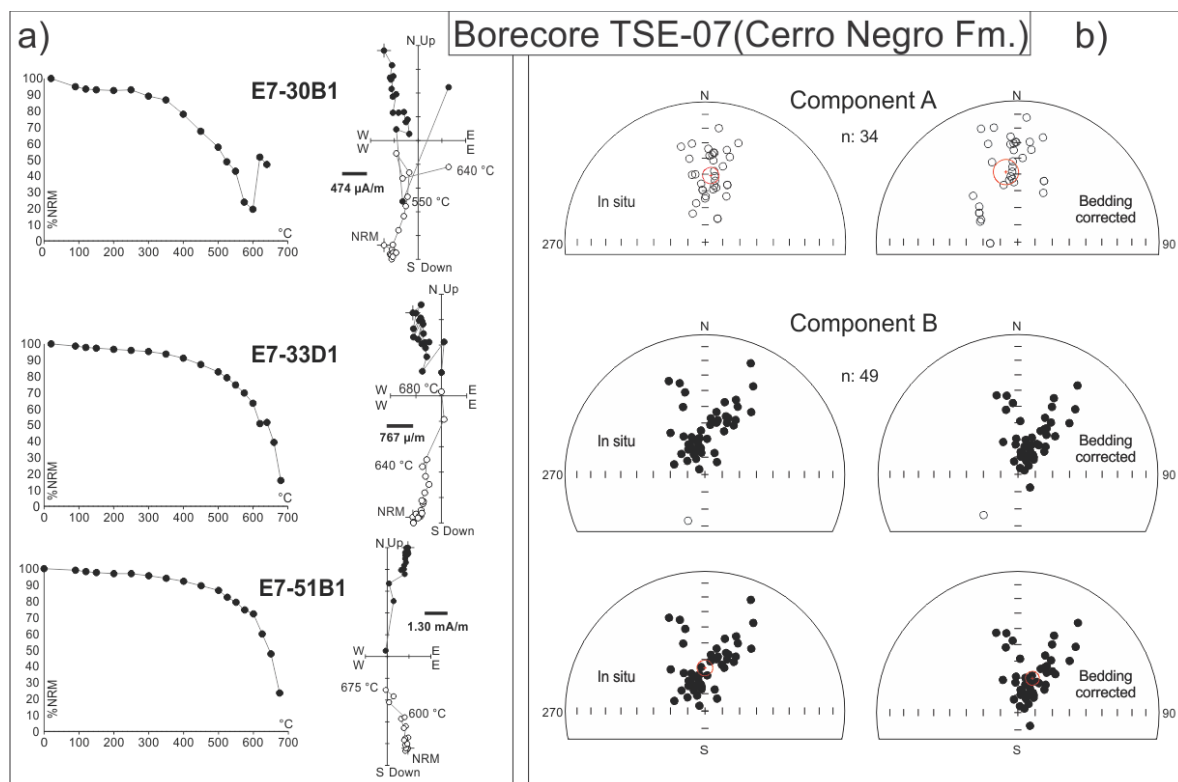


Figure 4.8: a) Representative specimens of the Cerro Negro formation in TSE-07 bore core demagnetized by high temperatures. Demagnetization plots and Zijderveld diagrams are shown; b) Stereographic projections of the specimens directions obtained from the low coercivity component "a" and high temperature component "b". The components are shown in "in situ" geographic coordinates and after bedding correction. Lowermost stereonet show specimen ChRM directions after inverting a single one of negative inclinations. More references in Figure 4.7.

## 4.5. Directional analysis

### 4.5.1. Mean directions determined on a specimen basis

From the study carried out at the outcrop level at site AV1 and in drill cores E34, H09 and E07, a mean direction for the ChRM can be obtained considering the total of specimens for the Avellaneda formation. This yields an "in situ" direction (after azimuthal rotation) of: Dec:  $6.6^\circ$ , Inc:  $59.3^\circ$ ,  $\alpha_{95}$ :  $2.4^\circ$ , k: 15.1, n: 246. After application of the respective bedding correction an improvement in the statistical parameters is observed: Dec:  $18.6^\circ$ , Inc:  $65.1^\circ$ ,  $\alpha_{95}$ :  $2.2^\circ$ , k: 18.3 (Figure 4.9). These results indicate a statistically significant tilt test at a 99% confidence (McElhinny et al., 1964). Since this test has been generally considered as of low sensitivity, the results obtained strongly suggest that the ChRM of the Avellaneda Formation is pre-tilting.

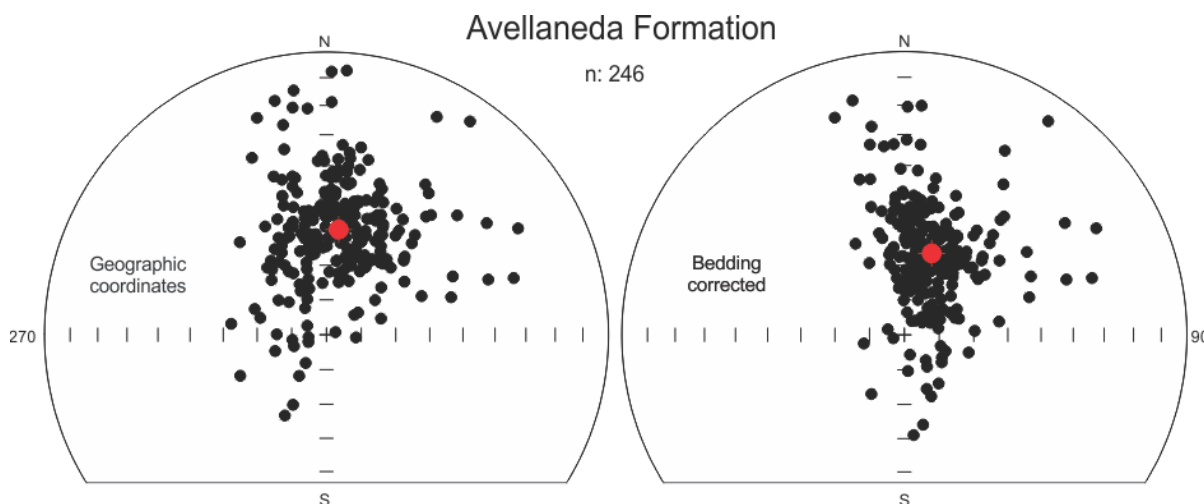


Figure 4.9: Stereographic projections of the characteristic remanence directions and the overall mean direction (full red circle) obtained at a specimen level for the Avellaneda formation. The directions are represented in in situ geographic coordinates (left) and after bedding correction (right). Specimen directions of negative inclinations have been inverted into its antipodal hemisphere.

#### 4.5.2. Mean direction determined on a sample basis

The mean direction for the Avellaneda formation was also determined by averaging the specimen ChRM directions per core segment in order to obtain a single direction for each independent sample of the drill cores and the outcrop. In this way, each sample (approximately 10 to 30 cm long segments of the cores) resembles a more traditional paleomagnetic site. This procedure was carried out either considering all samples regardless of the number of specimens contributing to each mean one or selecting only those samples with a number of specimens  $\geq 3$  (Figure 4.10a). The mean direction obtained considering the total of the samples in “in situ” geographic coordinates is: Dec:  $6.5^\circ$ , Inc:  $59.1^\circ$ ,  $\alpha_{95}$ :  $4.2^\circ$ , k: 17.3, N: 69, and after applying the bedding correction the statistical parameters improve slightly: Dec:  $18.8^\circ$ , Inc:  $64.2^\circ$ ,  $\alpha_{95}$ :  $3.8^\circ$ , k: 20.8. This improvement is not significant at 99% confidence. On the other hand, the mean direction from samples with three or more specimens in “in situ” geographic coordinates is: Dec:  $7.0^\circ$ , Inc:  $60.9^\circ$ ,  $\alpha_{95}$ :  $4.8^\circ$ , k: 18.3, N: 51 and when applying the bedding correction is: Dec:  $21.4^\circ$ , Inc:  $67.0^\circ$ ,  $\alpha_{95}$ :  $4.1^\circ$ , k: 24.2, again showing a slight improvement in the statistical parameters after bedding correction. Application of the McElhinny (1964) tilt test turns a significant pre-tilt magnetization at 90% but not-significant at 95%. In any case, the results suggest that a pre-tilting remanence is more likely. As shown in Table 4.3, the method for determining the mean direction of the

Avellaneda formation, whether by averaging all specimens, all samples or only samples with a number of specimens equal or greater than 3, does not yield significantly different results.

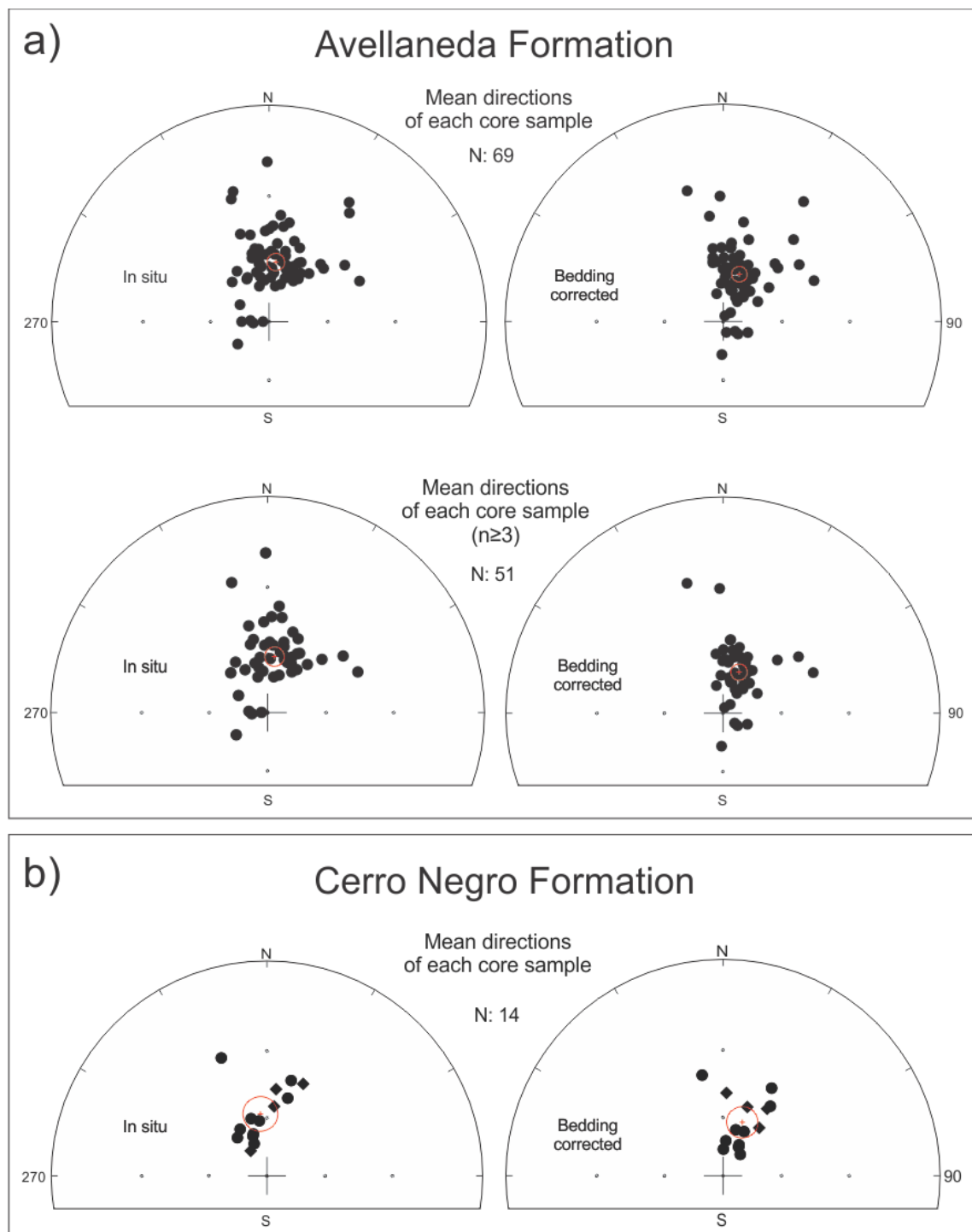


Figure 4.10: a) Stereographic projections of the characteristic remanence directions and mean directions obtained for the Avellaneda formation on a sample basis (upper diagrams), and excluding samples with less than 3 specimens (lower diagrams), in in situ coordinates (left) and after bedding corrections (right); b) idem a) for the Cerro Negro formation considering all the samples taken from the bore core TSE-07 and those directions reported in Rapalini et al. (2013) (black diamonds).

Table 4.1: Mean directions per sample with  $n(\text{specimens}) \geq 3$  obtained for the Avellaneda formation in borecores TDH-09, TSE-34, TSE-07 and site AV1. N: number of samples; n: number of specimens considered in each sample; Dec: declination; Inc: inclination; Lat: latitude; Long: longitude; alpha95 and A95: confidence ellipses for mean directions and VGPs at 95% confidence, respectively.

Sample	In situ							Bedding corrected						
	Dec	Inc	alpha95	n	Lat	Long	A95	Dec	Inc	alpha95	Lat	Long	A95	
H9-11	17.1	59.7	33.3	4	10.9	312.9								
H9-17	14.0	55.3	7.6	3	16.0	311.6								
H9-18	24.0	61.5	4.9	6	7.4	317.4								
H9-19	11.8	58.2	6.2	4	13.4	309.2								
H9-20	34.2	63.2	5.4	4	2.7	323.4								
H9-21	16.5	59.7	7.6	5	11.0	312.5								
H9-25	344.6	26.4	21.9	3	37.0	281.0								
H9-28	45.5	51.5	17.0	5	8.9	337.5								
H9-30	53.1	43.2	18.6	4	10.3	347.2								
H9-32	65.7	41.2	19.8	3	3.4	356.6								
H9-4	23.4	63.0	13.8	3	5.8	316.3								
H9-5	2.9	62.1	14.2	4	9.6	301.9								
H9-7	9.7	71.1	7.1	4	-3.0	305.3								
H9-8	30.7	65.5	12.7	4	1.0	319.9								
<b>All (N: 14)</b>	<b>24.4</b>	<b>58.1</b>	<b>8.8</b>	<b>56</b>	<b>10.0</b>	<b>318.5</b>	<b>10.3</b>							
E34-10	12.6	58.3	7.2	4	13.2	309.8		16.3	73.2		-6.8	308.2		
E34-11	20.7	63.0	5.4	5	6.4	314.5		34.8	77.3		-16.2	313.9		
E34-12	16.9	69.6	5.6	3	-1.5	309.8		39.1	84.0		-27.5	308.2		
E34-13	28.3	55.6	13.6	3	12.3	322.9		41.3	69.1		-6.5	323.6		
E34-14	39.5	58.0	17.1	3	6.0	329.7		59.9	69.4		-13.9	332.2		
E34-15	23.6	58.9	12.2	5	10.3	318.0		36.1	72.9		-10.0	318.1		
E34-16	26.5	56.4	16.2	4	12.1	321.2		39.0	70.1		-7.1	321.6		
E34-1	22.4	49.7	6.8	5	19.3	320.1		29.6	63.9		3.2	320.0		
E34-2	17.4	47.6	6.6	4	22.3	316.3		21.7	62.4		6.9	315.4		
E34-4	17.4	61.4	45.4	3	8.9	312.7		26.7	75.9		-12.6	311.7		
E34-5	357.6	44.7	14.8	3	26.6	297.4		353.3	59.3		12.7	294.5		
E34-6	6.2	37.6	4.0	3	31.7	306.6		5.6	52.6		19.6	304.8		
E34-7	2.4	42.4	1.9	4	28.4	302.3		0.4	57.3		15.1	300.1		
E34-8	8.6	42.3	7.0	6	28.0	308.7		8.8	57.3		14.7	307.0		
E34-9	13.0	53.2	4.7	3	18.2	311.1		16.1	68.1		0.7	309.8		
<b>All (N: 15)</b>	<b>15.7</b>	<b>53.7</b>	<b>5.3</b>	<b>58</b>	<b>16.3</b>	<b>313.7</b>	<b>6.0</b>	<b>20.5</b>	<b>68.5</b>	<b>5.3</b>	<b>-1.9</b>	<b>312.7</b>	<b>8.0</b>	
E7-11	352.2	61.3	8.6	5	10.3	293.9		25.6	64.7		3.3	317.1		

E7-12	349.0	52.2	10.0	3	19.5	290.0	12.4	58.0	13.5	309.7			
E7-13	345.9	54.2	10.0	3	17.1	287.7	11.0	60.6	10.8	308.1			
E7-14	317.2	62.1	12.2	3	0.7	270.2	346.7	75.1	-9.6	293.5			
E7-15	332.5	65.1	8.0	3	2.9	281.5	13.6	73.3	-6.7	306.8			
E7-20	347.8	45.6	15.1	4	2.4	287.8	6.0	52.4	19.8	305.1			
E7-21	334.1	64.5	6.7	6	3.5	282.2	14.0	72.5	-5.5	307.2			
E7-22	353.6	68.3	11.8	3	1.4	295.8	39.1	69.5	-6.4	322.1			
E7-23	327.7	59.3	8.1	3	7.4	275.4	356.8	70.2	-1.3	297.9			
E7-26	357.4	55.6	15.9	5	16.8	297.6	23.7	58.5	10.7	318.3			
E7-36	265.2	81.7	5.8	3	-36.6	279.4	130.3	79.9	-47.8	322.1			
E7-37	345.7	63.6	7.0	7	6.8	289.7	23.5	68.4	-1.0	314.1			
E7-38	344.7	70.8	8.6	4	-3.1	291.1	39.4	73.5	-11.7	319.1			
E7-40	273.9	80.2	13.5	3	-33.4	276.8	130.0	82.0	-45.9	317.1			
E7-42	348.9	66.2	17.9	3	3.9	292.4	31.2	69.4	-4.0	318.0			
E7-43	300.5	72.4	7.9	3	-16.9	270.9	15.1	86.9	-31.0	301.7			
E7-44	271.5	86.8	14.3	3	-36.6	291.8	114.2	76.0	-43.2	333.7			
E7-45	234.5	70.0	10.5	6	-49.4	252.3	182.5	72.8	-68.7	296.2			
<b>All (N: 18)</b>	<b>335.5</b>	<b>68.1</b>	<b>6.7</b>	<b>70</b>	<b>-3.0</b>	<b>284.4</b>	<b>10.7</b>	<b>24.5</b>	<b>74.5</b>	<b>6.7</b>	<b>-12.0</b>	<b>311.6</b>	<b>11.6</b>
AV1A	359.3	17.4	8.3	7	44.1	298.8	358.9	27.4	38.5	298.4			
AV1C	4.8	55.5	2.7	10	16.8	303.8	4.7	65.5	5.3	303.0			
AV1D	1.7	54.1	5.0	8	18.4	301.3	0.5	64.1	7.2	300.1			
AV1E	27.1	61.3	14.3	5	6.9	319.6	37.3	70.2	-6.7	320.7			
<b>All (N: 4)</b>	<b>6.1</b>	<b>47.8</b>	<b>25.0</b>	<b>30</b>	<b>21.6</b>	<b>306.5</b>	<b>21.0</b>	<b>6.4</b>	<b>57.8</b>	<b>25.0</b>	<b>11.0</b>	<b>305.9</b>	<b>25.3</b>
<b>All (N: 51)</b>	<b>7.0</b>	<b>60.9</b>	<b>4.8</b>	<b>214</b>	<b>8.7</b>	<b>304.3</b>	<b>6.6</b>	<b>21.4</b>	<b>67.1</b>	<b>4.2</b>	<b>-1.0</b>	<b>313.4</b>	<b>5.9</b>

In the Cerro Negro formation, an analysis was also carried out to determine the mean direction on a sample (and not specimen) basis. In this case, due to the low number of samples, no selection was made based on the number of specimens. A complete directional analysis was made considering the mean directions of the samples obtained in this work and those directions reported by Rapalini et al. (2013). The mean direction for the Cerro Negro Formation computed in this way is Dec: 353.9°, Inc: 57.9°,  $\alpha_{95}$ : 8.5°, k: 23.0, N: 14. When applying the bedding correction the mean direction is Dec: 19.8°, Inc: 60.7°,  $\alpha_{95}$ : 7.7°, k: 27.7, observing a slight improvement in the statistical parameters but not statistically significant (Figure 13b). However, Rapalini et al. (2013) reported a positive fold test for this formation.

Table 4.2 Mean directions per sample obtained for the Cerro Negro formation in borecore TSE-07. For references see Table 2. With (\*) sites previously reported by Rapalini et al. (2013).

Sample	In situ							Bedding corrected						
	Dec	Inc	alpha95	n	Lat	Long	A95	Dec	Inc	alpha95	Lat	Long	A95	
E7-27	340.5	68.0	7.9	5	0.3	287.7		28.6	73.0		-8.5	314.4		
E7-28	338.9	29.4	18.6	4	33.7	275.2		348.3	39.5		29.6	287.3		
E7-29	352.1	61.2	24.1	2	10.4	293.8		25.4	64.7		3.4	316.9		
E7-30	330.2	62.1	9.0	3	5.2	278.5		4.6	71.7		-3.6	302.3		
E7-31	338.4	71.8	4.7	4	-5.4	288.1		38.8	75.7		-14.7	316.9		
E7-32	14.2	41.1	32.9	2	28.0	314.5		29.0	40.6		23.9	328.9		
E7-33	342.1	67.0	10.3	3	1.9	288.3		27.4	71.9		-6.6	314.5		
E7-34	344.5	59.3	31.3	2	11.6	287.7		15.5	65.3		4.5	310.2		
E7-35	322.4	64.9	20.9	2	-0.4	275.1		1.0	76.1		-10.7	300.2		
E7-51	14.9	49.2	8.5	4	21.5	313.6		34.2	47.8		16.7	330.7		
<b>All (N: 10)</b>	<b>348.3</b>	<b>58.7</b>	<b>10.0</b>	<b>31</b>	<b>10.9</b>	<b>290.0</b>	<b>11.4</b>	<b>18.5</b>	<b>63.7</b>	<b>10.0</b>	<b>3.4</b>	<b>312.4</b>	<b>12.1</b>	
OV-9*	21.4	40.9	11.8	9	26.3	321.7		37.0	59.2		5.9	327.4		
OL-20*	6.0	46.1	-	1	25.3	305.7		2.4	48.3		23.7	302.0		
OL-21*	327.1	74.3	80.6	2	-11.3	284.0		33.3	49.6		15.7	329.2		
OV-22*	5.9	54.2	27.1	5	17.4	305.7		19.4	53.0		16.5	317.4		
<b>All (N: 4)</b>	<b>6.8</b>	<b>54.8</b>	<b>20.9</b>	<b>17</b>	<b>15.0</b>	<b>303.9</b>	<b>27.0</b>	<b>22.2</b>	<b>53.3</b>	<b>12.3</b>	<b>15.7</b>	<b>319.3</b>	<b>16.0</b>	
<b>All (N: 14)</b>	<b>353.9</b>	<b>57.9</b>	<b>8.5</b>	<b>48</b>	<b>12.1</b>	<b>293.8</b>	<b>10.1</b>	<b>19.8</b>	<b>60.7</b>	<b>7.7</b>	<b>7.0</b>	<b>314.4</b>	<b>9.5</b>	

Table 4.3: Mean ChRM directions determined for the Avellaneda and Cerro Negro formations. Mean directions obtained by averaging specimens, by considering sample/site, and samples with specimens  $\geq 3$  are shown. BP: bedding plane (strike/dip, right hand convention); N: number of samples taken from the core bores and in the outcrop at AV1; n: number of specimens; Dec: declination; Inc: inclination;  $\alpha_{95}$  and k: Fisherian statistical parameters. All the values in the table are expressed in ( $^{\circ}$ ), with the exception of the k parameter.

Geologic unit	Bore core/outcrop	BP ( $^{\circ}$ )	N	n	Geographic coordinates				Bedding corrected			
					Dec	Inc	$\alpha_{95}$	k	Dec	Inc	$\alpha_{95}$	k
Avellaneda Fm.	AV1	95/10	5	33	8.5	47.6	6.9	14.3	9.5	57.6	6.9	14.3
	TSE-34	98/15	15	58	15.7	53.3	3.2	35.4	20.4	68.1	3.2	35.4
	TDH-09	0/0	25	76	20.5	58	3.9	18.3	-	-	-	-
	TSE-07	20/17	24	79	336.9	66.1	3.7	19.5	20.5	72.8	3.7	19.5
	All (specimens)	-	-	246	6.6	59.3	2.4	15.1	18.6	65.2	2.2	18.0
	All (samples)	-	69	-	6.5	59.1	4.2	17.3	18.8	64.2	3.9	20.5
	All (samples with $n \geq 3$ )	-	51	-	7.0	60.9	4.8	18.3	21.4	67.1	4.2	23.9
Cerro Negro Fm.	TSE-07 (specimens)	20/17	-	48	359.8	55.8	5.9	13.0	22.9	60.4	5.2	16.1
	TSE-07 (samples)	20/17	14	-	353.9	57.9	8.5	23	19.8	60.7	7.7	27.7

## 5. Reversal tests

The paleomagnetic records of the Avellaneda Formation suggest a dominant reverse polarity with some short reversal periods (see Afonso et al., companion paper). A reversal test was applied to the Avellaneda Formation ChRM directions after bedding correction (McFadden and McElhinny, 1990, Koymans et al., 2016). In two cores the reversal test yielded negative results (E34, angle between directions of  $12.3^{\circ}$  vs. critical angle of  $8.3^{\circ}$ , E07, angle between directions of  $29.0^{\circ}$  vs critical angle of  $6.7^{\circ}$ ). At core H09 the result was classified as indeterminate, with an angle between directions of  $12.3^{\circ}$  and a critical angle of  $31.2^{\circ}$ . When the reversal test was determined for all specimens ( $n$ : 246), both in geographic coordinates and after bedding correction, the result was still negative. In geographic coordinates, the angle between directions was  $22.9^{\circ}$  vs critical angle  $7.8^{\circ}$ , meanwhile after bedding correction the angle between directions was  $23.9^{\circ}$  vs critical angle  $6.3^{\circ}$ . Failure of the reversal test may indicate that the sampling of normal intervals was not sufficient to fully average paleosecular variation.

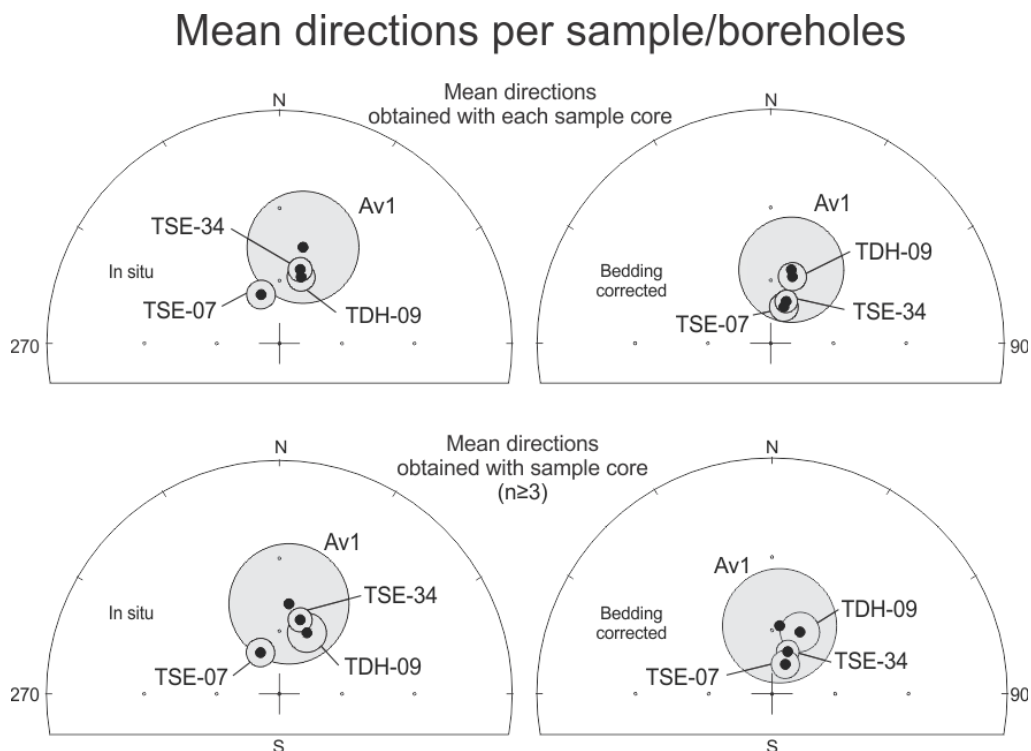


Figure 4.11: Stereographic projections of the mean directions obtained per bore core and site AV1 for the Avellaneda formation. It is analyzed considering all samples and with those samples with  $n \geq 3$  specimens. The directions are shown in geographic coordinates and after bedding correction.

## 6. Rock magnetism

Rock magnetism studies were carried out in representative samples from the three drill cores and from the outcrop of the Avellaneda and Cerro Negro formations. The studies consisted of K (bulk susceptibility) vs. T, IRM (isothermal remanent magnetization) acquisition and back-field curves, hysteresis cycles and FORCs diagrams.

### 6.1. Thermomagnetic curves

The K vs. T curves were performed at low and high temperatures in the AV1D-3 sample (marl) taken from the AV1 site (Avellaneda formation). The low temperature susceptibility curve (Figure 4.12a) shows the typical behavior of paramagnetic minerals as the main responsible for susceptibility, however, a minor jump in K at around  $-180^{\circ}\text{C}$  might be related to a Verwey transition (Verwey, 1939; Walz, 2002) and the presence of magnetite. However, this needs to be further substantiated. On the other hand, the high temperature curve (Figure 4.12b), carried out under argon atmosphere, shows a minor drop in K between  $540^{\circ}\text{C}$  and  $580^{\circ}\text{C}$ , consistent with the presence of magnetite. Cooling curve shows an irreversible cycle indicating mineralogical changes in response to heating. The peaks in susceptibility

observed in the high temperature cooling curve indicate the formation of new ferromagnetic (*sensu lato*) phases (magnetite?, maghemite?) as a product of the alteration during heating. The same happens in the high temperature curves from samples of the Avellaneda formation in TDH-09 (sample H9-29, shale) and TSE-34 (sample E34-7, marl) bore cores (Figure 4.12c, d). In these latter cases, production of magnetite seems obvious due to the steep increase in susceptibility with cooling just below 580°C. In all these cases a five to ten fold increase in K at room temperature is observed after heating. A different behavior is observed in the sample E7-14 (marl) taken from the Avellaneda formation in bore core TSE-07 (Figure 4.12e), with a noisy but basically reversible cycle. During heating an apparent Hopinson peak (Dunlop and Özdemir, 1997) develops followed by a steep delay in K around 540-580 °C compatible with (Ti poor) magnetite. Finally, the sample E7-29 (sandstone) from the Cerro Negro formation (bore core TSE-07) presents a behavior similar to that of most of the samples analyzed in the Avellaneda formation, with irreversible cycle and neo formation of magnetite producing a five-fold increase in K at room temperature (Figure 4.12f).

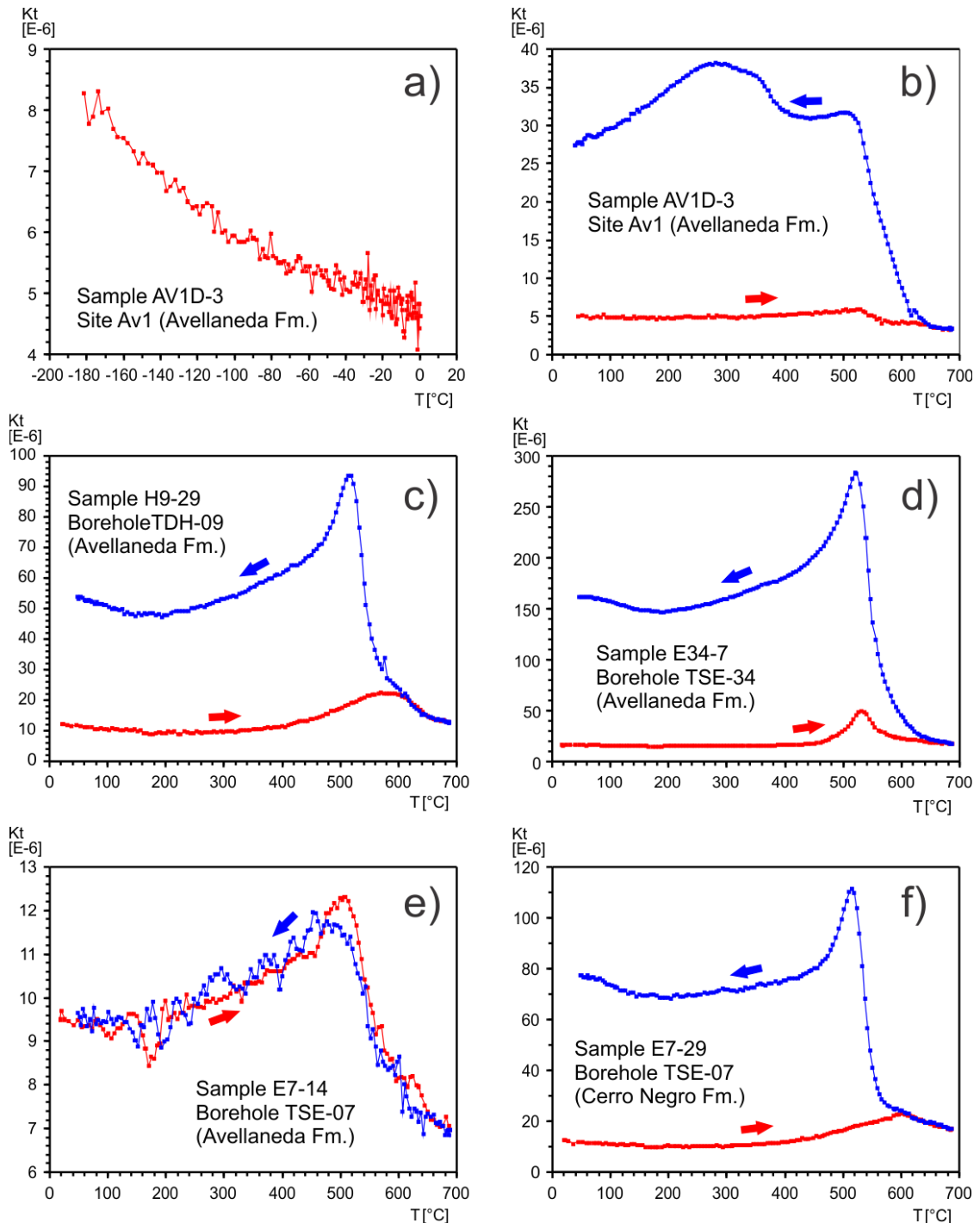


Figure 4.12: Low and high temperature thermomagnetic curves. a) Normalized low temperature curve for a sample of the Avellaneda formation from site AV-1 (outcrop); b) high temperature curves for the same sample; c), d) and e) high temperature curves from samples of the Avellaneda formation from TDH-09; TSE-34 and TSE-07 borecores, respectively; f) high temperature curves for a sample from the Cerro Negro formation, taken from borecore TSE-07. The red (blue) lines correspond to the heating (cooling) curves. Most samples generally show irreversible curves with possibly neo formation of magnetite.

## 6.2. IRM and IRM back-field

The IRM and IRM back-field curves were performed on 12 specimens from the Avellaneda formation, at TSE-34, four specimens from TDH-09 and TSE-07, each, and one specimens from AV1 (Table 4.4). Three specimens of the Cerro Negro formation collected from TSE-07 bore core were also analyzed. The samples from the bore core TSE-34 showed behaviors associated to ferrimagnetic minerals, reaching saturation at fields lower than 1T in all the samples analyzed and a steep increase in the curve at low fields (Figure 4.13a, sample E34-2b, marl). However, in most cases there is clear evidence of an additional antiferromagnetic contribution (Figure 4.13a, sample E34-12a, marl). The remanence coercivity ( $B_{cr}$ ) yielded a wide range of values, between 56.1 and 434.9 mT. As can be seen in Table 4.4, low  $B_{cr}$  values are observed in the lower stratigraphic levels (samples E34-1 and E34-2) while in the upper levels, values of a higher order of magnitude are consolidated, with a more stratigraphic correlation prevailing than lithological with the value of  $B_{cr}$ . Statistical unmixing of different phases contributions was achieved using MAXunMix application (Maxbauer et al., 2016 and references therein). The result for some selected samples is presented in Figures 16 b and c for bore core samples E34. The qualitative interpretation just described is confirmed by this analysis. Both samples show the presence of two components with significantly different coercive forces ( $B_c$ ) likely corresponding to magnetite (41-39 mT) and hematite (620-477 mT), respectively, with medium to strong predominance of hematite.

Table 4.4: Coercitive force (Bc) and remanence coercivity (Bcr) values for samples of the Avellaneda formation in boreholes TSE-34, TSE-07 and TDH-09 and site AV1. The values obtained for the Cerro Negro formation in the borehole TSE-07 are also shown. Note that there is not a clear correlation between lithology and the values obtained. Bc and Bcr in mT.

Borehole (formation)	Lithology	Core	Bc	Bcr
TSE-34 (Avellaneda formation)	marl	E34-1	44.6	74.8
	marl	E34-2	29.1	56.1
	marl	E34-3	70.4	290.8
	marl	E34-4	37.0	85.5
	marl	E34-5	316.0	422.8
	marl	E34-6	308.0	434.9
	marl	E34-7	312.2	414.6
	shale	E34-8	187.6	385.7
	shale	E34-9	370.5	433.7
	marl	E34-10	100.9	359.8
	shale	E34-11	180.7	364.7
	marl	E34-12	94.3	298.7
TSE-07 (Avellaneda formation)	marl	E7-22	361.8	456.1
	marl	E7-26	348.2	439.3
	marl	E7-37	21.2	47.1
	marl	E7-40	33.9	84.8
TDH-09 (Avellaneda formation)	marl	H9-9	52.7	242.9
	marl	H9-18	78.7	351.4
	marl	H9-21	297.5	404.6
	shale	H9-26	361.0	452.6
AV1 (Avellaneda formation)	shale	AV1A-1C	-	469.9
	shale	AV1A-4B	-	467.5
	shale	AV1D-3	41.7	108.2
	shale	AV1E-4B	-	395.7
TSE-07 (Cerro Negro formation)	shale	E7-29	305.7	403.9
	sandstone	E7-32	51.0	307.2
	shale	E7-35	277.8	360.3

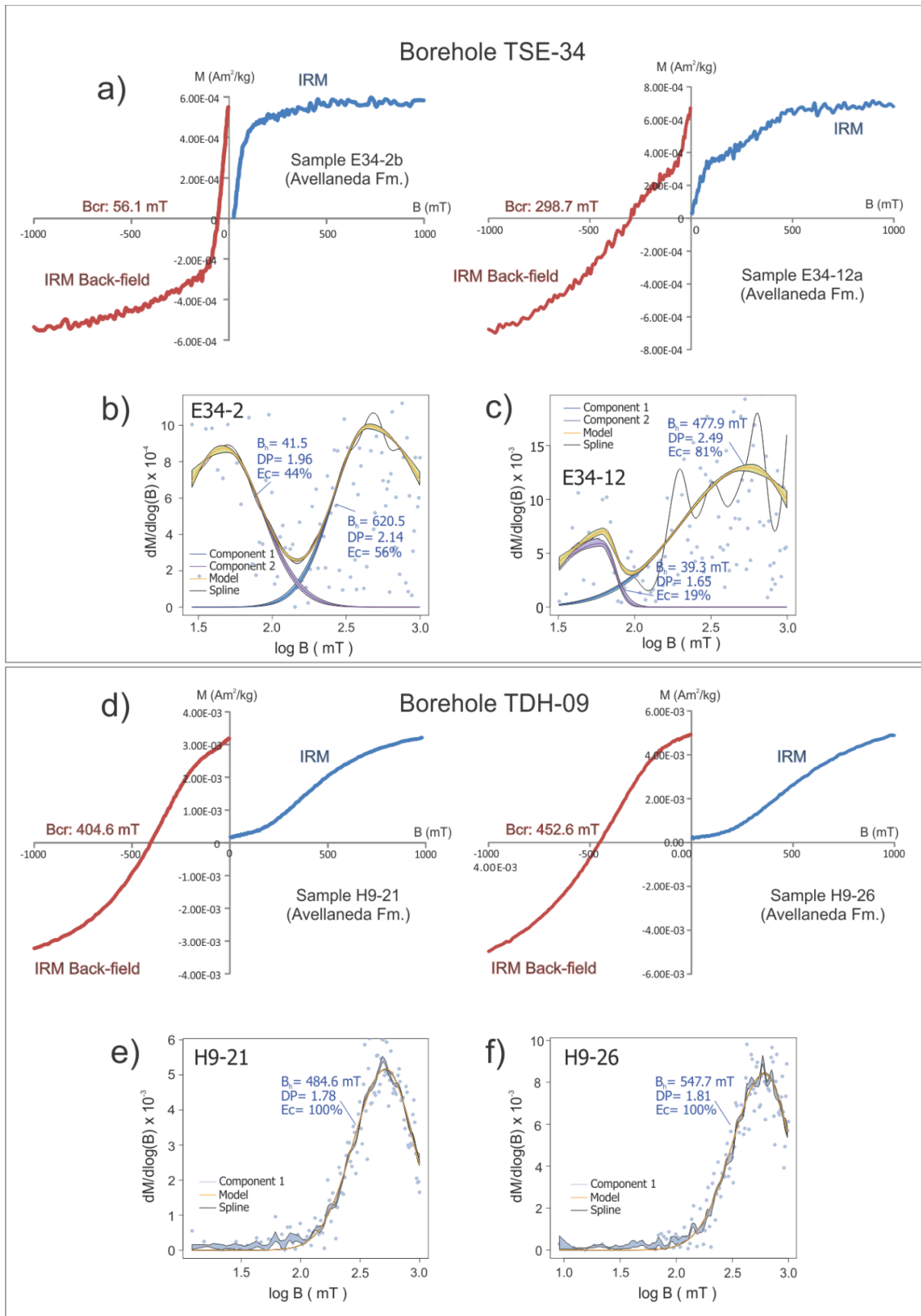


Figure 4.13: Isothermal remanent magnetization (IRM) and IRM back-field acquisition curves, a) Curves belonging to representative samples of the Avellaneda formation from bore core TSE-34; b) and c) MaxUnmix modeling from IRM data showing coercivity component from the previous samples; d) idem a) for representative samples from bore core TDH-09; e) and f) idem b) and c) for the samples of the bore core TDH-09. Bcr: coercivity of remanence.

In bore core TDH-09, a behavior opposite to the previous bore core is observed (Figure 4.13d) with a predominance of the antiferromagnetic fraction, easily identifiable from the less abrupt increase in magnetization at low fields and from non-saturation at smaller fields than 1 T. This behavior is observed in rocks of different lithology, being the samples H9-9, H9-18 y H9-21, marls and the sample H9-26 a shale. The remanence coercivity values obtained were similar to each other, between 242.9 and 452.6 mT (Table 4.4). The analysis using the MAXunMix application showed consistent results with the IRM method, based on the predominance of an antiferromagnetic component (Figure 4.13e, f).

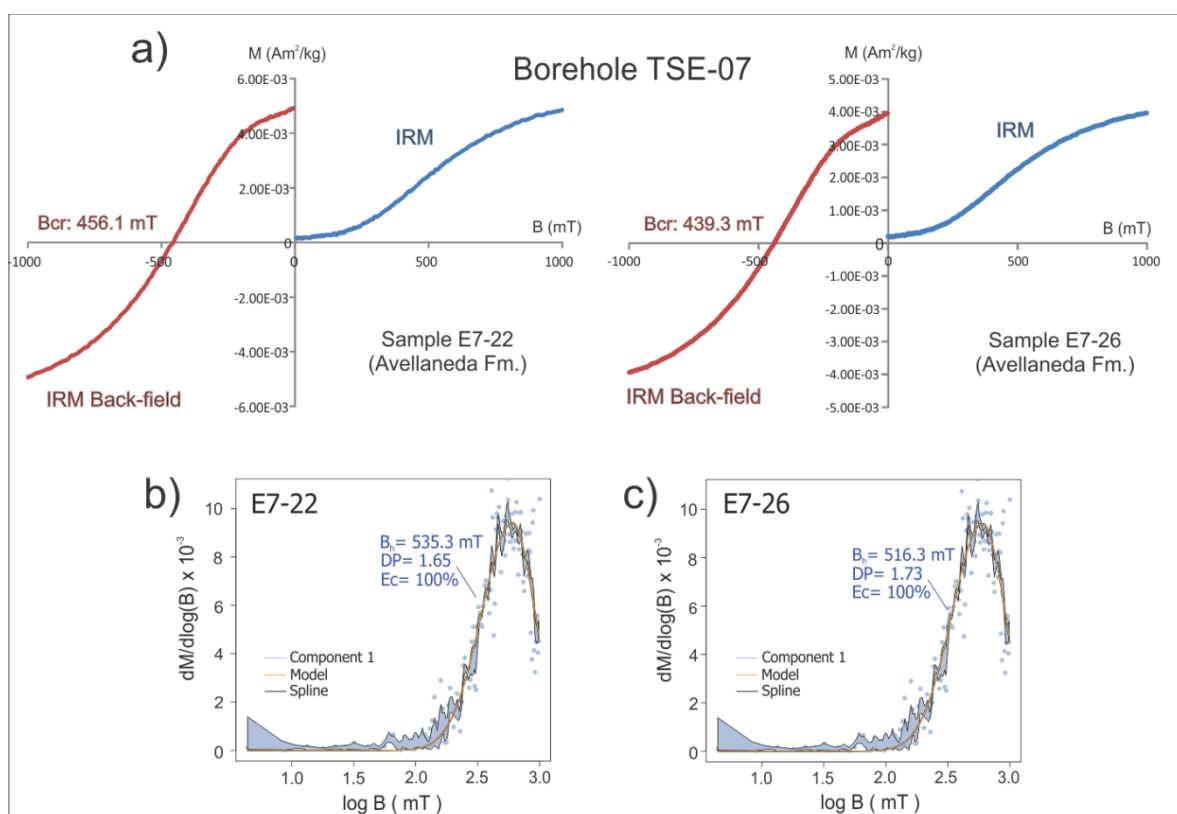


Figure 4.14: Isothermal remanent magnetization (IRM) and IRM back-field acquisition curves, a) Curves belonging to representative samples of the Avellaneda formation from bore core TSE-07; b) and c) MaxUnmix modeling from IRM data showing coercivity component from the previous samples. Bcr: coercivity of remanence.

As in the previous case, bore core TSE-07 showed antiferromagnetic fraction in samples E7-22 and E7-26 located in the upper section of the stratigraphic column (Figure 4.2 and Figure 4.14) but a ferrimagnetic fraction was observed in the other two samples located in the lower part (E7-37 and E7-40, Figure 4.2 and Table 4.4). In both cases, the lithology remains the same with the presence of marls. The remanence coercivity varied between 47.1 and 456.1 mT (Table 4.4). Finally, at the AV1 site, a marked predominance of the

antiferromagnetic fraction is seen (Figure 4.15a), with remanence coercivity values between 108.2 and 469.9 mT (Table 4.4). It is important to mention that the determination of IRM and IRM back-field in this case was carried out by an ASC Scientific IM-10-30 pulse magnetizer applying the following steps to IRM: 15, 29, 44, 61, 74, 100, 150, 200, 300, 450, 600, 800, 1000, 1310, 1970 and 2300 mT. On the other hand, the pulses applied for the IRM back-field were: 15, 25, 35, 65, 100, 250, 350, 450, 500 and 550 mT. The study of the AV1D-3 sample (not shown in Figure 4.15) was carried out using a VSM magnetometer (Molspin Ltd.).

In the Cerro Negro Formation there is a clear predominance of the antiferromagnetic fraction (Figure 4.15b). The IRM back-field curves yielded remanence coercivity values between 307.2 and 403.9 mT (Table 4.4).

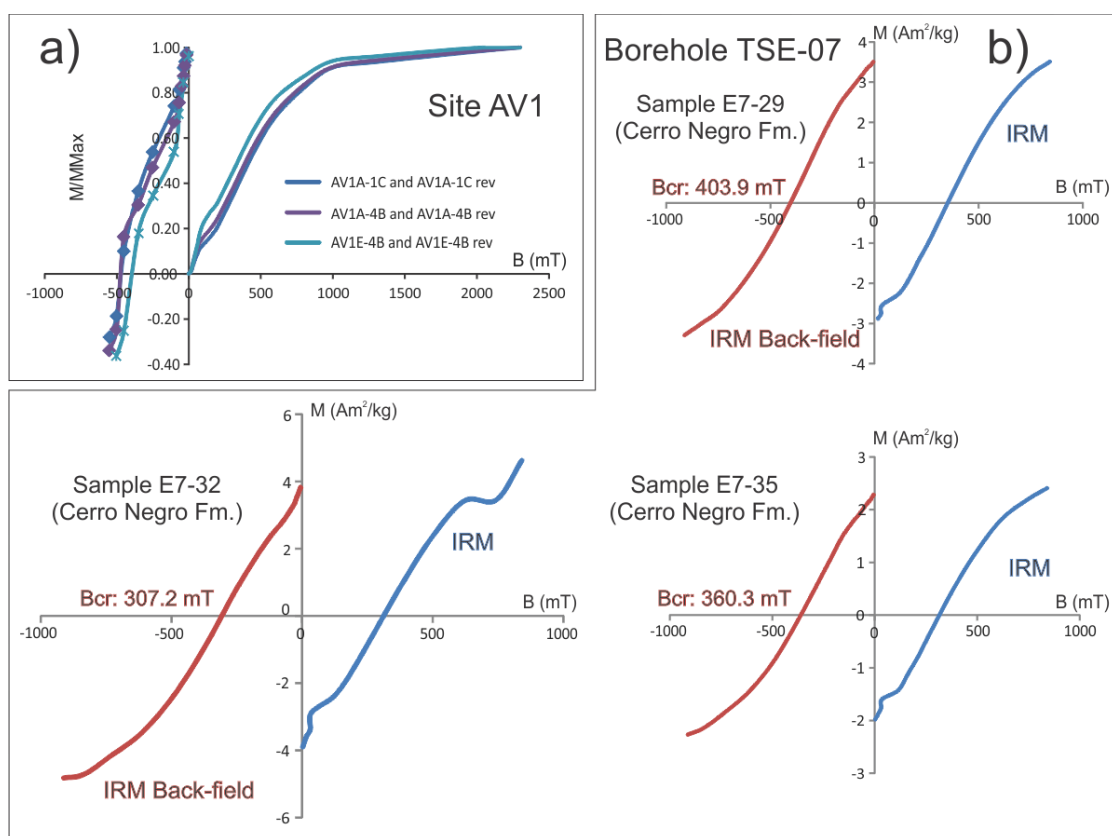


Figure 4.15: Isothermal remanent magnetization (IRM) and back-field acquisition curves, a) Curve belonging to the Avellaneda formation at site AV1; b) Curves belonging to representative samples of the Cerro Negro formation from bore core TSE-07. Bcr: coercivity of remanence.

### 6.3 Hysteresis cycles

The hysteresis cycles, performed on the same IRM samples, showed an important contribution of paramagnetic minerals (Figure 4.17 and 4.18), in all the analyzed samples and in the two formations studied. After subtracting the paramagnetic contribution, moderate to

high coercive forces were observed in the Avellaneda formation, with a wide range of values between 29.1 and 370 mT in bore core TSE-34, between 52.7 and 297.5 mT in bore core TDH-09, and between 21.2 and 361.8 mT in bore core TSE-07 (see Table 4.4). Finally, a single hysteresis cycle was performed at the AV1 site, obtaining a moderate coercivity  $B_c$ : 41.7 mT. In the Cerro Negro formation, the coercivity values were also moderate to high (between 51.0 and 411.0 mT, Table 4.4) with a slightly higher mean value ( $B_c$  mean: 211.5 mT). From Figure 4.16 and 4.17, it is possible to observe a significant disparity in the shapes of the hysteresis curves within each borehole and in both formations. This is analyzed based on the stratigraphic height and by comparison with the IRM and thermomagnetic curves. In borehole TSE-34, hysteresis curves show “pseudo-single domain” loops (sample E34-2b, Figure 4.16a), shapes determined by the presence of hematite (sample E34-9c, Figure 4.16a) and “goose-neck” loops, following the classification proposed by Tauxe (2005). These curves are coherent with the behaviors observed in the IRM curves (Figure 4.15a) where a predominance of magnetite was observed (80-54%) with a subordinate antiferromagnetic (hematite) fraction (20-46%). In borehole TDH-09, hysteresis curves showed “goose-neck” loops (sample H9-18, Figure 4.16b) and shapes determined by the presence of hematite (sample H9-26, Figure 19b), which is corroborated with the coercivity spectra (Figure 16f). Finally, the borehole TSE-07 has hysteresis curves with shapes determined by the presence of hematite (sample E7-22, Figure 4.16c) and “pseudo-single domain” loops (sample E7-37, Figure 4.16c). Stratigraphic height does not show a clear correlation with magnetic mineralogy (Table 4.4, Figure 4.2). In the boreholes TSE-34 and TSE-07 the predominance of marls is almost absolute, with pelitic levels near the top of the Avellaneda formation. In the case of the former, the predominance of magnetite does not change with lithology (marl or pelite), being the exception sample E34-10 (predominance of hematite in marl). In the second, the analyzed samples that are in the upper levels (E7-22 and E7-26) show a predominance of hematite while for the samples analyzed in lower levels (E7-37 and E7-40) a predominance of magnetite is inferred. Finally, in borehole TDH-09, a greater contribution of detrital material is observed in the upper part of the Avellaneda formation between 63.5 to 58 meters (below surface), approximately. All samples showed a predominance of hematite, irrespective of them belonging to marls or to shales (sample H9-26). The Cerro Negro formation, only represented in borehole TSE-07, shows hysteresis curves with shapes determined by the presence of hematite (sample E7-29 and E7-35, Figure 4.17b) and “pseudo-single domain” loops (sample E7-32, Figure 4.17b). The IRM curves show the presence of antiferromagnetic

minerals (Figure 4.15b) and the high temperature thermomagnetic curve is consistent with the presence of hematite and magnetite.

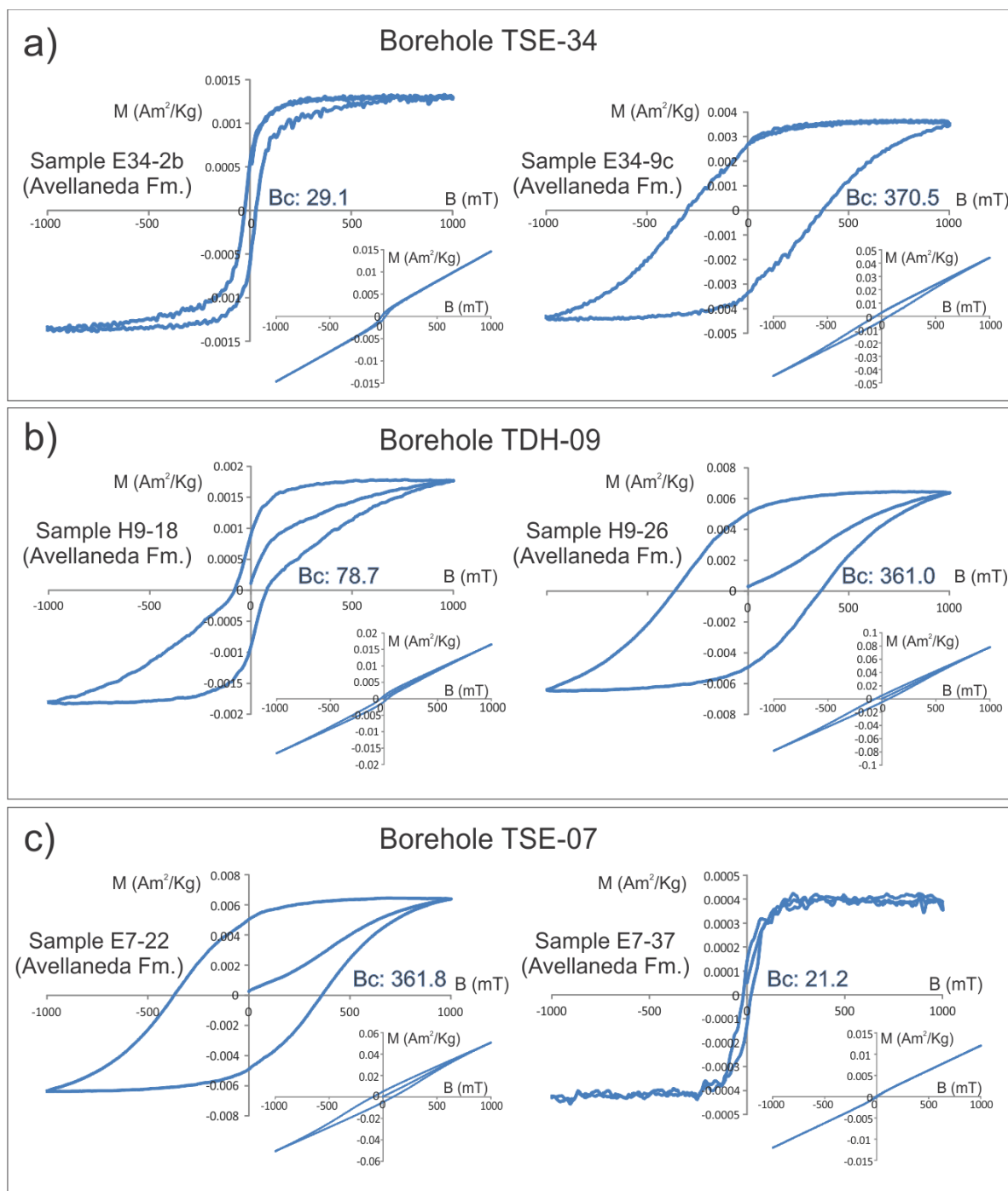


Figure 4.16: a) Representative hysteresis cycles of the Avellaneda formation in bore core TSE-34; b) and c) idem a) for bore cores TDH-09 and TSE-07, respectively, after subtraction of the paramagnetic contribution. In the insets, the original “uncorrected” cycles are shown.  $B_c$ : coercive force in mT.

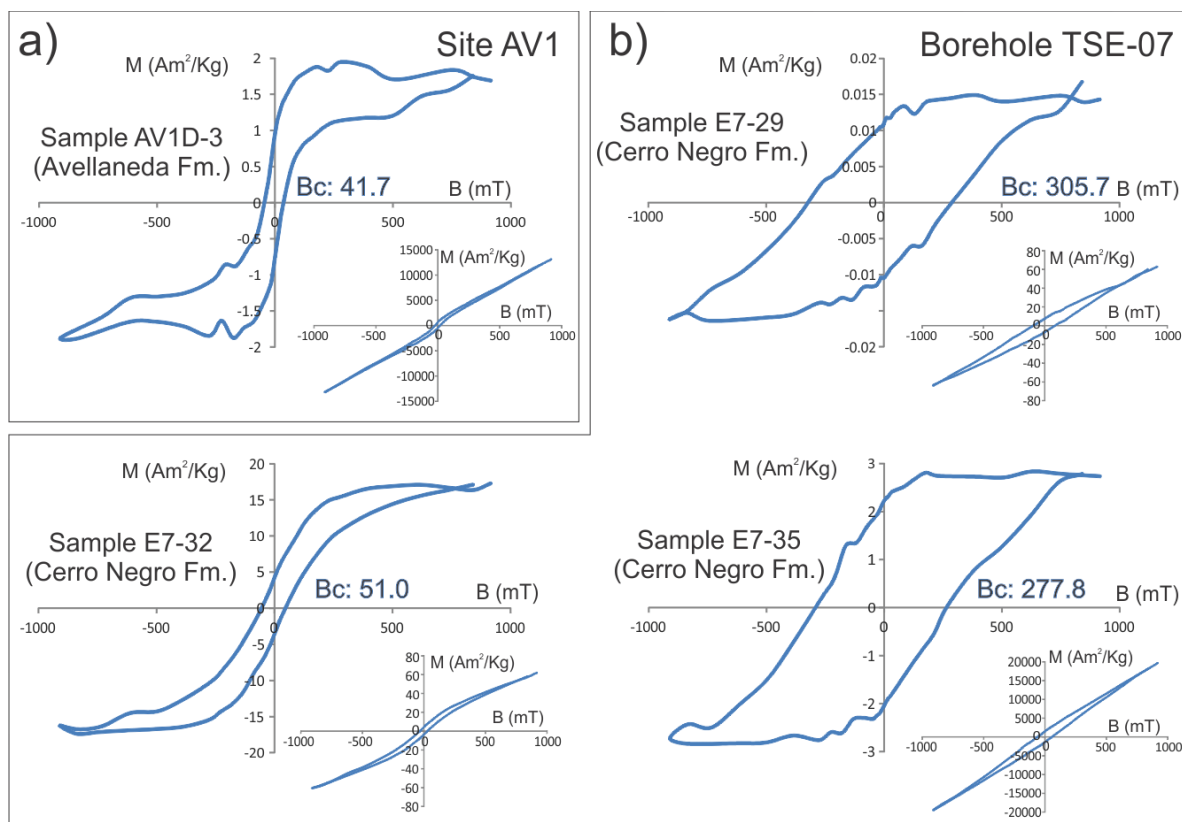


Figure 4.17: a) Representative hysteresis cycle of the Avellaneda formation at the AV1 site; b) representative hysteresis curves of the Cerro Negro formation in bore core TSE-07. References as in Figure 4.16.

#### 6.4. First-order reversal curve (FORC) analyses

FORC studies were carried out in six samples from TSE-07 (E7-37 and E7-40), TDH-09 (H9-9 and H9-21) and TSE-34 (E-34-1 and E34-10) boreholes providing more details about the magnetic remanence in the Avellaneda Formation. All representative samples show a highly peaked lie on the  $B_u = 0$  axis with contours elongated across  $B_c$  axis. The presence of a lobe extending along the negative  $B_u$  axis (Figure 4.18) is characteristic of interacting SD magnetite. Similar distributions have been observed for experimentally disaggregated magnetosome particles (Kopp and Kirschvink, 2008; Moskowitz et al., 1993) and for some magnetofossil-bearing sediments (Egli et al., 2010; Roberts et al., 2011, 2012; Yuan et al., 2019). The sample E34-12 show a broader vertical spread close to the origin of the  $B_c$  axis indicating some contributions of superparamagnetic fractions (Roberts et al., 2014).

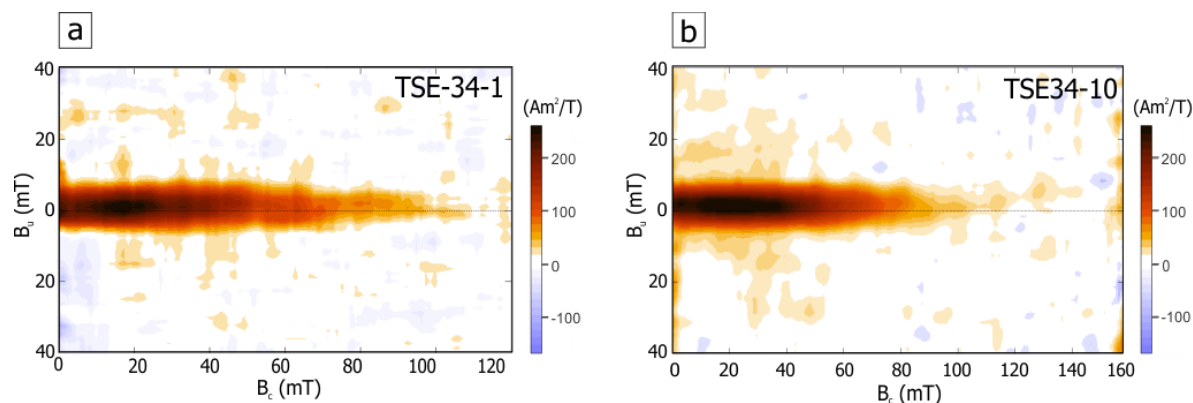


Figure 4.18: FORCs diagrams from the E34-1 and E34-10 samples.

## 7. Discussion

Our study of the Ediacaran Avellaneda and Cerro Negro formations allowed us to compute two new paleomagnetic poles for the Río de la Plata craton. The directional analysis of the Avellaneda formation was carried out with two methodologies: by averaging the specimens and by considering the mean directions obtained in each sample. From this last methodology, mean directions were determined from samples with  $n \geq 3$  specimens and without such restriction. In the case of the Cerro Negro formation, the directional analysis was performed in the same way but without applying any restriction to the number of specimens per sample. As seen in Table 4.3, the final mean directions obtained either by averaging specimens or samples do not vary significantly. In the two studied formations, the specimens directions and mean directions per sample were converted into VGPs in order to compute the respective paleomagnetic poles. In all three bore core analyzed dominant reverse polarity is significant. However, some short intervals of opposite polarities have been found. For a detailed discussion on the magnetostratigraphy of the Avellaneda formation the reader is referred to the companion paper of Afonso et al. (submitted). No reversals were observed in the outcrop sampled at AV1, however such small sampling only encompassed 6 meters of stratigraphic thickness. The Cerro Negro formation exhibits a similar behavior to the underlying Avellaneda formation, with a total predominance of specimens with reverse polarity (a single specimen showed normal polarity).

In the Avellaneda formation, the degree of anisotropy is low to moderate, with a sedimentary fabric predominantly oblate. The same characteristics are observed for the Cerro Negro formation.  $K_{min}$  axis coincide in most cases with pole to bedding and  $K_{max}$  and  $K_{int}$

are distributed on the bedding plane. This is interpreted as a sedimentary or early diagenetic pre-tectonic fabric.

The paleomagnetic poles determined for the Avellaneda (1.0°S, 313.4° W, A95: 5.9°) and the Cerro Negro (7.0° N, 314.4° E, A95: 9.5°) formations are located close to each other. They are presented in Figure 4.19 in West Africa coordinates in a Western Gondwana reconstruction (Torsvik et al, 2012), and Table 4.5, together with other Ediacaran poles from Western Gondwana cratons (i.e. Río de la Plata, Amazonia, West Africa and Congo-Sao Francisco). As has been already published several times (see Rapalini, 2018) a simple and long apparent polar wander path seems to accommodate all previous poles and VGPs from the Rio de la Plata craton between around 600 and 575 Ma. These are mainly based on the well-dated poles of Playa Hermosa formation (PH, ca. 594 Ma) and Sierra de las Animas Complex (ca. 578 Ma) plus the Los Barrientos (LB) pole, with a less well constrained age, but likely around 580 to 585 Ma from stratigraphic considerations as it belongs to the Cerro Largo Fm. (see Gómez Peral et al., 2018). This fast section of the Rio de la Plata craton APWP is supported by the position of the Nola dykes pole (ND, ca. 571 Ma) from the Congo-Sao Francisco craton and the Adrar-n-Takoucht volcanics pole (C, ca. 577 Ma) from West Africa. A few VGPs from the Sierras Bayas Group (Rapalini et al., 2013, 2021) consistently fall along this path.

The positions of the Avellaneda (AV) and Cerro Negro (CN) Formations poles obtained in our study suggest that the Late Ediacaran path for the Rio de la Plata (and West Gondwana?) should be modified. The Avellaneda formation paleomagnetic pole has a more likely age, limited by stratigraphic constraints, between 580 and 560 Ma. A negative C<sup>13</sup> anomaly in the upper levels of the Avellaneda Formation (e.g. Gómez Peral et al., 2018, Afonso et al, submitted) may be correlative of the Shuram global isotopic excursion, dated at 570 Ma (Pu et al., 2016). An age of 570 Ma or younger for the AV pole is also suggested for its position nearly 60° apart from the SAn, LB, ND and C poles of ca. 585-575 Ma. In any case, this implies a fast polar drift of CRP in the early Late Ediacaran and a path that turns into northern central Africa, different from most previously proposed (Trindade et al., 2006; Rapalini et al., 2013). The less robust paleomagnetic pole obtained for the Cerro Negro Formation falls very close to AV pole. The age of this formation is restricted from the discoidal structures reported by Arrouy et al. (2016) in its upper levels. These structures were assigned to the genus *Aspidella* sp. and have been interpreted as corresponding to the “White Sea” fauna (Arrouy et al., 2016) for which a more likely age of 558-550 Ma has been

proposed (Boag et al., 2016). CN pole was obtained from lower levels of the Cerro Negro Formation. These considerations suggest that AV and CN poles are more likely encompassed in the 570-560 Ma. Of course, this is based on the acceptance of a primary magnetization, as suggested by the positive tilt-test and rock magnetic data plus a coherent magnetostratigraphic pattern as described in the companion paper (Afonso et al., submitted).

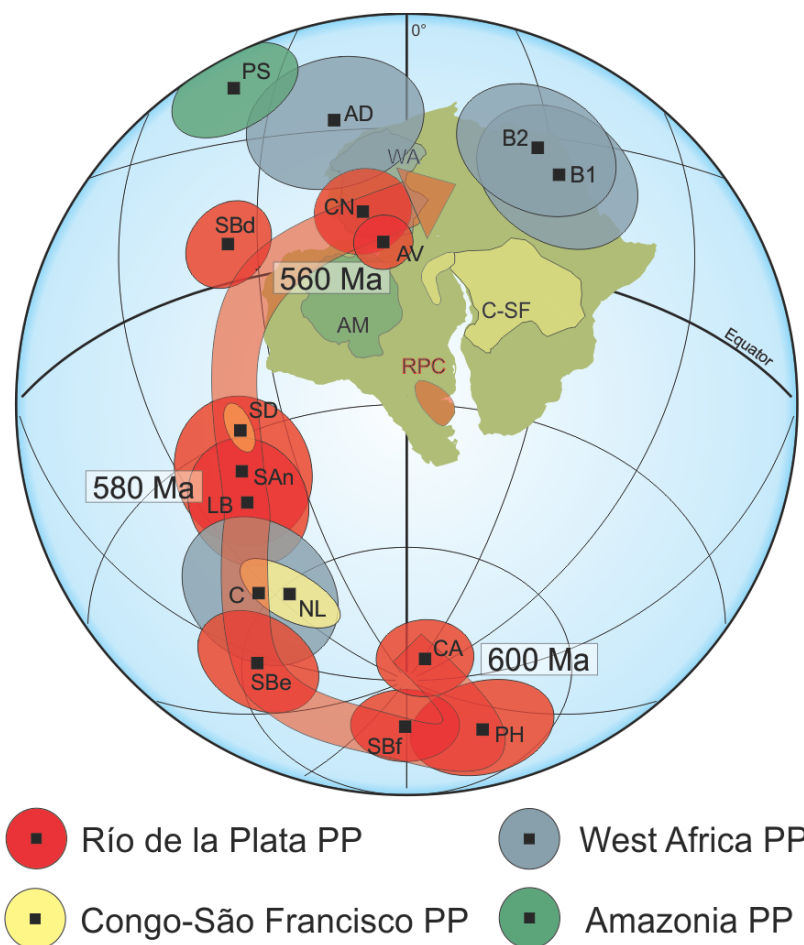


Figure 4.19: Proposed APWP for the RPC in the 600-560 Ma interval. The paleomagnetic poles of other Western Gondwana cratons for the same interval are also shown. The RPC and Congo-São Francisco poles were rotated to Africa according to the Euler pole  $47.5^\circ$  N,  $33.3^\circ$  W,  $56.2^\circ$  ccw (Torsvik et al., 2012), while the Amazonia pole was rotated according to  $50^\circ$  N,  $32.5^\circ$  W,  $55.1^\circ$  ccw (Torsvik et al., 2012). For the acronyms used in the poles see Table 4.5. The white boxes next to the APWP indicate approximate ages in that section.

Robert et al. (2017) conducted paleomagnetic studies on well-dated volcanics in the West African craton. The authors proposed the existence of two events of inertial interchange true polar wander (IITPW) occurring in the Neoproterozoic. In particular, the second

proposed event occurred between 575 and 565 Ma and would explain the very distant paleomagnetic poles of the Adrar-n-Takoucht and Fajjoud and Taddoughast volcanics (Robert et al., 2017) of approximately those ages, respectively. Robert et al. (2018) further developed this model comparing approximately coeval paleomagnetic poles from West Africa, Laurentia, Baltica, West Gondwana and Australia that were interpreted to be compatible with the IITPW hypothesis. Ediacaran poles from West Africa (AD, B1, B2 and C, see Table 4.5, Figure 4.19) show a long and fast track as well as an abrupt change in its direction determined by pole C of ~577 Ma. This pole is approximately consistent with poles of similar ages in RPC (SAn and LB) and Congo-São Francisco (ND), suggesting that these blocks were close to each other or even already united at that time. The AV and CN poles imply a fast apparent polar displacement for the RPC (and other West Gondwana blocks?) between ca. 580 and 570-560 Ma (Figure 4.19). This seems consistent at a first sight with the IITPW proposal, although the RPC track falls short of a ca. 90° swath apparently found in other continents (Robert et al., 2018). Whether this is invalidating such model or just the recording of superposed independent movements along the track due to final Gondwana assembly should be investigated further. The role of long-lived large non-dipole contributions in the Late Ediacaran Earth magnetic field remain ambiguous. Consistent paleopole positions from different continents at around 580-575 Ma, as already discussed, suggest that the GAD hypothesis was likely valid at least near the end of the Early Ediacaran.

With the new paleomagnetic information for RPC, and assuming a basically valid GAD hypothesis up to ca. 560 Ma it is possible to infer a gross picture of the drift of this block during the late Early and early Late Ediacaran (Figure 4.20). At ~600 Ma the craton might have been at a paleo latitude of ~19° S (as computed for the Olavarría city in the Tandilia System), according to the paleomagnetic pole from the Playa Hermosa Formation (Rapalini et al., 2015). Relative location of other Western Gondwana blocks are not well constrained paleomagnetically, particularly Congo- São Francisco lacks any paleomagnetic pole of similar age. Slightly older poles from West Africa and Amazonia (see Table 4.5) at 610-615 Ma, suggest that both blocks were probably a single plate relatively far-away from CRP. By ~580 Ma (Figure 4.20), the RPC, Congo-São Francisco and West Africa cratons are reconstructed as already assembled, although relative movements among them are allowed from the data. They are the already mentioned SAn, LB, ND and C poles (Table 4.5). Although there is no paleomagnetic information on the Amazonia craton for this time, it is indirectly inferred that it was part of the same continent together with the RPC given the

paleoreconstructions that locate Amazonia attached to West Africa since the Paleoproterozoic (see D'Agrella-Filho et al., 2016 and references therein) and the consistent early Ediacaran poles already mentioned. By this time, the paleolatitude of the Olavarría locality in the CRP was at  $\sim 46^\circ$  S, drifting about  $27^\circ$  in 20 Ma. The Western Gondwana forming blocks may have drifted afterwards towards even higher latitudinal positions within a large counterclockwise rotation (Figure 4.20c). Deposition of the marls and shales of the Avellaneda formation took place at those times at latitude of  $\sim 50^\circ$ S. The CN pole suggests slightly lower paleolatitudes ( $\sim 42^\circ$ S) an around 560 Ma.

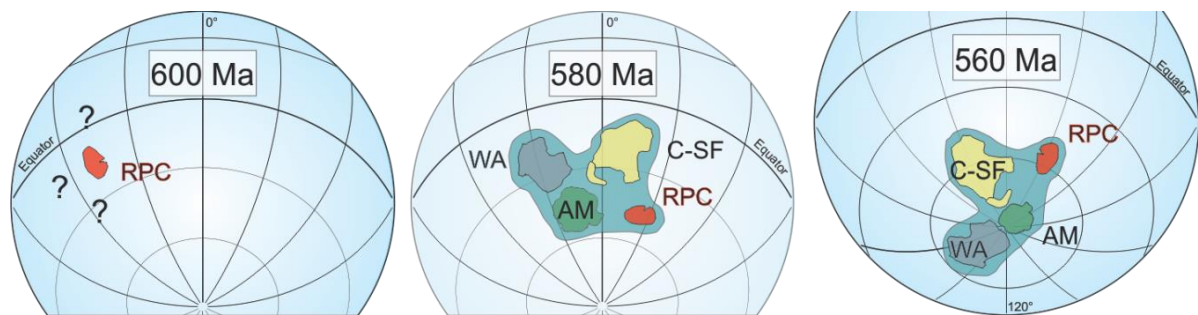


Figure 4.20: Paleogeography of the RPC at 600, 580 and 560 Ma. At 600 Ma there is no paleomagnetic evidence that supports the RPC together with another Gondwana craton. From  $\sim 575$  Ma, paleomagnetic information allows more complete paleoreconstructions. WA: West Africa; AM: Amazonia; C-SF: Congo-São Francisco.

Table 4.5: Ediacaran poles belonging to the Río de la Plata, Congo-São Francisco, West Africa and Amazonia cratons. They are reported in current coordinates and in Gondwana coordinates. The rotations of the paleomagnetic poles were made according to the Euler poles (Torsvik et al., 2012): RPC (47.5°N, 33.3°W, 56.2° ccw) y Amazonia (50.0°N, 32.5°W, 55.1° ccw). Pole references: 1- This paper; 2- Rapalini et al. (2013); 3- Rapalini (2006); 4- Rapalini et al. (2015); 5- D'Agrella-Filho and Pacca (1988); 6- Meert and Van der Voo (1996); 7- Moloto-A-Kenguemba et al. (2008); 8- Morel (1981); 9- Robert et al. (2017); 10- García et al. (2013). Lat: latitude, Long: longitude.

Craton	Unit	Pole	Present-day coordinates		Pole position (Gondwana coordinates)		A95 (°)	Age ( )	Ref.
			Lat.	Long.	Lat.	Long.			
RPC	Cerro Negro Fm.	CN	7.0	314.4	11.2	351.3	9.5	560 (APWP and paleontology)	1
	Avellaneda Fm.	AV	-1.0	313.4	4.1	355.3	5.9	570 (APWP and stratigraphy)	1
	Olavarría Fm.	SBd	21.0	290.4	8.2	323.9	8.9	560 (APWP)	2
	Los Barrientos	LB	-16.2	253.9	-42.4	312.6	12.9	570 (APWP)	3
	Sierra de Animas Complex	SAn	-12.2	258.9	-36.5	315.3	14.9	578 ± 4 (U-Pb SHRIMP, zircon)	4
	Cerro Largo Fm.	SBe	-25.9	219.0	-62.9	265.7	11.3	580 (APWP)	2
	Villa Mónica Fm.	SBf	-49.0	198.2	-78.6	181.4	9.2	590 (APWP)	2
	Playa Hermosa Fm.	PH	-58.8	183.1	-71.2	137.1	12.1	590 (U-Pb SHRIMP, detrital zircons)	4
	Campo Alegre Fm.	CA	-57.0	223.0	-83.9	33.9	9.0	600 (APWP)	5
CSF	Sinyai Dolerite	SD	-29.0	319.0	-	-	3/5	547 ± 4 (Ar-Ar, biotite)	6
	Nola Dyke	NL	-61.8	304.8	-	-	5.4/10.7	571 ± 6 (Ar-Ar, amphibole)	7
	Adma Diorite	AD	32.5	344.7	-	-	15.9	616 ± 11 (U-Pb, zircon)	8
WA	Fajjoud and Tadoughast Volc.	B1	21.9	31.0	-	-	15.6	572-551 (U-Pb SHRIMP, zircon)	9
	Djebel Boho Volc.	B2	27.3	27.1	-	-	14.9	547-526 (U-Pb SHRIMP, zircon)	9
	Adrar-n-Takoucht Volc.	C	-57.6	295.6	-	-	15.7	577-564 (U-Pb SHRIMP, zircon)	9
AM	Planalto da Serra	PS	49.7	313.4	42.6	319.8	10.8	615 ± 5 (Ar-Ar, phlogopite)	10

## 8. Conclusions

Detailed paleomagnetic studies were conducted in the Avellaneda (~570 Ma) and Cerro Negro (~560 Ma) formations. In the first unit, sampling was carried out at an outcrop and in samples extracted from three different boreholes. In the second, the sampling was carried out in only one borecore. In both cases, new paleomagnetic poles were obtained: (AV, 1.0° S, 313.4° E, A95: 5.9°) for the Avellaneda formation and (CN, 7.0° N, 314.4°E, A95: 9.5°) for the Cerro Negro formation. AMS studies confirm a sedimentary and pre-tectonic origin for the magnetic fabrics. Rock magnetism analyses suggest that both magnetite and hematite, in variable proportion, carry the remanence. The new poles allow a more robust APWP for the RPC in the 600-560 Ma interval. A drift of the RPC from low latitude positions at 600 Ma (~19°S for the Olavarría city) towards positions of moderately high paleolatitudes (between around 50° and 42°S) for the interval 580- 560 Ma. This illustrates that the long APWP between around 580 and 570 Ma for the RPC mainly involved a very large counterclockwise rotation with minor paleolatitudinal change. Whether this movement can be associated, and therefore supports, proposals of IITPW during the transition between the Early and Late Ediacaran awaits more in deep analyses and more importantly further paleomagnetic data of such age from different Western Gondwana forming blocks.

## Acknowledgments

This study was supported by the CONICET (Argentina)-FAPESP (Brazil) 2016 agreement and the CONICET (Subsidio Unidad Ejecutora-IGEBBA 2016) grant and FAPESP Thematic Project 2016/06114-6. Universidad de Buenos Aires (Grant 20020170100290BA) and ANPCyT (PICT 2018-01330) gave additional financial support. GMAP software by Torsvik (NGU) and Anisoft and Remasoft programs (AGICO, Inc.) were used to analyse the data. Matias Naselli and Fernando Almaraz kindly collaborated during preparation of samples and running of thermomagnetic and hysteresis curves. A special thanks to Cementos Avellaneda S.A. for facilitating access to the Cabañita quarry for field work and the study of the borecores.

## **CHAPTER V**

## 5. Paleomagnetism of the Ediacaran Avellaneda Formation (Argentina), Part II: Magnetic and chemical stratigraphy constraints on the onset of the Shuram carbon excursion

**Jhon W.L. Afonso**, Pablo Franceschinis, Augusto E. Rapalini, María Julia Arrouy, Lucía E. Gómez-Peral, Daniel G. Poiré, Sergio Caetano-Filho, Ricardo I.F. Trindade

**Abstract:** Magnetostratigraphy turn out to be a few reliable methods in high resolution correlations studies. Still, magnetostratigraphic studies have been underexploited in the Ediacaran successions. Here, we performed a magnetostratigraphy coupled carbon isotope study in the Ediacaran Avellaneda Formation (~570 Ma), a sedimentary cover of the Tandilia region, in the Río de la Plata craton. Paleomagnetic data and  $\delta^{13}\text{C}$  curves were obtained from three drill cores that cut enterally sedimentary record of the Avellaneda Formation. Paleomagnetic results plotted against stratigraphic allowed identify a prevalent reverse separated by normal polarity interval.  $\delta^{13}\text{C}$  values demonstrate that magnetostratigraphic polarity pattern is laterally consistent. Furthermore, C-isotope curves show a transition from positive to negative values near the top of the Avellaneda Formation. This excursion is likely correlate to the onset of the global Shuram excursion (ca. 570 Ma). Our findings suggest that Shuram excursion, took place during a reverse polarity chron. Comparison with other coeval sequences can be validate this consistency. Geomagnetic polarity reversals preserved in the Avellaneda Formation provide a rare opportunity to better constrain magnetostratigraphy as a tool method to correlation of Precambrian strata. Our results shed further light on the possible use of magnetic polarity reversals to correlated Ediacaran succession.

### 5.1. Introduction

The Ediacaran Period (~ 635–541 Ma) comprises a critical interval of Earth (Knoll, 2000; Knoll et al., 2006). During this time, drastic paleoenvironment changes were registered, as well as fast movements of continental blocks (Li et al., 2008). Besides, fluctuations in biogeochemical cycles at global scale have been reported by variations in seawater chemistry and likely in atmospheric redox conditions (Li et al., 2010). A very weak geomagnetic field (Bono et al., 2019) and high reversal frequency were apparently characteristic during the Ediacaran (Shatsillo et al., 2015; Bazhenov et al., 2016; Meert et al., 2016). Within these major transformations happening, first appearance of complex animals occurs in the

Ediacaran record followed by their spread and dominance of the marine benthic environments (Grotzinger et al., 2000).

Recently, studies focused on the Ediacaran Period have tried to establish the connection between paleoenvironmental, geochemical changes and the appearance of modern life. Among other paleocontinents, Rio de La Plata craton plays an important role in documenting Earth's critical changes in terminal Ediacaran Period (Rapalini et al., 2013; 2015). The Ediacaran strata from Rio de La Plata craton have exceptional preservation of oldest metazoan fossils (Arrouy et al., 2016), acritarchs and multicellular algae (Arrouy et al., 2015), as well as large variations in seawater chemistry which indicate significant transitions in oceanic and atmospheric redox conditions (Gómez-Peral et al., 2019).

Great progress has been made in understanding the events of the Ediacaran Period (Xiao and Narbonne, 2020). However, a well-defined chronological structure of events is still not well understood to compare and correlate them throughout different basins. Due to the limitation in applied biostratigraphy techniques to correlate globally sedimentary successions, prior to the widespread appearance of cosmopolitan biotic assemblages, and the lack of robust age constrains, a straightforward interpretation of eventual interplay between the main events is a hard task. In this scenario, magnetostratigraphy provides one of a few reliable methods to build a chronostratigraphic framework for the Ediacaran strata. Here, we combine a magnetic polarity stratigraphy with carbon isotope curves from marlstones of the Avellaneda Formation (580-560 Ma), a sedimentary cover unit from Rio de La Plata craton in Argentina. The main goal of this research is to explore the potential use of magnetostratigraphy as a tool for correlating Ediacaran successions, and thus, to contribute for a better chronostratigraphic framework.

## 5.2. General setting

The Tandilia System comprises a 350 km long orographic belt trending northwest-southeast in the Province of Buenos Aires (Figure 5.1). This belt consists of Paleoproterozoic igneous–metamorphic basement known as Buenos Aires Complex (Marchese and Di Paola, 1975) cut by a swarm of tholeiitic dykes of 1.6 Ga (Hartmann et al., 2002; Pankhurst et al., 2003; Cingolani et al., 2005, 2010; Rapela et al., 2011). Crystalline basement rocks are unconformably covered by a thick sedimentary package of Neoproterozoic to Lower Paleozoic age (Poiré and Gaucher, 2009; Arrouy et al., 2015; 2019).

Quarries near the city of Olavarría (Figure 5.1c) preserve one of the most expressive records of sediments in the Tandilia System comprising a ~450 m thick sedimentary pile (Poiré and Spalletti, 2005; Gómez-Peral et al., 2011; Arrouy et al., 2015). Much of this sedimentary column is formed by unmetamorphosed rocks from Neoproterozoic age divided into two groups: Sierras Bayas Group (Poiré, 1993) and La Providencia Group (Arrouy et al., 2015). The Sierras Bayas Group lay directly above the crystalline basement and is fashioned mainly by carbonate rocks (Poiré, 1993; Gómez Peral et al., 2011). This group includes five units, named from base to top, Villa Mónica, Colombo, Cerro Largo, Olavarría and Loma Negra formations (Figure 5.1d). An erosional karstic surface, named "Barker surface", separates La Providencia Group from the underlying Sierras Bayas Group (Figure 5.1d). The La Providencia Group was proposed by Arrouy et al., (2015) and consists mainly of fine-grained siliciclastic sediments with some contribution of carbonate. The La Providencia Group encompasses from base to top, the Avellaneda, Alicia and Cerro Negro formations (Figure 5.1d). The Lower Paleozoic succession is represented by the Balcarce Formation (Zimmermann and Spalletti, 2009).

The Avellaneda Formation corresponds to the basal section of the La Providencia Group. It consists mainly of massive and laminated marls that turn into fine-grained siliciclastic material at top, mainly composed of massive red clays (Arrouy et al., 2015). Recently, some sulfate occurrences attributed to evaporites, likely calcium sulfate, were reported in the Avellaneda Formation (Afonso et al., submitted). This unit lay on top of the Barker surface. The depositional setting interpreted for the Avellaneda Formation is tidal-influenced shallow-marine and protected coastal lagoons (Arrouy et al., 2015; Gómez--Peral et al., 2019). Until now, no absolute radiometric ages constraints are available for the Avellaneda Formation. The fossil index *Aspidella* sp. correlated to the White Sea assemblage found in the overlying Cerro Negro Formation provides an age constraint for that unit to 550-560 Ma (Arrouy et al., 2016), which is consistent with the Middle Ediacaran acritarchs recovered from the Alicia Formation (Arrouy et al., 2019).  $\delta^{13}\text{C}$  and  $^{87}\text{Sr}/^{86}\text{Sr}$  isotopes data suggest ages of 600-580 Ma for the underlying Loma Negra Formation (Gómez-Peral et al., 2007; Gómez-Peral et al., 2019;). Therefore, an age between 580 and 560 Ma is considered here as the most likely for the Avellaneda Formation.

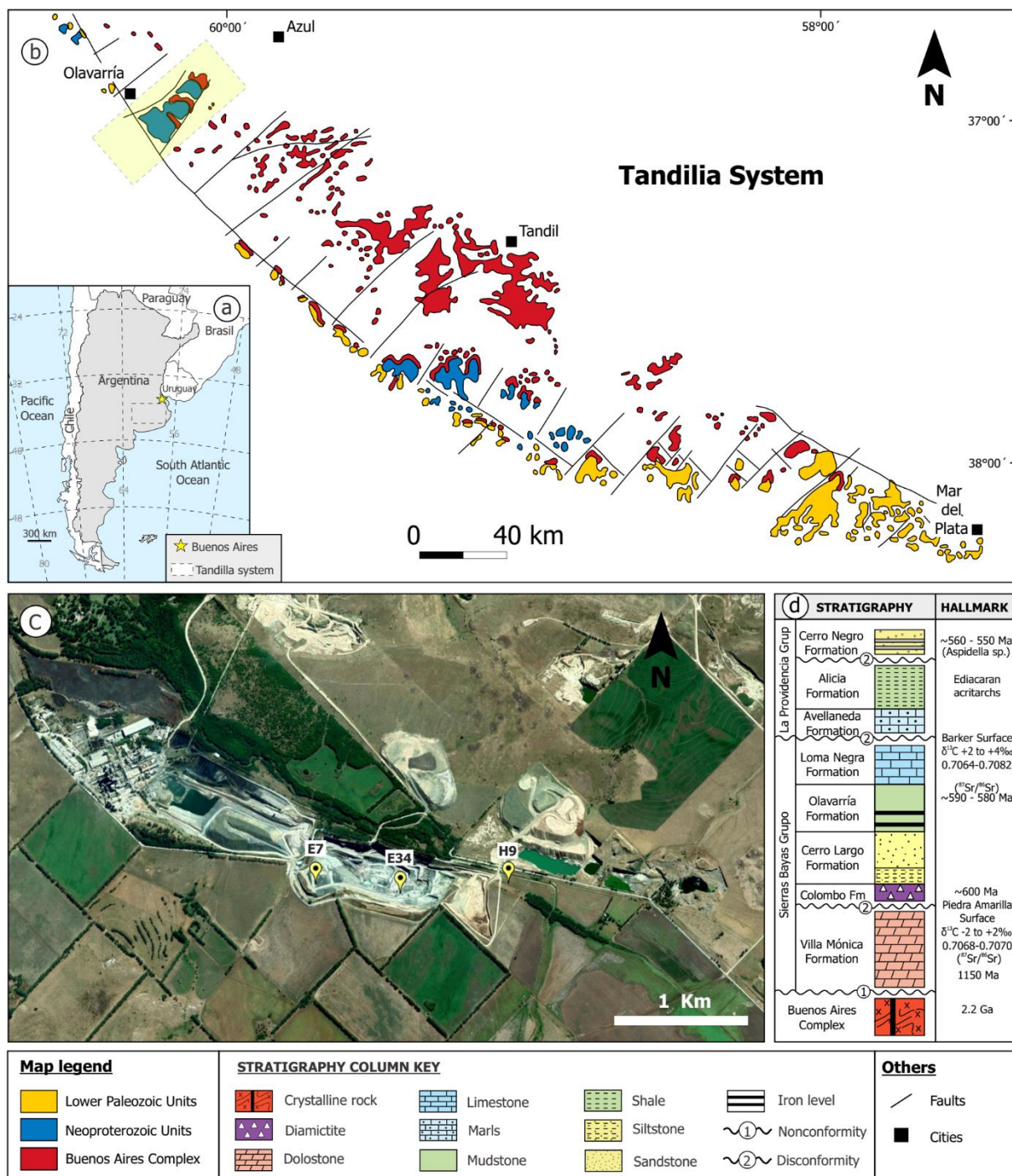


Figure 5.1: Map of the studied area (Buenos Aires Province, Argentina). (a) Map of southern of South America showing the location of the Tandilia System present in Figure 5b. (b) Simplified geological map of the Tandilia System exhibiting the main outcrop distributions of the Paleoproterozoic crystalline basement rocks (Buenos Aires Complex) and sedimentary units from Neoproterozoic-Lower Paleozoic age (modified from Iñiguez et al.1989). (c) Satellite images of mining and quarrying areas close to city of Olavarría (image from Google Earth), with drill core location marked with yellow pins. (d) Lithostratigraphic column, key stratigraphic surfaces and main geochronological, geochemical and biostratigraphy hallmarks used to order the events recorded in the Rio de la Plata craton (adapted from Iñiguez et al., 1989; Poiré and Spalletti, 2005; Gómez-Peral et al., 2007; 2014).

### **5.3. Sampling and analytical methods**

#### **5.3.1. Core description**

The Avellaneda Formation was accessed from three vertical drill cores labeled E34, E7 and H9 performed in La Cabañita quarry, located in the city of Olavarría (see figure 5.1). The drill cores were provided by Cementos Avellaneda S.A. Each one of these drill cores span the entire Avellaneda Formation which vary in thickness from ~11 to 22 meters. The drilling was performed at an altitude of 215 m for borehole E7, 215 m for E34 and 212 m for H9. Sedimentological and petrographic studies were performed in each core, and this record was used to correlate laterally the three cores. In addition, thin sections were prepared for rock classification and to assess petrographic details. Thin sections were also used to evaluate diagenetic overprinting on magnetic and geochemical signals.

#### **5.3.2. Paleomagnetic sampling**

The three boreholes from the Avellaneda Formation were studied for high-resolution magnetostratigraphy. Cylindrical cores 25 mm in diameter were collected using a drill press from boreholes E34 (68 cores), E7 (147 cores) and H9 (163 cores). These cylindrical samples were then cut into 22 mm-height standard paleomagnetic specimens. The average sampling spacing was from 0.2 to 0.7 m. Sampling was guided by the lithology and the preservation status of the boreholes; for example, fractured and veined intervals were skipped, and friable sediments were avoided. Analyzed samples were mainly collected from the center of the cores to avoid drilling induced remanence effects. The cores were not oriented in-situ, although relative azimuthal correlation between samples was obtained by fine lamination dip. In order to obtain absolute azimuthal oriented paleomagnetic records, we used a viscous paleomagnetic component as a reference (see companion paper by Franceschinis et al.). The results were further tested against the paleomagnetic record of some sites collected with a gasoline-powered drilling in nearby outcrops of the quarry.

#### **5.3.3. Paleomagnetism**

Natural remanent magnetization (NRM) for each specimen was measured, followed by stepwise demagnetization. Two protocols were used for a set of pilot specimens. Alternating field (AF) treatment followed the steps: 3 mT, 6 mT, 9 mT, 12 mT, 15 mT, 20 mT, 25 mT, 30 mT, 40 mT, 50 mT, 60 mT, 70 mT, 80 mT, 90 mT, 100 mT. Thermal treatment followed the

steps: 90 °C, 120 °C, 150 °C, 200 °C, 250 °C, 300 °C, 350 °C, 400 °C, 425 °C, 450 °C, 475 °C, 500 °C, 525 °C, 550 °C, 575 °C, 600 °C, 620 °C, 640 °C, 660 °C, 680 °C. Paleomagnetic data for E-34 were acquired in the automated RAPID model, DC SQUID magnetometer from 2G Enterprises, whereas the results for E7 and H9 boreholes were obtained from a u-channel DC SQUID magnetometer also from 2G Enterprises. Both equipments are housed into a magnetically-shielded room with ambient field <500 nT at the Laboratory of Paleomagnetism of the University of São Paulo (USPMag). AF demagnetization was performed with three orthogonal coils coupled with the magnetometers, whereas thermal demagnetization was done with a 48SC paleomagnetic furnace from ASC Scientific. Demagnetization results were represented in orthogonal diagrams (Zijderveld, 1967), and the characteristic components were isolated using the principal component analysis (PCA) routine of Kirschvink (1980) implemented in the REMASOFT 3.0 software (Chadima and Hrouda, 2006).

#### ***5.3.4. Anisotropy of magnetic susceptibility (AMS)***

Anisotropy of magnetic susceptibility (AMS) for all samples was measured, prior to any paleomagnetic processing, using a MFK1-FA Multi-Function Kappabridge at the Paleomagnetic Laboratory of São Paulo University (USPmag). AMS is defined by an ellipsoid with three mutually orthogonal axes of maximum (K1), intermediate (K2), and minimum (K3) susceptibility which provide the orientation and degree of alignment of magnetic minerals in rocks and sediments (Hrouda, 1982). In sedimentary rocks, AMS ellipsoids are used to infer primary controls on their depositional environment/processes (e.g., hydrodynamic conditions, transportation) and/or post-depositional processes (e.g., compaction, diagenesis, deformation) (Borradaile, 1991; Borradaile and Henry, 1997; Parés, 2015; Parés et al., 1999; Rochette et al., 1992; Tarling & Hrouda, 1993). The AMS parameters examined in this study are the lineation (L, determined by  $L = K1/K2$ ) and foliation (F, determined by  $F = K2/K3$ ). These parameters were plotted on a Flinn-type diagram (Jelinek, 1981). We also analyzed the AMS parameters Pj and T (Jelinek, 1981). The parameter Pj reflects the degree of anisotropy of the ellipsoid, which in general is a function of both mineralogy and alignment. The parameter T reflects the shape of the anisotropy ellipsoids.

### 5.3.5. Rock magnetism

Magnetic hysteresis loops, isothermal remanent magnetization (IRM), and first order reversal curves (FORCs) were measured on representative samples to characterize the magnetic mineralogy (see Franceschinis et al., this issue). Here, we present only IRM data in order to provide details about magnetic minerals. IRM were acquired using a Princeton Measurements Corporation MicroMag 3900 vibrating sample magnetometer (VSM) from USPmag.

### 5.3.6. Carbon and oxygen isotopes

Carbon and oxygen stable isotope compositions were measured in carbonate minerals from the three cores in order to precisely tie the magnetostratigraphic measurements between cores. The same samples collected for the paleomagnetic study were used for isotopic measurements. About 10 mg of carbonate powder was extracted with the help of a micro drilling device. We focused on well-preserved carbonate rich-layers, free of fractures or any post-depositional feature. Layers with siliciclastic grains were also avoided. Carbonate powders were reacted with  $\text{H}_3\text{PO}_4$  at 72 °C and the released  $\text{CO}_2$  was extracted through a continuous flow in a Thermo Finnigan GasBench II. All samples were analyzed at the Stable Isotope Laboratory of the Center for Geochronological Research, University of São Paulo (CPGeo/USP). The carbonate carbon and oxygen isotope ratios ( $\delta^{13}\text{C}_{\text{carb}}$  and  $\delta^{18}\text{O}_{\text{carb}}$ ) are reported in ‰ relative to Vienna Peedee Belemnite (VPDB). Standard deviations in the analyzed samples are 0.04 ‰ for carbon and 0.04 to 0.06 ‰ for oxygen.

### 5.3.7 Elemental geochemistry

In order to assess the potential post-depositional overprint in our samples, we performed geochemical analysis by measuring Ca, Sr, Fe and Mn to evaluate Fe/Sr, Mn/Sr and Ca/Sr ratios relationships against carbon and oxygen isotope compositions. Elemental concentrations were measured using a portable device Olympus Delta XRF Analyzer in the Marine Inorganic Chemistry Laboratory of the Institute of Oceanography at the University of São Paulo. Polished slabs were prepared, and the most homogeneous surfaces were selected for XRF analyses. A blank (pure  $\text{SiO}_2$ ) and the reference material NIST SRM 2711A were measured each 30 samples. The blank for Ca, Mn, Fe, and Sr contents were below the detection limit of the equipment. The standard material NIST SRM 2711A was measured 35

times during the period of analyses, with average uncertainties below  $\pm 0.4\%$  for Ca and Fe,  $\pm 92$  mg/kg for Mn and below  $\pm 7$  mg/kg for Sr. Reproducibility are in a range below  $\pm 0.05\%$  for Ca and Fe,  $\pm 9$  mg/kg for Mn, and  $\pm 5$  mg/kg for Sr.

## 5.4. Results

### 5.4.1. Core description and petrography

The Avellaneda Formation occurs in different depth levels and its thickness also varies throughout the three studied cores (Figure 5.2). In E7 the Avellaneda Formation is 18 meters thick, beginning around 40 mbs and ending at 58 mbs (Figure 5.2a). In the drill core E34 the Avellaneda Formation is 11 meters thick and occurs between 80 and 91 mbs (Figure 5.2b). The core H9 contains the thickest record of the Avellaneda Formation with 22 meters between 55 and 77 mbs (Figure 5.2c). Notwithstanding, sedimentary succession described in the three drill cores is very similar and allows straightforward lateral correlations.

Sedimentary succession investigated here comprises mainly reddish to brown and grayish to green mud limestone rocks with a variable content of detrital impurities (Figure 5.2). Sedimentary facies are dominated by monotonous massive to poorly laminated layers and/or thin parallel laminated layers (Figure 5.2). These facies generally occur interlayered and vertically grade into each other (Figure 5.2). Laminations are sharply defined, which imparts a characteristic striped appearance to the rock in vertical section. The thickness of each lamination varies from millimeters to centimeters. Erosional or truncated surfaces are rare and may be observed locally. The upper portion of drill core H9 show brown and green colored beds composed mainly by fine to very fine-grained siliciclastic rocks (Figure 5.2).

Petrographic analyses of thin sections (Figure 5.3) show that carbonate facies are the major constituent. In general, carbonate is microcrystalline calcite ( $<4 \mu\text{m}$  in size; Figure 5.3a) usually with low degree of recrystallization to microspar (Figure 5.3b). Carbonate facies are massive (Figure 5.3a and 5.3b) or can show a pervasive and thin irregular horizontal lamination (Figure 5.3c). Samples can contain thin laminated facies characterized by alternating light and dark millimeter laminae (Figure 5.3d). Dark laminae are putative rich in organic matter, whereas the light laminae are light carbonate-rich (Figure 5.3d). Dispersed detrital quartz grains can be found in carbonate facies (Figure 5.3c). Expressive occurrence of detrital grains is reported only in the upper part of drill core H9, where siliciclastic sediments are dominant from 59 to 65 mbs. Siliciclastic sediments (Figure 5.3f) include detrital quartz,

micaceous minerals and minor feldspar grains. More details about microfacies can be found in Afonso et al., (submitted).

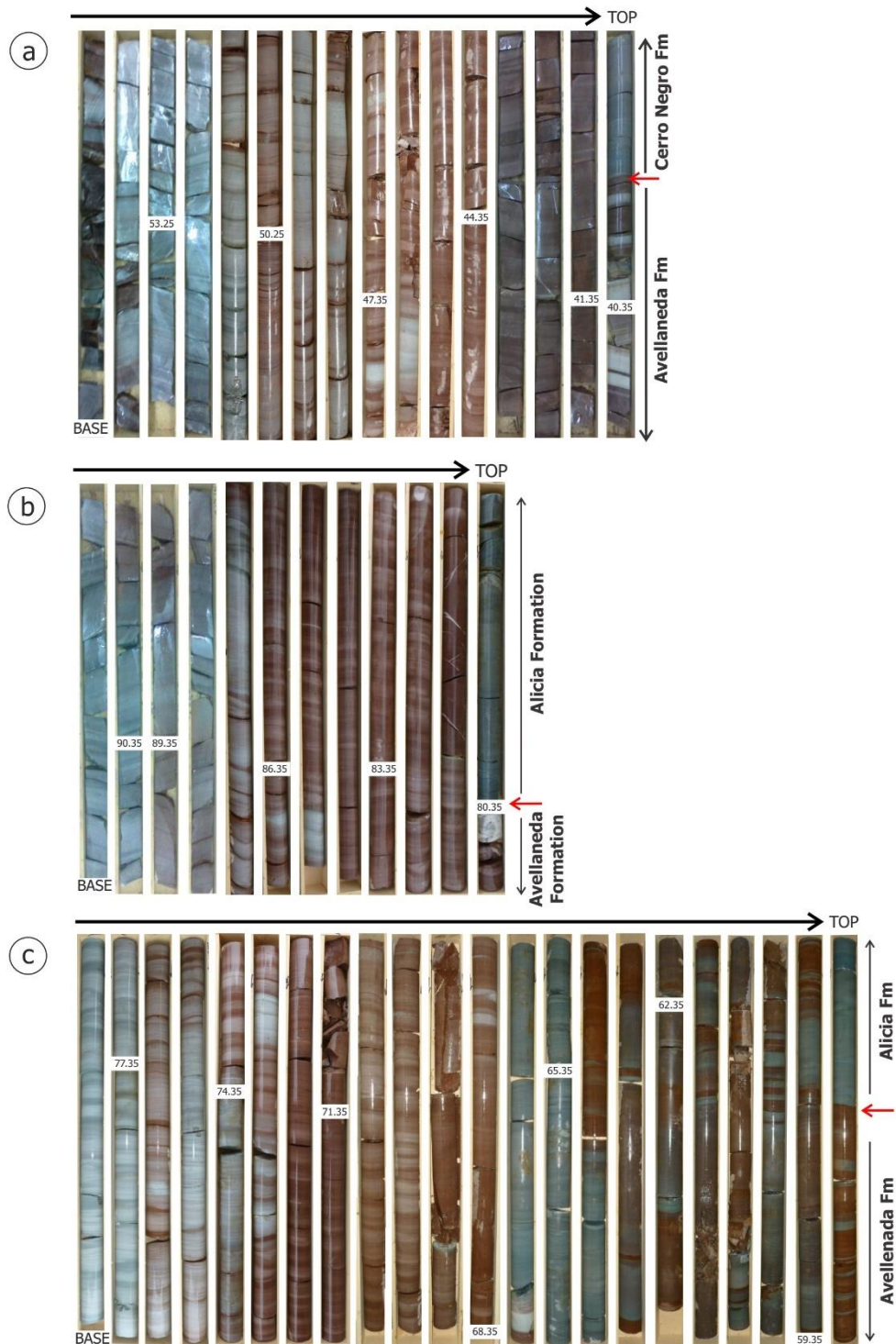


Figure 5.2: Drill cores recovered from three stratigraphic holes sited on the Olavarría region. Each drill core cut entire Avellaneda Formation. Red arrow indicates the geological boundary which separates one lithostratigraphic unit (formation) from another. Base and top to each borehole are shown in the first and last boxes. As well as the depth markings. In letter (a) are exposed drill cores from E7, (b) show rocks from E34 and in (c) are exposed drill cores from H9.

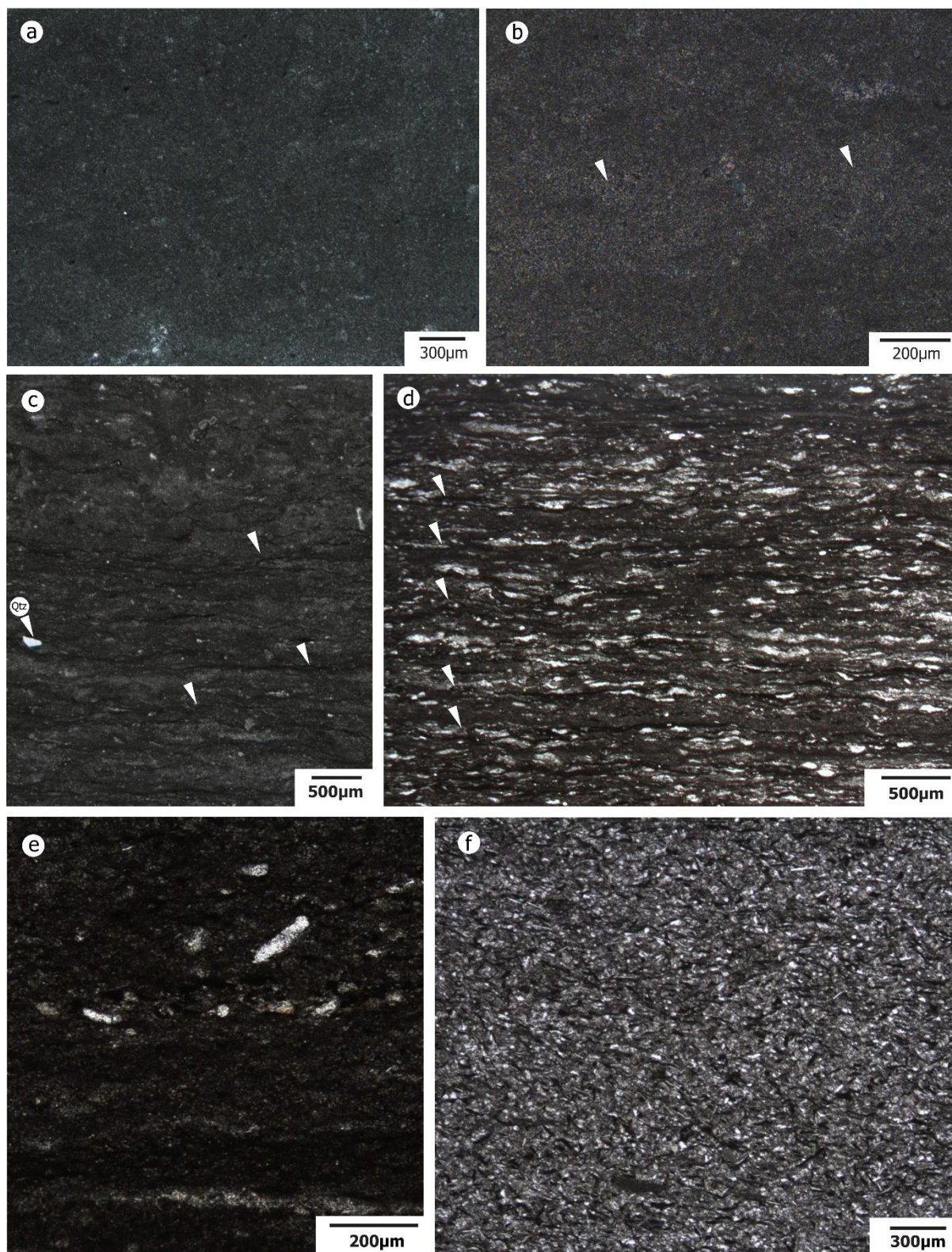


Figure 5.3: Petrographic details of the Avellaneda Formation. (a) Massive microcrystalline limestone. (b) Microcrystalline limestone showing low grade of recrystallization (white arrow). (c) Laminated limestone (pointed by arrows) showing dispersed quartz grains (Qtz). (d) Thin and crinkly lamination associated to microbial mats record. (e) Prismatic shaped crystal inferred as paedomorphic evaporite minerals. (f) Fine grained siliciclastic deposits.

#### 5.4.2 - Carbon and oxygen isotopes and elemental geochemistry

Measurements of carbon and oxygen isotope values were obtained across the three boreholes and span the entire interval of the Avellaneda Formation. Table 4.4.1 displays the carbon and oxygen isotopes data, Ca, Fe, Mn and Sr contents, as well as Sr/Ca, Fe/Sr and Mn/Sr ratios. From base to top of the Avellaneda Formation, the  $\delta^{13}\text{C}$  and  $\delta^{18}\text{O}$  isotopic composition displays coherent variations between the three studied cores. All sections are characterized on the basal portion by positive values around +4.5‰, followed by a marked negative  $\delta^{13}\text{C}$  excursion. Drill core E7 shows  $\delta^{13}\text{C}$  values varying from approximately +4.7‰ to -2.5‰.  $\delta^{18}\text{O}$  values for the same samples vary from -13.6‰ to -15.5‰. In E34,  $\delta^{13}\text{C}$  values are exclusively positive and vary between +4.5‰ and +0.1‰, whereas  $\delta^{18}\text{O}$  values for the same samples vary from -14.7‰ to -15.5‰. Finally, in the H9, the  $\delta^{13}\text{C}$  values range from +4.5‰ to -3.1‰ and the  $\delta^{18}\text{O}$  values vary from -11.8‰ to -15.0‰. The carbon and oxygen isotope data were useful to establish reliable correlations between the three drill cores (Figure 5.4).

Regarding the assessment of post-depositional alteration of isotope compositions, Figure 5.5a shows the  $\delta^{18}\text{O}$  vs  $\delta^{13}\text{C}$  cross plot, as well as the diagrams of  $\delta^{13}\text{C}$  against Sr/Ca, Fe/Sr and Mn/Sr which enable one to track possible trends associated with diagenetic processes (e.g. Banner, 1995; Jacobsen and Kaufman, 1999).  $\delta^{18}\text{O}$  vs  $\delta^{13}\text{C}$  displays no clear correlation that would suggest significant influence of meteoric diagenesis. Frequently, isotope signal from carbonate rocks is considered to be “intact” when  $\delta^{18}\text{O} > -10\text{‰}$  and when values  $\delta^{18}\text{O} < -14\text{‰}$  is considerable altered (Fölling and Frimmel, 2002). Notwithstanding, special conditions for the Neoproterozoic seawater are postulated to explain depleted values of  $\delta^{18}\text{O}$  up to -14‰ often found in these successions (Tahata et al., 2013; Veizer and Prokhoph, 2015).

We further explore here the relationship between carbon isotope compositions with geochemical ratios based on the mobility of Ca, Sr, Mn and Fe during diagenesis (e.g. Banner, 1995; Jacobsen and Kaufman, 1999). During diagenesis and carbonate neomorphism, especially during meteoric diagenesis, a decrease in Sr/Ca ratios is expected and relative enrichments in Mn and Fe, resulting in higher Mn/Sr and Fe/Sr ratios. Figures 5.7b, 5.7c and 5.7d do not show any trend with statistical significance between these ratios and  $\delta^{13}\text{C}$  ratios, suggesting that the carbon isotope trends are close to their primary composition, thus allowing their use for lateral stratigraphic correlation between these sections.

A previous detailed carbon and oxygen isotope study on the marls-rich interval from Avellaneda Formation had already proved the efficacy of carbon and oxygen isotopes chemostratigraphy for regional correlations between quarries in the Olavarría region (Gómez-Peral et al., 2007; 2019). The  $\delta^{13}\text{C}$  values and systematic variations observed in those studies are broadly comparable to those reported here. The same studies also corroborate a primary origin for these trends (Gómez-Peral et al., 2007; 2019). The geochemical data suggest minimal interaction of the original carbonates with diagenetic fluids or, alternatively, that the diagenetic system was buffered by the rock composition (low water–rock ratio).

Table 4.4.1: Carbon and oxygen isotopes data obtained from marls of the Avellaneda Formation.

Sample	Rock	$\delta^{13}\text{C}$ (V-PDB) ‰	Error $\delta^{13}\text{C}$ ‰	$\delta^{18}\text{O}$ (V-PDB) ‰	Error $\delta^{18}\text{O}$ ‰
E7-10B	Carbonate	3.40	0.10	-13.61	0.10
E7-11B	Carbonate	3.79	0.06	-13.59	0.07
E7-12A	Carbonate	4.18	0.06	-14.13	0.06
E7-13D	Carbonate	4.43	0.06	-14.44	0.04
E7-14A	Carbonate	4.51	0.07	-14.73	0.06
E7-15A	Carbonate	4.65	0.04	-14.65	0.04
E7-16A	Carbonate	4.19	0.05	-15.12	0.05
E7-17A	Carbonate	3.85	0.07	-15.27	0.06
E7-18A	Carbonate	2.62	0.09	-15.42	0.06
E7-19B	Carbonate	2.67	0.09	-15.44	0.09
E7-20B	Carbonate	2.71	0.07	-15.47	0.08
E7-21B	Carbonate	3.28	0.05	-15.42	0.05
E7-22C	Carbonate	2.75	0.04	-15.35	0.04
E7-23C	Carbonate	2.04	0.07	-15.43	0.08
E7-24B	Carbonate	-0.84	0.10	-15.04	0.10
E7-25B	Carbonate	-1.93	0.06	-15.31	0.08
E7-26E	Carbonate	-2.51	0.05	-15.37	0.06
E7-27E	Carbonate	-2.73	0.07	-15.40	0.04
E34-1A	Carbonate	4.24	0.06	-14.72	0.08
E34-2B	Carbonate	4.45	0.04	-14.91	0.05
E34-3C	Carbonate	3.67	0.08	-15.20	0.08
E34-4D	Carbonate	3.31	0.09	-15.24	0.09
E34-5A	Carbonate	3.23	0.08	-15.36	0.10

---

E34-6B	Carbonate	2.44	0.08	-15.24	0.09
E34-7B	Carbonate	1.97	0.09	-15.22	0.10
E34-8F	Carbonate	2.15	0.07	-15.18	0.09
E34-9C	Carbonate	2.07	0.08	-15.26	0.05
E34-10A	Carbonate	2.34	0.07	-15.49	0.08
E34-11B	Carbonate	2.12	0.07	-15.13	0.06
E34-12A	Carbonate	0.97	0.06	-15.13	0.05
E34-13B	Carbonate	4.15	0.05	-14.97	0.06
E34-14A	Carbonate	4.04	0.07	-15.02	0.05
E34-15C	Carbonate	3.98	0.05	-15.06	0.05
E34-16B	Carbonate	3.84	0.06	-15.10	0.07
<hr/>					
H9-2B2	Carbonate	3.39	0.06	-12.65	0.06
H9-3D	Carbonate	3.79	0.07	-11.75	0.06
H9-4D	Carbonate	4.32	0.06	-13.44	0.06
H9-5E	Carbonate	4.38	0.03	-13.61	0.04
H9-6A	Carbonate	4.45	0.05	-13.59	0.10
H9-7A	Carbonate	4.40	0.10	-13.99	0.09
H9-8D	Carbonate	4.49	0.05	-13.92	0.05
H9-9D	Carbonate	4.38	0.06	-14.37	0.06
H9-10B	Carbonate	4.16	0.08	-14.57	0.08
H9-11A	Carbonate	3.42	0.10	-14.77	0.09
H9-12A	Carbonate	3.02	0.10	-14.90	0.08
H9-13B	Carbonate	2.73	0.07	-14.83	0.08
H9-14B	Carbonate	2.78	0.10	-14.70	0.09
H9-15B	Carbonate	2.42	0.09	-14.84	0.09
H9-16B	Carbonate	2.61	0.10	-14.70	0.07
H9-17A	Carbonate	2.75	0.06	-14.64	0.06
H9-18E	Carbonate	2.76	0.05	-14.77	0.05
H9-19B	Carbonate	2.41	0.07	-14.84	0.07
H9-20A	Carbonate	1.75	0.09	-14.98	0.08
H9-21E	Carbonate	-2.32	0.09	-14.96	0.06
H9-22B	Carbonate	-3.05	0.06	-14.88	0.06

---

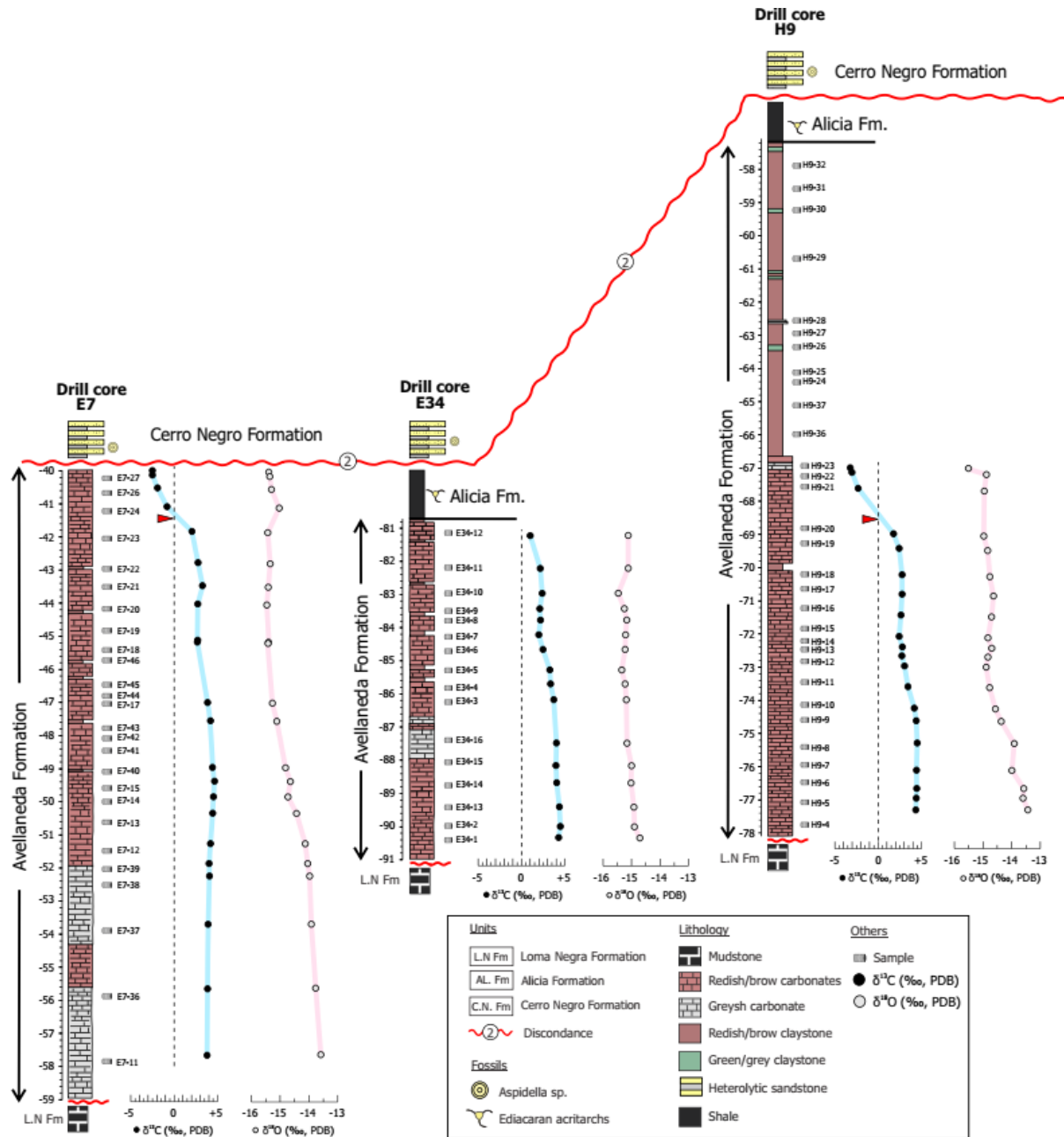


Figure 5.4: Simplified sedimentary profiles coupled with stable isotopes recorded in the Avellaneda Formation. Drill-cores are spatially oriented from east (left) to west (right). Red arrow indicates the turning point from negative to positive  $\delta^{13}\text{C}$  ratios.

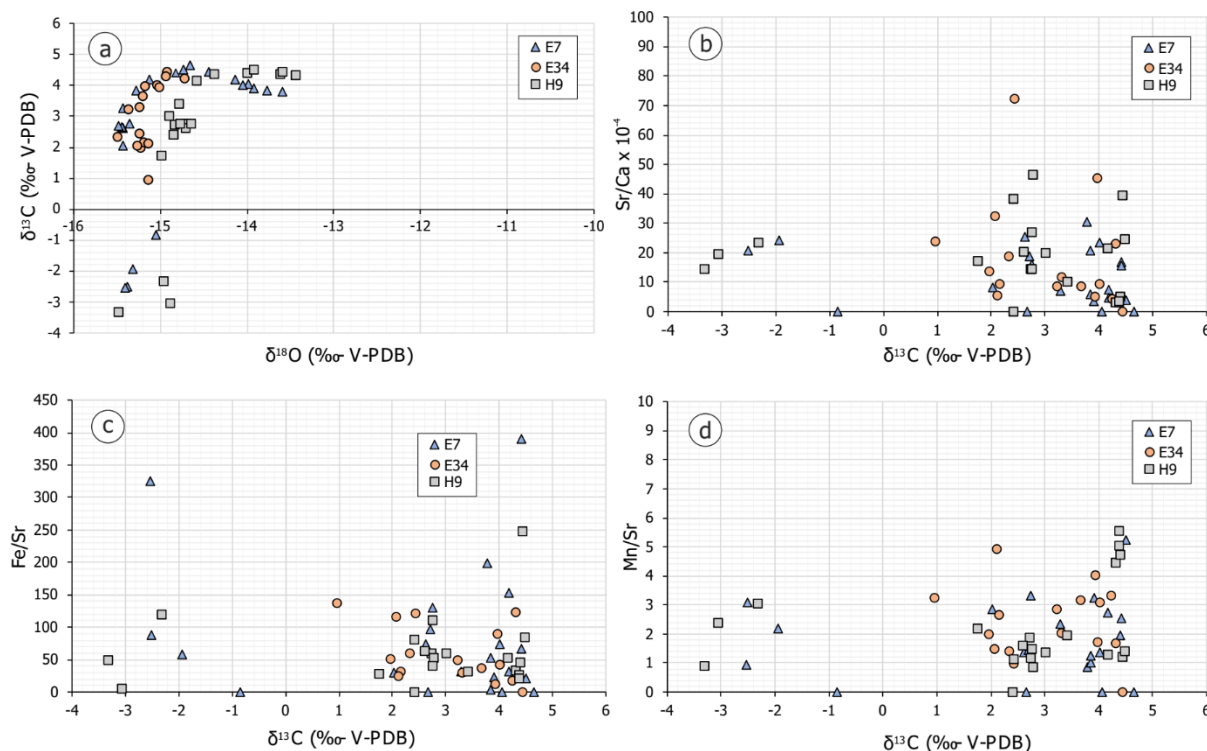


Figure 5.5: Stable isotopes and elemental geochemical analysis of samples from the Avellaneda Formation. (a) Cross-plot of the  $\delta^{18}\text{O}$  vs  $\delta^{13}\text{C}$ ; (b)  $\delta^{13}\text{C}$  vs Sr/Ca ratio; (c)  $\delta^{13}\text{C}$  vs Fe/Sr ratio and (d)  $\delta^{13}\text{C}$  vs Mn/Sr ratio.

### 5.4.3. Anisotropy of magnetic susceptibility (AMS)

The results obtained from AMS measurements display similarities between the three drill cores. The main AMS parameters are summarized on Table 4.4.2. The mean bulk susceptibility  $K_m$  ranges from  $3.32 \times 10^{-5}$  to  $2.12 \times 10^{-4}$  SI with an average ( $\pm$  standard deviation) of  $1.18 \pm 0.385 \times 10^{-4}$  SI ( $n = 92$ ) in drill core E7 (Table 4.4.2, Figure 6). Measures performed in samples collected in E34 show bulk susceptibility  $K_m$  ranging from  $6.20 \times 10^{-5}$  to  $1.97 \times 10^{-4}$  SI with an average ( $\pm$  standard deviation) of  $1.43 \pm 0.377 \times 10^{-4}$  SI ( $n = 65$ ). For H9 the bulk susceptibility  $K_m$  ranges from  $6.17 \times 10^{-5}$  to  $5.21 \times 10^{-4}$  SI showing an average ( $\pm$  standard deviation) of  $2.37 \pm 1.18 \times 10^{-4}$  SI ( $n = 114$ ).

The AMS data is used to infer the strain imprint on sedimentary rocks (Pares et al., 2015). Principal-axes orientations of AMS were estimated for each drill core. In order to facilitate visualization, the  $K_2$  axis was suppressed and the equal-area projections in Figure 6 exhibit only  $K_1$  and  $K_3$  axes. In the Avellaneda Formation, the  $K_1$  axis is distributed along a girdle close to the horizontal plane (i.e., the bedding plane), whereas the  $K_3$ , which is the pole to the magnetic foliation, shows steep inclinations ranging predominantly between  $75$ - $90^\circ$  (Figures 5.6a-5.6c), revealing a nearly horizontal magnetic foliation. This configuration is

typical of a primary sedimentary fabric without apparent disorder and disturbance (Hrouda & Kahan, 1991; Rochette et al., 1992). All drill cores display an oblate magnetic fabric, with the magnetic foliation (F) exceedingly higher than the magnetic lineation (L) (Table 4.4.2, Figures 5.6d – 5.6f). The parameter T almost always displays positive values, also indicating an oblate shape for the AMS ellipsoids. This type of relationship is considered as evidence for undisturbed sediments in all drill cores. The degree of anisotropy  $P_j$  averages 1.012 ( $\pm 0.018$ ), 1.022 ( $\pm 0.019$ ) and 1.073 ( $\pm 0.067$ ) for E7, E34 and H9, respectively (Table 4.4.2, Figures 5.6d-5.6f). In addition, the  $P_j$  and T values display a positive curvilinear relationship (Figures 5.6g-5.6i), so that samples with a high  $P_j$  value always possess an oblate fabric. These results are again typical of the magnetic fabrics in undisturbed sediments, the oblate sub horizontal magnetic fabric resulting from sediment settling and further compaction (Rochette et al., 1992; Weil and Yonkee, 2009; Yang et al., 2019).

The AMS data were also plotted against sedimentary logs to track variability of  $K_m$  and the orientation of principal axes across the Avellaneda Formation (Figure 5.7).  $K_m$  values reveal a progressive increase of susceptibility towards the top of the sections. In general, these increases are smooth, except for H9 core which displays an abrupt displacement with  $K_m$  values jumping from  $\sim 2 \times 10^2$  to  $\sim 5 \times 10^2$ . The highest mean value of magnetic susceptibility coincides with the start of the fine-grained siliciclastic facies. The  $P_j$  parameter shows a similar behavior, with highest values and major variations observed in the detrital facies of H9 core (Figure 5.7).

The AMS pattern observed in the three cores can be explained by the well-developed sedimentary bedding (Figure 5.7). For almost all samples, the  $K_3$  axis shows a steep inclination, predominantly higher than  $75^\circ$ . However, at the top of E7 and at some depths in the other cores, we note a series of  $K_3$  axis very close to the border of the stereoplot (Figures 5.6 and 5.7), i.e. the magnetic foliation in these samples is almost vertical. This unusual behaviour for sedimentary rocks may be explained by the presence of very fine magnetic grains (Ferre et al., 2002) or recrystallization of carbonate with preferred c-axis orientation as siderite/ankerite (Hounslow, 2001) or yet by presence of Mn-carbonate (English 1999). The cause of "inverse" magnetic fabric in Avellaneda Formation needs to be further investigated.

Table 4.4.2: Anisotropy of magnetic susceptibility (AMS) data from Avellaneda Formation.

Drill Core		AMS parameters						Mean eigenvectors		
Code	Bedding Plane		Km ( $10^{-4}$ )	L	F	Pj	T	K <sub>max</sub> (D/I) (Conf. ellip)	K <sub>int</sub> (D/I) (Conf. ellip)	K <sub>min</sub> (D/I) (Conf. ellip)
E7 n = 87	20/17	Mean	0.332-2.12	1.004	1.008	1.012	0.396	288.8/5.6	19.1/2.8	135.9/83.8
		Average	1.18	1.006	1.018	1.026	0.252	(56.6/16.0)	(56.9/36.7)	(38.9/17.9)
		std.	0.385	0.002	0.017	0.018	0.508			
E34 n = 65	98/15	Mean	0.620-1.97	1.001	1.018	1.022	0.856	29.8/3.2	299.7/2.1	177.2/86.2
		Average	1.43	1.005	1.020	1.026	0.436	(57.9/14.3)	(58.0/7.9)	(14.2/9.5)
		std.	0.377	0.003	0.016	0.019	0.361			
H9 n = 114	0/0	Mean	0.617-5.17	1.001	1.063	1.073	0.976	309.0/1.4	39.0/0.0	129.7/88.6
		Average	2.37	1.004	1.065	1.079	0.677	(70.6/6.8)	(70.6/7.9)	(8.0/6.9)
		std.	1.18	0.003	0.057	0.067	0.397			

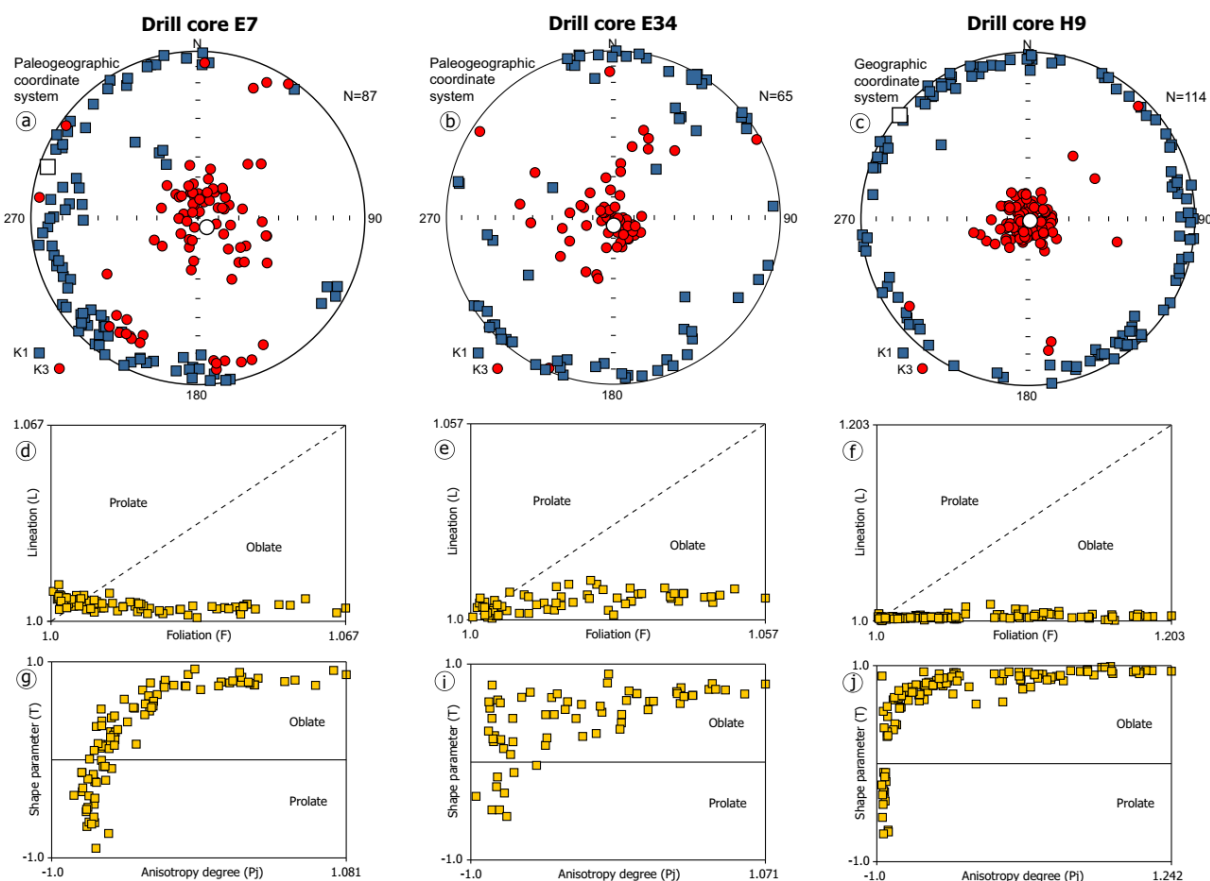


Figure 5.6: AMS data from investigated drill cores. Diagrams exposed in a, d and g are render from E-07. Figure b, e and h were performed from E-07. And c, f and i were produced from H-09. From (a) to (c) equal area projections in lower hemisphere, showing the directions of K<sub>1</sub> and K<sub>3</sub> axes for each drill core. All projections were plotted in geographic coordinate system. Large open symbols show the mean directions of the three principal susceptibility axes calculated with Jelínek's statistics (according Jelínek, 1981). Lineation (L) is plotted versus foliation (F) in a Flinn-type diagram for each drill core are exhibit in boxes from (d) to (f). Boxes (g) to (i) show the relationship between the corrected anisotropy degree Pj and the shape parameter T

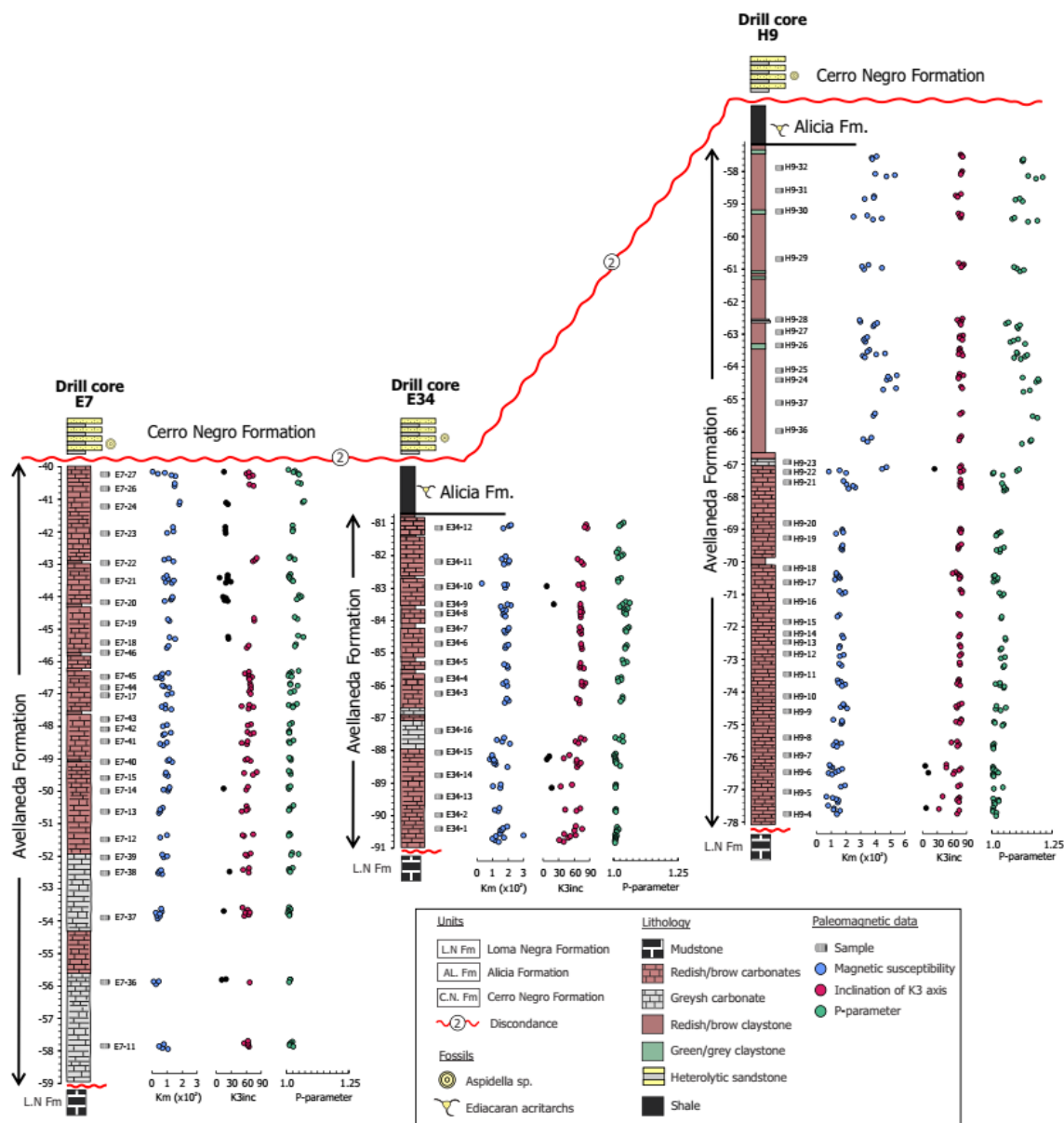


Figure 5.7: Variations of AMS parameters plotted against vertical sedimentary facies. AMS parameters plotted include magnetic susceptibility (SI), inclination of K3 axis and degree of anisotropy (Pj).

#### 5.4.4. Magnetic mineralogy

The magnetic properties of samples from the drill cores range from soft to hard coercivity behaviour (Figure 5.8). Soft coercivity phase exhibits a rapid increase in IRM acquisition curves for fields smaller than 0.1 T and an almost complete saturation around 0.3 T (Figure 5.8). This type of behavior is typical of rocks magnetically dominated by low-coercivity phases, such as Ti-poor magnetite or maghemite (e.g E34-2). A second type of behavior is marked by a rapid increase under 0.2 T, followed by a slow acquisition until

saturation over 0.6 T (Figure 5.8). This magnetic behavior suggests the coexistence of two magnetic components with strongly contrasting coercivities (Roberts et al., 1995). The third magnetic behavior correspond to concave-up IRM acquisition curves, which do not reach saturating even after our peak field of 1 T (Figure 5.8). This last behavior is likely due to the presence of high-coercivity phases like hematite (Roberts et al., 2013). More detailed about magnetic properties of samples from the sections and drill cores are described in the companion paper by Franceschinis et al., (this issue).

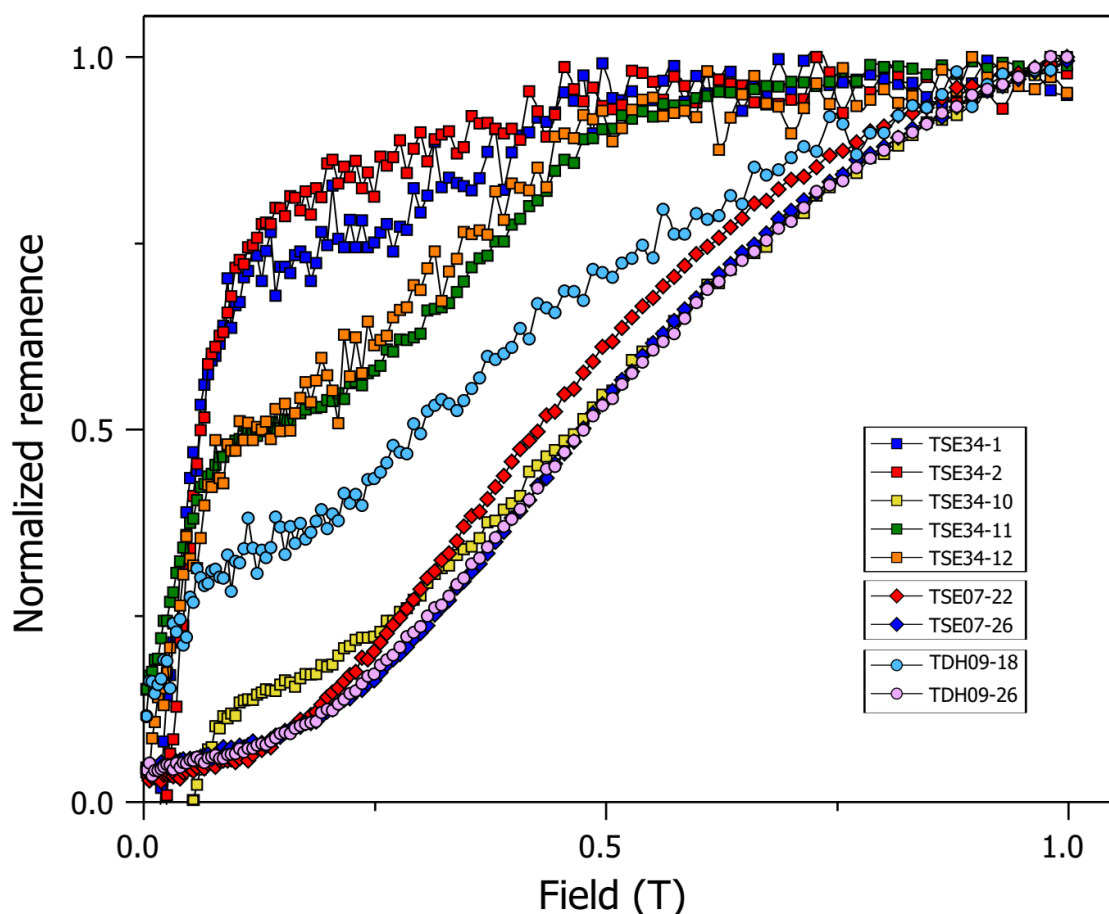


Figure 5.8: IRM acquisition curves performed in representative samples selected in distinct intervals of the Avellaneda Formation.

#### 5.4.5 - Palaeomagnetic analysis

Progressive alternating field and thermal demagnetization techniques were applied first to a set of pilot samples. Alternating field demagnetization was usually unable to fully demagnetize the NRM and isolate its most stable component. On the other hand, pilot samples

submitted to thermal demagnetization clearly isolated a characteristic component, and so it was used as a standard procedure.

The measured NRM intensities in sedimentary rocks of the Avellaneda Formation with stable magnetic directions varied from  $10^{-4}$  to  $10^{-6}$  A/m. These samples showed a very stable demagnetization pattern. Overall, all specimens were able to produce reliable paleomagnetic results in spite of their weak NRM. Remanence intensities gradually decayed with increasing demagnetization temperatures (Figure 5.9). The first major decay occurs at around 250-350 °C, which may indicate the existence of some amount of iron sulfide in these rocks (Roberts, 1995; Sagnotti and Winkler, 1999; Roberts et al., 2011). The magnetic intensities of most samples display a steady decrease after 350 °C and show a second major decay at 580 °C, related to the presence of magnetite. A few samples achieved complete demagnetization at 580 °C, but most of them reached complete demagnetization only at 650 °C (Figure 5.9), which is typical of hematite, consistent with the results of IRM acquisition curves.

A consistently observed paleomagnetic direction is isolated by stepwise heating to between temperatures 100 to 300 °C. This low temperature component (labelled “a”) is present in nearly every sample from the three drill cores analyzed. Here, we use the low temperature component to refine the azimuthal orientation of the sample fragments of the drill cores, using the low temperature component mean direction isolated at a nearby outcrop in the same quarry (see Franceschinis et al., this issue). The maximum angular deviation (MAD) values were always below 12°. The component “a” is well grouped and show a single normal polarity. The component “a” recovery from each drill core is plotted in Figure 9a for a direct comparison. The mean direction of magnetic component “a” point to NW or NE and display a moderate negative inclination. Component “a” has a mean direction “in situ” of Dec = 5.4° and Inc = - 56.0° ( $\alpha = 1.5^\circ$ , n = 88; Figure 10a) measured for core E7, Dec = 5.5° and Inc = - 51.0° ( $\alpha = 2.1^\circ$ , n = 67; Figure 10a) for core E34, and Dec = 5.4° and Inc = - 48.2° ( $\alpha = 2.8^\circ$ ; n = 89; Figure 10a) for core H9. The mean direction after clustered all drill cores specimens is about Dec = 5.4° and Inc = - 52.0° ( $\alpha = 1.3^\circ$ , n = 244; Figure 10a).

The higher laboratory unblocking temperature magnetization was named component “b”. This component is present in nearly every sample and is stable within the temperature interval ranging from 350-575 °C, for most samples. However, a small number of samples, probably dominated by high coercivity minerals as hematite bearing, show maximum unblocking temperatures higher than 600 °C. Overall, samples collected across different drill

cores from Avellaneda Formation show a very similar behavior during demagnetization (Figure 5.9). The component “b” displays positive (negative) northeast (southwest) directions (Figure 5.9). For samples that record both the “a” component and a normal polarity “b” component, the demagnetization diagrams display a little change in inclination. In contrast, for samples with a “a” component and a reversed polarity “b” component, this inflection is much more pronounced (Figure 5.9). The “b” component after bedding correction yields a mean direction with Dec = 20.5° and Inc = 66.1° ( $\alpha_{95}$  = 3.7°, n = 79; core E7, Figure 10b), Dec = 20.4° and Inc = 68.1° ( $\alpha_{95}$  = 3.2°, n = 58; core E34, Figure 5.10b). For specimens collected from core H9 tilt correction was unnecessary, as lamination was measured to be subhorizontal, and mean direction points to Dec = 20.5° and Inc = 58.0° ( $\alpha_{95}$  = 3.9°, n = 76; Figure 5.10b).

Component “b” was interpreted as the Characteristic Remanent Magnetization (ChRM) for the Avellaneda Formation and was used for the magnetic polarity stratigraphy and magnetostratigraphic correlation across this unit.

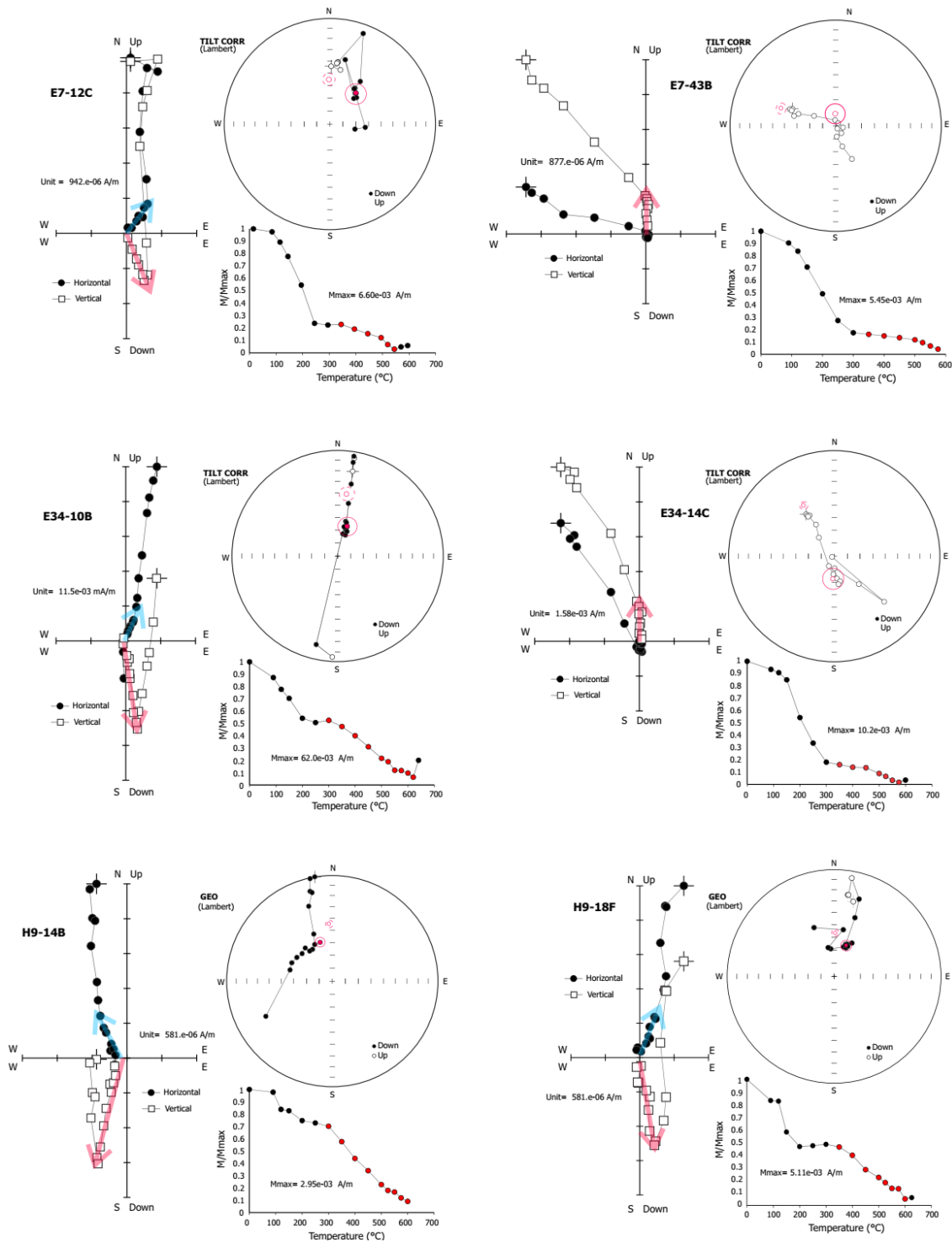


Figure 5.9: Orthogonal demagnetization diagrams (Zijderveld diagrams) and evolution of the remanence intensity during thermal demagnetization treatment. Remanence intensity is normalized to the maximum of each sample. Representative demagnetization diagrams for samples (identified by code) from the Avellaneda Formation. NRM—natural remanent magnetization. Magnetic intensity ( $M/M_{max}$ ) plots against temperature showing thermal demagnetization behavior with red dots indicating the “b” component. In Zijderveld diagrams the high-temperature component (“b” component) that decays to the origin is traced with a blue arrow and red filled shapes.

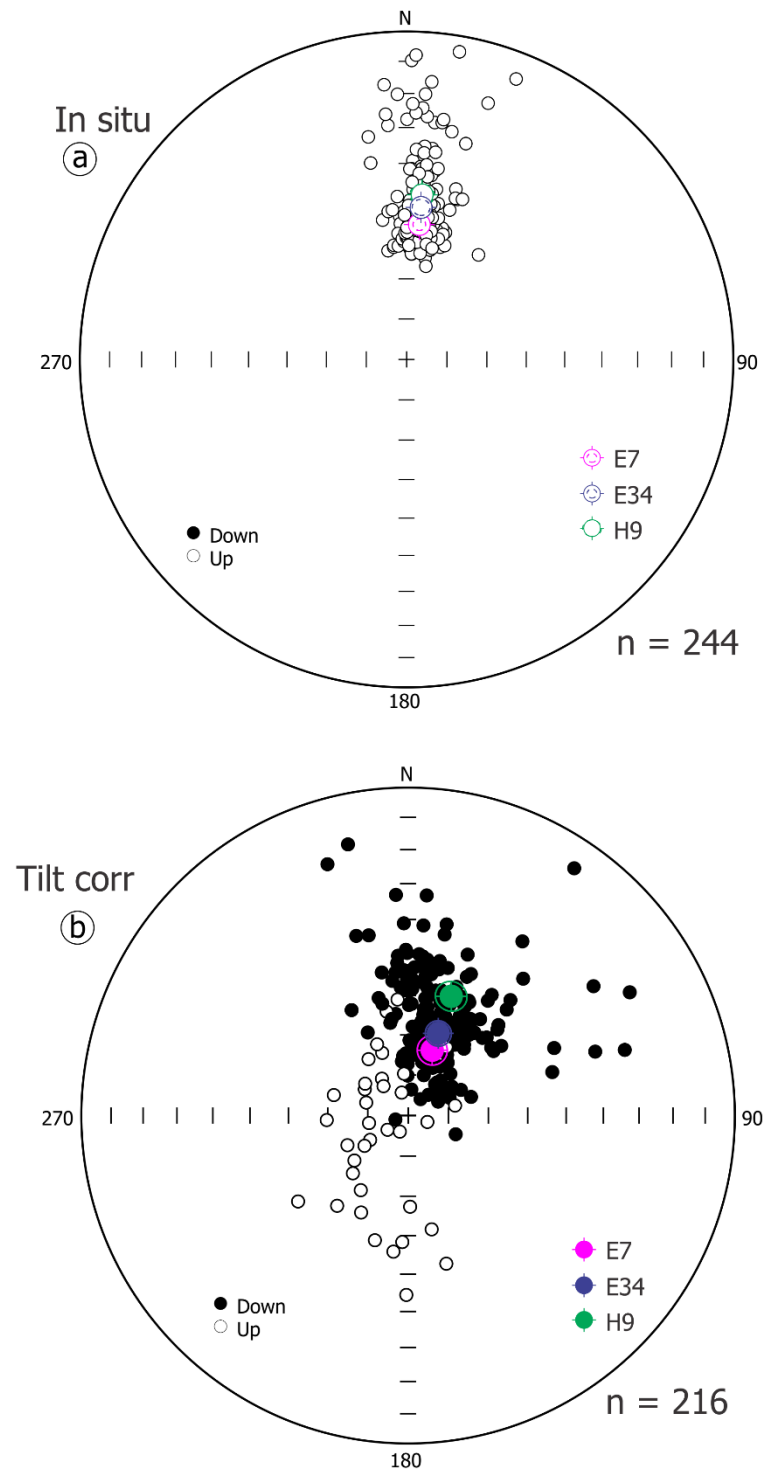


Figure 5.10: Equal area stereonet displaying the (a) mean directions of component “a” from the Avellaneda Formation at Olavarria. Component “a” shows an overlap in the three drill cores. (b) Equal area stereonet displaying the ChRM direction (component “b”) of the Avellaneda Formation at Olavarria. Up (down) pointing palaeomagnetic directions are indicated by open (closed) circles in the stereoplots. Circle symbols were calculated from samples that reach stable endpoints. Coloured ovals represent the cone of 95 per cent confidence about the mean direction for each drill core.

## 5.5. Discussion

### 5.5.1. On the primary nature of the Avellaneda characteristic magnetic component

Carbonate sediments display weak magnetization and are reputable to be prone to remagnetization mostly due to syn-depositional and post-depositional interaction with formation fluids (Jackson and Swanson-Hysell, 2012). Yet, several lines of evidence support the hypothesis that sediments in the Avellaneda Formation were well preserved and spared from significant alteration. Petrographic observations suggest only an incipient recrystallization of carbonate mud to microspar (Figure 5.3). Unrecrystallized mud calcite are most consistent with peak temperatures around  $\sim 150$  °C (Heydari and Wade, 2002). Furthermore, sedimentary rocks still contain well-preserved parallel lamination, including delicate thin lamination associated to microbial mats combined with occurrence of casts of evaporitic minerals. These features argue for good preservation state of the studied sediments. We also note that the presence of drusy and blocky calcite cement are exclusively restricted to veins and fluid interactions. Elemental and isotope geochemistry analysis also indicate that sediments from Avellaneda may have passed unscathed from significant alterations.

Rock magnetic data also provide some evidence for stability and the primary nature of the characteristic magnetization component isolated in the studied samples. Rock magnetic analysis and thermal demagnetization spectrum both indicate fine-grained magnetite and hematite as the main magnetic carries in the Avellaneda Formation. These minerals are capable of preserve a magnetic remanence over suitable long periods of time. The thermal demagnetization spectrum is also similar among the three analyzed sections.

Our detailed magnetostratigraphic study shows that the high-temperature stable magnetization component presents both positive and negative inclinations. This dual-polarity component was easily recognized in all drill cores along the entirety of the Avellaneda Formation and present good agreement of the reversal stratigraphy between sections, after independent correlations using sedimentology and stable isotopes data (Figure 13). The polarity pattern observed in the Avellaneda Formation, agree reasonably well from section to section which is consistent with a remanent acquisition during sediment deposition or immediately after, during early diagenesis. In opposite, if the magnetization had been acquired during late diagenetic processes, a reproduction of the polarity pattern observed in the Avellaneda Formation seems unlikely.

Drill cores from the Avellaneda Formation investigated here are dominated by fine-grained sediments without conglomeratic intraformational facies, making it impossible to perform a classic conglomerate test. The presence of dual polarity was used by Francischinis et al., (submitted) to apply reversal test (McFadden and McElhinny, 1990; Koymans et al., 2016). The reversal test was performed to each drill core individually and in a sum of all specimens. However, this reversal test is failed in all tested scenarios. Francischinis et al., (submitted) argue that due to small set of samples for each normal polarity interval, they were likely too short to fully average paleosecular variations. Francischinis et al., (submitted) demonstrate that ChRM directions recovery in Avellaneda Formation likely was acquired before tilting and does not resemble any expected Phanerozoic direction for the study locality.

Paleomagnetic investigations have been previously performed on the Cryogenian to Ediacaran–Cambrian sedimentary successions from Tandilia system (Valencio et al., 1980; Rapalini et al., 2013) as well in other correlative sedimentary units from Río de La Plata Craton (Rapalini & Sanchez-Bettucci, 2008). Furthermore, some works found a widespread remagnetization event that affected several sedimentary units of the Neoproterozoic cover of the Río de la Plata Craton (Font et al., 2012). However, others have escaped remagnetization (e.g. Los Barrientos claystones, Rapalini, 2006).

### **5.5.2. Magnetic polarity stratigraphy and chemostratigraphy of the Avellaneda Formation**

To determine a polarity zone, we used at least two consecutive samples with the same polarity (Figure 5.11). Paleomagnetic results plotted against the stratigraphy show that the Avellaneda Formation is dominated by long lasting intervals with positive inclination separated by short intervals of negative inclinations (Figure 5.11). Furthermore, relatively short intervals show transition from positive-negative inclination (and vice-versa) that may represent excursions of the Ediacaran geomagnetic field (Figure 5.11). We are aware of the inherent uncertainty in merely trying to match magnetic polarity patterns among analyzed drill cores, then, it is important to note that the magnetostratigraphic correlation among the three drill cores is guided not solely by the lithostratigraphy, but also anchored by carbon isotope stratigraphy (Figure 5.11).  $\delta^{13}\text{C}$  values show a progressive decrease upward through in the succession.  $\delta^{13}\text{C}$  profile started with positive values at the base showing progressively less positive values upward and moving into negative records up in the section. These trends are identified in all investigated drill cores (although negative values are not reached in E-34

due to apparent truncation of the Avellaneda Fm in contact with the overlying Alicia Fm). The primary nature of carbon isotopes is supported by elemental geochemistry data (Figure 5.5).

At the Avellaneda Fm, the most positive values of  $\delta^{13}\text{C}$  are reported in basal section.  $\delta^{13}\text{C}$  profile indicate values close or slightly up to +4‰. These  $\delta^{13}\text{C}$  values are laterally consistent in all drill cores. Values of  $\delta^{13}\text{C} > +4\text{‰}$  are almost exclusively found within the reverse polarity basal levels in the Avellaneda Formation. In the intermediate portion of this unit, we note a good consistency of  $\delta^{13}\text{C}$  values that show a slight downward trend. In addition,  $\delta^{18}\text{O}$  show a major offset in this same stretch. These trends are better observed in drill cores E7 and H9. For drill core E34 isotope data appears more monotonous. However, correlation based on magnetostratigraphic polarity is consistent and shown by stratigraphic position of normal polarity intervals. The negative ~3‰ excursion near the top of the Avellaneda Formation within a relatively long reverse interval is also correlated among drill cores. These correlations assume likely intervals of relative condensations or surges of sedimentation (e.g., see magnetic stratigraphy data from H9), but their broad consistency throughout the three profiles show there are no major gaps in the composite stratigraphy among the studied drill cores. Mapping mine fronts and adjacent drill cores previously studied provide critical information confirming the near-completeness of rock records and their attainable temporal resolutions (Arrouy et al., 2015; Gómez-Peral et al., 2017; 2019). Although not imposing like other coeval succession, this isotopic excursion can be interpreted as an expression of the initial stages of the globally synchronous Shuram Excursion (Afonso et al., submitted). Shuram excursion is thought as a singular chemostratigraphic worldwide record reported in multiple paleocontinents (Grotzinger et al., 2011; Rooney et al., 2020). If this interpretation is valid, our results on the Avellaneda Formation suggest that the onset of the Shuram Excursion can be constrained by a reverse polarity interval.

### 5.5.3. Towards a magnetic polarity chart for the Ediacaran

Correlating and dating of sedimentary rock sequences is critical in Earth sciences. For this reason, recent extensive magnetostratigraphic studies have significantly furthered the updating of the geomagnetic polarity time scale (GPTS) back into the Early Paleozoic and the Precambrian. To build the GPTS from sedimentary sequences on the continents requires good data coverage and careful work to correlate the sequence independently of the paleomagnetism and to remove the effects of remagnetization on the data. At the same time, our knowledge of

the magnetic field polarity in the more ancient epochs is non-systematic and fragmentary. A necessary condition for successfully solving this problem is to establish a reliable biostratigraphic or any high-precision age constrain useful to correlate section by section. However, the use of biostratigraphy is substantially unworkable by their practical absence in a number of the largest regions as well as for most of Proterozoic successions. Lack of reliable radioisotopic age constraints of purely sedimentary series are also a challenge. Conversely, there are numerous excursions, both negative and positive, in  $\delta^{13}\text{C}$  during late Neoproterozoic times. These  $\delta^{13}\text{C}$  fluctuations are key for global correlations (Halverson et al., 2005).

Despite of potential limitations concerning the results of this study, we attempt to draw a comparison of these result with those reported for sedimentary rocks across the late Ediacaran and early Cambrian. We are aware that correlation based on polarity magnetic by pattern matching is ambiguous due to lack of available accurate age scheme. In addition, the Ediacaran geomagnetic field behavior is poorly known and more complicated as it appears to show periods of low and high reversal frequency. Sedimentary succession from 635 Ma to 570 Ma report a stable magnetic field with low reversal frequency according to a rather large number of studies on terrigenous red beds (Schmidt and Williams, 2010). Contrarily, a high reversal frequency was reported around 550 Ma and decreasing into Middle Cambrian (Bazhenov et al., 2016; Robert et al., 2017; Gallet et al., 2019). By comparison, results for the Avellaneda Formation document a relatively low or very modest frequency rate of polarity reversals which suggests that the studied sections shouldn't be far from the interval  $\sim 570$  Ma. We should stress that despite of age uncertain, deposition of the Avellaneda Formation is constrained to the 580–560 Ma interval by correlation, fossils and isotopic ages of overlying and underlying units (Arrouy et al., 2016; Gómez-Peral et al., 2017; 2019).

The lack of precise age constrains turns difficult a straightforward comparison of our data with any particular previous late Ediacaran paleomagnetic data set. We try to do that using carbon isotopes curves (Figure 11). A similar approach is used to help correlations in multiple, globally separated localities. Rock magnetic records coupled with  $\delta^{13}\text{C}$  logs were applied on exposures in South Australia, South China, and the United States (Minguez et al., 2015; Minguez and Kodama, 2017; Gong et al., 2017, 2019) to correlate successions that record the Shuram isotopic excursion. In these studies, it was shown that the examined rocks contain ancient stable magnetization of both normal and reversed polarity. This component is easily isolated and is probably primary. Interestingly, the same geomagnetic reversal that was identified right at the nadir of the Shuram Excursion in sections from South Australia and the

United States also indicates that the Shuram Excursion was globally synchronous (Minguez and Kodama, 2017). Furthermore, these records suggest that time elapsed from onset to nadir of the excursion was or about 1 million years, with a slow recovery to normal values of several million years.

Recently Afonso et al., (submitted) based in sedimentary facies and carbonate isotope data proposed that Avellaneda Formation records the onset of the Ediacaran Shuram carbon isotope excursion. This fact allows to assign the sedimentary record from the Avellaneda Formation around ~570 Ma (Rooney et al., 2020). Furthermore, the age constraints based on the isotope profile provide the possibility to compare magnetostratigraphic record of the Avellaneda Formation with other coeval units. Matching of the  $\delta^{13}\text{C}$  pattern of our results with those from other localities suggest an accumulation rate of around 100 kyr/m for the carbonatic levels of the Avellaneda Formation. Extrapolating these values indicate that deposition of this unit probably lasted no more than 2 Ma. Our regional magnetostratigraphy data suggests the onset of the isotope  $\delta^{13}\text{C}$  excursion (change from positive to negative values) during a reverse polarity interval, some 4 to 6 meters (500 kyrs?) on top of the last normal interval. These observations provide an opportunity to test the synchronicity and duration of the excursion on a global scale, and possibly to contribute to the global magnetic polarity chart in the late Ediacaran.

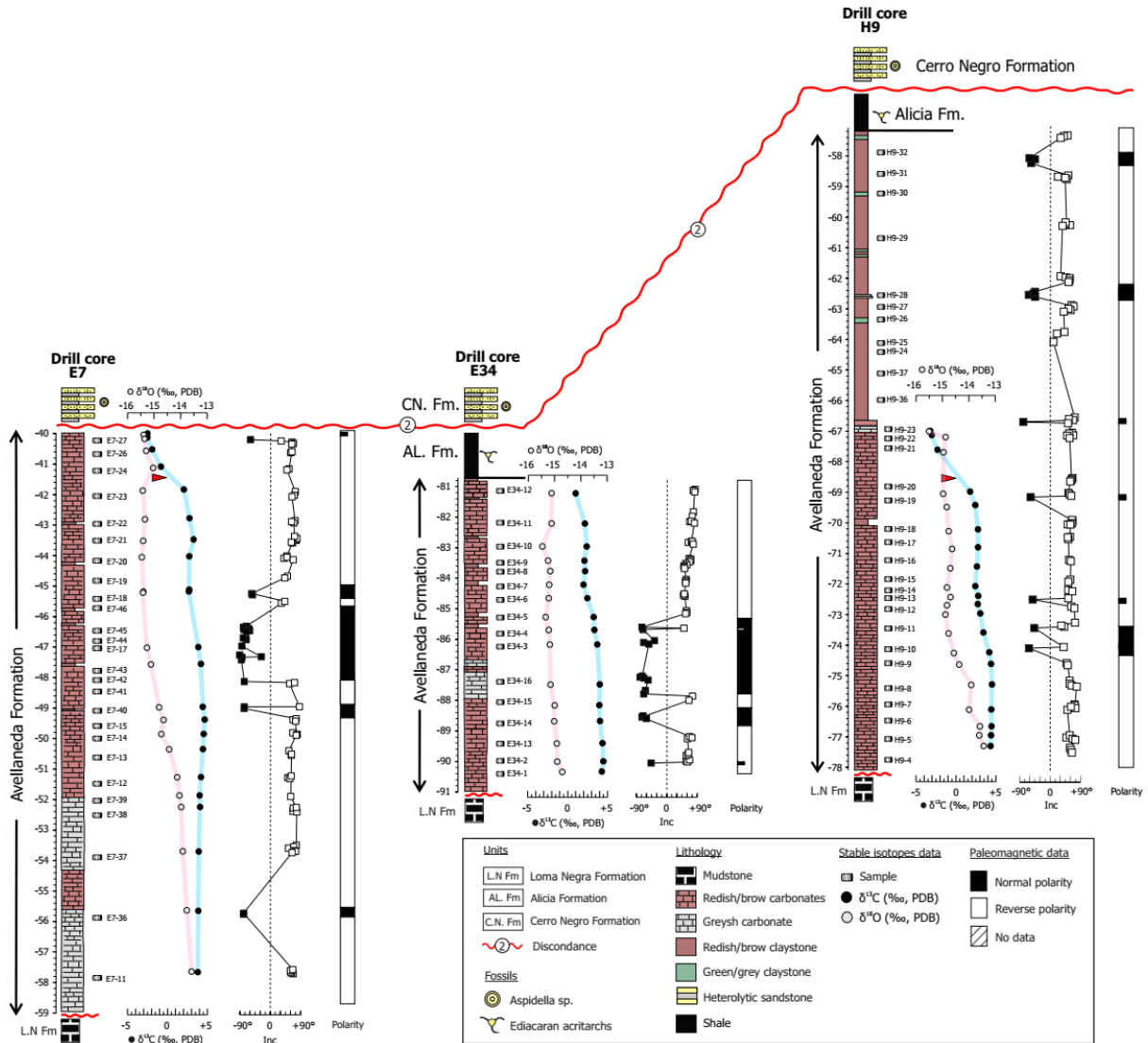


Figure 5.11: Magnetostratigraphy combined with stable isotope variations of the Avellaneda Formation. ChRM inclination (polarity) data are plotted against stratigraphic sampling level and lithology. Closed (open) squares represent stable directions isolated using thermal demagnetized treatment of normal (reverse) polarity. Red arrows indicate the stratigraphic levels of the turning point in C-isotope signal that pass from positive to negative values.

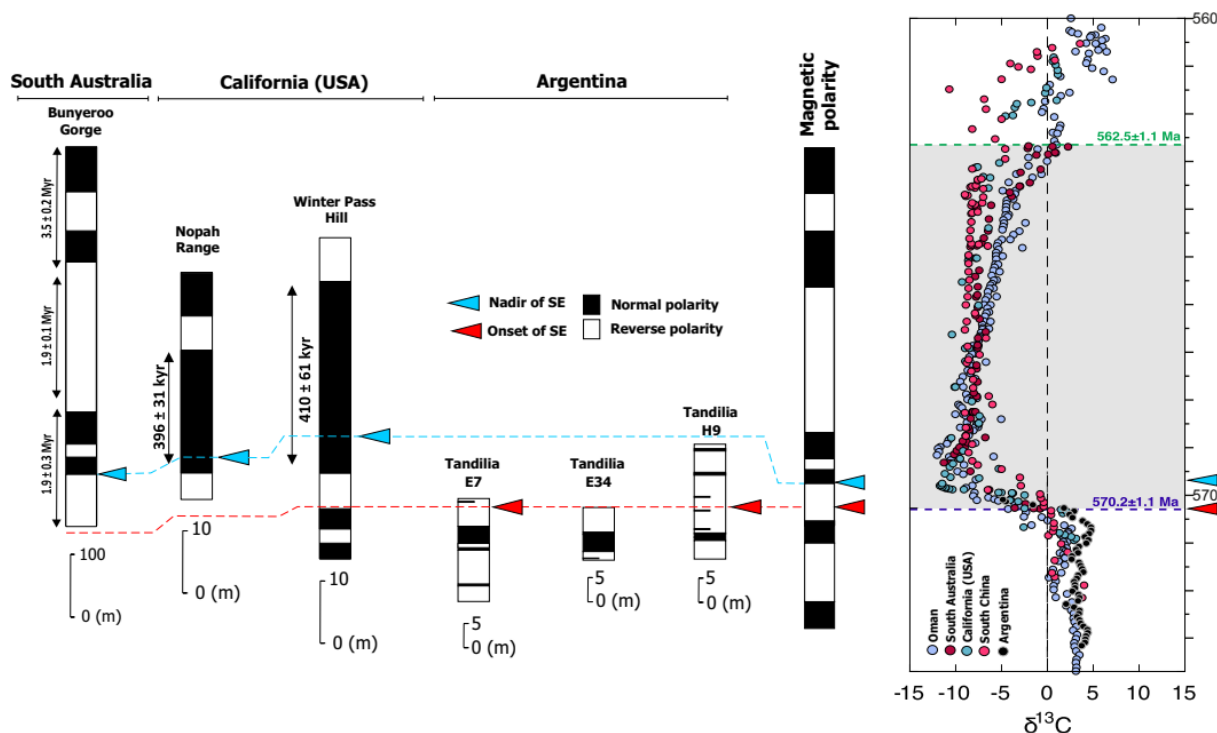


Figure 5.12: Polarity stratigraphy and carbon isotope stratigraphy for the globally separated coeval sections related to the interval 580-560 Ma. Results obtained in Avellaneda Formation are compared with Wonoka Formation from the Flinders Ranges in South Australia and with results from Death Valley, California, USA (Minguez et al., 2015). Note that the onset of Shuram isotope excursion is consistently positioned in a reverse polarity interval. The nadir of the Shuram excursion reported in the Flinders Ranges (excursion occurs at 80 m) is constrained stratigraphically by the polarity transition between the reverse and normal sites.

## 5.6. Conclusion

Magnetic polarity and stable isotopic stratigraphy were performed in sedimentary succession from the mid-Ediacaran Avellaneda Formation at Olavarria (Buenos Aires Province). Samples were systematically collected from three drill cores that cut entirely this unit. After thermal demagnetization treatment a low “a” and a high-temperature “b” magnetic component were successfully isolated. The “a” -component is exclusively of normal polarity and corresponds to a secondary post-tectonic overprint. On the other hand, the “b” -component displays both normal and reverse polarities and is interpreted as a primary remanence. We use this dual polarity component to build the magnetostratigraphy column and a correlation scheme through the Avellaneda Formation. Correlation among the three sections is supported by  $\delta^{13}\text{C}$  values obtained. Directional results indicate the prevalence of reverse polarity magnetozones with an intercalated normal magnetozones. A few very short intervals of normal polarity were also observed. Our data show a transition from positive to negative

values of  $\delta^{13}\text{C}$  near the top of the carbonatic section of the Avellaneda Formation. We correlate this to the onset of the global Shuram excursion which, therefore, took place during a reverse polarity chron. Comparison with other coeval sequences that recorded this excursion shows consistency in the polarity patterns. Isotopic correlation also provides a minimum depositional age constraint of ca. 570 Ma for the Avellaneda Formation. At present only few continuous magnetostratigraphic sequences can be considered to constrain the geomagnetic field behavior during the Ediacaran. Our new results contribute to such ambitious goal.

## **CHAPTER VI**

## 6. Conclusion and perspectives

This chapter presents the main contributions arising from this Thesis, whose main goal is to contribute for a better understanding of the Ediacaran Period (635 to 539 Ma), a pivotal period in Earth history. This interval began in the aftermath of extreme glaciations (Snowball Earth events) and witnessed the rise of complex macroscopic life amid several perturbations in the carbon cycle. These are recorded by pronounced carbon-isotope excursions (CIEs) in marine carbonate records, defined as negative and positive deviations in the stratigraphic trend of carbonate-carbon isotope ( $\delta^{13}\text{C}_{\text{carb}}$ ) profiles. These perturbations have been documented worldwide and are commonly used to establish regional to global stratigraphic correlations. At the same time, the paleogeographic configuration of the planet also changed dramatically due to the final dispersion of the Rodinia supercontinent and the formation of Gondwana. In addition, the Ediacaran could have experienced non-actualistic geomagnetic and/or geodynamic phenomena such as inertial interchange polar wander (IIPW) or an anomalously weak geomagnetic field. All these events appear to be connected and claim the attention of the scientific community.

In this context, the mid-Ediacaran Avellaneda Formation (580-560), deposited at the margin of a Gondwana paleocontinent still in construction, provides the opportunity to investigate some of the unusual events of the Ediacaran. The data obtained from the Avellaneda Formation provides new information on the depositional setting and paleogeography of that unit and the Rio de la Plata craton, refine their carbon and oxygen isotopes curves and demonstrate the potential for magnetostratigraphic correlations on the Ediacaran period.

Chapter 3 provides a detailed microfacies analyses, combining electron microscope observations, cathodoluminescence, elementary geochemistry and carbon-oxygen stable isotopes in the Avellaneda Formation. These tools refine the depositional setting by recognizing subtidal/intertidal and intertidal/supratidal environments. This study reports for the first time the presence of evaporite textures and sulfate minerals (gypsum-anhydrite) in the Avellaneda Formation. Despite the partial to full replacement of calcium by barium in sulfate minerals phases, evaporite textures and minerals are considered diagnostic of arid conditions prevailing during deposition. Furthermore, the carbon isotope profile reveals a transient positive to negative isotope excursion. Geochemical and oxygen isotopes evidence suggests the carbon isotopes excursion is primary in nature. Given the age of the Avellaneda

formation, and the extent of the isotopic shift, this excursion is interpreted as the expression of the Shuram negative carbon isotope excursion, the largest carbon isotope excursion ever recorded in Earth's history. Although not reaching extreme nadir values, the Shuram isotopic excursion reported in the Avellaneda Formation reinforces the hypotheses of an interplay between C, S, and Ba cycles with increased continental weathering and oxygenation of the Earth's surface during the SE.

Chapter 4 uses the sedimentary rocks of the Avellaneda formation and the upper unit, the Cerro Negro formation, to improve the apparent polar wander path (APWP) of the Río de la Plata craton (RPC), and better constrain reconstruct the paleogeography of the Gondwana paleocontinent. Both units provide well-defined magnetic directions at specimens and site level, defining a characteristic magnetization likely carried by magnetite and at some places also hematite. In both cases, new paleomagnetic poles were obtained: AV, 1.0° S, 313.4° E, A95: 5.9° for the Avellaneda formation and CN, 7.0° N, 314.4°E, A95: 9.5° for the Cerro Negro formation. The new poles contribute to define a more robust APWP for the RPC across the interval between 600 to 560 Ma. These results demonstrate a rapid drift of the RPC from low latitude positions at 600 Ma (~19°S for the Olavarría city) towards positions of moderately high paleolatitudes (between around 50° and 42°S) for the interval 580-560 Ma. Paleomagnetic data suggest a very large counterclockwise rotation with minor paleolatitudinal change for the RPC during 580 and 570 Ma. The new poles also provide a critical constraint from RPC, one of most important tectonic piece of Western Gondwana. Interestingly, unusually fast movements have been speculated in the Early to Late Ediacaran. Results reported here, although revealing a displacement of the RPC, are not consistent with an IITPW. The analysis of other coeval units from different West Gondwana blocks may provide a better assessment of this process.

In Chapter 5, a magnetostratigraphy for the Avellaneda Formation is presented. Magnetic stratigraphy is a powerful tool to perform reliable correlations of local and global sections, however, it is still underexploited in the Precambrian. For the Ediacaran, a high-resolution stratigraphic correlation is critical in the establishment of temporal links between the different phenomena occurring in this period. Several authors have proposed causal links between isotope excursions, climate, life evolution and changes in the paleogeography and the composition of oceans and atmosphere, but the lack of a robust time-frame hinders a more thorough test of these hypotheses. Here, the magnetostratigraphic correlation was coupled with a detailed sedimentary facies description and was anchored by carbon isotopes. Results

obtained in the Avellaneda formation demonstrate a consistent polarity pattern characterized by a major reverse interval separated by normal polarity zones. The presence of the Shuram carbon isotopes excursion allows the correlation of the results obtained here with magnetic stratigraphic results from other cratons, beyond the RPC. Indeed, magnetostratigraphy results and carbon isotopes reported in the Avellaneda Formation appear to be useful to extend the correlation with the coeval Ediacaran units of Wonoka Formation (Australia) and Johnny Formation (Death Valley, California, USA). Together, these data provide a magnetic stratigraphic framework for the onset, apex and decay of the Shuram excursion. In addition, the polarity pattern observed in the Avellaneda Formation also suggests that, at least, during 580-565 Ma the Earth's magnetic field was stable, with a reversal rate more akin to that observed in most of the Phanerozoic.

Several issues still remain unsolved concerning the Avellaneda formation and the processes reigning during the Ediacaran period. Below, I summarize some recommendations for future investigations and open-ended questions:

1) It is recommended that more sedimentological investigations, integrating chemical and biological information together with detailed microscope observations must be performed in the Avellaneda formation and coeval units. Further investigations centered in redox-sensitive geochemical proxies can be able to explore the seawater chemistry and biogeochemical cycles during apparently pulsed oxygenation events that accompanied the Shuram Excursion. In the case of Avellaneda, there is a great opportunity for studies in the well-preserved sulfate phases likely formed in the early diagenetic realm. Furthermore, Ba-proxies are able to show if the biological productivity at the time operated like the modern oxygenated oceans or in a different form, or yet and even more interestingly, if the Avellaneda Formation records the transition from the anoxic paleo-oceans to the oxygenated modern oceans.

2) Paleogeographic reconstructions of Gondwana in the Ediacaran times are problematic. The sparse data are ambiguous and give rise to a myriad of scenarios and models. Therefore, the acquisition of new key poles is important to solve some inconsistencies enabling the construction of APWP for several of the main cratonic blocks that formed that paleocontinent. Moreover, new data are essential to confront the actualistic versus non-actualistic hypotheses proposed for the Ediacaran, including the existence of inertial interchange true polar wander, equatorial dipole or a very weak geodynamo with permanent non-dipole configurations of the field.

3) Magnetic stratigraphy combined with stable carbon isotopes in the Avellaneda Formation provided tight constraints for the onset of the Shuram carbon excursion that can be used for global correlations. Obtaining paleomagnetic data across stratigraphic successions may be viewed as a necessary complimentary data to the key poles approach based on the paleomagnetism of magmatic units. Coupling magnetic data on the sedimentary record with isotopes and sedimentary facies data are key to disambiguate the different non-actualistic hypotheses proposed for the Ediacaran, enabling one to check for the synchronicity of movements predicted by IITPW events, the stability of the field and its relative strength through time. The magnetic and isotopic data can be complemented with cyclostratigraphy studies to refine the time-frame for the onset of the Shuram excursion, also providing a “chronometer” to estimate the duration of isotope excursions and polarity intervals in the whole Ediacaran period.

## REFERENCES

- Abrajevitch, A., Van der Voo, R., 2010. Incompatible Ediacaran paleomagnetic directions suggest an equatorial geomagnetic dipole hypothesis. *Earth and Planetary Science Letters*, 293, 164-170.
- Ader, M., Macouin, M., Trindade, R. I. F., Hadrien, M., Yang, Z. Y., Sun, Z. M., Besse, J., 2009. A multilayered water column in the Ediacaran Yangtze platform? Insights from carbonate and organic matter paired  $\delta^{13}\text{C}$ . *Earth and Planetary Science Letters*, 288, 213-227.
- Ader, M., Sansjofre, P., Halverson, G. P., Busigny, V., Trindade, R. I., Kunzmann, M., Nogueira, A. C., 2014. Ocean redox structure across the Late Neoproterozoic Oxygenation Event: a nitrogen isotope perspective. *Earth and Planetary Science Letters*, 396, 1-13.
- Algeo, T.J., Luo, G.M., Song, H.Y., Lyons, T.W., Canfield, D.E., 2015. Reconstruction of secular variation in seawater sulfate concentrations. *Biogeosciences*, 12(7), 2131-2151.
- Allan, J.R., and Matthews, R.K., 1982. Isotope signatures associated with early meteoric diagenesis. *Sedimentology*, 29(6), 797-817.
- Alsharhan, A.S., and Kendall, C.S.C., 2003. Holocene coastal carbonates and evaporites of the southern Arabian Gulf and their ancient analogues. *Earth-Science Reviews*, 61(3-4), 191-243.
- Amthor, J.E., Grotzinger, J.P., Schröder, S., Bowring, S.A., Ramezani, J., Martin, M.W., Matter, A., 2003. Extinction of *Cloudina* and *Namacalathus* at the Precambrian-Cambrian boundary in Oman. *Geology*, 31(5), pp.431-434.
- Antonio, P.Y.J., Trindade, R.I.F., Giacomini, B., Brandt, D., Tohver, E. 2021. New high-quality paleomagnetic data from the Borborema Province (NE Brazil): Refinement of the APW path of Gondwana in the Early Cambrian. *Precambrian Research*, 360, p.106243.
- Arrouy, M.J., 2015. *Sedimentología y estratigrafía de los depósitos ediacarano-paleozoicos suprayacentes a las calizas del Precámbrico del Sistema de Tandilia, Provincia de Buenos Aires, Argentina*. PhD Thesis. Facultad de Ciencias Naturales y Museo, Universidad Nacional de La Plata, pp. 285.
- Arrouy, M.J., Poiré, D., Gómez Peral, L.E., Canalicchio, J.M., 2015. *Sedimentología y estratigrafía del grupo La Providencia (nom. nov.): cubierta superior neoproterozoica, Sistema de Tandilia, Argentina*. *Latin American Journal of Sedimentology and Basin Analysis*, 22, 171–189.
- Arrouy, M.J., Warren, L. V., Quaglio, F., Poiré, D.G., Simões, M.G., Rosa, M.B., Peral, L.E.G., 2016. Ediacaran discs from South America: Probable soft-bodied macrofossils unlock the paleogeography of the Clymene Ocean. *Scientific Reports*, 6, 1–10.
- Arrouy, M.J., Gaucher, C., Poiré, D.G., Xiao, S., Gómez Peral, L., Warren, L.V., Bykova, N., Quaglio, F., 2019. A new record of late Ediacaran acritarchs from La Providencia group (Tandilia System, Argentina) and its biostratigraphical significance. *Journal of South American Earth Sciences*, 93, 283-293.
- Arrouy, M.J., Gómez-Peral, L.E., 2020. Exposing the inside of the fine-grained siliciclastic tidal shelf deposits of the Alicia Formation, Tandilia Basin, during the Ediacaran anoxia in the

Clymene Ocean, *Journal of South American Earth Sciences*, doi: <https://doi.org/10.1016/j.jsames.2020.102945>.

Arrouy, M.J., Gómez-Peral, L., Penzo, V., Ferreyra, C., Poiré, D.G., 2021. Fossil bubble structure related to microbial activity coeval with the middle Ediacaran Oceanic Oxygenation Event in the Tandilia System. *Latin American Journal of Sedimentology and Basin Analysis*, 28(2), 101-120.

Banner, J.L., and Hanson, G.N., 1990. Calculation of simultaneous isotopic and trace-element variations during water-rock interaction with applications to carbonate diagenesis. *Geochimica et Cosmochimica Acta* 54, 3123–3137.

Banner, J.L. 1995. Application of the trace element and isotope geochemistry of strontium to studies of carbonate diagenesis. *Sedimentology*, 42(5), 805-824.

Barrio, C.A., Poiré, D.G., Iñiguez Rodríguez, A.M., 1991. El contacto entre la Formación Loma Negra (Grupo Sierras Bayas) y la Formación Cerro Negro: un ejemplo de paleokarst, Olavarría, provincia de Buenos Aires. *Revista de la Asociación Geológica Argentina* 46, 69–76.

Bazhenov, M.L., Levashova, N.M., Meert, J.G., Golovanova, I.V., Danukalov, K.N., Fedorova, N.M., 2016. Late Ediacaran magnetostratigraphy of Baltica: evidence for magnetic field hyperactivity?. *Earth and Planetary Science Letters*, 435, pp.124-135.

Bengtson, S. 1992. Proterozoic and earliest Cambrian skeletal metazoans, in Schopf, J.W., and Klein, C., eds., *The Proterozoic Biosphere: A Multidisciplinary Study*: Cambridge, UK, Cambridge University Press, p. 1017–1033.

Bergmann, K.D., Al Balushi, S.A.K., Macley, T., Grotzinger, J.P., Eiler, J.M. 2018. A 600-million-year carbonate clumped-isotope record from the Sultanate of Oman. *Journal of Sedimentary Research*, v 88, 960–979.

Biggin, A.J., Steinberger, B., Aubert, J., Suttie, N., Holme, R., Torsvik, T.H., van der Meer, D.G., van Hinsbergen, D.J.J. 2012. Possible links between long-term geomagnetic variations and whole-mantle convection processes. *Nat. Geosci.* 5, 526–533.

Bishop, J. K. 1988. The barite-opal-organic carbon association in oceanic particulate matter. *Nature*, 332(6162), 341-343.

Bjerrum, C. J., and Canfield, D. E., 2011. Towards a quantitative understanding of the late Neoproterozoic carbon cycle. *Proceedings of the National Academy of Sciences*, 108(14), 5542-5547.

Blättler, C.L., Claire, M.W., Prave, A.R., Kirsimäe, K., Higgins, J.A., Medvedev, P.V., ... & Lepland, A. (2018). Two-billion-year-old evaporites capture Earth's great oxidation. *Science*, 360(6386), 320-323.

Blättler, C.L., Bergmann, K.D., Kah, L.C., Gómez-Pérez, I., Higgins, J.A., 2020. Constraints on Meso- to Neoproterozoic seawater from ancient evaporite deposits. *Earth and Planetary Science Letters*, 532, 115951.

Boag, T. H., Darroch, S. A., Laflamme, M., 2016. Ediacaran distributions in space and time: testing assemblage concepts of earliest macroscopic body fossils. *Paleobiology*, 42, 574-594.

Bono, R. K., Tarduno, J. A., Nimmo, F., Cottrell, R. D., 2019. Young inner core inferred from Ediacaran ultra-low geomagnetic field intensity. *Nature Geoscience*, 12, 143-147.

Borradaile, G.J., 1991. Correlation of strain with anisotropy of magnetic susceptibility (AMS). *Pure and applied geophysics*, 135(1), 15-29.

Borradaile, G.J., and Henry, B., 1997. Tectonic applications of magnetic susceptibility and its anisotropy. *Earth-Science Reviews*, 42(1-2), 49-93.

Borrello, A.V., 1966. Trazas, restos tubiformes y cuerpos fósiles problemáticos de la Formación La Tinta, Sierras Septentrionales de la Provincia de Buenos Aires. *Paleontografía Bonaerense*, Fasc. 5, Comisión de Investigaciones Científicas, Provincia de Buenos Aires 1-42.

Bosak, T., Bush, J.W.M., Flynn, M.R., Liang, B., Ono, S., Petroff, A.P., Sim, M.S., 2010. Formation and stability of oxygen-rich bubbles that shape photosynthetic mats. *Geobiology*, 8(1), 45-55.

Bose, P. K., Eriksson, P. G., Sarkar, S., Wright, D. T., Samanta, P., Mukhopadhyay, S., ... & Altermann, W., 2012. Sedimentation patterns during the Precambrian: A unique record?. *Marine and Petroleum Geology*, 33(1), 34-68.

Bottjer, D.J., Hagadorn, J.W., Dornbos, S.Q. 2000. The Cambrian substrate revolution. *GSA today*, 10(9), pp.1-7.

Bowyer, F., Wood, R. A., Poulton, S. W. 2017. Controls on the evolution of Ediacaran metazoan ecosystems: A redox perspective. *Geobiology* 15, 516–551.

Brand, U., and Veizer, J., 1980. Chemical diagenesis of a multicomponent carbonate system; 1, Trace elements. *Journal of Sedimentary Research*, 50(4), 1219-1236.

Bristow, T.F., and Grotzinger, J.P., 2013. Sulfate availability and the geological record of cold-seep deposits. *Geology*, 41(7), 811-814.

Budd, D.A., Hammes, U., Ward, W.B., 2000. Cathodoluminescence in calcite cements: new insights on Pb and Zn sensitizing, Mn activation, and Fe quenching at low trace-element concentrations. *J. Sed. Res.* 70, 217–226.

Calver, C.R. 2000. Isotope stratigraphy of the Ediacarian (Neoproterozoic III) of the Adelaide Rift Complex, Australia, and the overprint of water column stratification. *Precambrian Research*, 100, 121–150.

Canfield, D.E., Poulton, S.W., Narbonne, G.M., 2007. Late-Neoproterozoic deep-ocean oxygenation and the rise of animal life. *Science*, 315(5808), pp.92-95.

Canfield, D. E., Poulton, S. W., Knoll, A. H., Narbonne, G. M., Ross, G., Goldberg, T., Strauss, H., 2008. Ferruginous conditions dominated later Neoproterozoic deep-water chemistry. *Science*, 321, 949-952.

Canfield, D.E., and Farquhar, J., 2009. Animal evolution, bioturbation, and the sulfate concentration of the oceans. *Proceedings of the National Academy of Sciences*, 106(20), 8123-8127.

Canfield, D.E., Knoll, A.H., Poulton, S.W., Narbonne, G.M., Dunning, G.R. 2020. Carbon isotopes in clastic rocks and the Neoproterozoic carbon cycle. *American Journal of Science*, 320(2), pp.97-124.

Chadima, M., and Hrouda, F., 2006. Remasoft 3.0 a user-friendly paleomagnetic data browser and analyzer. *Trav. Geophys.*, 27, 20–21.

Cheng, M., Wang, H., Li, C., Luo, G., Huang, J., She, Z., ... and Algeo, T. J., 2022. Barite in the Ediacaran Doushantuo Formation and its implications for marine carbon cycling during the largest negative carbon isotope excursion in Earth's history. *Precambrian Research*, 368, 106485.

Cingolani, C.A., Hartmann L.A., Santos J.O.S., McNaughton N.J., 2002. U–Pb SHRIMP dating of zircons from the Buenos Aires complex of the Tandilia belt, Río de La Plata cratón, Argentina. *Proc 15 Congreso Geológico Argentino (El Calafate, Santa Cruz)*. Actas 1:149–154.

Cingolani, C., 2011. The Tandilia System of Argentina as a southern extension of the Río de la Plata craton: an overview. *Int. J. Earth Sci.* 100, 221–242.

Claes, H., Miranda, T., Falcão, T. C., Soete, J., Mohammadi, Z., Zieger, L., Erthal, M. M., Aguillar, J., Schmatz, J., Busch, A., Swennen, R., 2021. Model for calcite spherulite formation in organic, clay-rich, lacustrine carbonate shales (Barbalha Formation, Aptian, Araripe Basin, NE Brazil). *Marine and Petroleum Geology*, 128, 104988.

Cohen, P.A., Schopf, J.W., Butterfield, N.J., Kudryavtsev, A.B., Macdonald, F.A. 2011. Phosphate biomineralization in mid-Neoproterozoic protists. *Geology*, 39(6), pp.539-542.

Collins, A. S., Pisarevsky, S. A., 2005. Amalgamating eastern Gondwana: the evolution of the Circum-Indian Orogens. *Earth-Science Reviews*, 71, 229-270.

Collinson J.D., and Thompson, D.B., 1982. *Sedimentary Structures*. Georae Allen & Unwi" Pobl. Ltd., Iondo.

Condon, D., Zhu, M., Bowring, S., Wang, W., Yang, A., Jin, Y. 2005. U-Pb ages from the Neoproterozoic Doushantuo Formation, China. *Science*, 308 (5718), pp.95-98.

Cordani, U.G., Pimentel, M.M., Araújo, C.E.G. de, Fuck, R.A., 2013. The significance of the Transbrasiliano-Kandi tectonic corridor for the amalgamation of West Gondwana. *Brazilian Journal of Geology*, 43, 583–597.

Cordani, U.G., Fairchild, T.R., Ganade, C.E., Babinski, M., Leme, J.D.M. 2020. Dawn of metazoans: to what extent was this influenced by the onset of “modern-type plate tectonics”?. *Brazilian Journal of Geology*, 50.

Corsetti, F.A. and Kaufman, A.J., 2003. Stratigraphic investigations of carbon isotope anomalies and Neoproterozoic ice ages in Death Valley, California. *Geological Society of America Bulletin*, 115, 916–932.

Cracknell, K., García-Bellido, D. C., Gehling, J. G., Ankor, M. J., Darroch, S. A., Rahman, I. A., 2021. Pentaradial eukaryote suggests expansion of suspension feeding in White Sea-aged Ediacaran communities. *Scientific reports*, 11, 1-9.

Cui, H., Kaufman, A.J., Xiao, S., Zhou, C. and Liu, X.-M. 2017. Was the Ediacaran Shuram Excursion a globally synchronized early diagenetic event? Insights from methane-derived authigenic carbonates in the uppermost Doushantuo Formation, South China. *Chemical Geology*, 450, 59–80.

Cui, H., Kaufman, A.J., Peng, Y., Liu, X.M., Plummer, R.E., Lee, E.I. 2018. The Neoproterozoic Hüttenberg  $\delta^{13}\text{C}$  anomaly: genesis and global implications. *Precambrian Research*, 313, pp.242-262.

Cui, H., Kaufman, A.J., Xiao, S., Zhou, C., Zhu, M., Cao, M., ..., Guan, C., 2022. Dynamic interplay of biogeochemical C, S and Ba cycles in response to the Shuram oxygenation event. *Journal of the Geological Society*, 179(2).

D'Agrella Filho, M.S. y Pacca, I.G., 1988. Palaeomagnetism of the Itajai, Castro and Bom Jardim groups from southern Brazil. *Geophysical Journal International*, 2, 365–376.

D'Agrella Filho, M.S., Trindade, R.I.F., Queiroz, M.V.B., Meira, V.T., Janikian, L., Ruiz, A.S., Bispo-Santos, F., 2016. Reassessment of Aguapeí (Salto do Céu) paleomagnetic pole, Amazonian Craton and implications for Proterozoic supercontinents. *Precambrian Research*, 272, 1–17.

Darroch, S.A., Smith, E.F., Laflamme, M., Erwin, D.H., 2018. Ediacaran extinction and Cambrian explosion. *Trends in ecology & evolution*, 33(9), 653-663.

De Putter, T., Rouchy, J.-M., Herbosch, A., Keppens, E., Pierre, C., & Groessens, E., 1994. Sedimentology and palaeo-environment of the Upper Visean anhydrite of the Franco—Belgian Carboniferous basin (Saint-Ghislain borehole, southern Belgium). *Sedimentary Geology*, 90(1-2), 77–93.

Derry, L.A., Kaufman, A.J., Jacobsen, S.B., 1992. Sedimentary cycling and environmental change in the Late Proterozoic: evidence from stable and radiogenic isotopes. *Geochimica et Cosmochimica Acta*, 56(3), 1317-1329.

Derry, L.A. 2010. A burial diagenesis origin for the Ediacaran Shuram–Wonoka carbon isotope anomaly. *Earth and Planetary Science Letters*, 294(1-2), pp.152-162.

Derry, L.A., 2010. On the significance of  $\delta^{13}\text{C}$  correlations in ancient sediments. *Earth and Planetary Science Letters*, 296(3-4), 497-501.

Dickson, J.A.D., 1966. Carbonate identification and genesis as revealed by staining. *Journal Sedimentary Petrology*, 36, 491-505.

Driscoll, P. E., 2016. Simulating 2 Ga of geodynamo history. *Geophysical Research Letters*, 43, 5680-5687.

Droser, M. L., and Gehling, J.G. 2015. The advent of animals: the view from the Ediacaran. *Proceedings of the National Academy of Sciences*, 112(16), 4865-4870.

Droser, M.L., Tarhan, L.G., Gehling, J.G. 2017. The rise of animals in a changing environment: global ecological innovation in the late Ediacaran. *Annual Review of Earth and Planetary Sciences*, 45, 593-617.

Duda, J. P., Van Kranendonk, M. J., Thiel, V., Ionescu, D., Strauss, H., Schäfer, N., & Reitner, J., 2016. A rare glimpse of Paleoproterozoic life: Geobiology of an exceptionally preserved microbial mat facies from the 3.4 Ga Strelley Pool Formation, Western Australia. *PLoS One*, 11(1), e0147629.

Egli, R., Chen, A. P., Winklhofer, M., Kodama, K. P., Horng, C. S., 2010. Detection of noninteracting single domain particles using first-order reversal curve diagrams. *Geochemistry, Geophysics, Geosystems*, 11.

Erwin, D.H., Laflamme, M., Tweedt, S.M., Sperling, E.A., Pisani, D., Peterson, K.J. 2011. The Cambrian conundrum: early divergence and later ecological success in the early history of animals. *science*, 334(6059), pp.1091-1097.

Etienne, J.L., Allen, P.A., Rieu, R., Le Guerroué, E., Hambrey, M.J. 2007. Neoproterozoic glaciated basins: a critical review of the Snowball Earth hypothesis by comparison with Phanerozoic glaciations. *Special publication-IAS*, 39, p.343.

Evans, D.A.D., 2003. True polar wander and supercontinents. *Tectonophysics*, 362, 303–320.

Evans, D.A.D. and Raub, T.D. 2011. Neoproterozoic glacial palaeolatitudes: A global update. *Geological Society, London, Memoirs*, 36(1), pp.93-112.

Fairchild, I.J. and Kennedy, M.J. 2007. Neoproterozoic glaciation in the Earth System. *Journal of the Geological Society*, 164(5), pp.895-921.

Ferré, E.C., 2002. Theoretical models of intermediate and inverse AMS fabrics. *Geophysical Research Letters*, 29, 31-1.

Fike, D.A., Grotzinger, J.P., Pratt, L.M., Summons, R.E. 2006. Oxidation of the Ediacaran Ocean. *nature*, 444(7120), pp.744-747.

Flügel, E., 2010. *Microfacies of Carbonate Rocks. Analysis, Interpretation and Application*.

Fölling, P.G., & Frimmel, H.E., 2002. Chemostratigraphic correlation of carbonate successions in the Gariiep and Saldania Belts, Namibia and South Africa. *Basin Research*, 14(1), 69-88.

Font, E., Rapalini, A.E., Tomezzoli, R.N., Trindade, R.I.F., Tohver, E., 2012. Episodic remagnetizations related to tectonic events and their consequences for the South America Polar Wander Path. *Geological Society, London, Special Publications*, 371(1), 55-87.

Forjanés, P., Astilleros, J. M., Fernández-Díaz, L. 2020. The formation of barite and celestite through the replacement of gypsum. *Minerals*, 10(2), 189.

Franceschinis, P. R., Rapalini, A. E., Bettucci, L. S., Dopico, C. M., Milanese, F. N., 2019. Paleomagnetic confirmation of the “unorthodox” configuration of Atlantica between 2.1 and 2.0 Ga. *Precambrian Research*, 334, 105447.

Franks, J., and Stolz, J. F., 2009. Flat laminated microbial mat communities. *Earth-Science Reviews*, 96(3), 163-172.

Gallet, Y., Pavlov, V., Courtillot, V. 2003. Magnetic reversal frequency and apparent polar wander of the Siberian platform in the earliest Palaeozoic, inferred from the Khorbusuonka river section (northeastern Siberia). *Geophysical Journal International*, 154, p. 829-840.

Gallet, Y., and Pavlov, V. 2016. Three distinct reversing modes in the geodynamo. *Izvestiya Phys. Solid Earth* 52, 291–296.

Gallet, Y., Pavlov, V., Korovnikov, I. 2019. Extreme geomagnetic reversal frequency during the Middle Cambrian as revealed by the magnetostratigraphy of the Khorbusuonka section (northeastern Siberia). *Earth Planet. Sci. Lett.* 528.

Garcia, M.S.R., Trindade, R.I.F., D'Agrella-Filho, M.S.D., Pinho, F.E.C., Paulo, S., 2013. Paleomagnetismo do complexo alcalino Planalto da Serra (Mato Grosso): Implicações para a Formação do Gondwana. *Latinmag Letters*, 3, 1–8.

Garret, P., 1970. Phanerozoic stromatolites: noncompetitive ecologic restriction by grazing and burrowing animals. *Science*, 169: 171–173.

Gaucher, C., Sial, A.N., Poiré, D., Gómez-Peral, L., Ferreira, V.P., Pimentel, M.M., 2009. Chemostratigraphy. Neoproterozoic–Cambrian evolution of the Río de la Plata Palaeocontinent. In: Gaucher, C., Sial, A.N., Halverson, G.P., Frimmel, H.E. (Eds.), *Neoproterozoic-Cambrian tectonics, global change and evolution: a focus on southwestern Gondwana*. *Developments in Precambrian Geology*. Elsevier, pp. 115–122.

Gómez-Peral, L.E., Poiré, D.G., Strauss, H., Zimmermann, U., 2007. Chemostratigraphy and diagenetic constraints on Neoproterozoic carbonate successions from the Sierras Bayas Group, Tandilia System, Argentina. *Chem. Geol.* 237, 127–146.

Gómez-Peral, L.E., Kaufman, A.J., Poiré, D.G., 2014. Paleoenvironmental implications of two phosphogenic events in Neoproterozoic sedimentary successions of the Tandilia System, Argentina. *Precamb. Res.* 252, 88–106.

Gómez-Peral, L.E., Sial, A.N., Arrouy, M.J., Richiano, S., Ferreira, V.P., Kaufman, A.J., Poiré, D.G., 2017. Paleo-climatic and paleo-environmental evolution of the Neoproterozoic basal sedimentary cover on the Río de La Plata Craton, Argentina: insights from the  $\delta^{13}\text{C}$  chemostratigraphy. *Sediment. Geol.* 353, 139–157.

Gómez-Peral, L.E., Kaufman, A.J., Julia, M., Richiano, S., Sial, A.N., Poiré, D.G., Ferreira, V.P., 2018. Preglacial palaeoenvironmental evolution of the Ediacaran Loma Negra Formation, far southwestern Gondwana, Argentina. *Precambrian Research*, 315, 120–137.

Gómez-Peral, L.E., Arrouy, M.J., Poiré, D.G., & Cavarozzi, C.E., 2019. Redox-sensitive trace element distribution in the Loma Negra Formation in Argentina: The record of an Ediacaran oxygenation event. *Precambrian Research*, 332, 105384.

Gomes, J.P., Bunevich, R.B., Tedeschi, L.R., Tucker, M.E., Whitaker, F.F., 2020. Facies classification and patterns of lacustrine carbonate deposition of the Barra Velha Formation, Santos Basin, Brazilian Pre-Salt. *Marine and Petroleum Geology*, 113, 104176.

Gómez-Peral, L.E., Arrouy, M.J., Richiano, S., Cereceda, A., Alé, S.A., Poiré, D.G., 2021. Unravelling hidden glacial effects in the Cryogenian marine depositional settings of the Tandilia Basin, Argentina. *Precambrian Research*, (361), 106261.

Gong, Z., Kodama, K.P., and Li, Y.X., 2017. Rock magnetic cyclostratigraphy of the Doushantuo Formation, South China and its implications for the duration of the Shuram carbon isotope excursion. *Precambrian Research*, 289, 62–74.

Gong, Z., Kodama, K.P., Li, Y.X. 2019. Paleomagnetism and rock magnetic cyclostratigraphy of the Ediacaran Doushantuo Formation, South China: Constraints on the remagnetization mechanism and the encoding process of Milankovitch cycles. *Palaeogeography, Palaeoclimatology, Palaeoecology*, 528, 232–246.

Gong, Z. and Li, M. 2020. Astrochronology of the Ediacaran Shuram carbon isotope excursion, Oman. *Earth and Planetary Science Letters*, 547, p.116462.

Gonzalez-Muñoz, M.T., Martinez-Ruiz, F., Morcillo, F., Martin-Ramos, J. D., Paytan, A., 2012. Precipitation of barite by marine bacteria: A possible mechanism for marine barite formation. *Geology*, 40(8), 675-678.

Gostin, V.A., McKirdy, D.M., Webster, L.J., Williams, G.E. 2010. Ediacaran ice-rafting and coeval asteroid impact, South Australia: insights into the terminal Proterozoic environment. *Australian Journal of Earth Sciences*, 57(7), pp.859-869.

Götze, J., 2012. Application of Cathodoluminescence Microscopy and Spectroscopy in Geosciences. *Microscopy and microanalysis: the official journal of Microscopy Society of America, Microbeam Analysis Society, Microscopical Society of Canada*. 18. 1-15.

Gradstein, F.M., Ogg, J.G., and Smith, A.G., Bleeker, W., Lourens, L. 2004. A new geologic time scale with special reference to Precambrian and Neogene. *Episodes*, 27(2), p. 83-100.

Griffith, E. M., & Paytan, A., 2012. Barite in the ocean—occurrence, geochemistry and palaeoceanographic applications. *Sedimentology*, 59(6), 1817-1835.

Grotzinger, J.P., and Kasting, J.F., 1993. New constraints on Precambrian ocean composition. *The Journal of Geology*, 101(2), 235-243.

Grotzinger, J.P., and Knoll, A.H., 1999. Stromatolites in Precambrian carbonates: Evolutionary Mileposts or Environmental Dipsticks? *Annual Review of Earth and Planetary Sciences* 1999 27:1, 313-358.

Grotzinger, J.P., Watters, W.A., and Knoll, A.H., 2000. Calcified metazoans in thrombolite-stromatolite reefs of the terminal Proterozoic Nama Group, Namibia. *Paleobiology*, 26(3), 334-359.

Grotzinger, J.P., Fike, D.A., Fischer, W.W. 2011. Enigmatic origin of the largest-known carbon isotope excursion in Earth's history. *Nature Geoscience*, 4(5), 285-292.

Györi, O., Haas, J., Hips, K., Lukoczki, G., Budai, T., Demény, A., & Szócs, E., 2020. Dolomitization of shallow-water, mixed siliclastic-carbonate sequences: The Lower Triassic ramp succession of the Transdanubian Range, Hungary. *Sedimentary Geology*, 395, 105549.

Hagadorn, J. W., & Bottjer, D. J. 1997. Wrinkle structures: Microbially mediated sedimentary structures common in subtidal siliciclastic settings at the Proterozoic-Phanerozoic transition. *Geology*, 25(11), 1047-1050.

Halverson, G.P., Hoffman, P.F., Schrag, D.P., Maloof, A.C., Rice, A.H.N., 2005. Toward a Neoproterozoic composite carbon-isotope record. *Geological Society of America Bulletin*, 117(9-10), 1181-1207.

Halverson, G.P., Wade, B.P., Hurtgen, M.T., Barovich, K.M. 2010. Neoproterozoic chemostratigraphy. *Precambrian Research*, 182(4), pp.337-350.

Hamilton, W.B., 2011. Plate tectonics began in Neoproterozoic time, and plumes from deep mantle have never operated. *Lithos*, 123(1-4), pp.1-20.

Hardie, L.A., 2003. Anhydrite and gypsum. In: Middleton, G.V., Church, M.J., Coniglio, M., Hardie, L.A. and Longstaffe, F.J. (eds). *Encyclopedia of Sediments and Sedimentary Rocks*. Springer Netherlands, Dordrecht, 16–19.

Hartmann, L.A., Santos J.O.S., Cingolani C.A., McNaughton N.J., 2002. Two Paleoproterozoic Orogenies in the Evolution of the Tandilia Belt, Buenos Aires, as evidenced by zircon U-Pb SHRIMP geochronology. *Int Geology Rev* 44:528–543. doi:10.2747/0020-6814.44.6.528.

Hebert, C.L., Kaufman, A.J., Penniston-Dorland, S.C., Martin, A.J. 2010. Radiometric and stratigraphic constraints on terminal Ediacaran (postGaskiers) glaciation and metazoan evolution. *Precambrian Research*, 182(4), pp.402-412.

Hernández, M., Arrouy, M. J., Scivetti, N., Franzese, J. R., Canalicchio, J. M., Poiré, D. G., 2017. Tectonic evolution of the Neoproterozoic Tandilia sedimentary cover, Argentina: New evidence of contraction and extensional events in the southwest Gondwana margin. *Journal of South American Earth Sciences*, 79, 230-238.

Heydari, E., and Wade, W.J. 2002. Massive recrystallization of low-Mg calcite at high temperatures in hydrocarbon source rocks: Implications for organic acids as factors in diagenesis. *AAPG bulletin*, 86(7), 1285-1303.

Hiatt, E.E., and Pufahl, P.K., 2014. Cathodoluminescence petrography of carbonate rocks: a review of applications for understanding diagenesis, reservoir quality and pore system evolution. *Mineralogical Association of Canada, Short Course 45 pp.* 75–96.

Hodych, J.P., Buchan, K.L., 1994. Early Silurian palaeolatitude of the Springdale Group redbeds of central Newfoundland: a palaeomagnetic determination with a remanence anisotropy test for inclination error. *Geophysical Journal International*, 117, 640–652.

Hoffman, P.F., Kaufman, A.J., Halverson, G.P., Schrag, D.P. 1998. A Neoproterozoic snowball earth. *science*, 281(5381), pp.1342-1346.

Hoffman, P.F. and Schrag, D.P. 2002. The snowball Earth hypothesis: testing the limits of global change. *Terra nova*, 14(3), pp.129-155.

Hoffman, P.F., Halverson, G.P., Domack, E.W., Husson, J.M., Higgins, J.A., Schrag, D.P. 2007. Are basal Ediacaran (635 Ma) post-glacial “cap dolostones” diachronous? *Earth and Planetary Science Letters*, 258(1-2), pp.114-131.

Hoffman, P.F., and Li, Z.X. 2009. A palaeogeographic context for Neoproterozoic glaciation. *Palaeogeography, Palaeoclimatology, Palaeoecology*, 277(3-4), 158-172.

Homann, M., Heubeck, C., Airo, A., Tice, M.M., 2015. Morphological adaptations of 3.22 Ga-old tufted microbial mats to Archean coastal habitats (Moodies Group, Barberton Greenstone Belt, South Africa). *Precambrian Research*, 266, 47-64.

Hounslow, M.W., 2001. The crystallographic fabric and texture of siderite in concretions: implications for siderite nucleation and growth processes. *Sedimentology*, 48(3), 533-557.

Hrouda, F., 1982. Magnetic anisotropy of rocks and its application in geology and geophysics. *Geophysical Surveys*, 5, 37-82.

Husson, J.M., Maloof, A.C., Schoene, B., Chen, C.Y. and Higgins, J.A., 2015. Stratigraphic expression of Earth’s deepest  $\delta^{13}\text{C}$  excursion in the Wonoka Formation of South Australia. *American Journal of Science*, 315, 1–45.

Iñiguez, R.A.M. y P.E. Zalba, 1974. Nuevo nivel de arcilitas en la zona de Cerro Negro, Partido de Olavarría, Provincia de Buenos Aires. *Anales del LEMIT, Serie 2*: 95-100.

Iñiguez R.A.M., 1999. La Cobertura Sedimentaria de Tandilia. In: Caminos R. (Ed), Geología Argentina. (SEGEMAR). pp 101–106.

Jackson, M., and Swanson-Hysell, N.L., 2012. Rock magnetism of remagnetized carbonate rocks: Another look. Geological Society, London, Special Publications, 371(1), 229-251.

Jacobsen, S. B., and Kaufman, A. J., 1999. The Sr, C and O isotopic evolution of Neoproterozoic seawater. Chemical Geology, 161(1-3), 37-57.

Jahnert, R.J., and Collins, L. B. 2012. Characteristics, distribution and morphogenesis of subtidal microbial systems in Shark Bay, Australia. Mar. Geol., 303–306, 115–136.

James, N., and Jones, B., 2015. Origin of carbonate sedimentary rocks (1st ed). John Wiley and Sons.

Jelinek, V., 1981. Characterization of the magnetic fabric of rocks. Tectonophysics, 79, 63–67.

Jewell, P.W., and Stallard, R.F., 1991). Geochemistry and paleoceanographic setting of central Nevada bedded barites. The Journal of Geology, 99(2), 151-170.

Jiang, G., Sohl, L.E. and Christie-Blick, N. 2003b. Neoproterozoic stratigraphic comparison of the Lesser Himalaya (India) and Yangtze block (south China): paleogeographic implications. Geology, 31, 917–920.

Kah, L.C., Lyons, T.W. Chesley, J.T. 2001. Geochemistry of a 1.2 Ga carbonate-evaporite succession, northern Baffin and Bylot Islands: implications for Mesoproterozoic marine evolution. Precambrian Research, 111, 203–234,

Kah, L.C., Lyons, T.W., Frank, T.D., 2004. Low marine sulphate and protracted oxygenation of the Proterozoic biosphere. Nature, 431(7010), 834-838.

Kasting, J.F., Howard, M.T., Wallmann, K., Veizer, J., Shields, G., Jaffrés, J., 2006. Paleoclimates, ocean depth, and the oxygen isotopic composition of seawater. Earth and Planetary Science Letters, 252(1-2), 82-93.

Kaufman, A.J. and Knoll, A.H. 1995. Neoproterozoic variations in the C-isotopic composition of seawater: stratigraphic and biogeochemical implications. Precambrian research, 73(1-4), pp.27-49.

Kaufman, A.J., and Knoll, A.H., 1995. Neoproterozoic variations in the C-isotopic composition of seawater: stratigraphic and biogeochemical implications. Precambrian research, 73(1-4), 27-49.

Kaufman, A.J., Corsetti, F.A. and Varni, M.A., 2007. The effect of rising atmospheric oxygen on carbon and sulfur isotope anomalies in the Neoproterozoic Johnnie Formation, Death Valley, USA. Chemical Geology, 237, 47–63.

Kendal, J.K., 1985. On the significance of evaporite lamination, in Schreiber, B.C., ed., Proc. of 6th Int'l Symp. on Salt: Salt Inst., Alexandria, Va., v. 1, p. 161-170.

Kendall, A.C., 2010, Marine evaporites, in James, N. P., and Dalrymple, R. W., eds., Facies Models 4: GEOtext 6, Geological Association of Canada pp 505–540.

King, R.F., 1955. The remanent magnetism of artificially deposited sediments. Geophysical Supplements to the Monthly Notices of the Royal Astronomical Society, 7, 115–134.

- Kinsman, D.J. 1969. Modes of formation, sedimentary associations, and diagnostic features of shallow-water and supratidal evaporites. *AAPG Bulletin*, 53(4), 830-840.
- Kirkham, A., 1997. Shoreline evolution, aeolian deflation and anhydrite distribution of the Holocene, Abu Dhabi. *GeoArabia*, 2(4), 403-416.
- Kirschvink, J., 1980. The least-squares line and plane and the analysis of paleomagnetic data. *Geophysical Journal of the Royal Astronomical Society*, 62, 699–718.
- Kirschvink, J.L., 1992. Late Proterozoic low-latitude global glaciation: the snowball Earth.
- Knauth, L.P., and Kennedy, M.J., 2009. The late Precambrian greening of the Earth. *Nature* 460, 728–732.
- Knoll, A.H. 2000: Learning to tell Neoproterozoic time. *Precambrian Research* 100, 3-20.
- Knoll, A., Walter, M., Narbonne, G., Christie-Blick, Nicholas. 2006. The Ediacaran Period: a new addition to the geologic time scale. *Lethaia*, 39(1), pp.13-30.
- Kodama, K.P., 2012. Paleomagnetism of sedimentary rocks: Process and interpretation. Willey-Blackwell, Chichester, pp 164.
- Kopp, R. E., Kirschvink, J. L., 2008. The identification and biogeochemical interpretation of fossil magnetotactic bacteria. *Earth-Science Reviews*, 86, 42-61.
- Koymans, M.R., Langereis, C.G., Pastor-Galan, D., and van Hinsbergen, D.J.J., 2016. Paleomagnetism.org: An online multi-platform open source environment for paleomagnetic data analysis. *Computers and Geosciences*, 93, 127–137.
- Lakhdar, R., Soussi, M., Talbi, R. 2020. Modern and Holocene microbial mats and associated microbially induced sedimentary structures (MISS) on the southeastern coast of Tunisia (Mediterranean Sea). *Quaternary Research*, 100, 77–97.
- Le Guerroué, E., Allen, P.A., Cozzi, A. 2006. Chemostratigraphic and sedimentological framework of the largest negative carbon isotopic excursion in Earth history: The Neoproterozoic Shuram Formation (Nafun Group, Oman). *Precambrian Research*, 146(1-2), pp.68-92.
- Le Guerroué, E., Allen, P.A., Cozzi, A., Etienne, J.L., Fanning, M. 2006. 50 Myr recovery from the largest negative  $\delta^{13}\text{C}$  excursion in the Ediacaran Ocean. *Terra Nova*, 18(2), pp.147-153.
- Leanza, C.A., and Hugo, C.A., 1987. Descubrimiento de fosforitas sedimentarias en el Proterozoico Superior de Tandilia, Buenos Aires, Argentina. *Revista de la Asociación Geológica Argentina* 42 (3–4), 417–428.
- Levashova, N.M., Golovanova, I.V., Rudko, D.V., Danukalov, K.N., Rudko, S.V., Salmanova, R.Y., Meert, J.G. 2021. Late Ediacaran magnetic field hyperactivity: Quantifying the reversal frequency in the Zigan Formation, Southern Urals, Russia. *Gondwana Research*, 94, pp.133-142.
- Li, Z.X., Bogdanova, S., Collins, A.S., Davidson, A., De Waele, B., Ernst, R. E., ... and Vernikovsky, V., 2008. Assembly, configuration, and break-up history of Rodinia: a synthesis. *Precambrian research*, 160(1-2), 179-210.
- Li, C., Love, G.D., Lyons, T.W., Fike, D.A., Sessions, A.L., Chu, X., 2010. A stratified redox model for the Ediacaran ocean. *Science*, 328(5974), 80-83.

Li, Z. X., Evans, D. A., Halverson, G. P., 2013. Neoproterozoic glaciations in a revised global palaeogeography from the breakup of Rodinia to the assembly of Gondwanaland. *Sedimentary Geology*, 294, 219-232.

Li, Z., Cao, M., Loyd, S. J., Algeo, T. J., Zhao, H., Wang, X., Zhao, L., Chen, Z. Q., 2020. Transient and stepwise ocean oxygenation during the late Ediacaran Shuram Excursion: Insights from carbonate  $\delta^{238}\text{U}$  of northwestern Mexico. *Precambrian Research*, 344, 105741.

Lindholm, R.C., 1987. *A practical Approach to Sedimentology*. Allen and Unwin, London, p. 276

Liu, P., Xiao, S., Yin, C., Chen, S., Zhou, C., Li, M., 2014. Ediacaran acanthomorphic acritarchs and other microfossils from chert nodules of the upper doushantuo Formation in the yangtze gorges area, south China. *J. Paleontol.* 88 (72), 1–139.

Liu, Y., Chen, W., Foley, S.F., Shen, Y.A., Chen, C., Li, J., ... & Lin, J., 2021. The largest negative carbon isotope excursions in Neoproterozoic carbonates caused by recycled carbonatite volcanic ash. *Science Bulletin*, 66(18), 1925-1931.

Lluehliier, F., Hulot, G., Gallet, Y., Schweiger, T. 2019. Impact of inner-core size on the dipole behavior of numerical dynamo simulation. *Geophys. J. Int.* 218, 179–189.

Lokier, S.W., 2013. Coastal sabkha preservation in the Arabian Gulf. *Geoheritage*, 5(1), 11-22.

Loyd, S.J., Marenco, P.J., Hagadorn, J.W., Lyons, T.W., Kaufman, A.J., Sour-Tovar, F., Corsetti, F.A., 2012. Sustained low marine sulfate concentrations from the Neoproterozoic to the Cambrian: Insights from carbonates of northwestern Mexico and eastern California. *Earth and Planetary Science Letters*, 339, 79-94.

Loyd, S.J., Marenco, P.J., Hagadorn, J.W., Lyons, T.W., Kaufman, A.J., Sour-Tovar, F., Corsetti, F.A. 2013. Local  $\delta^{34}\text{S}$  variability in ~ 580 Ma carbonates of northwestern Mexico and the Neoproterozoic marine sulfate reservoir. *Precambrian Research*, 224, 551-569.

Lyons, T. W., Reinhard, C. T., Planavsky, N. J., 2014. The rise of oxygen in Earth's early ocean and atmosphere. *Nature*, 506, 307-315.

Macdonald, F. A., Strauss, J. V., Sperling, E. A., Halverson, G. P., Narbonne, G. M., Johnston, D. T., Kunzmann, M., Schrag, D.P., Higgins, J. A., 2013. The stratigraphic relationship between the Shuram carbon isotope excursion, the oxygenation of Neoproterozoic oceans, and the first appearance of the Ediacara biota and bilaterian trace fossils in northwestern Canada. *Chemical Geology*, 362, 250-272.

Maloof, A.C., Porter, S.M., Moore, J.L., Dudás, F.Ö., Bowring, S.A., Higgins, J.A., Fike, D.A., Eddy, M.P. 2010. The earliest Cambrian record of animals and ocean geochemical change. *Bulletin*, 122(11-12), pp.1731-1774.

Marchese H.G., Di Paola, E., 1975. Reinterpretación estratigráfica de la Perforación Punta Mogotes N° 1, Provincia de Buenos Aires. *Revista de la Asociación Geológica Argentina*, 30, 17–44

Martín-Hernández, F., Hirt, A.M., 2004. A method for the separation of paramagnetic, ferrimagnetic and haematite magnetic subfabrics using high-field torque magnetometry. *Geophysical Journal International*, 157, 117–127.

Martinez-Ruiz, F., Paytan, A., Gonzalez-Muñoz, M.T., Jroundi, F., Abad, M. D. M., Lam, P.J., ... & Kastner, M., 2019. Barite formation in the ocean: Origin of amorphous and crystalline precipitates. *Chemical Geology*, 511, 441-451.

McElhinny, M. W., 1964. Statistical significance of the fold test in palaeomagnetism. *Geophysical Journal International*, 8, 338-340.

McFadden, P.L., and McElhinny, M.W., 1990. Classification of the reversal test in palaeomagnetism. *Geophysical Journal International*, 103, 725-729.

McFadden, K.A., Huang, J., Chu, X., Jiang, G., Kaufman, A.J., Zhou, C., Yuan, X., Xiao, S. 2008. Pulsed oxidation and biological evolution in the Ediacaran Doushantuo Formation. *Proceedings of the National Academy of Sciences*, 105(9), pp.3197-3202.

McIlroy, D. and Logan, G.A. 1999. The impact of bioturbation on infaunal ecology and evolution during the Proterozoic-Cambrian transition. *Palaios*, 14(1), pp.58-72.

McMahon, S., Matthews, J.J., Brasier, A., Still, J. 2021. Late Ediacaran life on land: desiccated microbial mats and large biofilm streamers. *Proceedings of the Royal Society B*, 288(1962), 20211875.

Meert, J.G., Van der Voo, R., 1996. Study of the Sinyai Dolerite, Kenya: Implications for Gondwana Assembly. *The Journal of Geology*, 104, 131–142.

Meert, J.G., 2014. Strange attractors, spiritual interlopers and lonely wanderers: The search for pre-Pangean supercontinents. *Geoscience Frontiers*, 5, 155–166.

Meert J.G., Levashova N.M., Bazhenov M.L., Landing E. 2016. Rapid changes of magnetic Field polarity in the late Ediacaran: Linking the Cambrian evolutionary radiation and increased UV-B radiation. *Gondwana Research*, 34:149-157.

Melezhik, V.A., Fallick, A.E., Rychanchik, D.V. and Kuznetsov, A.B. 2005. Palaeoproterozoic evaporites in Fennoscandia: implications for seawater sulphate, the rise of atmospheric oxygen and local amplification of the  $\delta^{13}\text{C}$  excursion. *Terra Nova*, 17, 141–148, <https://doi.org/10.1111/j.1365-3121.2005.00600.x>.

Melezhik, V.A., Pokrovsky, B.G., Fallick, A.E., Kuznetsov, A.B. and Bujakaite, M.I. 2009. Constraints on  $87\text{Sr}/86\text{Sr}$  of Late Ediacaran seawater: insight from Siberian high-Sr limestones. *Journal of the Geological Society, London*, 166, 183–191.

Melott, A.L., Pivarunas, A., Meert, J.G., Lieberman, B.S. 2018. Does the planetary dynamo go cycling on? Re-examining the evidence for cycles in magnetic reversal rate. *International Journal of Astrobiology*, 17(1), pp.44-50.

Melvin, J.L. (Ed.), 1991. *Evaporites, petroleum and mineral resources*. Elsevier.

Mercedes-Martín, R., Brasier, A.T., Rogerson, M., Reijmer, J.J., Vonhof, H., Pedley, M., 2017. A depositional model for spherulitic carbonates associated with alkaline, volcanic lakes. *Mar. Petrol. Geol.* 86, 168–191.

Mercedes-Martín, R., Ayora, C., Tritlla, J., Sánchez-Román, M., 2019. The hydrochemical evolution of alkaline volcanic lakes: A model to understand the South Atlantic Pre-Salt mineral assemblages. *EarthScience Reviews*, 198, 102938.

Mercedes-Martín, R., Rao, A., Rogerson, M., Sánchez-Roman, M., 2021. Effects of salinity, organic acids and alkalinity in the growth of calcite spherulites: implications for evaporitic lacustrine sedimentation. *The Depositional Record*. doi.org/10.1002/dep2.136.

Minguez, D., Kodama, K.P., Hillhouse, J.W. 2015. Paleomagnetic and cyclostratigraphic constraints on the synchronicity and duration of the Shuram carbon isotope excursion, Johnnie Formation, Death Valley Region, CA. *Precambrian Research*, 266, 395-408.

Minguez, D. and Kodama, K.P. 2017. Rock magnetic chronostratigraphy of the Shuram carbon isotope excursion: Wonoka Formation, Australia. *Geology*, 45(6), pp.567-570.

Mitchell, R. N., Kilian, T. M., Evans, D. A., 2012. Supercontinent cycles and the calculation of absolute palaeolongitude in deep time. *Nature*, 482, 208-211.

Mitchell, E.G., Bobkov, N., Bykova, N., Dhungana, A., Kolesnikov, A.V., Hogarth, I.R., ... & Grazhdankin, D.V., 2020. The influence of environmental setting on the community ecology of Ediacaran organisms. *Interface focus*, 10(4), 20190109.

Moloto-A-Kenguemba, G., Trindade, R.I.F., Monié, P., Nédélec, A., Siqueira, R., 2008. A late Neoproterozoic paleomagnetic pole for the Congo craton: Tectonic setting, paleomagnetism and geochronology of the Nola dike swarm (Central African Republic). *Precambrian Research*, 164, 214–226.

Morel, P., 1981. Palaeomagnetism of a Pan-African diorite: a Late Precambrian pole for western Africa. *Geophysical Journal of the Royal Astronomical Society*, 65, 493–503.

Moskowitz, B. M., Frankel, R. B., Bazylinski, D. A., 1993. Rock magnetic criteria for the detection of biogenic magnetite. *Earth and Planetary Science Letters*, 120, 283-300.

Mossman, DJ. and Brown, MJ., 1986. Stratiform barite in sabkha sediments, Walton-Cheverie, Nova Scotia, *Eon. Geol.*,81:2Q16-202.

Nabhan, S., Marin-Carbonne, J., Mason, P.R., & Heubeck, C., 2020. In situ S-isotope compositions of sulfate and sulfide from the 3.2 Ga Moodies Group, South Africa: A record of oxidative sulfur cycling. *Geobiology*, 18(4), 426-444.

Narbonne, G.M., Kaufman, A.J., Knoll, A.H., 1994. Integrated chemostratigraphy and biostratigraphy of the Windermere Supergroup, northwestern Canada: Implications for Neoproterozoic correlations and the early evolution of animals. *Geological Society of America Bulletin*, 106(10), 1281-1292.

Narbonne, G.M., Xiao, S., Shields, G.A., Gehling, J.G. 2012. The Ediacaran Period. *The geologic time scale*, 1, pp.413-435.

Noffke, N., Gerdes, G., Klenke, T., 2003. Benthic cyanobacteria and their influence on the sedimentary dynamics of peritidal depositional systems (siliciclastic, evaporitic salty, and evaporitic carbonatic). *Earth-Science Reviews*, 62(1-2), 163-176.

Noffke, N., Eriksson, K.A., Hazen, R. M., Simpson, E.L., 2006. A new window into Early Archean life: Microbial mats in Earth's oldest siliciclastic tidal deposits (3.2 Ga Moodies Group, South Africa). *Geology*, 34(4), 253-256.

Noffke, N., Christian, D., Wacey, D., Hazen, R.M., 2013. Microbially induced sedimentary structures recording an ancient ecosystem in the ca. 3.48-billion-year-old Dresser Formation, Pilbara, Western Australia. *Astrobiology*. (12):1103-24. doi: 10.1089/ast.2013.1030.

Och, L.M. and Shields-Zhou, G.A., 2012. The Neoproterozoic oxygenation event: Environmental perturbations and biogeochemical cycling. *EarthScience Reviews*, 110(1-4), pp.26-57.

Okubo, J., Muscente, A. D., Luvizotto, G. L., Uhlein, G. J., Warren, L. V., 2018. Phosphogenesis, aragonite fan formation and seafloor environments following the Marinoan glaciation. *Precambrian Research*, 311, 24-36.

Opdyke, N.D. and Channel, J.E.T. 1996. *Magnetic Stratigraphy*. New York: Academic Press.

Palin, R.M., Santosh, M., Cao, W., Li, S.S., Hernández-Uribe, D., Parsons, A. 2020. Secular change and the onset of plate tectonics on Earth. *EarthScience Reviews*, 207, p.103172.

Parés, J.M., van der Pluijm, B.A., Dinarès-Turell, J., 1999. Evolution of magnetic fabrics during incipient deformation of mudrocks (Pyrenees, northern Spain). *Tectonophysics*, 307(1-2), 1-14.

Parés, J.M., 2015. Sixty years of anisotropy of magnetic susceptibility in deformed sedimentary rocks. *Frontiers in Earth Science*, 3, 4.

Paulsen, T., Deering, C., Sliwinski, J., Bachmann, O., Guillong, M., 2017. Evidence for a spike in mantle carbon outgassing during the Ediacaran period. *Nature Geoscience*, 10(12), 930-934.

Pavlov, V., and Gallet, Y. 2001. Middle Cambrian high magnetic reversal frequency (Kulumbe River section, northwestern Siberia) and reversal behaviour during the Early Palaeozoic. *Earth Planetary Science Letters*, 185, p. 173-183.

Paytan, A., Kastner, M., Martin, E. E., Macdougall, J. D., Herbert, T., 1993. Marine barite as a monitor of seawater strontium isotope composition. *Nature*, 366(6454), 445-449.

Paytan, A., Mearon, S., Cobb, K., Kastner, M., 2002. Origin of marine barite deposits: Sr and S isotope characterization. *Geology* 30, 747–750.

Pisarevsky, S.A., McCausland, P.J., Hodych, J.P., O'Brien, S.J., Tait, J.A., Murphy, J.B. 2012. Paleomagnetic study of the late Neoproterozoic Bull Arm and Crown Hill formations (Musgravetown Group) of eastern Newfoundland: implications for Avalonia and West Gondwana paleogeography. *Canadian Journal of Earth Sciences*, 49(1), pp.308-327.

Plotnick, R.E., Dornbos, S.Q., Chen, J. 2010. Information landscapes and sensory ecology of the Cambrian Radiation. *Paleobiology*, 36(2), pp.303-317.

Poch, R.M., Artieda, O., Herrero, J., Lebedeva-Verba, M., 2010. Gypsic Features. In: *Interpretation of Micromorphological Features of Soils and Regoliths*, pp. 195–216.

Poiré, D.G., 1987. *Mineralogía y sedimentología de la Formación Sierras Bayas en el Núcleo Septentrional de las sierras homónimas, partido de Olavarría, provincia de Buenos Aires*. Unpublised PhD Tesis 494, Facultad de Ciencias Naturales y Museo, Universidad Nacional de La Plata, 271 pp.

Poiré, D.G., 1993. *Estratigrafía del Precámbrico sedimentario de Olavarría, Sierras Bayas, Provincia de Buenos Aires, Argentina*. XII Congreso Geológico Argentino y II Congreso de Exploración de Hidrocarburos Actas II, pp. 1–11.

Poiré, D.G., and Spalletti, L.A., 2005. La cubierta sedimentaria precámbrica/paleozoica inferior del Sistema de Tandilia. In: De Barrio, R.E., Etcheverry, R.O., Caballé, M.F., Llambías, E.J. (Eds.), *Geología y Recursos Minerales de la provincia de Buenos Aires. Relatorio del XVI Congreso Geológico Argentino*, pp. 51–68.

Poiré D.G., Gaucher, C., Germs, G., 2007. La superficie ‘Barker’ y su importancia regional, Neoproterozoico del Cratón del Río de La Plata. VI Jornadas Geológicas y Geofísicas Bonaerenses. *Actas 36. Mar del Plata, Argentina*.

Poiré, D., and Gaucher, C., 2007. Lithostratigraphy and correlations of two Neoproterozoic basins from the Río de la Plata Craton, SW Gondwana. En: III Symposium on neoproterozoic-early palaeozoic events in Southwestern Gondwana, Programme and Short Papers, Stellenbosch, 23–27.

Poiré, D., and Gaucher, C., 2009. Lithostratigraphy. Neoproterozoic- Cambrian evolution of the Río de la Plata Palaeocontinent. En: Gaucher C., Sial, A.N., Halverson, G.P., Frimmel, H.E. (Eds), *Neoproterozoic–Cambrian Tectonics, Global Change and Evolution: a focus on southwestern Gondwana. Developments in Precambrian Geology*, 16, 87–101.

Poiré, D.G., Peral, L.E.G., Arrouy, M.J., 2018. The Glaciations in South America. En: Siegesmund, S., Basei, M.A.S., Oyhantçabal, P., Oriolo, Sebastián (Eds.), *Geology of Southwest Gondwana, Regional Geology Reviews*. Springer International Publishing, Cham, 527-541.

Porter, S. M., & Knoll, A. H. 2000. Testate amoebae in the Neoproterozoic Era: evidence from vase-shaped microfossils in the Chuar Group, Grand Canyon. *Paleobiology*, 26(3), 360-385.

Pratt, B.R., 1982. Stromatolite decline - a reconsideration. *Geology* 10, 512 – 515.

Pratt, B.R., 2010. Peritidal carbonates. In: James NP, Dalrymple RW (eds) *Facies models 4. GEOText6*, Geological Association of Canada, pp 401–420.

Prince, J.K.G., Rainbird, R.H. Wing, B.A., 2019. Evaporite deposition in the mid-Neoproterozoic as a driver for changes in seawater chemistry and the biogeochemical cycle of sulfur. *Geology*, 47, 375–379, <https://doi.org/10.1130/G45464.1>.

Pruss, S. B., Finnegan, S., Fischer, W. W., Knoll, A. H. 2010. Carbonates in skeleton-poor seas: new insights from Cambrian and Ordovician strata of Laurentia. *Palaios*, 25(2), 73-84.

Pu, J. P., Bowring, S. A., Ramezani, J., Myrow, P., Raub, T. D., Landing, E., Mills, A., Hodgin, E., Macdonald, F. A., 2016. Dodging snowballs: Geochronology of the Gaskiers glaciation and the first appearance of the Ediacaran biota. *Geology*, 44, 955-958.

Pufahl, P.K. and Hiatt, E.E. 2012. Oxygenation of the Earth's atmosphere–ocean system: a review of physical and chemical sedimentologic responses. *Marine and Petroleum Geology*, 32(1), pp.1-20.

Quijada, I.E., Benito, M.I., Suarez-Gonzalez, P., Rodríguez-Martínez, M., Campos-Soto, S., 2020. Challenges to carbonate-evaporite peritidal facies models and cycles: insights from Lower Cretaceous stromatolite-bearing deposits (Oncala Group, N Spain). *Sedimentary Geology*, 408, 105752.

Rapalini, A.E., 2006. New late Proterozoic paleomagnetic pole for the Rio de la Plata craton: Implications for Gondwana. *Precambrian Research*, 147, 223–233.

Rapalini, A.E. and Sánchez Bettucci, L., 2008. Widespread remagnetization of late Proterozoic sedimentary units of Uruguay and the apparent polar wander path for the Rio de La Plata craton. *Geophysical Journal International*, 174, 55–74.

Rapalini, A.E., Trindade, R.I., Poiré, D.G. 2013. The La Tinta pole revisited: paleomagnetism of the Neoproterozoic Sierras Bayas Group (Argentina) and its implications for Gondwana and Rodinia. *Precambrian Research*, 224, 51-70.

Rapalini, A.E., Tohver, E., Bettucci, L.S., Lossada, A.C., Barcelona, H., Pérez, C. 2015. The late Neoproterozoic Sierra de las Ánimas Magmatic Complex and Playa Hermosa Formation, southern Uruguay, revisited: Paleogeographic implications of new paleomagnetic and precise geochronologic data. *Precambrian Research*, 259, 143-155.

Rapalini, A.E., 2018. The Assembly of Western Gondwana: Reconstruction Based on Paleomagnetic Data. In: Siegesmund, S., Basei, M.A.S., Oyhantçabal, P., Oriolo, Sebastián (Eds.), *Geology of Southwest Gondwana. Regional Geology Reviews*, Springer International Publishing, Cham, 3-18.

Rapalini, A. E., Franceschinis, P. R., Bettucci, L. S., Arrouy, M. J., Poiré, D. G., 2021. The Precambrian drift history and paleogeography of Río de la Plata craton. In: Pesonen, L.J., Salminen, J., Sten-Åke, E., Evans, D., Veikkolainen, T. (Eds.), *Ancient Supercontinents and the Paleogeography of Earth*. Elsevier, pp. 243-261.

Rapela, C.W., Pankhurst, R.J., Casquet, C., Fanning, C.M., Baldo, E.G., González-Casado, J.M., Galindo, C., Dahlquist, J., 2007. The Río de La Plata craton and the assembly of sw gondwana. *Earth Sci. Rev.* 83, 49–82.

Reuschel, M., Melezhik, V., Whitehouse, M., Lepland, A., Fallick, A., Strauss, H. 2012. Isotopic evidence for a sizeable seawater sulfate reservoir at 2.1 Ga. *Precambrian Research*, 192, 78–88, <https://doi.org/10.1016/j.precamres.2011.10.013>.

Roberts, A. P., Chang, L., Heslop, D., Florindo, F., Larrasoaña, J. C., 2012. Searching for single domain magnetite in the “pseudo-single-domain” sedimentary haystack: Implications of biogenic magnetite preservation for sediment magnetism and relative paleointensity determinations. *Journal of Geophysical Research: Solid Earth*, 117.

Robert, B., Besse, J., Blein, O., Greff-Lefftz, M., Baudin, T., Lopes, F., Meslouh, S., Belbadaoui, M., 2017. Constraints on the Ediacaran inertial interchange true polar wander hypothesis: A new paleomagnetic study in Morocco (West African Craton). *Precambrian Research*, 295, 90–116.

Robert, B., Greff-Lefftz, M., Besse, J., 2018. True polar wander: A key indicator for plate configuration and mantle convection during the late Neoproterozoic. *Geochemistry, Geophysics, Geosystems*, 19, 3478-3495.

Roberts, A.P., 1995. Magnetic characteristics of sedimentary greigite (Fe<sub>3</sub>S<sub>4</sub>), *Earth Planet. Sci. Lett.*, 134, 227–236.

Roberts, A.P., Cui Y., Verosub K.L. 1995. Wasp-waisted hysteresis loops: mineral magnetic characteristics and discrimination of components in mixed magnetic systems. *J. Geophys. Res.* 100, 17909-17924.

Roberts, A. P., Florindo, F., Villa, G., Chang, L., Jovane, L., Bohaty, S. M., Larrasoaña, J.C., Heslop, D., Gerald, J. D. F., 2011. Magnetotactic bacterial abundance in pelagic marine environments is limited by organic carbon flux and availability of dissolved iron. *Earth and Planetary Science Letters*, 310, 441-452.

- Roberts, A.P., Chang, L., Rowan, C.J., Horng, C.S., Florindo, F., 2011. Magnetic properties of sedimentary greigite (Fe<sub>3</sub>S<sub>4</sub>): An update. *Reviews of Geophysics*, 49(1).
- Roberts, A.P., Florindo, F., Chang, L., Heslop, D., Jovane, L., Larrasoana, J.C., 2013. Magnetic properties of pelagic marine carbonates. *Earth-science reviews*, 127, 111-139.
- Roberts, A. P., Heslop, D., Zhao, X., Pike, C. R., 2014. Understanding fine magnetic particle systems through use of first-order reversal curve diagrams. *Reviews of Geophysics*, 52, 557-602.
- Rochette, P., Jackson, M., Aubourg, C., 1992. Rock magnetism and the interpretation an isotropy of magnetic susceptibility. *Reviews of Geophysics*, 30, 209–226.
- Rodriguez-Navarro, C., Jimenez-Lopez, C., Rodriguez-Navarro, A., Gonzalez-Muñoz, M.T., Rodríguez-Gallego, M., 2007. Bacterially mediated mineralization of vaterite. *Geochim. Cosmochim. Acta* 71:1197–1213
- Rooney, A.D., Cantine, M.D., Bergmann, K.D., Gómez-Pérez, I., Al Baloushi, B., Boag, T.H., Busch, J.F., Sperling, E.A., Strauss, J.V. 2020. Calibrating the coevolution of Ediacaran life and environment. *Proceedings of the National Academy of Sciences*, 117(29), pp.16824-16830.
- Rothman, D.H., Hayes, J.M., Summons, R.E. 2003. Dynamics of the Neoproterozoic carbon cycle: *National Academy of Sciences Proceedings*, v. 100, p. 8124–8129.
- Sagnotti, L., and Winkler, A., 1999. Rock magnetism and palaeomagnetism of greigite-bearing mudstones in the Italian peninsula, *Earth Planet. Sci. Lett.*, 165, 67–80.
- Sanchez-Navas, A., Martín-Algarra, A., Rivadeneyra, M.A., Melchor, S., Martín-Ramos, J. D., 2009. Crystal-growth behavior in Ca-Mg carbonate bacterial spherulites. *Cryst. Growth Des.* 9 (6), 2690–2699.
- Sawaki, Y., Ohno, T., Tahata, M., Komiya, T., Hirata, T., Maruyama, S., Windley, B.F., Han, J., Shu, D., Li, Y. 2010. The Ediacaran radiogenic Sr isotope excursion in the Doushantuo Formation in the three Gorges area, South China. *Precambrian Research*, 176(1-4), pp.46-64.
- Schieber, J. 1999. Microbial mats in terrigenous clastics; the challenge of identification in the rock record. *Palaios*, 14(1), 3-12.
- Schieber, J., Bose, P. K., Eriksson, P. G., Banerjee, S., Sarkar, S., Altermann, W., & Catuneanu, O. (Eds.). 2007. *Atlas of microbial mat features preserved within the siliciclastic rock record*. Elsevier.
- Schmidt, P.W., & Williams, G.E., 2010. Ediacaran palaeomagnetism and apparent polar wander path for Australia: no large true polar wander. *Geophysical Journal International*, 182(2), 711-726.
- Schrag, D.P., Higgins, J.A., Macdonald, F.A., Johnston, D.T., 2013. Authigenic carbonate and the history of the global carbon cycle. *science*, 339(6119), 540-543.
- Schreiber, B. C., Friedman, G. M., Decima, A., & Schreiber, E., 1976. Depositional environments of Upper Miocene (Messinian) evaporite deposits of the Sicilian Basin. *Sedimentology*, 23(6), 729-760.
- Schreiber, B.C., 1988. Subaqueous evaporite deposition. In: B.C. Schreiber (Editor), *Evaporites and Hydrocarbons*. Columbia Univ. Press, New York, pp. 182-255.

Schreiber, B.C., and El Tabakh, M., 2000. Deposition and early alteration of evaporites [Review]: *Sedimentology*, v. 47, p. 215–238.

Schröder, S., Bekker, A., Beukes, N.J., Strauss, H. and Van Niekerk, H.S. 2008. Rise in seawater sulphate concentration associated with the Paleoproterozoic positive carbon isotope excursion: evidence from sulphate evaporites in the ~2.2–2.1 Gyr shallow-marine Lucknow Formation, South Africa. *Terra Nova*, 20, 108–117, <https://doi.org/10.1111/j.1365-3121.2008.00795.x>.

Scotese, C.R., Song, H., Mills, B.J. and van der Meer, D.G., 2021. Phanerozoic paleotemperatures: The earth's changing climate during the last 540 million years. *Earth-Science Reviews*, 215, p.103503.

Seilacher, A., and Pflüger, F. 1994. From biomats to benthic agriculture: a biohistoric revolution: Krumbein, W.E., Paterson, D.M., and Stal, L.J., eds., *Biostabilization of Sediments: Bibliotheks- und Informationssystem der Universität Oldenburg*, p. 97–105.

Seilacher, A. 1999. Biomat-related lifestyles in the Precambrian. *Palaios*, 14(1), 86-93.

Shatsillo, A.V., Kuznetsov, N.B., Fedonkin, M.A., Priyatkina, N.S., Serov, S.G. 2015. First magnetostratigraphic data for the stratotype of the Upper Neoproterozoic Lopata Formation (the north east Yenisei Ridge): problems of its age and paleogeography of the Siberian Platform at the boundary of the Phanerozoic and Proterozoic. *Dokl. Earth Sci.*, 465:121-124.

Shcherbakova, V.V., Bakhmutov, V.G., Thallner, D., Shcherbakov, V.P., Zhidkov, G.V., Biggin, A.J. 2020. Ultra-low palaeointensities from East European Craton, Ukraine support a globally anomalous palaeomagnetic field in the Ediacaran. *Geophysical Journal International*, 220(3), pp.1928-1946.

Shi, W., Li, C., Luo, G., Huang, J., Algeo, T. J., Jin, C., ... & Cheng, M. 2018. Sulfur isotope evidence for transient marine-shelf oxidation during the Ediacaran Shuram Excursion. *Geology*, 46(3), 267-270.

Shields, G. A., Carden, G.A., Veizer, J., Meidla, T., Rong, J.Y., Li, R.Y., 2003. Sr, C, and O isotope geochemistry of Ordovician brachiopods: A major isotopic event around the Middle-Late Ordovician transition. *Geochimica et Cosmochimica Acta*, 67(11), 2005-2025.

Shields, G.A., Mills, B.J.W., Zhu, M., Raub, T.D., Daines, S.J. and Lenton, T.M. 2019. Unique Neoproterozoic carbon isotope excursions sustained by coupled evaporite dissolution and pyrite burial. *Nature Geoscience*, 12, 823–827.

Shinn, E.A., 1968. Practical significance of birdseye structures in carbonate rocks. *Journal of Sedimentary Research*, 38, 215–223.

Shinn, E.A., 1983a. Tidal flat environment. In: *Carbonate Depositional Environments* (Ed. by P.A. Scholle, O.O. Bebout and C.H. Moore) *Met. At. Ass. petrol. Geol.* 33, 173-210.

Shinn, E. A., 1983b. Birdseyes, fenestrae, shrinkage pores, and loferites; a reevaluation: *Journal of Sedimentary Petrology*, v. 53, p. 619–628.

Shinn, E.A., 1986. Modern carbonate tidal flats: their diagnostic features. *Quart. J. Colorado Sch. Mines* 81, 7-35.

Sial, A.N., Gaucher, C., Misi, A., Boggiani, P.C., Alvarenga, C.J.S.D., Ferreira, V.P., Pimentel, M.M., Pedreira, J.A., Warren, L.V., Fernández-Ramírez, R., Geraldés, M., 2016. Correlations of some Neoproterozoic carbonatedominated successions in South America based on high-resolution chemostratigraphy. *Brazilian Journal of Geology*, 46, pp.439-488.

Smith, E. F., Macdonald, F. A., Petach, T. A., Bold, U., Schrag, D. P., 2016. Integrated stratigraphic, geochemical, and paleontological late Ediacaran to early Cambrian records from southwestern Mongolia. *Bulletin*, 128, 442-468.

Sperling, E. A., Wolock, C. J., Morgan, A. S., Gill, B. C., Kunzmann, M., Halverson, G. P., Macdonald, F.A., Knoll, A.H., Johnston, D. T., 2015. Statistical analysis of iron geochemical data suggests limited late Proterozoic oxygenation. *Nature*, 523, 451-454.

Sullivan, L. A., & Koppi, A. J. (1993). Barite pseudomorphs after lenticular gypsum in a buried soil from central Australia. *Soil Research*, 31(4), 393-396.

Sumner, D.Y., and Grotzinger, J.P., 2000. Late Archean aragonite precipitation: petrography, facies associations, and environmental significance. In: *Carbonate Sedimentation and Diagenesis in the Evolving Precambrian World* (Eds J.P. Grotzinger and N.P. James), SEPM Spec. Publ., 67, 123–144.

Sumner, D.Y., and Grotzinger, J.P., 2004. Implications for Neoproterozoic ocean chemistry from primary carbonate mineralogy of the Campbellrand-Malmani Platform, South Africa. *Sedimentology*, 51, 1273–1299.

Swart, P.K., and Eberli, G., 2005. The nature of the  $\delta^{13}\text{C}$  of periplatform sediments: Implications for stratigraphy and the global carbon cycle. *Sedimentary Geology*, 175(1-4), 115-129.

Tahata, M., Ueno, Y., Ishikawa, T., Sawaki, Y., Murakami, K., Han, J., ... & Komiya, T. 2013. Carbon and oxygen isotope chemostratigraphies of the Yangtze platform, South China: decoding temperature and environmental changes through the Ediacaran. *Gondwana Research*, 23(1), 333-353.

Tan, X., Kodama, K.P., 2002. Magnetic anisotropy and paleomagnetic inclination shallowing in red beds: Evidence from the Mississippian Mauch Chunk Formation, Pennsylvania. *Journal of Geophysical Research: Solid Earth*, 107, EPM 9-1-EPM 9-17.

Tarling, D., and Hrouda, F., 1993. *Magnetic anisotropy of rocks*. Springer Science & Business Media.

Tauxe, L., 2005. *Lectures in Paleomagnetism*. Electronic version, pp 341.

Teixeira, W., Iacumin, M., Piccirillo, E.M., Echeveste, H., Ribot, A., Fernandez, R., Renne, P.R., Heaman, L.M., 2002. Calc-alkaline and tholeiitic dyke swarms of Tandilia, Rio de la Plata craton, Argentina: U-Pb, Sm-Nd and Rb-Sr  $^{40}\text{Ar}/^{39}\text{Ar}$  data provide new clues for intraplate rifting shortly after the Trans-Amazonian orogeny. *Precambrian Research*, 119, 329-353.

Teixeira, W., D'Agrella Filho, M.S., Hamilton, M.A., Ernst, R.E., Girardi, V.A.V., Mazzucchelli, M., Bettencourt, J.S., 2013. U-Pb (ID-TIMS) baddeleyite ages and paleomagnetism of 1.79 and 1.59 Ga tholeiitic dyke swarms, and position of the Rio de la Plata Craton within the Columbia supercontinent. *Lithos*, 174, 157–174.

Thallner, D., Biggin, A. J., Halls, H. C., 2021. An extended period of extremely weak geomagnetic field suggested by palaeointensities from the Ediacaran Grenville dykes (SE Canada). *Earth and Planetary Science Letters*, 568, 117025.

Tohver, E., D'Agrella-Filho, M.S.D., Trindade, R.I.F., 2006. Paleomagnetic record of Africa and South America for the 1200–500 Ma interval, and evaluation of Rodinia and Gondwana assemblies. *Precambrian Research*, 147, 193–222.

Tohver, E., Cawood, P.A., Rossello, E.A., Jourdan, F., 2012. Closure of the Clymene Ocean and formation of West Gondwana in the Cambrian: evidence from the Sierras Australes of the southernmost Rio de la Plata craton, Argentina. *Gondwana Research*, 21(2-3), 394-405.

Tohver, E., Trindade, R. I., 2014. Comment on “Was there an Ediacaran Clymene Ocean in central South America?” by UG Cordani and others. *American Journal of Science*, 314, 805-813.

Torsvik, T.H., Van der Voo, R., Preeden, U., Mac Niocaill, C., Steinberger, B., Doubrovine, P. V., van Hinsbergen, D.J.J., Domeier, M., Gaina, C., Tohver, E., Meert, J.G., McCausland, P.J.A., Cocks, L.R.M., 2012. Phanerozoic Polar Wander, *Palaeogeography and Dynamics*. *Earth-Science Review*, 114, 325–368.

Tosca, N.J., and Wright, V.P., 2018. Diagenetic pathways linked to labile Mg-clays in lacustrine carbonate reservoirs: a model for the origin of secondary porosity in the Cretaceous pre-salt Barra Velha Formation, offshore Brazil. In: Armitage, P.J., Butcher, A.R., Churchill, J.M., Csoma, A.E., Hollis, C., Lamder, R.H., Omma, J.E. and Worden, R.H. (Eds.) *Reservoir Quality of Clastic and Carbonate Rocks: Analysis, Modelling and Prediction*. Geological Society, London, Special Publications, 435, 33-46

Trindade, R.I.F., D'Agrella Filho, M.S., Epof, I., Brito-Neves, B.B., 2006. Paleomagnetism of Early Cambrian Itabaiana mafic dikes (NE Brazil) and the final assembly of Gondwana. *Earth Planetary Science Letters*, 244, 361–377.

Tucker, M. E., 1976. Replaced evaporites from the late Precambrian of Finnmark, Arctic Norway: *Sedimentary Geology*, v. 16, p. 193–204.

Tucker, M., 1988. *Techniques in Sedimentology*. Blackwell Scientific Publications, Oxford, 394 p.

Tucker, M.E., and Wright, V.P., 1990. *Carbonate Sedimentology*. Blackwell, Oxford, 482p.

Tucker, M.E. 2001. *Sedimentary Petrology*. 3rd Edition, Blackwell Science, Oxford, 262p.

Valencio, D.A., Sinito, A.M., Vilas, J.F., 1980. Palaeomagnetism of Upper Precambrian rocks of the La Tinta Formation, Argentina. *Geophysical Journal of the Royal Astronomical Society*, 62, 563-575.

Veizer, J., 1983. Chemical diagenesis of carbonates: Theory and application, in Arthur, M., Veizer, J., and Land, L., eds., *Stable isotopes in sedimentary geology: SEPM Short Course*, v. 10, p. 3.1-3.100.

Veizer, J., and Prokoph, A., 2015. Temperatures and oxygen isotopic composition of Phanerozoic oceans. *Earth-Science Reviews*, 146, 92-104.

Verrecchia, E.P., Freytet, P., Verrecchia, K.E., Dumont, J.L., 1995. Spherulites in calcrete laminar crusts; biogenic CaCO<sub>3</sub> precipitation as a major contributor to crust formation. *J. Sediment. Res.* 65 (4a), 690–700.

- Verwey, E.J.W., 1939. Electronic conduction of magnetite (Fe<sub>3</sub>O<sub>4</sub>) and its transition point at low temperatures. *Nature*, 144, 327–328.
- Waggoner, B., 2003. The Ediacaran Biotas in space and time. *Integr. Comp. Biol.* 43: 104-113.
- Walker, R.G., (Ed) 1984. *Facies Models*. Geosci. Can. Reprint Ser., 1. Geol. Soc. Can., Waterloo, Ontario. 1.1
- Walz, F., 2002. The Verwey transition—a topical review. *Journal of Physics: Condensed Matter*, 14, R285.
- Warren, J. K. (1983). Tepees, modern (southern Australia) and ancient (Permian—Texas and New Mexico)—a comparison. *Sedimentary Geology*, 34(1), 1-19.
- Warren, J.K., 1982. The Hydrological setting, occurrence, and significance of gypsum in late Quaternary salt lakes in South Australia. *Sedimentology*, 24: 609-637.
- Warren, J.K., 1991. Sulfate Dominated Sea-Marginal and Platform Evaporative Settings: Sabkhas and Salinas, Mudflats and Salterns. In *Developments in Sedimentology* (Vol. 50, pp. 69-187). Elsevier.
- Warren, J.K., 2010. Evaporites through time: Tectonic, climatic and eustatic controls in marine and nonmarine deposits. *Earth-Science Reviews*, 98(3-4), 217-268.
- Warren, J.K., 2016. *Evaporites: A geological compendium*. Springer.
- Warren, J.K. 2021. Evaporite deposits. In: Alderton, D. and Elias, S.A. (eds). *Encyclopedia of Geology* (Second Edition). Academic Press, Oxford, 945–977, <https://doi.org/10.1016/B978-0-08-102908-4.00165-X>.
- Warren, J.K., and Kendall, C.G.St.C., 1985. Comparison of sequences formed in marine sabkha (subaerial) and salina (subaqueous) settings—modern and ancient. *Am. Assoc. Pet. Geol. Bull.*, 69 (6): 1013-1023.
- Warren, L.V., Simões, M.G., Fairchild, T.R., Riccomini, C., Gaucher, C., Anelli, L.E., Freitas, B.T., Boggiani, P.C., Quaglio, F. 2013. Origin and impact of the oldest metazoan bioclastic sediments. *Geology*, 41(4), pp.507-510.
- Warren, L. V., Quaglio, F., Riccomini, C., Simões, M. G., Poiré, D. G., Strikis, N. M., Anelli, L.E., Strikis, P. C., 2014. The puzzle assembled: Ediacaran guide fossil *Cloudina* reveals an old proto-Gondwana seaway. *Geology*, 42, 391-394.
- Wei, W., Zeng, Z., Shen, J., Tian, L.L., Wei, G.Y., Ling, H.F., Huang, F., 2021. Dramatic changes in the carbonate-hosted barium isotopic compositions in the Ediacaran Yangtze Platform. *Geochimica et Cosmochimica Acta*, 299, 113-129.
- Weil, A.B., and Yonkee, A., 2009. Anisotropy of magnetic susceptibility in weakly deformed red beds from the Wyoming salient, Sevier thrust belt: Relations to layer-parallel shortening and orogenic curvature. *Lithosphere*, 1(4), 235-256.
- Widanagamage, I.H., Waldron, A.R., Glamoclija, M., 2018. Controls on barite crystal morphology during abiotic precipitation. *Minerals*, 8(11), 480.
- Witkosky, R. and Wernicke, B.P. 2018. Subsidence history of the Ediacaran Johnnie Formation and related strata of southwest Laurentia: Implications for the age and duration of the Shuram isotopic excursion and animal evolution. *Geosphere*, 14(5), pp.2245-2276.

Wood, R.A. 2011. Paleocology of the earliest skeletal metazoan communities: implications for early biomineralization. *Earth-Science Reviews*, 106(1-2), pp.184-190.

Wood, R.A., Poulton, S.W. et al. 2015. Dynamic redox conditions control late Ediacaran metazoan ecosystems in the Nama Group, Namibia. *Precambrian Research*, 261, 252–271.

Wood, R. and Penny, A. 2018. Substrate growth dynamics and biomineralization of an Ediacaran encrusting poriferan. *Proceedings of the Royal Society B: Biological Sciences*, 285(1870), p.20171938.

Wood, R., Liu, A.G., Bowyer, F., Wilby, P.R., Dunn, F.S., Kenchington, C.G., Cuthill, J.F.H., Mitchell, E.G. and Penny, A., 2019. Integrated records of environmental change and evolution challenge the Cambrian Explosion. *Nature ecology & evolution*, 3(4), pp.528-538.

Wright, V.P., 1984. Peritidal carbonate facies models: a review. *Geological Journal*, 19(4), 309-325.

Xiao S., Narbonne G.M., Zhou C., Laflamme M., Grazhdankin D.V., Vidal M.M, Cui H. 2016. Towards an Ediacaran Time Scale: Problems, Protocols, and Prospects. *Episodes*; 39:540-555.

Xiao, S.H. and Narbonne, G.M., 2020. The Ediacaran Period. In *Geologic time scale 2020* (pp. 521-561). Elsevier.

Xiao, S., Knoll, A.H., Kaufman, A.J., Yin, L., Zhang, Y., 1997. Neoproterozoic fossils in Mesoproterozoic rocks? Chemostratigraphic resolution of a biostratigraphic conundrum from the North China Platform. *Precambrian Research*, 84(3-4), 197-220.

Zhou, C. and Xiao, S., 2007. Ediacaran  $\delta^{13}\text{C}$  chemostratigraphy of South China. *Chemical Geology*, 237(1-2), pp.89-108.

Yang, C., Rooney, A.D., Condon, D.J., Li, X.H., Grazhdankin, D.V., Bowyer, F.T., ... & Zhu, M., 2021. The tempo of Ediacaran evolution. *Science advances*, 7(45).

Yang, T., Zhao, X., Petronotis, K., Dekkers, M.J., and Xu, H., 2019. Anisotropy of magnetic susceptibility (AMS) of sediments from Holes U1480E and U1480H, IODP Expedition 362: sedimentary or artificial origin and implications for paleomagnetic studies. *Geochemistry, Geophysics, Geosystems*, 20(11), 5192-5215.

Yuan, W., Zhou, H., Yang, Z., Hein, J. R., Yang, Q., 2019. Magnetite magnetofossils record biogeochemical remanent magnetization in hydrogenetic ferromanganese crusts. *Geology*, 48, 298-302.

Zhang, F., Xiao, S. et al. 2019. Global marine redox changes drove the rise and fall of the Ediacara biota. *Geobiology*, 17, 594–610.

Zhou, C., Xiao, S., Wang, W., Guan, C., Ouyang, Q., Chen, Z. 2017. The stratigraphic complexity of the middle Ediacaran carbon isotopic record in the Yangtze Gorges area, South China, and its implications for the age and chemostratigraphic significance of the Shuram excursion. *Precambrian Research*, 288, pp.23-38.

Zhu, M.Y., Babcock, L.E., Peng, S.C. 2006. Advances in Cambrian stratigraphy and paleontology: integrating correlation techniques, paleobiology, taphonomy and paleoenvironmental reconstruction. *Palaeoworld*, 15(3-4), pp.217-222.

Zhu, M., Lu, M., Zhang, J., Zhao, F., Li, G., Aihua, Y., Zhao, X., Zhao, M. 2013. Carbon isotope chemostratigraphy and sedimentary facies evolution of the Ediacaran Doushantuo Formation in western Hubei, South China. *Precambrian research*, 225, pp.7-28

Zijderveld, J.D.A. 1967. AC Demagnetization of Rocks: Analysis of Results. In: Runcorn, S.K., Creer, K.M. and Collinson, D.W., Eds., *Methods in Palaeomagnetism*, Elsevier, Amsterdam, 254-286.

Zimmermann, U., and Spalletti, L.A. 2009. Provenance of the lower paleozoic balcarce formation (Tandilia System, Buenos Aires Province, Argentina): implications for paleogeographic reconstructions of SW Gondwana. *Sedimentary Geology*, 219(1-4), 7-23.

**Supplementary material 1.** Major elements (Ca, Fe e Mn) and Sr concentrations data of carbonate samples from the Avellaneda Formation.

Sample code	Ca (%)	Fe (%)	Mn (%)	Sr (ppm)
E34-1	68.81	0.53	0.10	287
E34-10	26.27	2.94	0.07	495
E34-11	67.30	0.87	0.18	364
E34-11A	45.33	0.97	0.06	221
E34-12	12.06	3.97	0.09	288
E34-13	13.50	3.83	0.05	310
E34-14	33.63	1.32	0.10	317
E34-15	62.32	0.39	0.12	307
E34-16	6.87	2.80	0.05	311
E34-3	35.05	1.12	0.09	299
E34-4	36.39	1.28	0.09	433
E34-5	40.53	1.73	0.10	353
E34-6	4.57	4.01	0.03	331
E34-7	33.41	2.37	0.09	458
E34-8	48.43	1.43	0.12	453
E34-9	9.85	3.70	0.05	318
E7-11	6.81	4.13	0.02	208
E7-12	37.48	0.89	0.08	277
E7-13	10.76	7.02	0.05	180
E7-14	60.75	0.52	0.13	241
E7-16	28.89	2.03	0.56	132
E7-17	18.05	1.97	0.05	372
E7-18	15.45	2.88	0.05	392
E7-20	17.51	3.17	0.05	329
E7-21	47.96	1.08	0.08	346
E7-22	15.64	3.25	0.08	251
E7-23	50.72	1.25	0.12	416
E7-25	22.55	3.17	0.12	549
E7-26	17.29	3.14	0.11	359
E7-27	0.33	5.39	0.02	166
E7-36	67.23	0.17	0.04	398
E7-37	63.06	0.50	0.07	215
E7-39	17.21	2.99	0.05	402
E7-40	16.03	1.68	0.05	251
E7-41	22.64	1.36	0.07	282
E7-42	49.45	0.75	0.11	302
E7-43	11.52	2.14	0.04	376
E7-44	11.63	0.78	0.03	180
E7-45	15.58	1.90	0.05	379
E7-46	30.56	1.49	0.07	258

E7-47	0.52	3.39	0.04	229
H9-10	19.29	2.20	0.05	417
H9-11	42.32	1.33	0.08	428
H9-12	22.93	2.72	0.06	461
H9-13	30.05	2.63	0.08	438
H9-14	11.83	2.91	0.05	552
H9-15	11.28	3.53	0.05	434
H9-16	18.96	2.46	0.06	385
H9-17	12.43	3.69	0.04	334
H9-18	27.43	1.57	0.06	394
H9-18A	25.03	0.47	0.07	146
H9-20	29.31	1.42	0.11	501
H9-21	13.81	3.90	0.10	324
H9-22	70.78	0.64	0.33	1371
H9-23	19.12	1.33	0.02	275
H9-24	0.23	8.45	0.03	92
H9-25	2.07	2.59	0.02	50
H9-26	0.12	8.11	0.02	80
H9-27	2.13	2.53	0.01	41
H9-28	0.58	7.61	0.05	116
H9-29	0.20	8.65	0.02	82
H9-30	0.11	4.43	0.02	87
H9-31	0.89	0.78	0.01	23
H9-32	0.13	11.61	0.03	86
H9-33	0.10	5.21	0.03	80
H9-36	0.13	4.50	0.02	101
H9-37	0.12	4.67	0.02	86
H9-4	62.67	0.69	0.09	201
H9-5	35.00	0.28	0.05	108
H9-6	4.43	4.35	0.02	175
H9-7	45.15	1.04	0.11	225
H9-8	14.18	2.90	0.05	347
H9-9	65.80	0.50	0.13	240